Nanopore Resistive Sensing: Bridging Theory and Experiments

Martin Charron

Thesis submitted to the University of Ottawa
in partial Fulfillment of the requirements for the
Doctorate in Philosophy Degree in Physics

Ottawa-Carleton Institute for Physics
Department of Physics
Faculty of Science
University of Ottawa

Contents

Summary

Nanopore sensing is a single molecule technique which consists in detecting molecules as they pass through a nanopore, i.e. a nanoscale hole, driven by an electric potential gradient applied across the pore. When in conductive aqueous solutions, the passage of a biomolecule is detected as a transient ionic current blockade, due to translocating molecules momentarily hindering the movement of ions across the pore. The characteristics of the blockade signals (e.g. average or maximum current blockage amplitude, signal duration, sequence of blockade sublevels, etc.) can contain rich information related to the physical and chemical properties of the passing biomolecule. The simplicity by which nanopore sensing operates has resulted in highly successful applications and exciting research endeavors including nucleic acid sequencing.

The application-driven nature of the nanopore sensing field has resulted in a separation between nanopore sensing theory and experiments. The rich physics of the polymer capture and translocation through nanopores has yet to be extensively characterized experimentally. As such, the work in this thesis aims to bridge the gap existing between nanopore theory and experiments by providing new mathematical frameworks by which to analyze and interpret complex nanopore signals, or by providing clear experimental demonstrations of the forces underlying nanopore capture and translocation. Namely, the subjects covered in this thesis either attempt to characterize the electric field inside nanopores and in their vicinity, or attempt to characterize the response of polymers to this field, whether confined inside nanopore during translocation or outside the pore during capture. More precisely, in Chapter 2 a novel framework by which to model the blocked-state access region contributions is introduced. Chapter 3 studies the capture and translocation kinetics in the presence of salt concentration gradients across the nanopore membrane, conditions which allow the non-uniform modulation of the electric field in the nanopore system. Chapter 4

introduces a patterned nanostructure whose blockade signal allows estimating its instantaneous translocation velocity which, accompanied by simple physical insights, allows probing the underlying forces driving and opposing translocation. Lastly, Chapter 5 investigates the folding kinetics of a rigid DNA nanostructure, providing interesting insights into the structure's composition and the role of rigidity on translocation dynamics. The work presented was highly motivated by the core idea that a clearly presented description of the physical principles of nanopore sensing will be greatly beneficial for assisting researchers in designing better experiments, thus enabling the development of more applications.

Sommaire

La détection par nanopore est une technique d'analyse unimoléculaire qui consiste à détecter les molécules passant à travers un nanopore, c'est-à-dire un trou de taille nanométrique, sous l'application d'un gradient de potentiel électrique appliqué à travers le pore. Dans les solutions aqueuses conductrices, le passage d'une biomolécule est détecté en mesurant le blocage transitoire du courant ionique, induit par l'obstruction momentanée du mouvement des ions. Les caractéristiques des signaux de blocage (par exemple, l'amplitude moyenne ou maximale du blocage du courant, la durée du signal, la séquence des sous-niveaux de blocage, etc.) peuvent contenir une grande quantité d'informations liées aux propriétés physiques et chimiques de la molécule passante. La simplicité du fonctionnement de la détection par nanopores a donné lieu à des applications qui ont connu un grand succès et à des projets de recherche prometteurs, notamment le séquençage d'ADN.

Le fait que les travaux dans le domaine de la détection par nanopore se soient tous concentrés sur les applications, a entraîné une séparation entre la théorie décrivant les principes de détection et les observations expérimentales fondamentales pouvant le démontrer. Certains aspects pourtant cruciaux de la physique de la capture et de la translocation des polymères à travers les nanopores n'a pas encore été suffisamment caractérisée expérimentalement. Le travail de cette thèse vise donc à combler le manque existant entre la théorie et les expériences des nanopores en fournissant de nouveaux cadres mathématiques permettant d'analyser et d'interpréter les signaux complexes provenant des nanopores, ainsi qu'en fournissant des démonstrations expérimentales claires des forces sous-jacentes à la capture et à la translocation. Notamment, les sujets abordés dans cette thèse tentent de caractériser le champ électrique à l'intérieur et à l'extérieur des nanopores, et de caractériser la réponse des polymères à ce champ, qu'ils soient confinés à

l'intérieur du nanopore lors de la translocation ou à l'extérieur du pore lors du processus de capture. Plus précisément, le Chapitre 2 présente un nouveau cadre permettant de modéliser les contributions de la région d'accès lorsqu'obstruée par une molécule. Le chapitre 3 étudie la cinétique de capture et de translocation en présence de gradients de concentration de sel à travers la membrane du nanopore, conditions qui permettent une modulation non uniforme du champ électrique. Le chapitre 4 présente une molécule d'ADN nano-structurée dont le signal de blocage permet l'estimation de sa vitesse instantanée de translocation, ce qui, appuyé par des concepts physiques simples, permet de sonder les forces sous-jacentes qui animent le processus de translocation. Enfin, le chapitre 5 étudie la cinétique de pliage d'une nanostructure d'ADN rigide, ce qui offre des indications intéressantes sur la composition de sa structure. Le travail présenté dans cette thèse a été fortement motivé par l'idée fondamentale qu'une description claire des principes physiques de la détection par nanopore sera grandement bénéfique pour aider les chercheurs à concevoir de meilleures expériences, permettant ainsi le développement davantage d'applications.

Acknowledgements

I wish to thank all the members of the T-Cossa and Godin lab who I have crossed paths with throughout the past few years and from who I've learned so much. I owe a great deal to everyone in our lab that has taken time out of their usually busy schedule to lend a hand to troubleshoot experiments or to explain concepts that I could not grasp on my own. Discussing, brainstorming and joking around with all of you was by far the favorite part of my time as a PhD student. That and the huge pile of money I've amassed.

I extend a special thank you to my supervisor, Vincent. I am very grateful for the opportunity you gave me years ago to discover the world of scientific research and all the experiences you have supported since. Ten years after setting foot in your lab, I come out with a head filled with a LOT of nanopore literature, but mostly filled with good memories.

A ma famille et mes amis, merci de toujours me faire sentir intelligent lorsque je me sens stupide, et stupide lorsque je me sens soudainement trop intelligent, mais surtout merci de me faire sentir aimé inconditionnellement, je vous aime.

A Alexandra, l'espace de cette page ne suffit pas pour t'exprimer l'admiration, la gratitude et l'amour que je ressens pour toi. L'idée d'avoir terminé ce long projet et de pouvoir enfin passer plus de temps à tes côtés me remplit de bonheur. Je te promets de te soutenir autant que tu as su le faire lorsque j'en avais tellement de besoin durant les quatre dernières années, et les cinq d'avant aussi, d'ailleurs. Je t'aime, tout simplement.

Cette thèse est dédiée à ma mère, Shirley.

Statement of Originality

The material presented in this thesis results from research performed under the supervision of Dr. Vincent Tabard-Cossa in the Department of Physics at the University of Ottawa.

Chapter 2 contains two closely related articles, [5] and [7], of which I am first author. Both articles comprise a theoretical conductance modeling technique which I have developed on my own. Finite-element simulations were performed by Dr. Zachary Roelen (Postdoctoral Fellow in the T.-Cossa Lab) to validate the model's accuracy. Web-based apps were developed by Deekshant Wadhwa (Computer Science MSc student in the T.-Cossa Lab) to make the intricate equations resulting from the model more approachable to the nanopore community.

Chapter 3 contains the first article I published as a first author as a PhD student.[2] I designed the experiments to be run and performed the experiments and analysis with the help of Lucas Philipp, an undergraduate student (UBC Biophysics) doing a coop work term at the time.

Chapter 4 is a manuscript written as a first author that is submitted, but not yet published.[8] I designed the experiments, and performed most of the experiments and analysis, with Breeana Elliott and Nada Kerrouri, undergraduate (uO Physics) students who helped performing experiments and analyzing data. Preliminary results were achieved with the help of Dr. Liqun He (when he was still a PhD student in the T.-Cossa Lab).

Chapter 5 is a published article, [4] on which I am a co-first author with Dr. Liqun He. My involvement with this project consisted of planning and designing experiments as well as analyzing and interpreting results.

Statement of Contributions

Publications

[1]. L. He, D. Tessier, K. Briggs, M. Tsangaris, **M. Charron,** E. McConnell, D. Lomovtsev & V. Tabard-Cossa. *Digital immunoassay for biomarker concentration quantification using solid-state nanopores.* Nat Commun 12, (2021). https://doi.org/10.1038/s41467-021-25566-8

[2]*. **M. Charron**, L. Philipp, L. He & V. Tabard-Cossa. *Elucidating the dynamics of polymer transport through nanopores using asymmetric salt concentrations*. Nano Res. **15**, 9943–9953 (2022). https://doi.org/10.1007/s12274-022-4886-3

[3]. M. Y. Bouhamidi, D. Lomovtsev, G. Mu, **M. Charron,** M. Waugh, & V. Tabard-Cossa. *Characterizing Surface Charge Density of Solid-State Nanopore Sensors for Improved Biosensing Applications*. in 2023 IEEE Sensors Applications Symposium, SAS 2023 - Proceedings (Institute of Electrical and Electronics Engineers Inc., 2023). doi:10.1109/SAS58821.2023.10254021.

[4]*. L. He,* **M. Charron,*** P. Mensing, K. Briggs, J. Adams, H. de Haan, & V. Tabard-Cossa. *DNA origami characterized via a solid-state nanopore: insights into nanostructure dimensions, rigidity and yield.* Nanoscale 15, 14043–14054 (2023). doi:10.1021/acs.nanolett.3c04997

[5]*. **M. Charron**, Z. Roelen, D. Wadhwa, & V. Tabard-Cossa. Improved Conductance Blockage Modeling of Cylindrical Nanopores, from 2D to Thick Membranes. Nano Lett (2024) doi:10.1021/acs.nanolett.4c02538.

[6]. B. Elliott, **M. Charron,** J. Pezacki, E. McConnell, & V. Tabard-Cossa. Solid-state nanopore counting of amplicons from recombinase polymerase isothermal amplification. Sensors and Diagnostics (2024) doi:10.1039/d4sd00159a.

[7]*. **M. Charron**, Z. Roelen, D. Wadhwa, & V. Tabard-Cossa. *Predicting Resistive Pulse Signatures in Nanopores by Accurately Modeling Access Regions*. (2024). *arXiv preprint arXiv:2411.05589*

[8]*. **M. Charron,** B. Elliott, N. Kerrouri, L. He, & V. Tabard-Cossa. *Velocity fluctuation and force scaling during driven polymer transport through a nanopore*. (2024). *arXiv preprint arXiv:2411.04261*

[9]. P. Mensing, **M. Charron,** M. Y. Bouhamidi & V. Tabard-Cossa. *Folding dynamics of linear ssDNA-dsDNA heterostructures through solid-state nanopores*. To be submitted.

[X]* : Included in the thesis.

Conference Presentations

[10]. **M. Charron,** L. Philipp, K. Briggs & V. Tabard-Cossa. Poster: Optimizing the Sensitivity of Concentration Measurements Using Nanopores in Salt Asymmetry. Biophysical Society, San Diego, February 2020.

[11]. **M. Charron,** L. Philipp, L. He & V. Tabard-Cossa. Virtual Poster: Dynamics of polymer Transport through Nanopores using Asymmetric Salt Concentrations. CECAM Workshop on "Nanopore Translocation and Nanochannel Confined Biopolymers", September 2021.

[12]. **M. Charron,** L. Philipp, B. Elliott & V. Tabard-Cossa. Poster: Experimental Investigation of Field-Driven Polymer Transport Dynamics. Biophysical Society of Canada Annual Meeting, Ottawa, May 2022.

[13]. **M. Charron,** L. Philipp, L. He, P. Mensing, K. Briggs & V. Tabard-Cossa. Talk: Elucidating Transport Dynamics in Solid-State Nanopores. From Solid State to Biophysics, Cavtat, Croatia, June 2022.

[14]. **M. Charron,** B. Elliott, D. Lomovtsev, P. Mensing, E. Majaesic, W. Houry & V. Tabard-Cossa. Poster: High-Bandwidth Temperature Control & Polymer Statistics during Nanopore Sensing. Single-Molecule Protein Sequencing 3, Delft, Netherlands, October 2022.

[15]. **M. Charron,** B. Elliott, L. He, P. Mensing, K. Briggs & V. Tabard-Cossa. Poster: Investigation of Forces Dictating Polymer Translocation through Solid-State Nanopores. Biophysical Society, San Diego, February 2023.

[16]. **M. Charron,** B. Elliott, W. McLeish, P. Mensing & V. Tabard-Cossa. Poster: Experimental Investigation of the Forces Governing DNA and Protein Transport through Nanopores. Black Forest Nanopore Meeting, November 2023.

[17]. **M. Charron** & V. Tabard-Cossa. Experimental Investigation of the Forces Governing DNA Transport through Nanopores. Ottawa-Carleton Institute for Physics, Ottawa, December 2023.

List of Figures

List of Tables

Chapter 1. Introduction

1.1 Nanopore Fundamentals

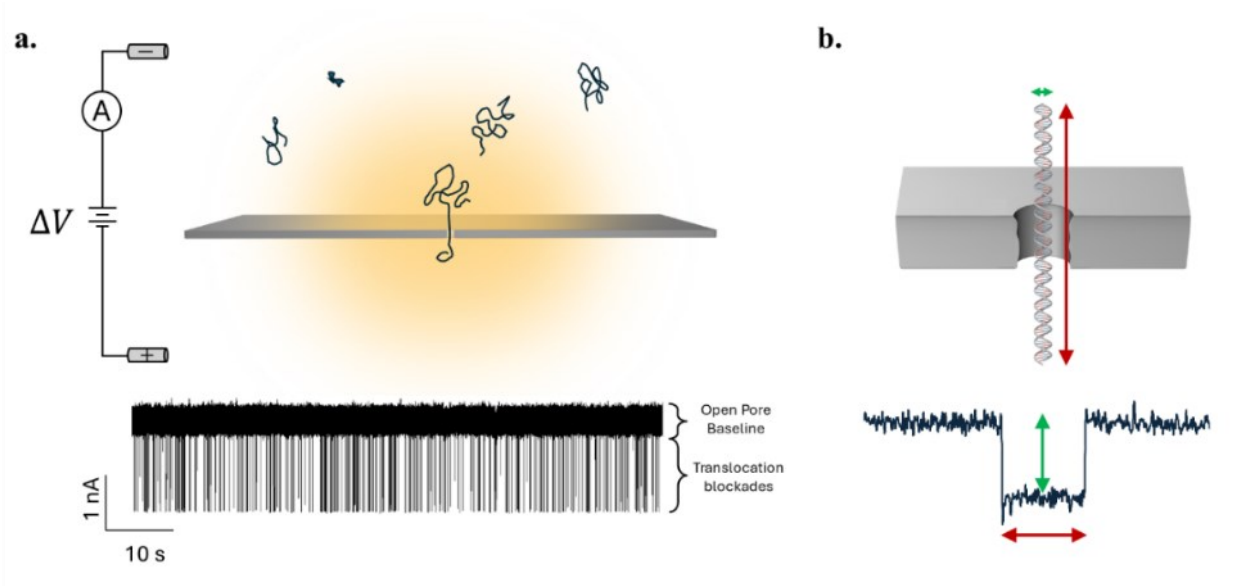

Figure 1.1. Nanopore sensing basics. a) A voltage is applied across a thin pore-containing membrane, creating an ionic current, which is transiently blocked when charged polymers translocate the pore. The yellow hue depicts the electric field in the vicinity of the pore. The current trace shown corresponds to passages of 50 base-pair DNA through a 4 nm wide nanopore. **b)** Characteristics of individual blockage events can be mapped to physical information of translocating molecules.

1.1.1 First Principles

Nanopores are holes of nanoscale dimensions. The passage of biomolecules through nanopores is central to many biological processes such as intercellular membrane transport, and central to highly successful biotechnological applications and research developments.[1–3] Namely, nanopores are commonly used as single-molecule resistive pulse sensors, wherein a pore is housed within an insulating membrane that separates two reservoirs filled with electrically conductive solutions;[4] When a potential difference is applied across the pore-containing membrane, a strong electric field is produced inside the pore and in its vicinity due to its nanoscale constriction, as depicted by the

yellow hue in Figure 1.1a. Under the right polarity, charged species in solution will thus be driven towards the pore, and pass, i.e. translocate, through the pore. When reservoirs contain salt solutions (most commonly KCl, LiCl, and NaCl) dissociated ions from each side of the pore move along or against the field lines and create a steady ionic current through the pore. Charged macromolecules suspended in solutions can also be captured and translocate through pores. The temporary presence of such molecules transiently hinders and reduces the steady ionic passage (Figure 1.1b). As shown in Figure 1.1c, the characterization of such current blockage pulses can give information on the translocating molecules. For instance, the amplitude of the current blockage gives information regarding the molecule's volume or dimensions. Sequences of different blockage sublevels within a single blockade can inform regarding a molecule's conformation or composition, as will be discussed and clarified throughout this thesis.

As summarized in Figure 1.2, there are three broad classes of nanopores: biological, solid-state and hybrid nanopores. Biological pores consist of proteins that spontaneously assemble and insert into lipid bilayers and contain inherent transmembrane channels that are permeable for ions and polymers to pass through.[5,6] Although naturally secreted proteins can be used for resistive sensing, in recent years much progress and effort has gone towards synthesizing proteins of various geometries with specific mutations or newly introduced functional groups that can optimize the passage and analysis of polymers of interest by modulating the pore's electrostatic or steric properties.[7–10] Figure 1.2b shows biological pores that were used in various nanopore sensing experiments.[5] Due to their structure being atomically consistent from one experiment to another, biological pores are the standard for measurement reproducibility and can thus provide ultra-precise measurements of sub-nanometer features of translocating polymers.

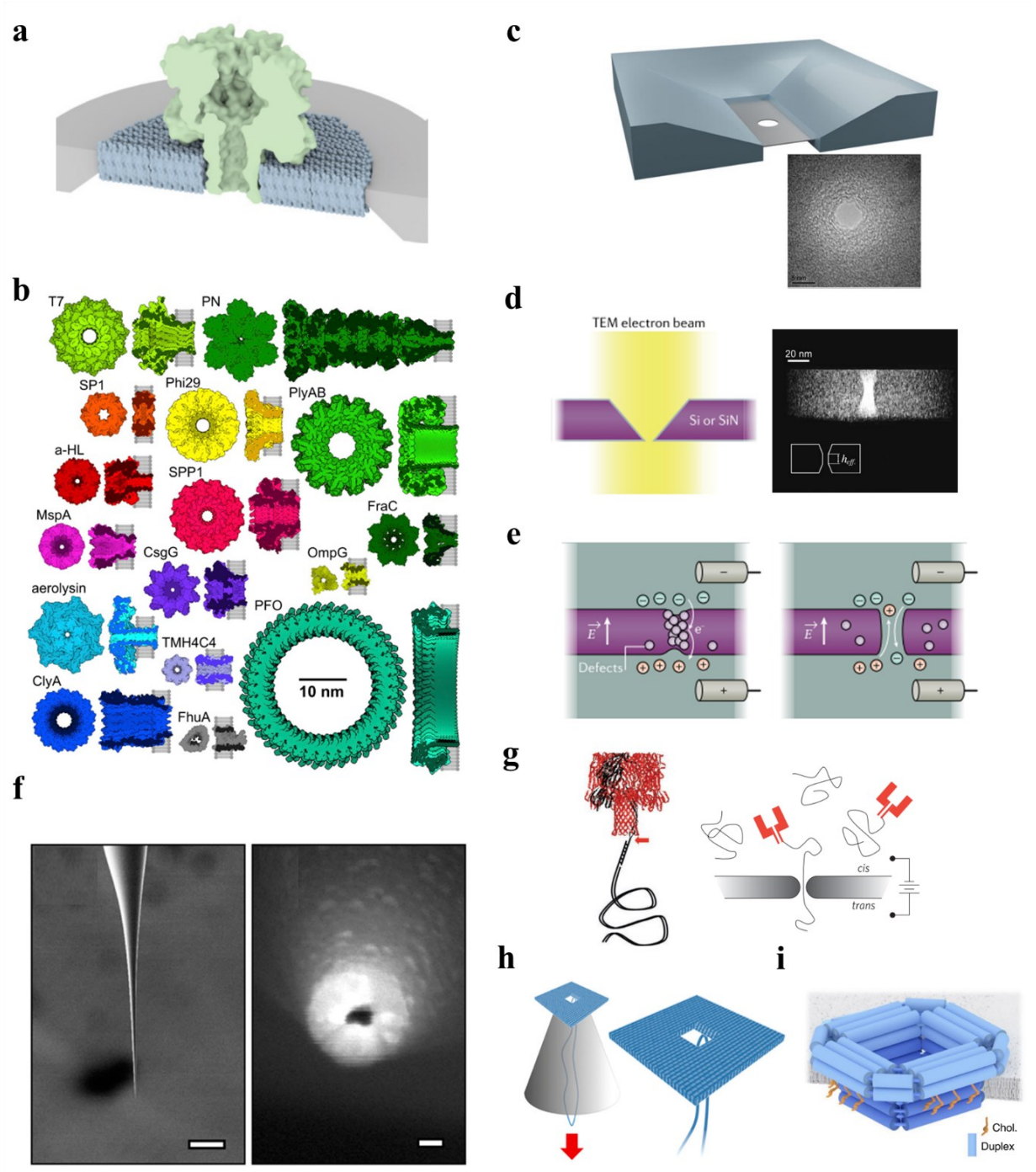

Figure 1.2. Types of nanopores. **a)** Schematic of a biological pore embedded in a lipid bilayer. Reprinted and adapted from Vincent Tabard-Cossa[11], Copyright 2013, with permission from Elviser. **b)** Various biological pores used in nanopore experiments. Adapted with permission from Mayer *et al.*[5] licensed under CC BY-NC-ND 4.0. **c)** Schematic of planar solid-state nanopore membrane setup[12] and TEM image of a pore drilled in SiNx membrane.[13] Adapted with permission from Xing *et al.*[12] licensed under CC BY 4.0, and from IOP Publishing, Ltd, from Lo *et al.*[13]; permission conveyed through Copyright Clearance Center, Inc. **d)** Pore fabrication by focused electron or ion beam.[4] TEM tomography image of nanopores, showing

double-cone structure of a pore fabricated by TEM.[14] Reproduced with permission from Springer Nature and Xue *et al.*[4] and from Kim *et al.* **e)** Pore fabrication by Controlled Dielectric Breakdown.[4,15] Reproduced with permission from Springer Nature and Xue *et al.*[4] **f)** SEM image of a nanopipette tip and of the nanopore at the tip. Left and right scale bars are 250 μm and 25 μm. Adapted with permission from Ivanov *et al*.[16] Copyright 2015 American Chemical Society. **g)** αHL hetero-heptamer with an attached 3 kbp dsDNA electrophoretically inserted through narrow SSNP. Reproduced with permission from Springer Nature and Hall *et al*.[17] **h)** DNA origami nanopore inserted and lying on nanopipette. Reproduced with permission from Hernández-Ainsa *et al*.[18] Copyright 2014 American Chemical Society. **i)** DNA-based nanopore inserted into a lipid membrane. Reproduced with permission from Springer Nature and Xing *et al*.[19]

Solid-state nanopores (SSNP) simply consist of pores fabricated in insulating solid-state materials. Planar membrane geometries (Figure 1.2c) are commonly used to house SSNP and have been made from silicon nitride (SiN), quartz, or ultra-thin 2D materials such as graphene or molybdenum disulfide, etc.[4] Multiple different techniques are used to fabricate pores in planar membranes. For instance, the first two established SSNP fabrication techniques involved focusing ion beams or electron beams on membranes,[20,21] resulting in the precise sculpting of nanopores (Figure 1.2d) with double-coned geometries.[14] Controlled BreakDown (CBD) is another well-established technique that consists in applying a strong voltage across a pristine dielectric membrane, until a localized material failure occurs resulting in a tunable nanoscale opening (Figure 1.2e).[15,22] The CBD technique is the fabrication method used throughout this thesis, and as such is discussed later in further details (Section 1.1.2). In addition to planar geometries, pipette pullers can be used to create nanopipettes, i.e. conically shaped capillaries with nanoscale openings (Figure 1.2f).[16] Because of the low capacitance of the glass pipette, current measurements with nanopipettes can achieve low ionic current noise.[23] Because of the higher mechanical stability provided by solid-state membranes compared to biological pores, sensing experiments can withstand higher voltages and salt concentrations and present the advantage of tunable pore sizes, wherein a pore can be grown or shrunk to a size comparable to that of a molecule of interest, thus maximizing the signal amplitudes. The operational flexibility and robustness of SSNPs has made

it possible to integrate nanopore sensing with different technologies like microfluidics,[24] plasmonics[25] and more.

Hybrid nanopores are a class of sensors that attempt to harness and combine the increased stability of SSNPs and the functionality and reproducibility of biological pores. For instance, as shown in Figure 1.2g, Hall *et al.* showed that a biological pore could be docked into a narrow SSNP resulting in a functional sensing platform, albeit with a poorer noise performance due to thermal fluctuations of the sensing protein pore.[17] It was also shown that DNA-origami pores could be docked on top of SSNPs, creating hybrid sensors (Figure 1.2h).[18] Lastly, recent years have seen the impressive development of DNA-origami pores that can be inserted into lipid membranes.[19] Due to the well-established chemistry and malleability of DNA, the shape and size of these pores are highly tunable, are easily functionalized (Figure 1.2i).

Resistive pulse sensing can be used at different scales to achieve different measurement modalities. For instance, when pores have a larger diameter and volume than the analyte of interest passing through it, the characteristics of the current blockade signals can be used to calculate information about the volume of the translocating analyte. First such examples were achieved by sizing and counting biological cells, microorganisms, etc.[26] with microscale channels. With their nanoscale resolution, nanopores have shown they are able to characterize the tertiary and quaternary structures of proteins.[27] For example, Figure 1.3a shows the current trace induced by the translocation of a non-spherical Immunoglobin G protein, from which its volume, shape and dipole moment could be extracted.[28]

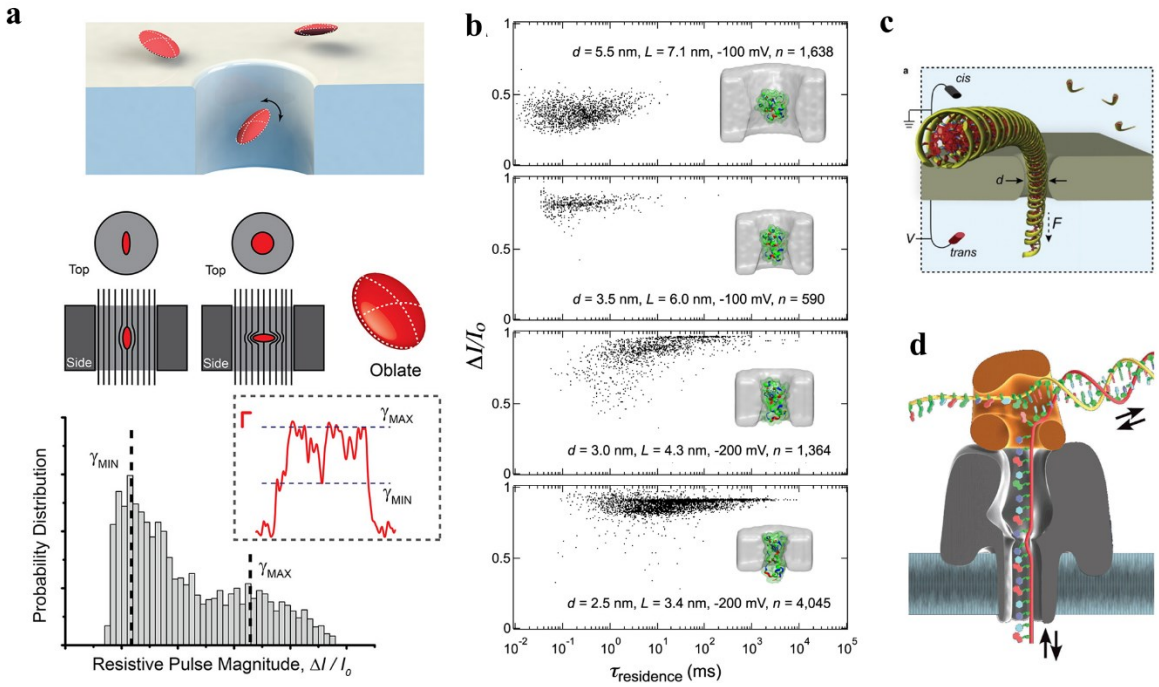

Figure 1.3. **Nanopore sensing at different scales. a)** Sensing proteins with volumes smaller than that of the pore, from which protein properties can be extracted. Adapted with permission from Houghtaling *et al*.[28] Copyright 2019 American Chemical Society. **b)** Squeezing proteins through nanopores allows studying protein folding kinetics. Adapted with permission from Tripathi *et al*.[29] **c)** When passing through small enough pores, DNA polymers must squeeze through pores by threading through the pore and translocating in a single-file manner. Reprinted from Carson *et al*.[30] with permission from Elsevier. **d)** Schematic of DNA sequencing method, wherein a ssDNA is sequentially fed into a biological pore. Reproduced with permission from Springer Nature and Schneider and Dekker.[31]

When pore diameters are smaller than the molecule of interest, they must squeeze inside the pores in order to initiate and complete translocations. For proteins larger than the pore, as shown in Figure 1.3b, partial or complete protein unfolding must occur to initiate translocation, the results of which allow for the study of protein folding energetics.[29,32,33] For DNA or any linear polymer with a gyration radius larger than the pore, the polymers cannot translocate through a pore without altering their relaxed conformations from bulk. In the limiting case that only one DNA strand fits inside a pore at once, a DNA end must find the pore for a single-file translocation to be initiated (Figure 1.3c). Single-file translocations are of particular interest given that, in addition to

extracting information about the polymer's dimensions, the nature and identity of the monomers along its contour can be analyzed sequentially, an idea at the heart of the now commercialized nanopore-assisted DNA sequencing technique (Figure 1.3d).

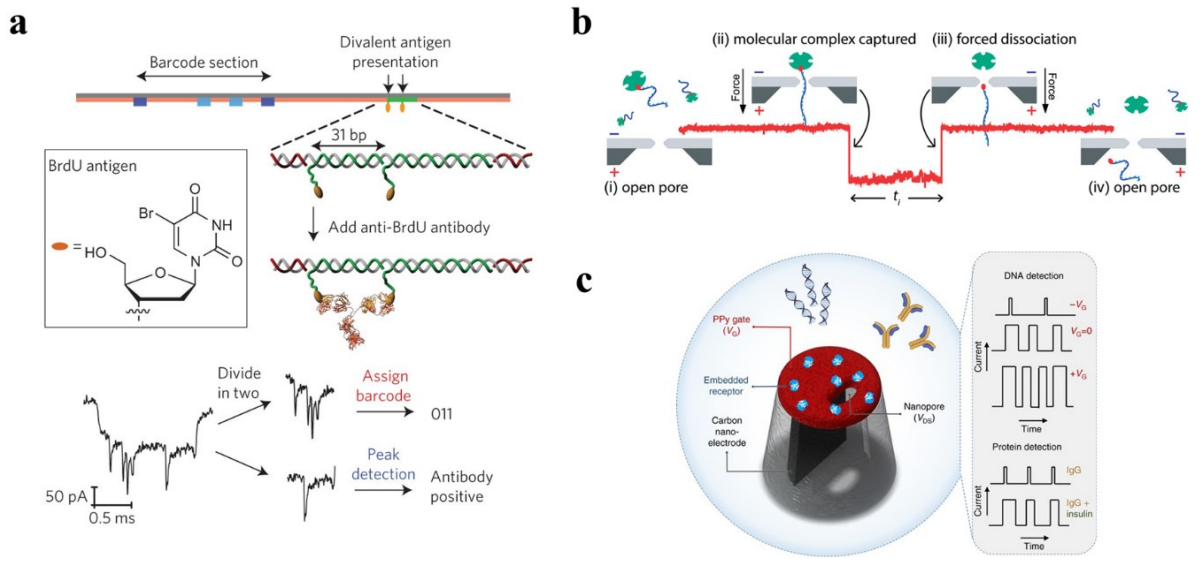

Figure 1.4. Different nanopore sensing modes. a) Carrier-assisted sensing method used to detect an IgG isotope antibody using a unique corresponding barcode signal. Reproduced with permission from Springer Nature and Bell *et al.*[34] **b)** Single-molecule force spectroscopy sensing used to determine the bond lifetime spectrum of the biotin-neutravidin complex. Reproduced with permission from Tabard-Cossa *et al.*[35] Copyright 2009 American Chemical Society. **c)** With controllable gate voltage, Nanopore extended field-effect transistor enables slower translocations and higher throughput. Reproduced from Ren *et al.*[36] licensed under CC BY 4.0.

An issue that can arise when sensing small or highly charged analytes is that the translocation blockades cannot be distinguished from the baseline noise or resolved temporally, respectively.[37] Moreover, the complex capture kinetics of heterogeneously charged molecules can result in hard-to-interpret current signals or simply in irreversible pore clogs. To avoid some of these issues, rather than sensing the hard-to-detect molecule by itself, it can instead be bound along the contour of a longer DNA carrier, after which the carrier-protein complex is detected and analyzed. The presence of the molecule of interest is thus simply detected as an extra transient blockage state during the single-file translocation of the carrier. This technique is at the heart of

many nanopore sensing schemes, since the translocation guided by the uniformly charged DNA is easier to detect and simpler to analyze. Figure 1.4a shows an example application from Bell *et al.*[34]

Nanopore sensing has been applied to a wide range of applications and is not limited to the detection of uninterrupted translocations. For instance, solid-state nanopores were used to performe force spectroscopy of single neutravidin-biotin chemical bonds, as shown in Figure 1.4b. One sensing modality which demonstrates well the versatility of nanopores is illustrated in Figure 1.4c and consists of a nanopore extended field-effect transistors which, as the name suggests, combine advantages of nanopores and field-effect transistors, and can even provide heightened selectivity via functionalization.

1.1.2 Controlled Breakdown Fabrication Method

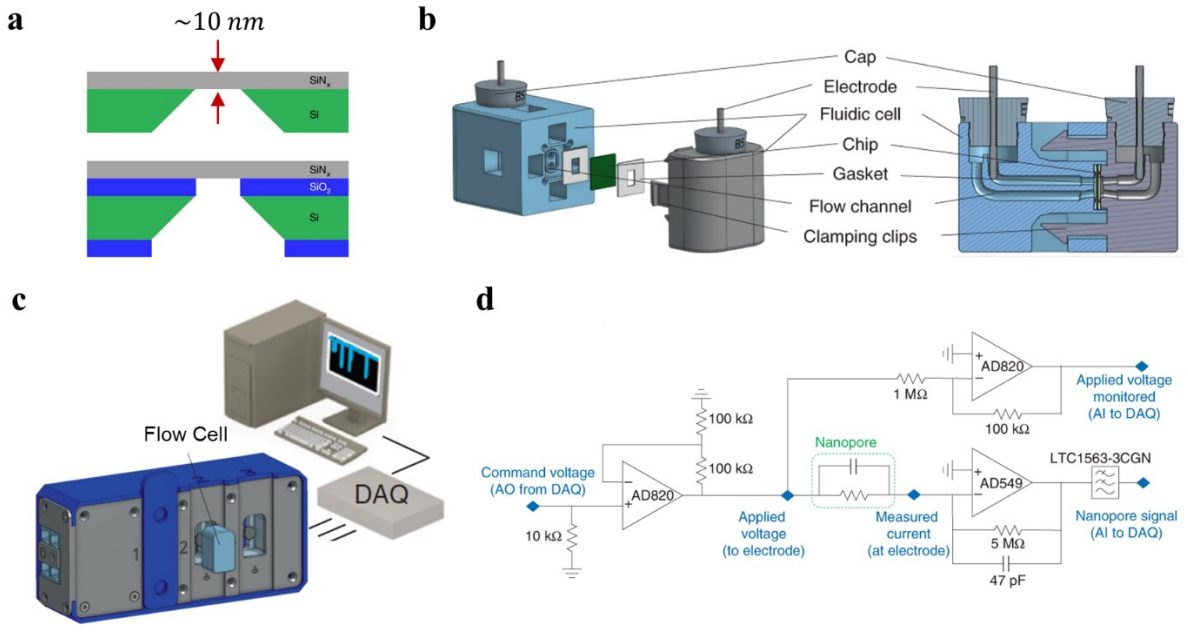

Figure 1.5. CBD nanopore fabrication setup. a) Schematic representation of silicon chips and free-standing membranes used in this work. **b)** Millifluidic flow cell design. **c)** Flow cell inserted into fabrication unit, connected to a computer setup through a DAQ card. **d)** Diagram of the electronic circuitry contained in the fabrication unit. Figure adapted with permission from Springer Nature and Waugh *et al.*[22]

The nanopores used in this work were all fabricated using the Controlled Breakdown (CBD) method,[15,22] a technique that has become widespread across the field owing to its simplicity, versatility, and lack of need of costly and cumbersome tools such as high energy electron and ion beams to name a few.[20,21] CBD nanopore fabrication is performed in aqueous salt solutions, i.e. in the same medium that sensing experiments are run in, which allows nanopores to be fabricated and integrated in complex device architectures, such as in microfluidic channels,[24] for example.

As depicted in Figure 1.5a, the membranes used in this work consist of silicon-nitride membranes (SiNx) of thicknesses varying between 10 and 20 nm. The SiN_x membranes sit on top of an etched silicon wafer resulting in a 40 μm × 40 μm free-standing SiNx window. To electrically isolate both of its sides, the membrane was sandwiched between two annular silicone gaskets providing fluidic access to the membrane surfaces, then compressed between two half millifluidic flow cells, thus sealing each membrane side. The channels in each half cell allow pipetting fluids and samples to the respective membrane surface, with the channel diameters made small enough to promote laminar flows, yet large enough to provide a decent hydraulic resistance. The cells were fabricated using the FormLabs Form 2 SLA 3D printer using Clear/Durable Resin. Multiple flow cell designs were used throughout this work, with one model depicted in Figure 1.5b. After assembling the flow cells as described above, the membrane was wetted, and Ag/AgCl electrodes placed in contact with the cell's channels such that voltages and currents can be applied and read, respectively. The setup and circuitry to achieve this are shown in Figures 1.5c-d.

As shown in Figure 1.6a, CBD pores are fabricated by applying a voltage across the thin membrane, creating a strong electric field stressing the material until a breakdown event occurs, indicating material being locally etched thus giving place to a nanopore. Figure 1.6b shows an example of the fabrication protocol commonly used, wherein a voltage ramp is applied, and the

induced current is monitored. Prior to fabrication, while the membrane is intact, a small current can be read which is attributed to capacitive response and a defect-assisted electron tunneling across the membrane. Once electrical breakdown occurs, a nanoscopic opening is created which allows ionic transport, which is indicated by a large surge of current. Using an adaptive threshold crossing algorithm,[22] voltage stops being applied after the current crosses the threshold.

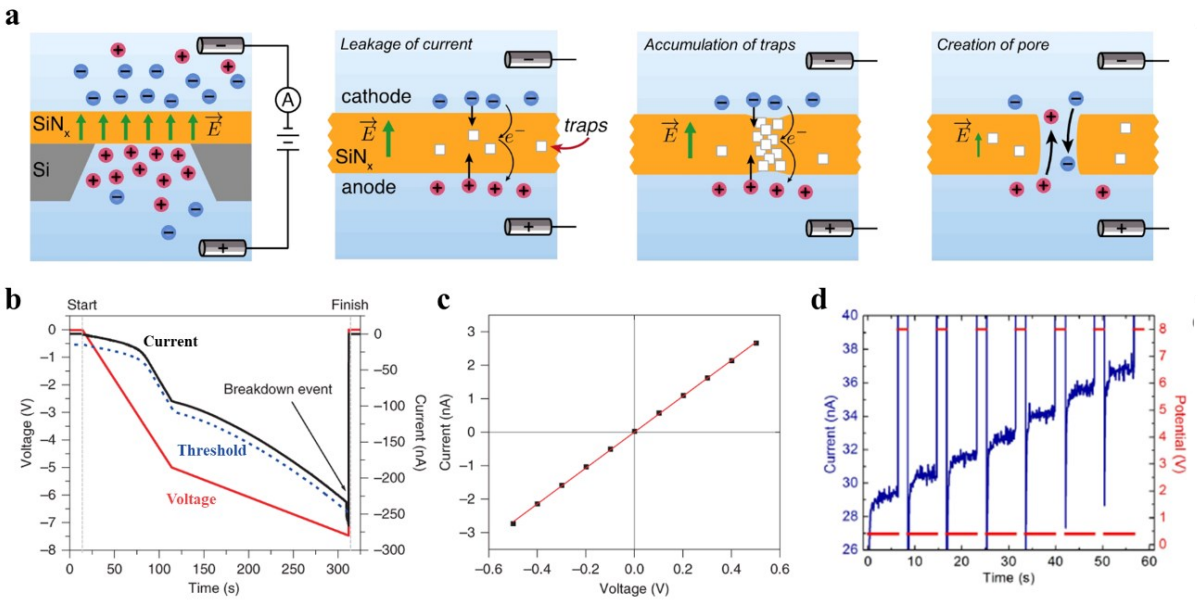

Figure 1.6. CBD fabrication & conditioning of nanopores. **a)** Controlled Breakdown mechanism and steps. Adapted with permission from Kwok *et al.*[15] licensed under CC BY 4.0. **b)** Applied voltage (red) and current (black - solid) measured throughout the fabrication of a nanopore. Adaptive current threshold shown in dashed black. **c)** Current vs Voltage measurements of a nanopore used to estimate the pore diameter.[22] Figures b) and c) adapted with permission from Springer Nature and Waugh *et al.*[22] **d)** Pore growth through application of AC voltage pulses. Used with permission of IOP Publishing, Ltd, from Beamish *et al.*[38]; permission conveyed through Copyright Clearance Center, Inc.

Directly after fabrication, pores tend to be small (d_{pore}<2 nm) and rectifying,[39] i.e. show polarity-dependent conductance. To address both issues, pores can be grown to desired sizes and conditioned by subjecting them to short AC voltage pulses for extended periods of time, as shown in Figure 1.6d.[38] Pulse amplitudes determine how quickly pores grow, with smaller voltage pulses sometimes being beneficial to the noise response of pores. Throughout the fabrication process,

pore size d is inferred from the conductance G of the pore (Figure 1.6c), using an equation involving the solution conductivity σ and membrane thickness L, as explained in Section 1.1.4:

$$d = \frac{G}{2\sigma}\left(1 + \sqrt{1 + \frac{4\sigma L}{\pi G}}\right). \tag{1.1}$$

1.1.3 Current Amplifiers

Figure 1.7. Current amplifiers. Chimera VC100 and the Axopatch 200B used in this work. Reproduced from: https://chimerainstruments.com/products/vc100/ and https://www.autom8.com/shop/mdcaxon-instruments/microelectrode-amplifiers/axopatch-200b-2-capacitor-feedback-patch-clamp-amplifier/.

Due to their nanoscale geometry, ionic currents through nanopores tend to be between 0.1 and 100 nA, and blockade durations can be as low as a few microseconds, under applied voltages ranging between 50 and 1000 mV. High bandwidth, low-current, and low-noise sensing are thus required for nanopore sensing experiments. To accurately read such small currents, at such temporal resolution, two different voltage clamp amplifiers were used throughout this work: The Axopatch 200B, which has 100 kHz bandwidth and can measure up to 200 nA, and the Chimera VC100, which has a 1 MHz bandwidth and can measure up to 10 nA. Analog output signals from such amplifiers are digitized through data acquisition cards (DAQ) at sampling rates of 500 kHz (Axopatch) and 4.17 MHz (Chimera), to then be read and analyzed on computer stations.

1.1.4 Current through nanopores

At the heart of resistive pulse sensing lies the challenge of identifying molecules by their translocation blockage characteristics. To achieve this, conduction models are commonly used to predict the conductance of pores in their open and blocked states,[40] the latter of which corresponds to pores blocked by insulating obstructions.

Open State

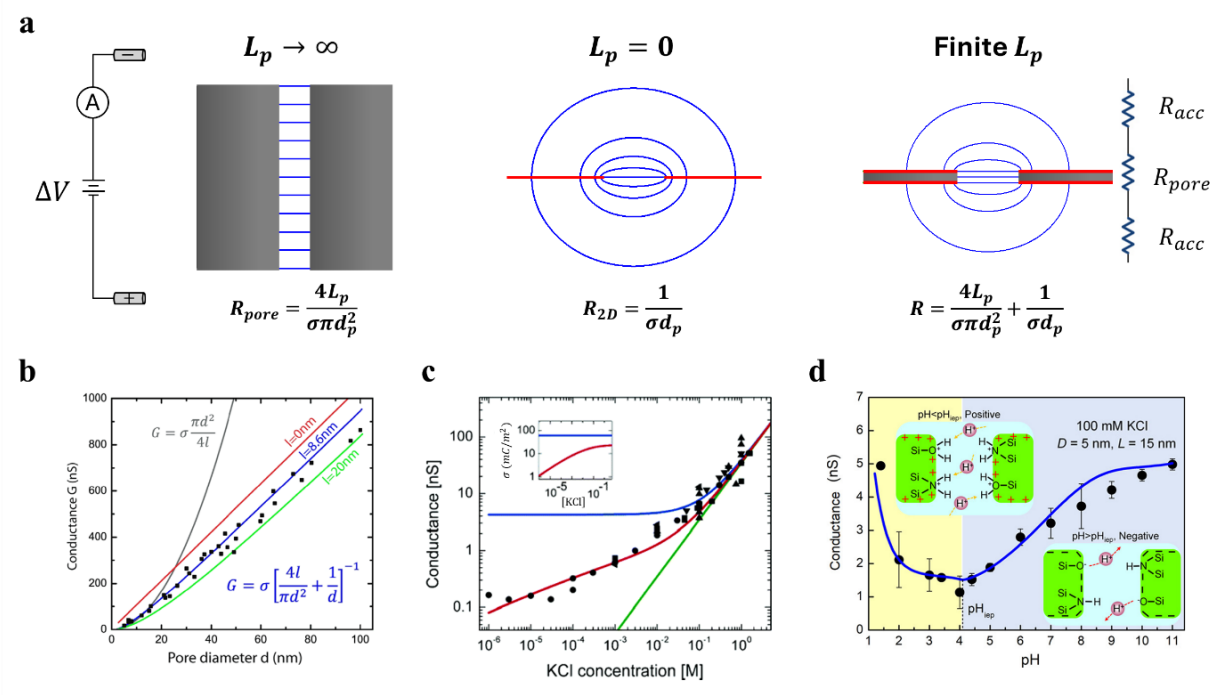

Figure 1.8. Open-pore conductance. a) Conductance modeling for different pore geometries, i.e. very long cylindrical channel, 2D pore and generalized finite-length pore. Blue lines correspond to equipotential lines. **b)** Measurements of conductance for different pore diameters. Measurements made in 1M KCl with 20 nm thick pores whose diameters were measured with TEM. Used with permission of IOP Publishing, Ltd, from Kowalczyk *et al.*[41]; permission conveyed through Copyright Clearance Center, Inc. **c)** Effect of salt concentration of conductance of 10 nm pores. Adapted with permission from Smeets *et al.*[42] Copyright 2006 American Chemical Society. **d)** Effect of solution pH on pore conductance. Reprinted with permission from Lin *et al.*[43] Copyright 2021 American Chemical Society.

The simplest case to conder is that of a long and narrow cylindrical pore of length L_p and diameter d_p ($L_p \gg d_p$ or $L_p \to \infty$). Under an applied voltage ΔV, the electric field in such channel

is well approximated as being uniform with amplitude $E = \Delta V / L_p$, and directed along the pore axis. The resistance of long cylindrical pores is thus

$$R_{cyl} = \frac{4L_p}{\sigma \pi d_p^2}. \tag{1.2}$$

The other limiting scenario to consider is that of a pore in a 2D membrane, i.e. $L_p = 0$. The resistance of a 2D pore can be found by assuming that the pore mouth is an equipotential disk, and so are the two infinitely large half-hemispheres far away from the pore, as reported by Hall:[44]

$$R_{2D} \equiv 2R_{acc} = \frac{1}{\sigma d_p}. \tag{1.3}$$

Note here that R_{acc} is the access resistance of half of the 2D pore system.

Interestingly, there exists no exact electric field solution for the intermediate case of finite-length pores with d_p and L_p, and thus no exact conductance equation. A very decent approximation for modeling the conductance of finite-length pores, as discussed in Chapter 2, is to make use of the two limiting cases in tandem: use the infinitely long channel solution for the interior of the pore, and use the 2D solution for the access regions, i.e. the regions outside the pore, and treat the regions as resistors in series, as depicted in Figure 1.8a:[41,45]

$$G_o = \left[R_{cyl} + 2R_{acc}\right]^{-1} = \left[\frac{4L_p}{\sigma \pi d_p^2} + \frac{1}{\sigma d_p}\right]^{-1}. \tag{1.4}$$

Figure 1.8b shows experimental results from Kowalczyk *et al.*[41] demonstrating the dependence of open pore conductance on pore size for nanopores drilled in 20 nm thick membranes, accompanied by Equation 1.4 evaluated for different values of L_p. Namely, for pores with large aspect ratios

($d_p/L_p > 1$) the access resistance dominates over the channel contributions, as demonstrated by a nearly linear dependence of G_o on d_{pore}, whereas the opposite is true for low aspect ratio pores.

When immersed in aqueous salt solutions, silicon nitride membranes are expected to be negatively (positively) charged for pHs higher (lower) than ~4. In addition to the contributions from the bulk pore and access regions, as per Equation 1.4, the movement of ions shielding the charged pore walls also contributes to the overall current. As showed in Figure 1.8c, studies of the open-pore conductance showed surface charge contributions to be significant mostly in lower salt concentrations, i.e. when the geometrical contributions proportional to conductivity σ are less important.[42] Given that solution pH alters the surface charge of the pore walls, electrokinetic contributions can also alter the open-pore conductance, as shown in Figure1.8d.[43] Since all experiments contained in this thesis were performed in high (> 1M) salt concentrations, the expressions and quantification of surface charge contributions are not further described.

Lastly, Equations 1.2-1.4 all pertain to cylindrical pores, however many fabrication techniques are known to result in non-cylindrical pore geometries (See Figure 1.2d),[14] in which case the above equations are ill suited. For rotationally symmetric pores with z-dependent diameters $d_p(z)$, wherein the z axis is aligned with the principal axis of the pore, it is common to model internal pore contributions by slicing it into disks of thickness dz and summing the z-dependent infinitesimal resistance $dR = 4dz/\sigma\pi d_p^2(z)$. Considering access resistance, a general expression for the open-pore conductance of finite-length non-cylindrical pores is thus:

$$G_o = \left[\frac{1}{2\sigma d_{bottom}} + \int_{-\frac{L_p}{2}}^{\frac{L_p}{2}} \frac{4dz}{\sigma\pi d_p^2(z)} + \frac{1}{2\sigma d_{top}}\right]^{-1}. \quad (1.5)$$

Here, $d_{bottom} = d_p(z = -L_p/2)$ and $d_{top} = d_p(L_p/2)$.This slice-partitioning method has been proposed and used since Maxwell's treatise,[46] and is known to overestimate conductance, yet result in accurate values for pores with smooth geometries not straying afar from cylinders.[40]

Blocked State

Just like the open state, the blocked state conductance of nanopores is more easily modeled for long channels with negligible access resistance, i.e. $L_p \gg d_p$, and nearly uniform electric fields. In such cases, as depicted in Figure 1.9a, the resistance R^b_{pore} of a rotationally symmetric pore can be well estimated by the slicing method discussed above:

$$G_b^{-1} = \int_{-\frac{L_p}{2}}^{\frac{L_p}{2}} dR(z) = \frac{4}{\pi\sigma}\int_{-\frac{L_p}{2}}^{\frac{L_p}{2}} \frac{dz}{d_p^2(z) - d_o^2(z)}. \tag{1.6}$$

Here $d_p(z)$ and $d_o(z)$ denote the z-dependent pore and obstruction diameter. This method is applicable to any pore and obstruction geometry; however, it relies on the assumption that the obstructions do not alter the electric field inside the pore. To this end, adjustments accounting for better electric field treatments have been achieved for spherical obstructions by Bean *et al*.[47]

From Equations 1.5 and 1.6, the conductance blockage ΔG expected of a pore in the presence of a specific obstruction can be calculated as

$$\Delta G = G_o - G_b. \tag{1.7}$$

The simplest solution to Equation 1.7 corresponds to the case of a cylindrical obstruction of diameter $d_o(z) = d_{DNA}$ inside a cylindrical pore of diameter $d_p(z) = d_p$, a geometry often used to describe DNA inside nanopores:

$$\Delta G_{DNA} = \frac{\sigma \pi d_{DNA}^2}{4L_p}. \tag{1.8}$$

Equations 1.6-1.8 are useful to help interpret the blockage distributions observed during DNA translocations: As shown in Figure 1.9b, DNA translocations result in quantized blockage values corresponding to folded translocations, i.e. translocations for which multiple segments of the same DNA strand are inside the pore at once. The quantized blockages are explained by the generalization of Equation 1.8: n DNA segments inside the pore result in $\Delta G_n = n \times \Delta G_{DNA}$. This observation allows identifying a DNA polymer's conformation as it underwent translocation.[48]

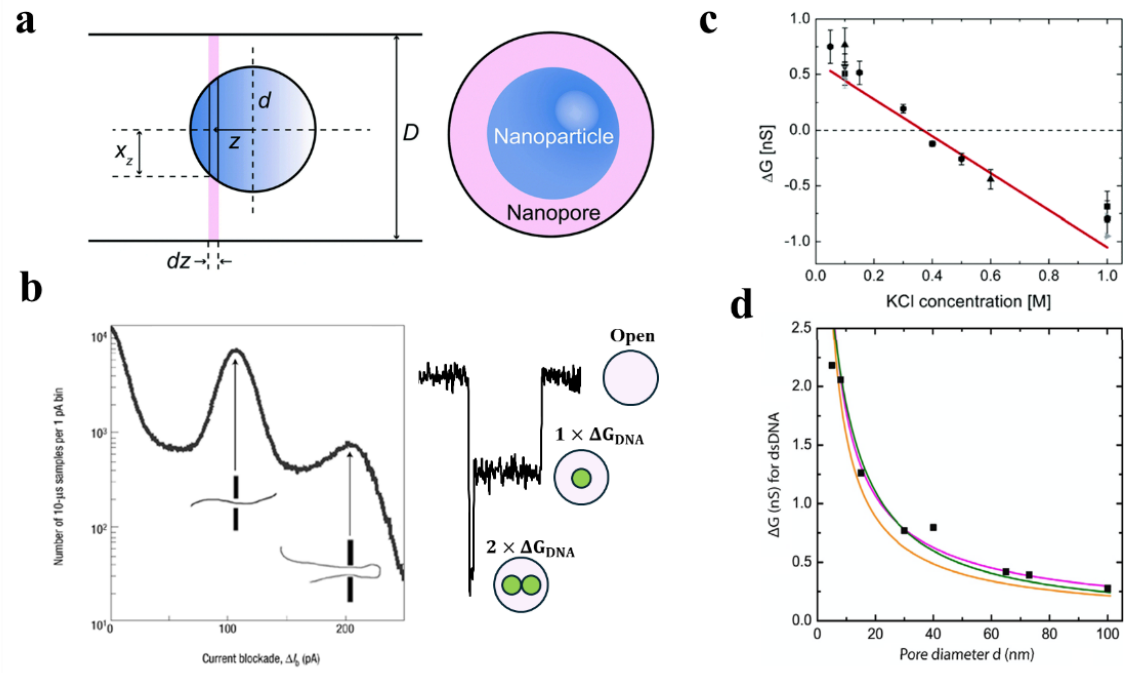

Figure 1.9. Blocked-state pore conductance. a) Modeling nanopore blockades using volume exclusion. Used with permission of Royal Society of Chemistry, from Tang *et al.*[40]*;* permission conveyed through Copyright Clearance Center, Inc. **b)** Quantized blockaded observed for DNA translocations arising from folded translocations. Reproduced with permission from Springer Nature and Li *et al.*[48] **c)** Effect of salt concentration on conductance blockages of DNA translocations.[42] Adapted with permission from Smeets *et al.*[42] Copyright 2006 American Chemical Society. **d)** Conductance blockage amplitude of DNA measured through nanopores of different sizes. Used with permission of IOP Publishing, Ltd, from Kowalczyk *et al.*[41]; permission conveyed through Copyright Clearance Center, Inc.

In addition to volume exclusion contributions, electrokinetic effects can also alter significantly blockage amplitudes, especially in low salt concentrations. Figure 1.9 c shows the dependence of ΔG_{DNA} on the bulk salt concentration, where current enhancements are observed in low concentrations instead of the blockages commonly observed in higher concentrations.[42] This enhancement results from the mobile counterions shielding the charged DNA backbone being introduced inside the pore alongside the polymer, and thus contributing to the overall conductance throughout the translocation process.

For pores with lengths and diameters of similar scale, access resistance contributions to the overall blockade can be significant. Kowalczyk *et al.*[41] demonstrated this by reporting the dependence of conductance blockage amplitude on pore diameter (Figure 1.9d), showing significantly smaller blockades in large pores, a phenomenon not predicted by the pore-size independent Equation 1.8. Modeling the resistance of blocked access regions is a non-trivial endeavour and not many methods exist to even approach this problem mathematically. This is the main subject of the second chapter of this thesis and as such is not described further here.

1.1.5 Current Fluctuations

A sought-after metric for nanopore sensing is high Signal-to-Noise Ratio (SNR), $\Delta I / I_{RMS}$, where ΔI is the translocation-induced ionic current blockage (signal), and I_{RMS} is the root mean square current (noise). The current RMS is related to the Power Spectral Density (PSD), through the relation $I_{RMS} = \int_0^B S_I(f) df$, where $S_I(f)$, is the PSD intensity at frequency f and B is the system's bandwidth. Figure 1.10a shows a typical PSD obtained from a device with a 23 nm pore

in 3.6 M LiCl solution under a 75 mV applied voltage, measured using the Chimera VC100 current amplifier (see Section 1.1.3).

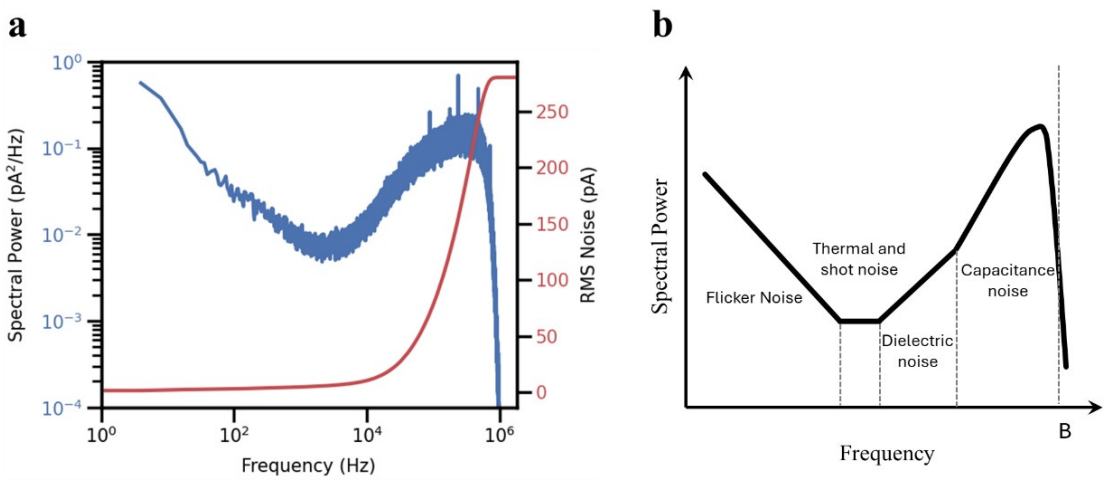

Figure 1.10. Sources of current fluctuations. a) Power Spectral Density obtained for a 23 nm nanopore device in 3.6 M LiCl under a 75 mV voltage. **b)** Illustration of the dominant sources of noise in the PSD at different frequencies.

Figure 1.10b shows that current fluctuations result from a nanopore system's electrical properties and from the measurement electronics. Namely, the PSD can be expressed as a polynomial of the form[11,49,50]

$$S_I(f) = \frac{a_0}{f} + a_1 + a_2 f + a_3 C_{total}^2 f^2 \frac{A^2}{Hz}. \quad (1.9)$$

Where the coefficients a_0, a_1, a_2, a_3 represent the contributions from the flicker,[51,52] thermal, dielectric, and capacitance noises, respectively.[11,49,50] Here C_{total} corresponds to the total capacitance comprising the nanopore membrane and chip, the parasitic capacitance and the amplifier feedback circuitry.

As noted in Figure 1.10b however, the current RMS of high bandwidth measurements are dominated by capacitance noise which, as per Equation 1.9, is expected to scale with the square of the system's capacitance C_{total}. The noise of nanopore signals can be thus significantly reduced by lowering the chip and membrane capacitance, which throughout this work was either achieved through painting the chips with PDMS,[49] or through using an oxide layer to decouple the Si support chip from the SiN membrane, as depicted in Figure 1.11a. A comparison of painted and unpainted SiNx chips is shown in Figure 1.11b-c.

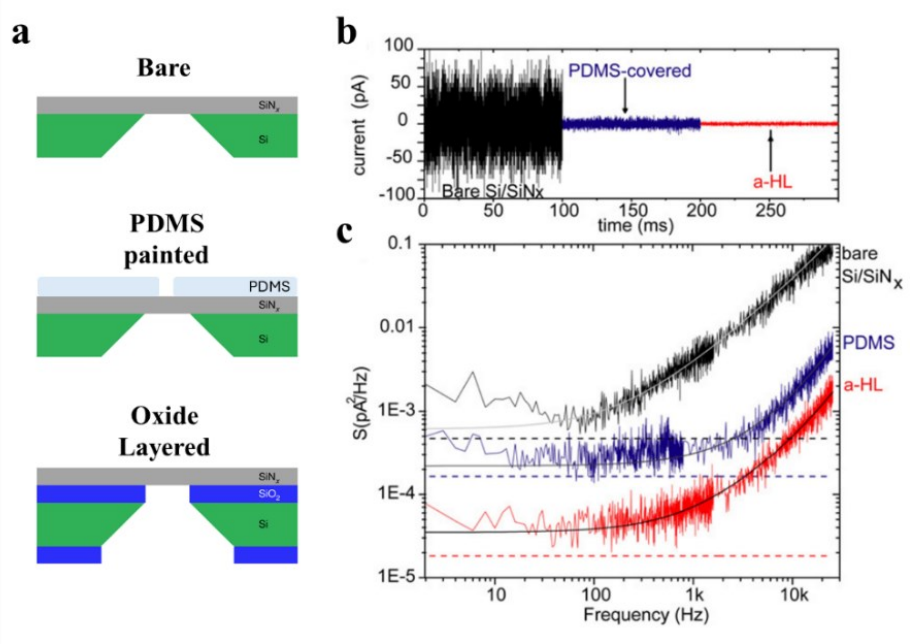

Figure 1.11. Lowering nanopore current noise. a) Depiction of methods used to lower the capacitance of nanopore chips: PDMS-painted and oxide underlayer chips. Adapted with permission from Springer Nature and Waugh *et al.*[22] **b)** Comparison of current traces obtained from a bare SiNx membrane (black) supported by Si support chip, a PDMS-painted SiNx chip (blue), and a α-hemolysin pore embedded in a lipid bilayer. **c)** PSDs of current traces of (b) showing reduced noise with PDMS-painted chips.[49] Figures b and c reproduced with permission from Tabard-Cossa *et al.* Copyright 2007 American Chemical Society.

1.1.6 Characteristic Response Time of Nanopore Systems

Because of the resistive and capacitive (RC) nature of the nanopore system and sensing circuitry, nanopore current fluctuations naturally have a non-zero rise time in response to a voltage or resistance impulse. As depicted in Figure 1.12a, single event traces with durations approaching that of the system's temporal resolution get altered with the amplitude of fast events even being attenuated and not reaching the full blockage expected from longer events.[53]

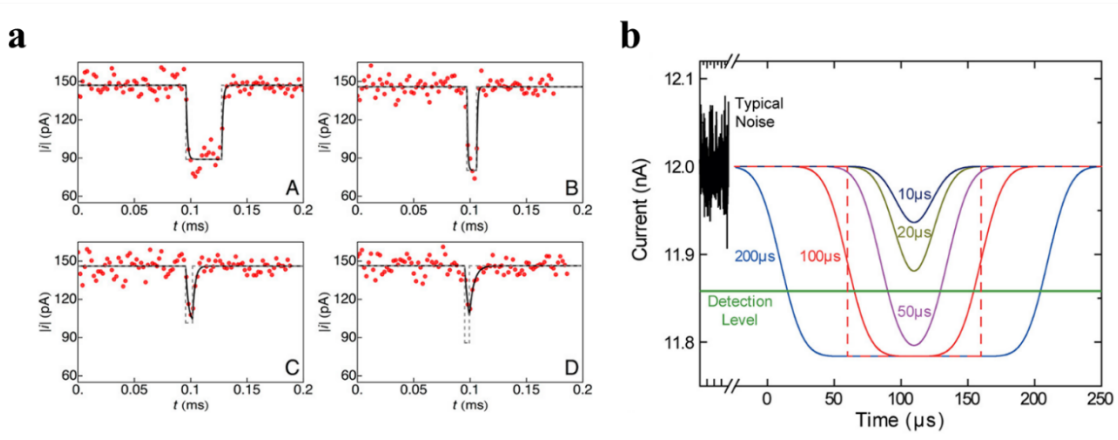

Figure 1.12. Nanopore signal rise time. a) Short lived current blockades caused by single PEG molecules interacting with an α-hemolysin nanopore. Adapted with permission from Balijepalli *et al*.[53] **b)** Distortion of rectangular pulses of varying durations by a 10 kHz Gaussian filter. Adapted with permission from Plesa *et al*.[37] Copyright 2013 American Chemical Society.

Since the noise of a nanopore increases with the system's bandwidth, the analysis of current measurements is most often realized on current traces that have been digitally filtered in order to obtain a better signal-to-noise ratio. Digitally filtering current data however increases the rise time constant of the signals, and thus further attenuates short-lived signals, as demonstrated in Figure 1.12b.[37] For the work presented in this thesis, filtering was performed using a Bessel low pass filter with a cutoff frequency chosen to balance good SNR and temporal resolution.

1.1.7 Capture Rate

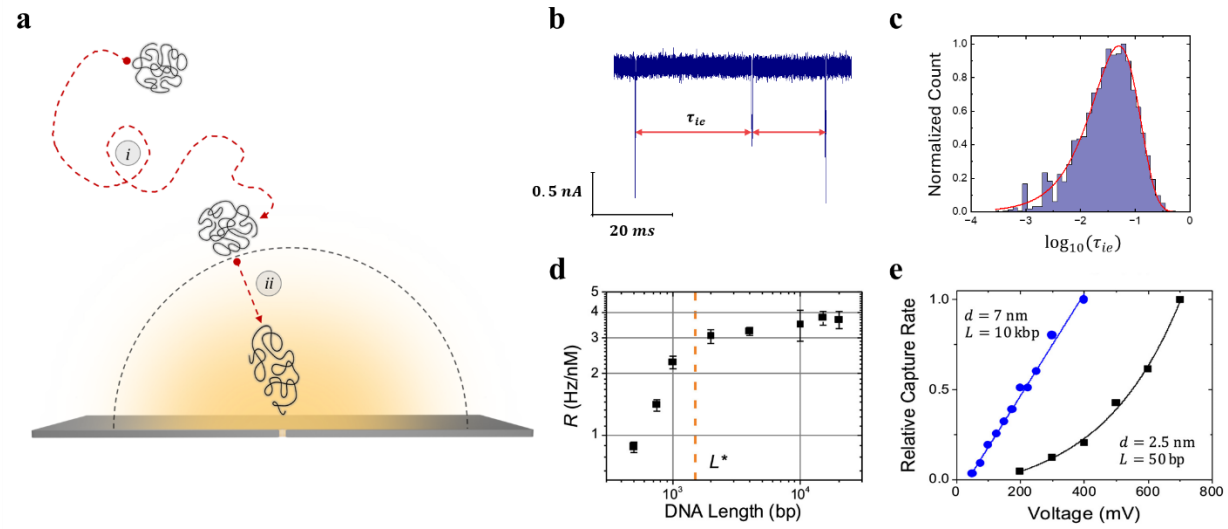

Figure 1.13. Nanopore capture analysis and kinetics. a) Sketch showing the steps of capture process. **b)** Current trace showing translocation inter-event times. Data acquired from 5 kbp DNA translocations through a 12 nm pore in 3.6 M LiCl under a 200 mV voltage. **c)** Distribution of logged inter-event times fitted to Equation 1.10 to extract the capture rate from experiment in b). **d)** Normalized capture rate R measured for different DNA lengths, showing two capture regimes described in text. **e)** Capture rate measured at different voltages for two different experimental conditions resulting in ΔV-dependences expected from two capture regimes. Figures d) and e) adapted with permissions from Charron *et al.*[54] Copyright 2019 American Chemical Society.

The frequency at which molecules translocate through nanopores, termed the nanopore capture rate, is an important metric used to determine the concentrations of analytes of interest. When working in low enough concentrations where inter-molecular interactions are negligible, the capture of an individual molecule occurs independently of others in solution, resulting in the capture rate J_c being linearly proportional to concentration, i.e. $J_c = R_c c$.[55] Here, R_c simply denotes the normalized capture rate, a useful metric to deconvolute the effects of concentration and the capture affinity of a pore in capturing an analyte of interest. The random and independent arrival of molecules at the pore mouth describes a Poisson point process, and as such the capture rate J_c of an experiment can be found by fitting the distribution of inter-event times τ_{ie} (Figure

1.13b) to a Poisson distribution, i.e. $P(\tau_{ie}) = J_c e^{-J_c \tau_{ie}}$. It has been shown that fitting the distribution of logged inter-event times to the corresponding log-transformed Poisson distribution provides an equally valid way of extracting J_c while being more robust to distribution outliers:[54]

$$P(x = \log_{10}(\tau_{ie})) = J_c e^{-J_c 10^x} 10^x \ln 10 \,. \tag{1.10}$$

As depicted in Figure 1.13a, for a molecule to be captured and translocate through a pore, it needs to first diffuse closer to the pore, at which point the non-uniform electric field attracts it towards the pore, and more significantly as it gets closer.[56,57] At the pore mouth, to initiate translocation a molecule must overcome a free energy barrier that arises from the nanoscale confinement imposed by the pore, thus significantly reducing the conformational entropy of linear polymers inserting into and threading through pores.[58,59] Two regimes are used to describe the kinetics of capture, the diffusion-limited and barrier-limited regimes (termed drift and entropic barrier regime by Muthukumar[59]). The former regime corresponds to scenarios wherein the energy barrier is insignificant, for which the rate-limiting process thus becomes the rate at which molecules diffuse close enough to be affected by the pore's electric field. Experimentally, diffusion-limited capture is characterized by a linear voltage dependence and DNA-length independence, as shown in Figures 1.13d-e.[54,56,57,60–63] The barrier-limited regime corresponds instead to scenarios where the rate-limiting step is the energy-barrier crossing at the pore mouth. Experimentally, as shown in Figure 1.13d-e,[54] this regime is characterized by exponential voltage dependence and DNA-length dependent capture and is observed mostly for smaller DNA lengths, pore sizes and applied voltage.

1.1.8 Translocation Time

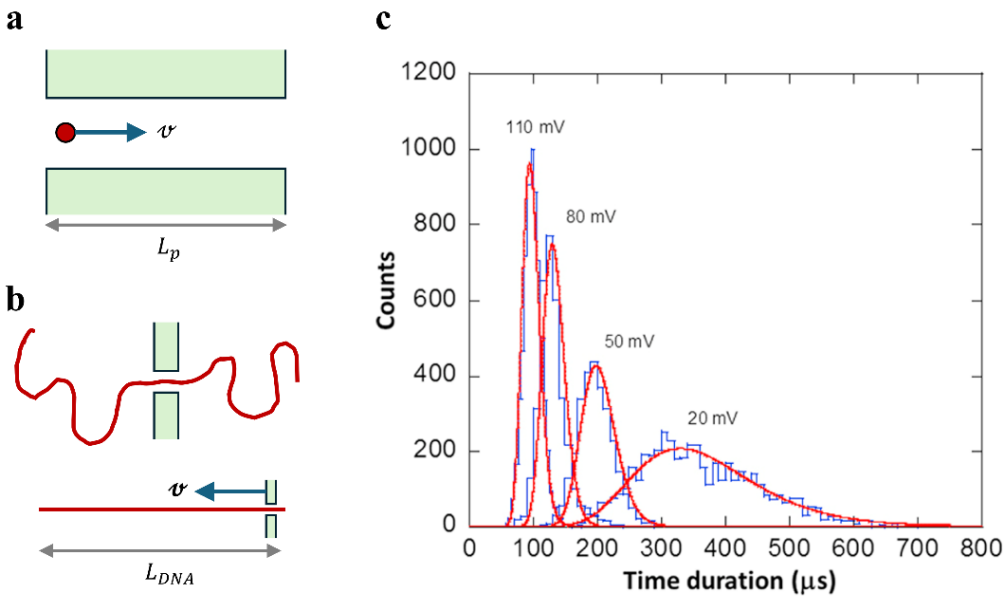

Figure 1.14. Translocation time distributions. a) Schematic of particle moving through a pore. **b)** Schematic of a polymer threading through a pore, and the equivalent interpretation, by which Equation 1.11 can be applied for constant-velocity translocations. **c)** Translocation time histograms for 4 kbp dsDNA in 1.6 M KCl with 20% glycerol at pH = 7.5 in an 8 nm pore, fitted to Equation 1.11. Used with permission of IOP Publishing, Ltd, from Ling *et al.*[64]; permission conveyed through Copyright Clearance Center, Inc.

As emphasized throughout this thesis, the passage of polymers through nanopores is a complex process. To gain some insight into the translocation process, first consider the simpler case of a spherical molecule moving through a long channel of length L_p at constant velocity v. The mean time it takes for the particle to migrate across the channel is simply $\tau = L_p/v$. Because of random thermal motion, some molecules will travel faster or slower across the channel. The distribution of translocation times τ can be found by solving the one-dimensional Fokker Planck equation and calculating the corresponding first-passage-time distribution.[64,65] For a molecule with a diffusion coefficient of D, the distribution of τ is expected to follow:

$$P(\tau) = \frac{L_p}{\sqrt{4\pi D\tau^3}} e^{-\frac{(L_p - v\tau)^2}{4D\tau}}. \qquad (1.11)$$

As shown in Figure 1.14c, Equation 1.11 has been applied to DNA translocation time histograms to study their average velocities v and diffusion coefficients D under various experimental conditions.[30,65] As shown in Figure 1.14b, although the translocation of linear polymers and spherical particles appear dissimilar, they can be made into congruous systems by changing the frame of reference, and considering the nanopore as drifting and diffusing along the contour of the polymer at a velocity v and with a diffusion coefficient D, respectively, thus replacing L_p with the polymer's contour lengths L_{DNA} as the relevant length scale.

Although Equation 1.11 typically fits experimental DNA translocation times distributions well,[30,65] the underlying assumption that velocity is constant throughout the translocation process is erroneous for double-stranded DNA translocations, as was demonstrated by extracted values of v and D clashing with well-established physical laws.[66] The disagreement stems from instantaneous translocation velocity partly depending on the time-dependent drag provided by monomers under motion outside the pore resulting in a non-constant velocity throughout the translocation process. The time-dependent drag forces occur since DNA translocation durations tend to be shorter than the polymer's relaxation time,[67] resulting in the polymer being out of equilibrium throughout its passage and its conformations being strongly correlated throughout the translocation process. As described by the Tension Propagation principles of Saito and Sakaue and others,[68–72] as translocation progresses, tension induced by the electrostatic pulling force inside the pore propagates through the polymer's contour, which engages segments into motion, in turn providing more drag opposing translocation. Once the tension front reaches the end of the molecule, its tail-end retracts, and the drag force decreases until the polymer is completely translocated. Figure 1.15 depicts the different steps of Tension Propagation principles.

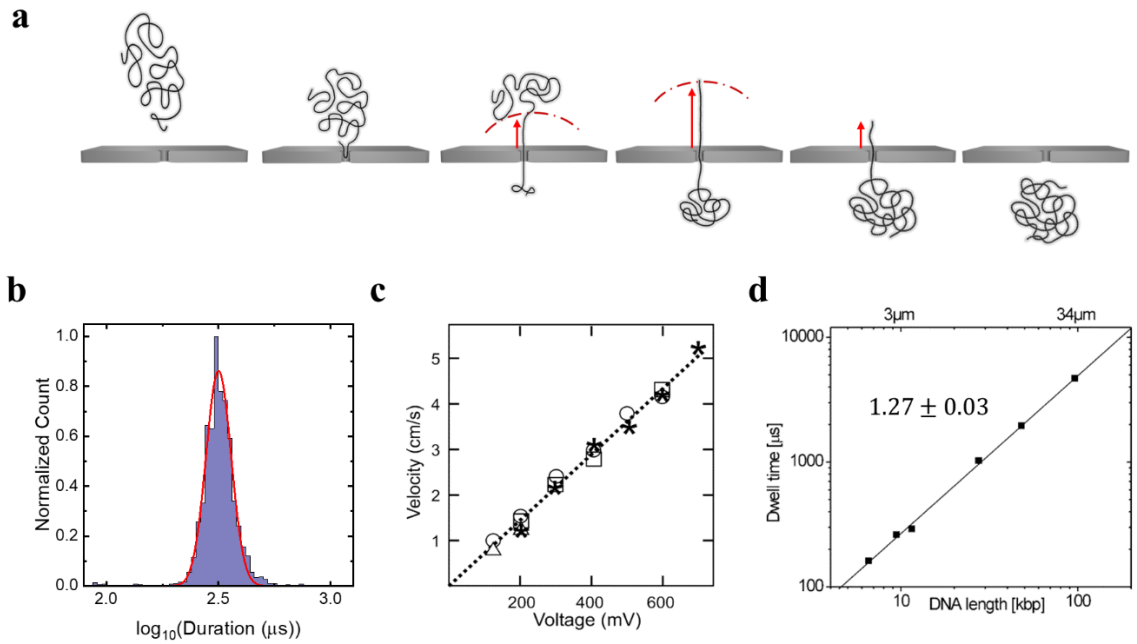

Figure 1.15. Translocation kinetics. a) Schematic showing the principles of tension propagation. **b)** Distribution of 5 kbp DNA translocation times through a 12 nm pore under 200 mV in 3.6M LiCl, fitted to a log-normal distribution. **c)** Average DNA translocation velocities measured across different voltages in 15 nm ion-beam sculpted pores in 1 M KCl solution. Different symbols represent different DNA lengths, as detailed in Chen *et al.*[61] Reproduced with permission from Chen *et al.*[61] Copyright 2004 American Chemical Society. **d)** Translocation times of different DNA lengths measured in 10 nm pores in 1 M KCl solution. Reproduced with permission from Storm *et al.*[73] Copyright 2004 American Chemical Society.

Instead of imposing Equation 1.11 and its incomplete description of the translocation process, the mean translocation durations $\bar{\tau}$ reported in this thesis were thus simply extracted by fitting the duration distributions to log-normal distributions, which were empirically found to describe experimental distributions adequately, as shown in Figure 1.15b. Experimentally, translocation kinetics are often studied by reporting the scaling of mean translocation times with voltage ΔV and polymer length L_{DNA}. As shown in Figures 1.15c-d, an inverse dependence on ΔV (equivalent to a linear dependence of velocity and applied voltage) and a super-linear dependence on DNA lengths such as $\bar{\tau} \sim L_{DNA}^{1.27}$ are expected and commonly reported.[54,73–75] The significance and origin of these scalings are central discussion points of Chapters 3 and 4.

1.2 DNA Properties

Although nanopores can sense a multitude of biomolecules, the work in this thesis is entirely achieved with double-stranded DNA polymers or DNA nanostructures. Just like many experimental studies prior to this thesis, DNA was used as a model polymer primarily because its physicochemical structure has been thoroughly studied owing to DNA's central role as the genetic foundation of living organisms. This section contains the information pertaining to DNA's structural and transport properties that will be useful for the study of the kinetics of nanopore capture and translocation.

1.2.1 Physicochemical Structure of DNA

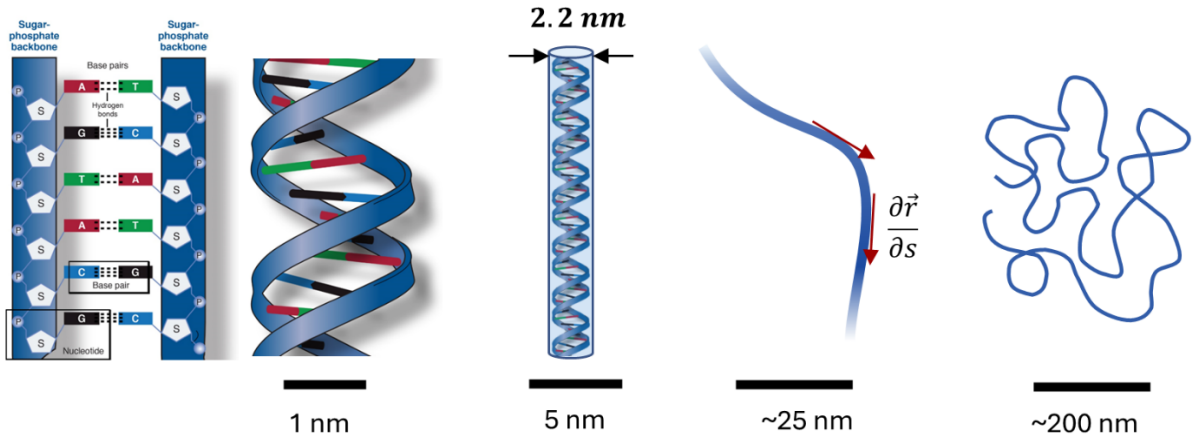

Figure 1.16. Sketches showing DNA chemistry and structure at different scales. Adapted from https://www.genome.gov/genetics-glossary/Phosphate-Backbone

Figure 1.16 shows how the structural properties of deoxyribonucleic acid, DNA, can be described and defined at different scales.[76,77] At the atomic scale, a double stranded DNA molecule is made up of two complementary single-stranded DNA (ssDNA) strands which form a double-helix structure by coiling around each other.[78] A ssDNA strand is a linear polymer made up of a series of monomers termed nucleotides, which individually consist of a single deoxyribose sugar,

a negatively charged phosphate group and a sequence of nitrogen-containing nucleobases: cytosine (C), guanine (G), adenine (A), or thymine (T). The sugar of one nucleotide is covalently bound the phosphate of the ensuing nucleotide, thus forming the sugar-phosphate backbone of the DNA. The nitrogenous bases of the strands are subject to Watson-Crick-Franklin pairing, wherein A forms a hydrogen bond with T, and C forms a hydrogen bond with G. As a result of base-pairing, two ssDNA polymers with complementary sequences are favored to bind together as dsDNA, thus forming the double-helix structure. X-ray diffraction measurements have shown that in this double-helical structure, the distance between successive bases is 0.34 nm, and the double-helix diameter is 2 nm.[77]

Across tens of base pairs (5-10 nm), dsDNA is quite rigid due base stacking interactions,[79] the interactions between successive base pairs. On the scale of the nanopores used in this work, the segments of dsDNA inside a pore can thus be treated as rigid rods. For simplicity, the geometry of dsDNA inside pores is thus assumed to be cylindrical, which is a useful assumption when modeling the conductance of pores in the presence of DNA, or even when considering pore-polymer hydrodynamic interactions, as later discussed. Note that nanopore measurements are performed in aqueous solutions, and as such a diameter of 2.2 nm is used for dsDNA's diameter, assuming its contour is surrounded by a non-conducting hydration shell of thickness 0.1 nm.

At a larger scale of ~25-100 nm, dsDNA behaves like a flexible rod. The persistence length ℓ_p is a characteristic length used to define the stiffness of the polymer. If a dsDNA polymer has a length of L_{DNA} and its contour is parametrized by $\vec{r}(s)$ with $s \in [0, L_{DNA}]$, the persistence length ℓ_p is defined as the characteristic contour distance over which the correlation of vectors tangent to the polymer contour are lost, i.e. decay significantly:

$$\left\langle \frac{d\vec{r}(s)}{ds} \cdot \frac{d\vec{r}(s+\delta s)}{ds} \right\rangle = e^{-\delta s/\ell_p}. \tag{1.12}$$

Here δs is the distance between two tangent vectors along the polymer contour. According to the wormlike chain model, dsDNA can be treated as a flexible beam with known mechanical properties of Y, the Young modulus, and I, the cross-sectional moment of inertia. Under this assumption, the persistence length can be written with respect to mechanical properties of dsDNA:

$$\ell_p = \frac{YI}{k_b T}. \tag{1.13}$$

Typical persistence lengths for dsDNA are measured around 50 nm, i.e. 150 base pairs (bp).[80]

From Equations 1.12-1.13, the mean end-to-end distance R_{ee} of dsDNA polymers can be calculated from the wormlike chain model to be:

$$R_{ee} = \langle |\vec{r}(L_{DNA}) - \vec{r}(0)|^2 \rangle^{\frac{1}{2}} = \sqrt{2\ell_p L_{DNA}\left(1 - \frac{\ell_p}{L_{DNA}}\left(1 - e^{-\frac{L_{DNA}}{\ell_p}}\right)\right)}. \tag{1.14}$$

For very short polymers, $L_{DNA} \ll \ell_p$, Equation 1.14 becomes $R_{ee} = L_{DNA}$, es expected for rigid rods, whereas for very long polymers, $L_{DNA} \gg \ell_p$, Equation 1.14 takes the form:

$$R_{ee} = \sqrt{2\ell_p L_{DNA}} = \sqrt{\ell_K L_{DNA}} = \ell_K N_K^{1/2}. \tag{1.15}$$

The rightmost expression of Equation 1.15 shows that the end-to-end statistics of long wormlike chains are equivalent to those of a random walk of N_k steps of length ℓ_k (s.t. $L_{DNA} \equiv \ell_K N_K$), from which a scaling $R_{ee} = \ell_k N_k^{1/2}$ is expected. The distance ℓ_K is known as the Kuhn length and corresponds exactly to twice the persistence length $\ell_k \equiv 2\ell_p$. Equation 1.15 therefore suggests

that at scales larger than $2\ell_p \approx 100\ nm$, dsDNA strands look increasingly like flexible, spaghetti-like coils, randomly distributed in space.[76]

Lastly, because the wormlike chain model ignores long range self-interactions, i.e. the inability of chain segments to overlap, it is known that Equation 1.15 underestimates the size of polymers, given that self-interactions are expected to swell real polymer chains. By considering the energetic and entropic contributions to the free energy, Flory theory dictates that the sizes of real chains should scale with their contour length L as:

$$R_{ee} \sim L^{\nu}. \tag{1.16}$$

Here ν is Flory's scaling coefficient, predicted to have a value of 3/5, and experimentally determined to be $\nu \approx 0.588$.[81]

1.2.2 DNA Transport Properties

Before studying the dynamics of electrophoretically driven dsDNA translocations through nanopores, this section describes the transport properties of dsDNA in bulk solution, namely its response to thermal motion and electric fields.

The diffusion of dsDNA polymers is described by Zimm dynamics, wherein the different segments of the polymer are tightly coupled to each other through hydrodynamic interactions. As such, the water contained inside the polymer coil moves along with the diffusing polymer, which can thus be treated as a solid sphere with a hydrodynamic radius R_H:

$$D = \frac{k_B T}{6\pi\eta R_H} \sim L_{DNA}^{-\nu}. \tag{1.17}$$

Note that the hydrodynamic radius R_H of a polymer is closely related and scales with its the end-to-end distance R_{ee} (Equation 1.16). The final expression of Equation 1.17 makes use of this and

shows the diffusion coefficient of DNA polymers should scale with $L^{-\nu}$. Figure 1.17a shows measurements of diffusion coefficients of various DNA lengths acquired during capillary electrophoresis experiments,[82] the scaling of which agrees well with Equation 1.17.

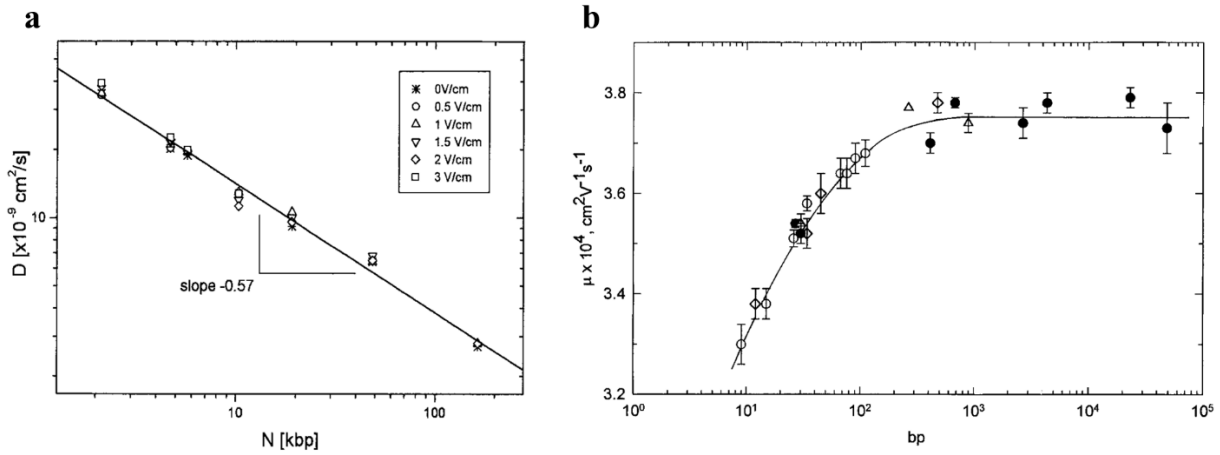

Figure 1.17. DNA transport. a) Diffusion coefficient measured for different dsDNA lengths undergoing capillary electrophoresis. Reproduced with permissions from John Wiley and Sons and Nkodo *et al*.[82] **b)** Electrophoretic mobility measurements for different dsDNA lengths. Reproduced with permissions from John Wiley and Sons and Stellwagen *et al.*[83]

Under an applied electric field, a DNA polymer behaves as a free-draining polymer and undergoes electrophoretic motion which is best described by Rouse dynamics, wherein interactions between different DNA segments are negligible. This is due to the hydrodynamic perturbations for each segment being contained within the diffuse layer of counterions shielding the charged DNA backbone. As a result, the electrophoretic mobility of dsDNA is a quantity determined locally by the balance of forces along the DNA, i.e. the electrostatic pulling force and the drag imparted by the counterion motion in the opposite direction, and is length-independent for long-enough polymers. Figure 1.17 b shows electrophoretic mobilities values experimentally measured for different dsDNA lengths,[83] showing length-independent measurements for longer strands, as expected from the above discussion.

1.2.3 DNA Origami

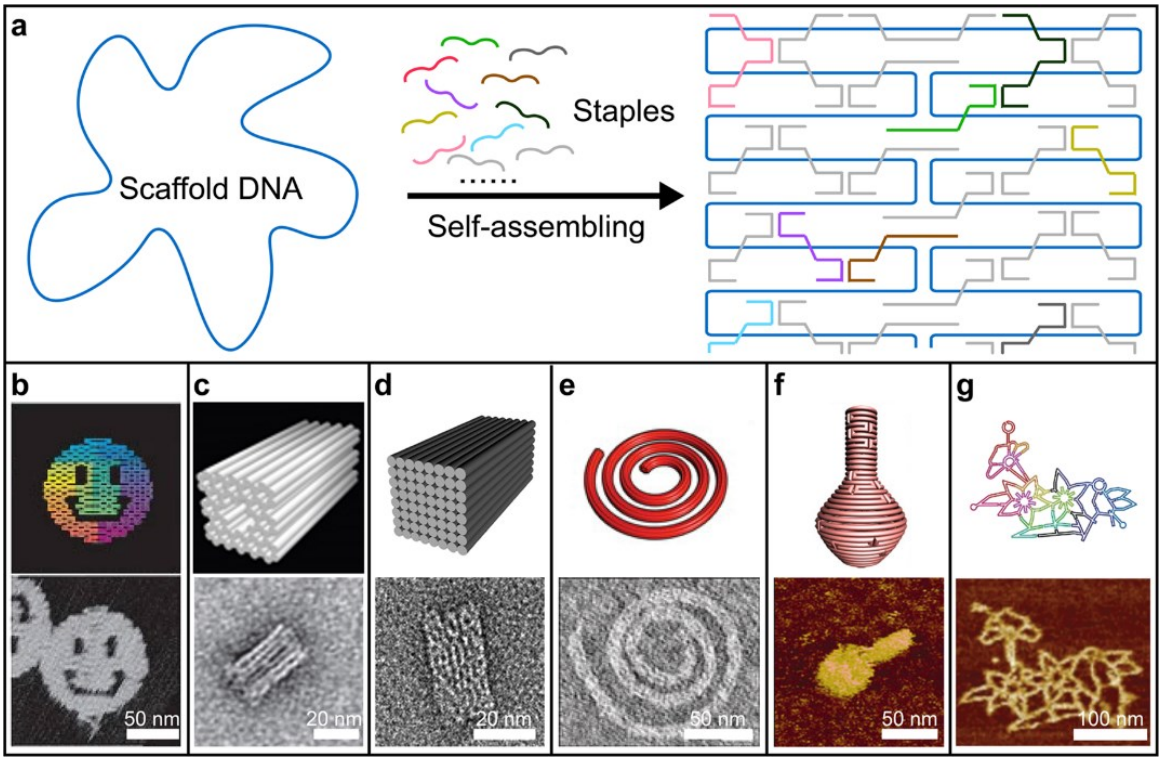

Figure 1.18. DNA origami structures. a) Schematic showing the principle of DNA origami assembly. Different origami structures **b)-g)** Examples of DNA origami structures. Figure reproduced with permission from Zhou *et al*.[84]

The stability of dsDNA and its programmability resulting from base-pairing mechanisms have given rise to the field of DNA nanotechnology, wherein DNA nanostructures can be self-assembled in a bottom-up fashion using ssDNA strands as structural components whose sequences guide the self-assembly process. One branch of DNA nanotechnology, DNA origami, has shown great robustness and yield for generating highly complex 3D nanostructures. DNA origami was first suggested in 2006 by Rothemund,[85] and consists in using a high number of short ssDNA to fold a long ssDNA scaffold into a desired shape. By carefully synthesizing the staple sequences, the folded scaffold can be made to form a wide variety of two- and three-dimensional shapes. For the nanostructures used in this thesis, the software caDNAno was used,[86] which provides the

ssDNA staple sequences required to accomplish any designed structure given the known scaffold sequence. Figure 1.18 shows examples of assembled DNA-origami nanostructures.[84]

1.3 Thesis Overview & Background Information

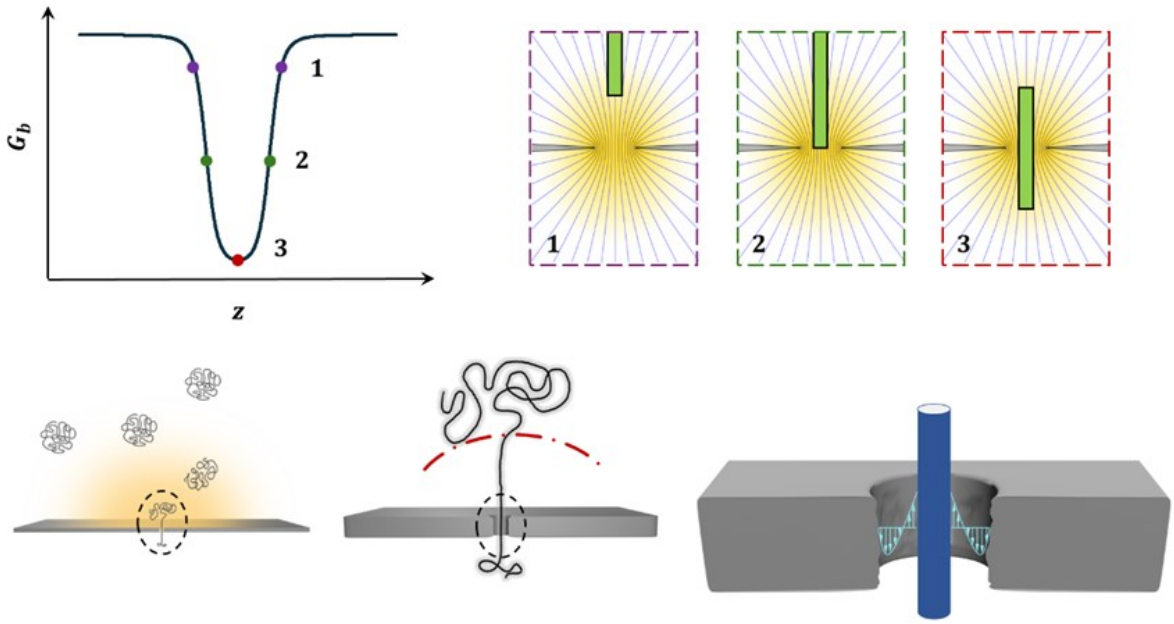

Figure 1.19. Thesis overview schematic. Schematic overview of the subjects addressed in this thesis: Modeling the conductance of blocked access resistances and studying the underlying forces of polymer capture and translocations at different scales.

The research contained in this thesis attempts to bridge the gap between nanopore sensing theory and experiment that has taken place mostly due to the application-driven nature of the nanopore research field and the rapid technological advancements and commercial success seen in past years. As such, there exists only a few experiments attempting to validate or test the different theories developed to describe the complex nature of the nanopore translocation process. Therefore, the different sections of this thesis provide either new theoretically-inclined ideas, as

per Chapter 2, or show experiments designed to test and demonstrate previously conceived theoretical concepts, as per Chapters 3, 4 and 5. The work introduced in this thesis aims to be useful for different types of researchers in the field, but most importantly attempts to paint from experiments and simple physical insights a very clear picture of nanopore transport dynamics and conductance modeling techniques. Before presenting original research, this chapter concisely discusses the subjects of each chapter and presents the existing body of work for each topic, thus giving background and motivation for further studying them.

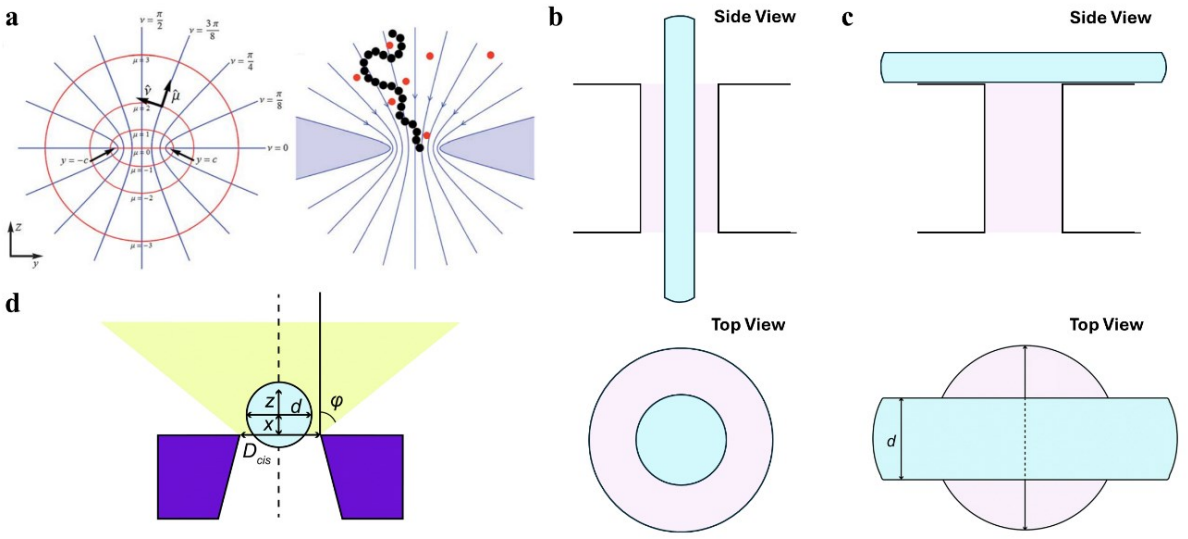

Figure 1.20. Access region modeling. a) Oblate spheroidal coordinates used to describe the potential and electric fields in the access regions. Used with permission of Royal Society of Chemistry, from Farahpour *et al.*[87]; permission conveyed through Copyright Clearance Center, Inc. **b)-d)** Schematics of scenarios where the conductance of blocked access regions was modeled. **b)** DNA inside nanopores has been modeled as a long cylinder blocking both the pore interior and the access regions.[41,88] **c)** DNA modeled lying on top of pores. **d)** Conical slices for access region.[40,89] Figures b) and d) used with permission of Royal Society of Chemistry, from Tang *et al.;* permission conveyed through Copyright Clearance Center, Inc.

In Chapter 2, a method by which to estimate and model the conductance of access regions blocked by insulating molecules is introduced and developed. The method is conceptually simple and builds on the idea that the resistance of a conducting region can be well estimated by partitioning the volume into thin slices in series and then summing up the corresponding

infinitesimal resistances.[46] Although the slicing method has been used profusely for the interior of blocked pores[40] (Equation 1.6), no robust equivalent method existed for modeling blocked access regions, whose contributions are known to be significant for low-aspect ratio pores (i.e., $d/L > 1$) (Figure 1.9d).[41] The original method introduced in Chapter 2 makes use of oblate spheroidal slices, inspired by Farahpour *et al.* who demonstrated that oblate spheroidal coordinates could be used to describe the electric field in the access regions in the absence of obstructions (Figure 1.20a).[87]

Prior to this work, a handful of access region conductance models were published, usually to address specific blockage scenarios. For instance, to predict blockages induced by DNA translocations, models were developed[41,88] for the conductance of long insulating cylinders blocking the pore interior and access regions, as depicted in Figure 1.20b. Similarly, a model was proposed by Carlsen *et al.*[90] to describe the conductance induced by DNA lying flat on the membrane above the nanopore mouth, as shown in Figure 1.20c. In 2011, Willmott and Parry introduced a slicing method to model the blocked access region by introducing an artificial cone constructed at the end of conical pores, in the access region, and using circular slices along the principal cone and pore axis (Figure 1.20d).[89] Generally, however, access region conductance blockage models are scarce and were recently described as being in their infancy, as per a 2022 article reviewing conductance modeling technique.[40]

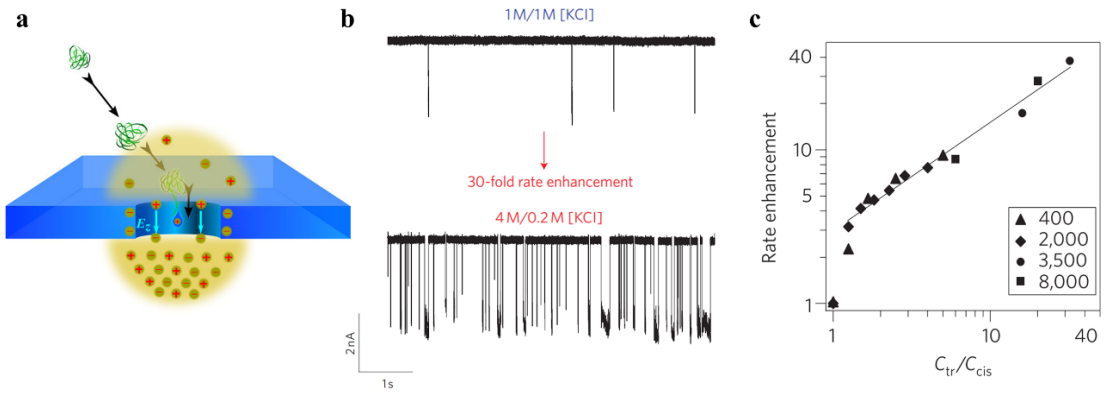

Figure 1.21. Sensing under salt gradients. a) Depiction of a nanopore separating two reservoirs of different salt concentrations. Adapted with permission from He *et al.*[91] Copyright 2016 American Chemical Society. **b)** Differing *cis* and *trans* salt can slow down translocation **(b)** and enhance capture rate **(c)** of DNA in nanopores. Figures b and c reproduced with permission from Springer Nature and Wanunu *et al*.[56]

In Chapter 3, the dynamics of DNA capture and translocation through nanopores are studied under asymmetric salt conditions, wherein the nanopore membrane partitions two reservoirs of different ionic concentrations (Figure 1.21a). In 2010, Wanunu *et al.* showed that asymmetric salt concentrations could be used to enhance capture rates and reduce translocation velocities when capturing DNA from the low concentration reservoir, as shown in Figures 1.21b and 1.21c.[56] Prior to this report, variations of experimental parameters such as voltage, salt concentration, temperature, etc., resulted in a coupled increase (or decrease) of both capture rate and velocity.[30,92–96] The observed decoupling of capture rate and translocation velocity in salt gradients hints at the non-uniform modulation of forces across the nanopore system and thus provides a great platform to study capture and translocation kinetics. Chapter 3 reports on the dependencies of capture rate and translocation times on DNA length, applied voltage, and salt gradients, to compare and test predictions from existing theoretical models, but also to provide additional experimental data to scarce body of nanopore experiments; Figure 1.22 shows all but one of the existing experimental measurements of capture rate and translocation times for different lengths of dsDNA.

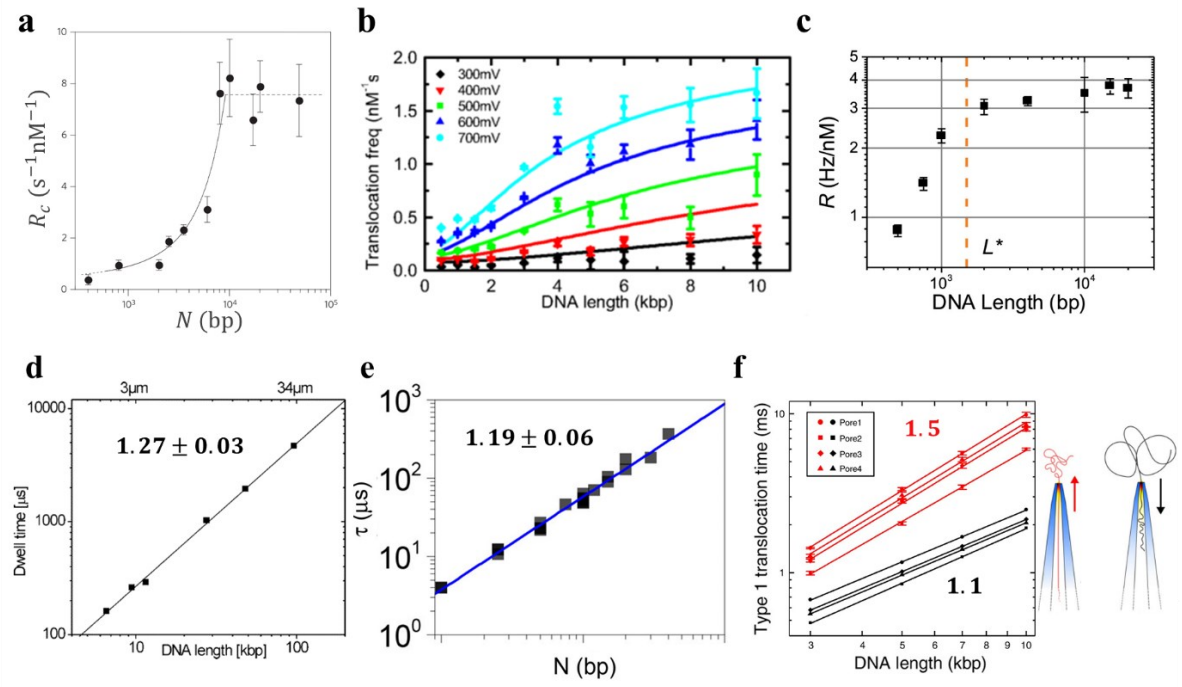

Figure 1.22. Existing experimental capture and translocation scaling data. Capture rate vs DNA length **a)** for a 4 nm pore in 1 M KCl under a voltage of 300 mV (Reproduced with permission from Springer Nature and Wanunu *et al*.[56]); **b)** for a 15 nm capillary in 4 M LiCl under different voltages (Reprinted figure with permission from Bell *et al.* [63] Copyright 2016); **c)** for a 7 nm pore in 1.8 M LiCl under a voltage of 300 mV (Adapted with permissions from Charron *et al*.[54] Copyright 2019 American Chemical Society). Translocation time vs DNA length **d)** for a 10 nm pore in 1 M KCl (Reproduced with permission from Storm *et al*.[73] Copyright 2004 American Chemical Society); **e)** for 8 nm pores in 3.6 M LiCl (Reproduced with permission from Briggs *et al*.[74] Copyright 2004 American Chemical Society); **f)** for 14 ± 3 nm capillaries in 4M LiCl (Adapted with permission from Bell *et al.* [97], licensed under CC BY 4.0).

In addition to modulating electrophoretic forces, nanopore sensing under asymmetric salt concentrations gives rise to diffusiophoresis and diffusioosmosis, two electrokinetic phenomena that take place due in part to the osmotic pressure gradients inside the double layer, and to the electro-osmotic response of charged surfaces to an electric field induced by the different diffusion coefficients of the ions in solution (Figure 1.23a). Experiments by McMullen *et al.* used salinity gradients across nanopore and showed that diffusioosmosis could thread DNA through nanopores without the need for applied voltages.[98] Recently, Xi *et al.* showed that the counteracting effects of diffusioosmosis and diffusiophoresis could even be harnessed to rotate a DNA-rotor nanostructure tethered into a nanopore.[99]

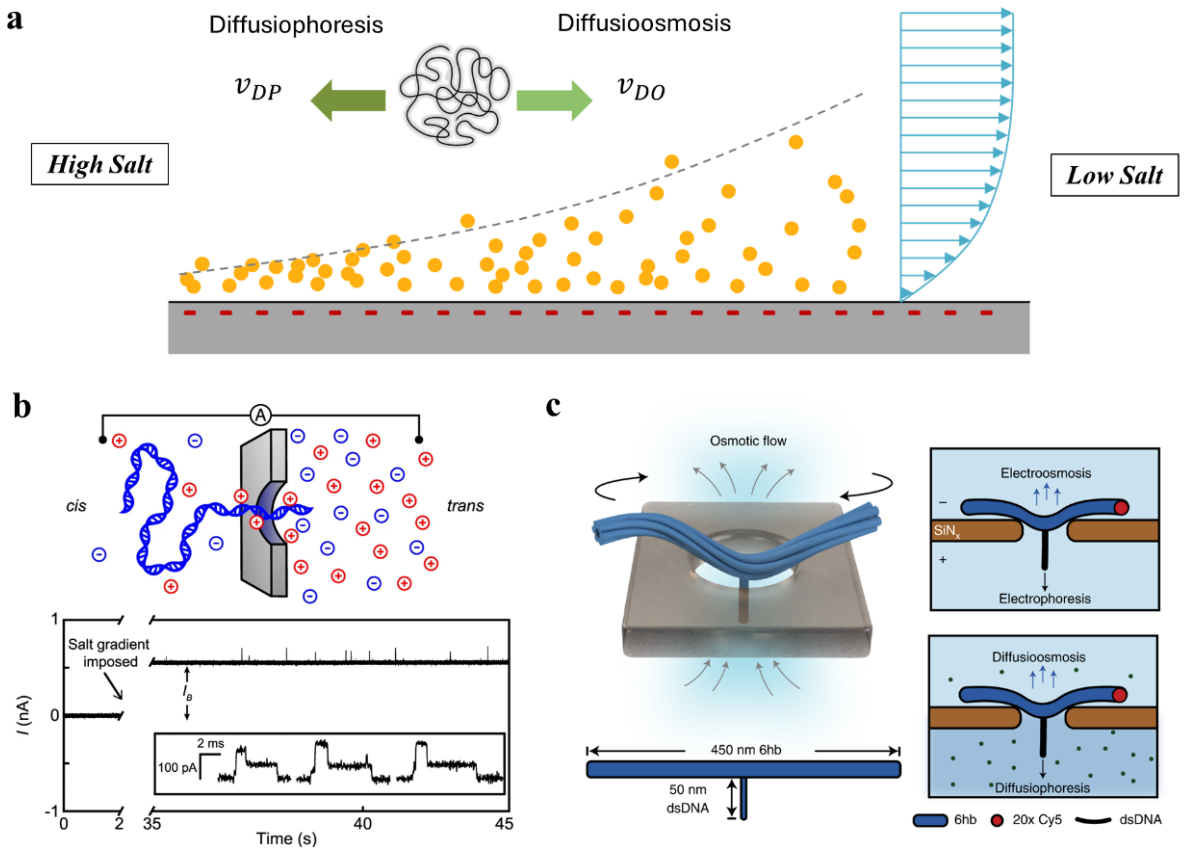

Figure 1.23. Diffusioosmosis and Diffusiophoresis. a) Depiction of diffusiophoresis and diffusioosmosis for a negatively charged DNA near a negatively charged surface. **b)** Diffusioosmosis used to drive polymer translocation through nanopores. Adapted from McMullen *et al.*[98] licensed under CC BY 4.0. **c)** Diffusiophoresis and diffusioosmosis harnessed to rotate a DNA rotor on a nanopore. Reproduced with permission from Springer Nature and Shin *et al.*[99]

Translocation kinetics are studied thoroughly in Chapter 4 using a patterned DNA nanostructure designed such that its instantaneous translocation velocity can be inferred from the blockade's current sublevels. As shown in Figures 1.24a-b, this project builds on the qualitative observations of two prior articles that utilised similar structures to demonstrate the non-uniform velocities expected throughout the translocation process.[67,100] In addition to providing an extensive report of the effects of experimental parameters (including, pore size, polymer length, applied voltage) on translocation velocity profiles, Chapter 4 demonstrates using simple physical insights that information about the forces at play during translocation can be inferred from the velocity

profiles, which allows multiple theoretical principles to be validated. Prior to this work, electrohydrodynamic forces had been characterized using optical tweezers stalling DNA strands into nanopores (Figure 1.24d),[101–105] but the time-dependent forces taking place in free translocations had not been probed. Furthermore, translocation-opposing pore-polymer interactions had been previously characterized in nanopores by measuring the dependence of translocation time on pore size, where significantly longer translocations were observed in smaller pores (Figure 1.24c).[30]

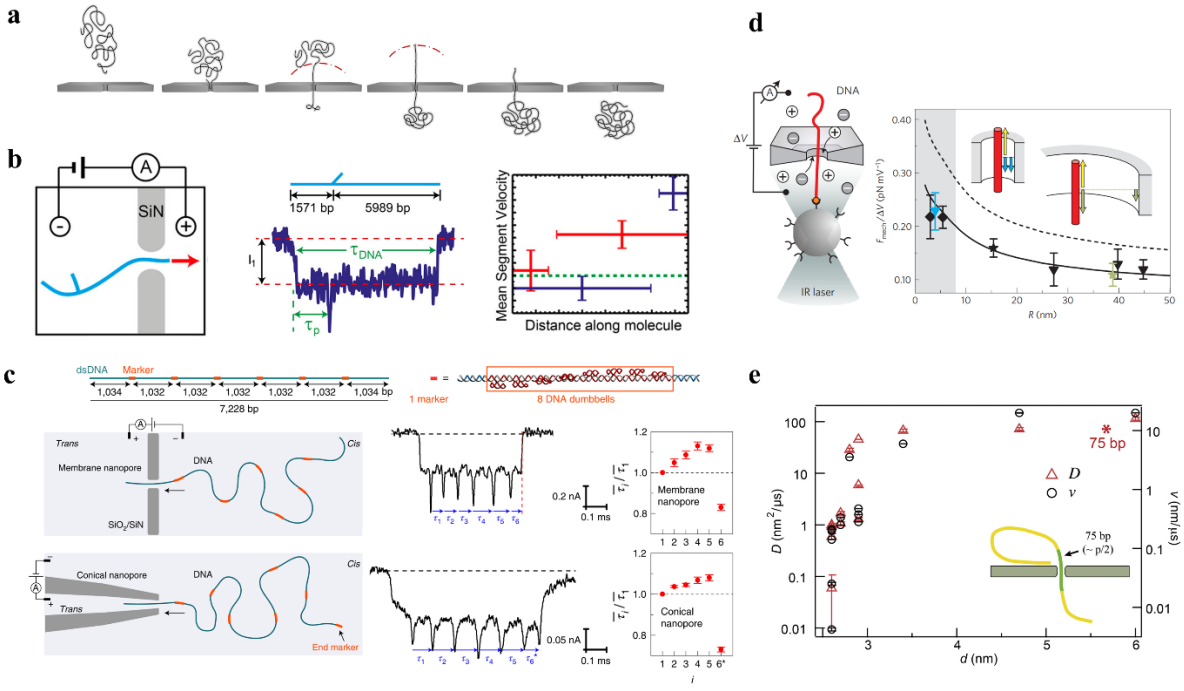

Figure 1.24. Existing experiments that characterized forces and velocities in nanopores. a) Tension propagation schematic. **b)** Translocation velocity extracted from passage of dsDNA strands with protruding markers along its contour. Adapted with permission from Plesa *et al.*[100] Copyright 2015 American Chemical Society. **c)** Patterned DNA nanostructure used to extract translocation velocity fluctuations single events. Reproduced with permission from Springer Nature and Chen *et al.*[67] **d)** Optical tweezer measurements of the force required to stall a DNA inside nanopores of different sizes. Reproduced with permission from Springer Nature and van Dorp *et al.*[101] **e)** Pore-polymer steric interactions probed by measuring the translocation times in different pore sizes. Velocities and diffusion coefficients are plotted instead of translocation times, since Equation 1.11 was used to fit time distributions. Reprinted from Carson *et al.* with permission from Elsevier.[30]

Lastly, Chapter 5 studies the kinetics of folded translocations by looking into the effects of increased polymer rigidity on folding behaviour. Given that many sensing applications require single-file translocations, a better understanding of folding dynamics would be beneficial for nanopore application development. Expanding on observations from Mihovilovic *et al.*[75] which showed that conformational entropic arguments could explain DNA folding statistics, the results from the folding of more rigid polymers show instead a search for energetically-favorable conformations, highlighting the role of rigidity when polymers enter pores.

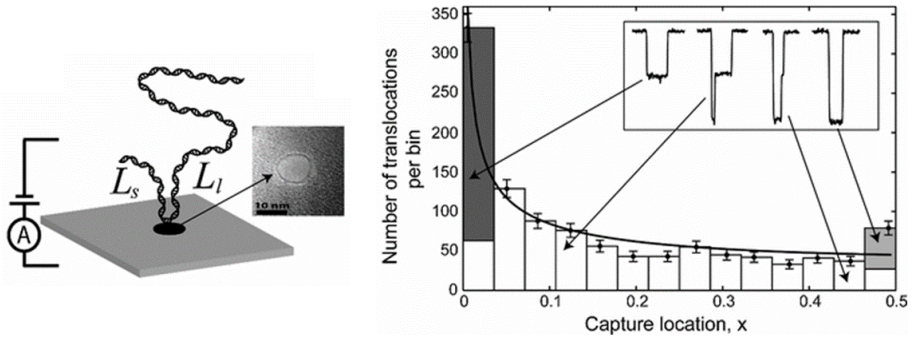

Figure 1.25. Existing studies of folding kinetics. The capture location of folded translocations can be estimated from their signals, the analysis of which shows that DNA prefers to fold near its ends. Reprinted and adapted with permission from Mihovilovic *et al*.[75] Copyright 2013 by the American Physical Society.

Chapter 2. Electric Field and Nanopore Conductance

This chapter contains two closely related manuscripts. Section 2.1 is from an article published in the *Nano Letters* scientific journal titled "Improved Conductance Blockage Modeling of Cylindrical Nanopores, from 2D to Thick Membranes" and authored by Martin Charron, Zachary Roelen, Deekshant Wadhwa and Vincent Tabard-Cossa.* The corresponding Supporting Information is provided in Section 2.2.

Section 2.3 is a submitted manuscript titled "Predicting Resistive Pulse Signatures in Nanopores by Accurately Modeling Access Regions" and is authored by Martin Charron, Zachary Roelen, Deekshant Wadhwa, and Vincent Tabard-Cossa.** The corresponding Supporting Information is provided in Section 2.4.

2.1 Improved Conductance Blockage Modeling of Cylindrical Nanopores, from 2D to Thick Membranes

Martin Charron, Zachary Roelen, Deekshant Wadhwa, Vincent Tabard-Cossa

Abstract

The ionic current blockage from a nanopore sensor is a fundamental metric for characterizing its dimensions and for sizing and identifying molecules translocating through it. Yet, most analytical models predicting the conductance of a nanopore in both open and obstructed states remain inaccurate. Here, using an oblate spheroidal coordinate framework to study the electrical response of nanopore access regions, we reveal that the widely used model from Kowalczyk *et al.* significantly overestimates access region contributions when blocked by a cylindrical object, like DNA. To address this, we present an improved analytical model for the obstructed access resistance, which we establish as highly accurate through finite-element simulations, especially for ultra-thin membranes and long narrow channels. Equipped with an improved nanopore conductance model, this work provides tools for more accurate calculation of the pore size and for the expected blockade from DNA, of high practical value for many biosensing applications.

2.2.1 Introduction

Nanopores have demonstrated their general applicability as part of a new generation of molecular sensing technology by playing a central role in the development of real-time, long-read DNA sequencing, and more recently, by showing a real promise toward disease biomarker detection as well as protein characterization and sequencing.[1–4] Their success relies in part on the simplicity of their operating principles: nanopores are nanoscale holes in thin insulating membranes that partition two electrolyte-filled reservoirs and, under an applied voltage, charged species such as ions and biopolymers are driven through the pore – the passage of the latter can be detected electrically by the momentary reductions in ionic current they create. Most nanopore applications rely on identifying and classifying molecules of interest through their current blockade characteristics, such as the magnitude and duration of different levels in the blockade signal. A physical model able to accurately predict the conductance blockages of biopolymers of known dimensions is therefore of great value in transducing individual nanopore signals into biomolecular identities or reporting on their conformations inside the pore.[48,106,107] Conversely, an accurate conductance model for open and blocked nanopores can be used to infer the dimensions of the nanopore with better accuracy given the known dimensions of the translocating molecule.[108–110] Such a model would thus allow accurate real-time nanopore sizing, which would be of great practical use for solid-state nanopore fabrication techniques that do not directly assess pore diameters visually during fabrication, such as the controlled breakdown method.[15,22]

Kowalczyk *et al.* introduced a model for calculating the conductance of a nanopore in an open and a blocked state, with the latter corresponding to the state wherein a cylindrical obstruction, such as a DNA polymer, is inserted into the nanopore.[41] Despite some of its shortcomings[40,88] (to be discussed in what follows), this model is used extensively in the nanopore

community for the prediction of the blockage depth. Here, we show that the model significantly overestimates the contribution to the conductance blockage from the access regions. Particularly, we use an oblate spheroidal coordinate framework to demonstrate that the expression from Kowalczyk *et al.* corresponds to the resistance of the access region blocked by a hyperboloid obstruction instead of a cylinder, as intended to model a DNA molecule. Using the same framework, we then describe a method to model the access resistance of nanopores in 2D and finite-length membranes in the presence of a true cylindrical obstruction, which we determine to be highly accurate through comparisons with finite element simulations. This improved conductance model also allows for more accurate pore size and length estimation through the open and blocked conductance data of a translocating cylinder-like molecular ruler, and as such a web-based pore size calculator is made available[111] to provide practical value to the nanopore community.

2.1.2 Existing Conductance Model for Open and Blocked States

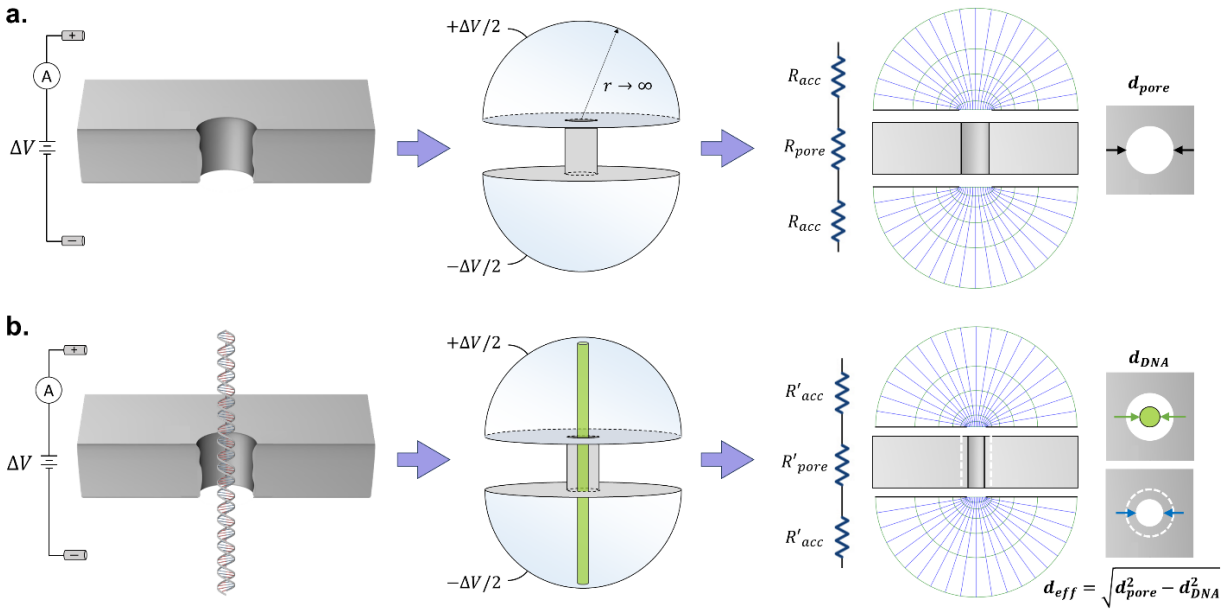

Figure 2.1.1. Depiction of Kowalczyk *et al.* [41] model for nanopore in open and blocked state. **a)** The nanopore is made of two hemispheres, i.e. the two pore access regions, and one cylindrical channel, i.e. the

pore itself. The conductance of the nanopore system is calculated by independently considering the in-series resistive contribution of each region. **b)** In a blocked state, the nanopore system is again considered as three resistances in series, but a reduced effective pore size $d_{eff} < d_{pore}$ is used to account for the presence of a cylindrical object obstructing the pore, like DNA.

Under an applied voltage, the nanopore system can be treated as three conductive regions in series:[45] a cylindrical channel modeling the interior of the pore, and two infinitely large hemispheres modeling the access regions, which span the regions from the nanopore mouth to infinitely far away, on either side of the membrane. If a nanopore with diameter d_{pore} and length L separates two reservoirs containing an ionic solution of conductivity σ, the electrical conductance G_o of the nanopore system is expected to be:

$$G_o(d_{pore}) = \left(R_{pore} + 2R_{acc}\right)^{-1} = \left(\frac{4L}{\sigma\pi d_{pore}^2} + \frac{1}{\sigma d_{pore}}\right)^{-1}. \quad (2.1.1)$$

Here the first resistance term, R_{pore}, corresponds to that of a cylinder of length L and diameter d_{pore}, whereas the second term corresponds to twice the access resistance, R_{acc}, i.e. the electrical resistance between a disk of diameter d_{pore} and an infinitely large hemisphere, as determined by Hall[44] in 1976 (see Figures 2.1.1a-b).

In 2011, Kowalczyk *et al.*[41] suggested that the blocked conductance G' of a nanopore in the presence of a linear polymer such as DNA with a cross-sectional diameter of d_{DNA} could be expressed as:

$$G' = \left(R'_{pore} + 2R'_{acc}\right)^{-1} = \left(\frac{4L}{\sigma\pi\left(d_{pore}^2 - d_{DNA}^2\right)} + \frac{1}{\sigma\sqrt{d_{pore}^2 - d_{DNA}^2}}\right)^{-1} = G_o\left(\sqrt{d_{pore}^2 - d_{DNA}^2}\right). \quad (2.1.2)$$

The blocked state conductance G' (Eq. 2.1.2) has the same form as the open-pore conductance G_o (Eq. 2.1.1), where d_{pore} is replaced by a reduced effective pore diameter corresponding to $d_{eff} = \sqrt{d_{pore}^2 - d_{DNA}^2}$. The use of this reduced effective diameter originates from the presence of a DNA molecule (modelled as a cylinder) inside the cylindrical channel increasing the resistance, R'_{pore}, to a value corresponding to the resistance of an unobstructed cylindrical channel R_{pore} of diameter d_{eff} (see Figure 2.1.1b). This effective diameter is then extended to the access resistance term, $R'_{acc} = R_{acc}(d_{eff})$, to estimate the effect of the presence of DNA in the hemispheres above and below the pore. Naturally, the conductance blockage ΔG expected from a cylindrical linear polymer like DNA fully inserted into a nanopore is simply obtained by subtracting Eq. 2.1.2 from Eq. 2.1.1:

$$\Delta G = G_o(d_{pore}) - G_o\left(\sqrt{d_{pore}^2 - d_{DNA}^2}\right). \tag{2.1.3}$$

Note that Equations 2.1.1-2.1.3 do not consider surface charge nor electro-osmotic flow conduction effects of the polymer or pore surface, which can be especially significant in low salt concentrations (< 1 M) or for small pores comparable in size to the Debye length.[42,96,112] The expressions derived for the rest of this work follow the same assumptions, and are therefore expected to be applicable mostly in the high-salt limit. Nonetheless, Equations 2.1.2-2.1.3 are still commonly used today by researchers to predict blockage amplitudes and to estimate nanopore sizes from conductance data.[110] Next, we mathematically show how this expression of the blocked conductance state overestimates the contribution from the blockage of the access region.

2.1.3. Oblate Spheroidal Coordinates Framework

Farahpour *et al.*[87] showed that the electrical properties of the access resistance in its open state could be calculated using oblate spheroidal coordinates. We now use and expand on this framework to re-interpret the use of the effective diameter, d_{eff}, and improve upon the model from Kowalczyk *et al.*[41], for the access resistance in the blocked state, R'_{acc}.

The oblate spheroidal coordinate system uses the variables $\mu \in [-\infty, \infty]$, $\nu \in [0, \pi/2]$, and $\phi \in [0, 2\pi]$, and is defined by the following coordinate transformations with the cartesian coordinates $(\mu, \nu, \phi) \rightarrow (x, y, z)$:

$$\begin{aligned} x &= c \cosh\mu \cos\nu \cos\phi \\ y &= c \cosh\mu \cos\nu \sin\phi \\ z &= c \sinh\mu \sin\nu. \end{aligned} \tag{2.1.4}$$

Note that the cylindrical coordinate, ρ, i.e. the radial distance from the z-axis, can be similarly defined as $\rho = \sqrt{x^2 + y^2} = c \cosh\mu \cos\nu$ (Figure 2.1.2a). In the oblate spheroidal system, constant-μ, and constant-ν surfaces correspond to oblate spheroids and to one-sheet hyperboloids with a focal ring of radius c, respectively. The reason this curvilinear coordinate system is useful in expressing the conductance of the nanopore is twofold. First, any one-sheet hyperboloid defined by $\nu = \nu_{pore}$ can be chosen to represent the surface of the pore-containing membrane, with the limit of $\nu_{pore} = 0$ corresponding to a pore embedded in a 2D membrane, in which case the focal distance c simply corresponds to the pore radius $c = d_{pore}/2$. Moreover, oblate spheroidal coordinates are useful because of the similarities between constant-μ surfaces and the equipotential surfaces described by Hall,[44] whose access resistance expression is derived from calculating the resistance between a disk electrode at the pore mouth and an infinitely large hemispherical electrode. Notably, since the surface of the oblate spheroid infinitely far from the

pore ($\mu \to \infty$) is congruent to that of an infinitely large sphere, whereas that at the pore mouth ($\mu = 0$) is congruent to that of a disk, the electrical properties of the access region can be determined by further assuming that all the intermediate constant-μ surfaces are also equipotential surfaces (see Figure 2.1.2a).[87]

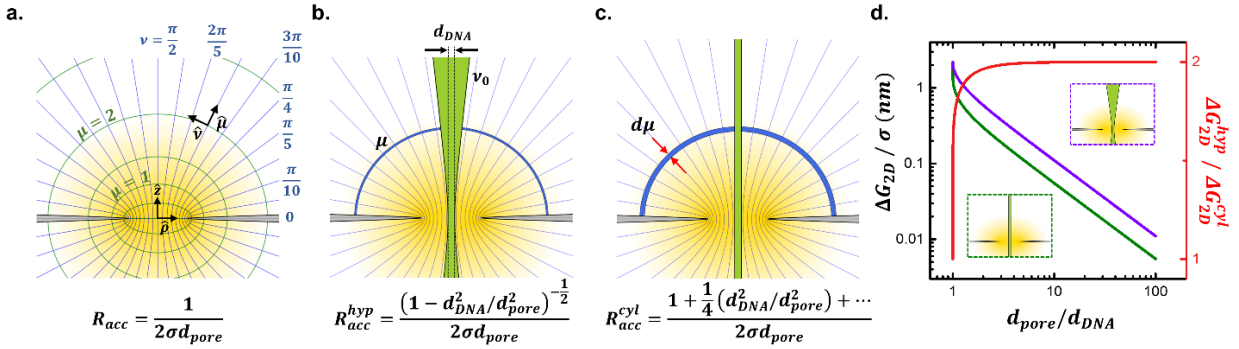

Figure 2.1.2. Calculation of the access region properties of 2D nanopores in different scenarios. The yellow hue depicts the electric field intensity. **a)** Depiction of oblate spheroidal coordinates and the electric field with unobstructed access regions. The open pore access resistance is obtained by integrating the electric flux through the surface of any oblate spheroid at fixed μ. **b)** Access resistance in the presence of a hyperboloidal obstruction (green) calculated by integrating the electric flux through the surface of a punctured oblate spheroid (blue). **c)** Access resistance in the presence of a cylindrical obstruction (green) calculated by integrating the infinitesimal contributions from oblate spheroidal slices (blue) from $\mu = 0$ to ∞. **d)** Comparison of the conductance blockage expected from a 2D nanopore, ΔG_{2D}, as a function of pore size, calculated using a cylindrical and a hyperboloidal obstruction.

Following this assumption and assuming no charge in the system, it is possible to find a solution to the curvilinear Laplace equation: $\nabla^2 V = \frac{\partial}{\partial \mu}\left(\frac{h_\nu h_\phi}{h_\mu}\frac{\partial V}{\partial \mu}\right) = 0$ to solve for the electrical potential $V(\mu)$ and the electric field $\vec{E}(\mu, \nu) = -\frac{1}{h_\mu}\frac{\partial V}{\partial \mu}\hat{\mu}$. Here, $h_\mu = h_\nu = c\sqrt{\sinh^2 \mu + \sin^2 \nu}$ and $h_\phi = c \cosh \mu \cos \nu$ are the scaling factors for oblate spheroidal coordinates. Using $V(0) = 0$ and $V(\mu \to \pm\infty) = \pm \Delta V/2$ as boundary conditions, the electric field between the disk electrode at the pore mouth and an infinitely large hemisphere electrode is found to be:

$$\vec{E}(\mu, \nu) = \frac{\Delta V}{\pi c \cosh \mu \sqrt{\sinh^2 \mu + \sin^2 \nu}}\hat{\mu}. \tag{2.1.5}$$

A detailed derivation of Equation 2.1.5 can be found in Section S2.2.1 of the SI. Note the electric field is directed along $\hat{\mu}$, and depends on both μ and ν, unlike $V(\mu)$.

The electric field can be used to determine the resistance of an unobstructed access region:[87]

$$R_{acc} = \frac{\Delta V/2}{\int_S j \cdot dA} = \frac{\Delta V/2}{\int_0^{2\pi}\int_0^{\frac{\pi}{2}} \sigma E \; h_\nu h_\phi d\phi d\nu} = \frac{1}{2\sigma d_{pore}}. \quad (2.1.6)$$

Here, the denominator corresponds to the total current going through the 2D nanopore system, calculated by integrating the current density $j = \sigma E$ over the surface of a constant-μ oblate spheroid. Equation 2.1.6 corresponds to the access resistance reported by Hall *et al.* and used in Equation 2.1.1 for the open pore conductance. See Section S2.2.2 of the SI for a complete derivation. Having validated the applicability of the oblate spheroidal coordinate system for the electrical response of unobstructed access regions, we now revisit the conductance blockage model from Kowalczyk *et al.*[41] using this new framework.

2.1.4 Hyperboloidal Obstruction of Access Region

We now study how the presence of a hyperboloid obstruction in the access region affects the access resistance, and further show that the resulting expression is identical to that of Kowalczyk *et al.* For a one sheet hyperboloidal obstruction delimited by the coordinate variable ν_0 (see Figure 2.1.2b), the blocked state access resistance R'^{hyp}_{acc} can be found:

$$R'^{hyp}_{acc} = \frac{\Delta V/2}{\int_0^{2\pi}\int_0^{\nu_0} \sigma E \; h_\nu h_\phi d\phi d\nu} = \frac{1}{2\sigma d_{pore}\sin\nu_0} = \frac{1}{2\sigma d_{pore}\sqrt{1-\frac{\rho^2}{c^2}\operatorname{sech}^2\mu\Big|_{\nu=\nu_0}}}. \quad (2.1.7)$$

As per R_{acc} (Eq. 2.1.6), the current is calculated by integrating the current density a fixed-μ oblate spheroid surface and limiting the integration bounds to $0 < \nu < \nu_0$ to account for the presence of the hyperboloid obstruction (See Section S2.2.3 of the SI for a complete derivation). The final expression of Equation 2.1.7 is obtained using the general relation $\sin\nu = \sqrt{1 - \frac{\rho^2}{c^2}\operatorname{sech}^2\mu}$ and restricting the coordinate pairs (ρ, μ) to those lying on the surface of a hyperboloid at $\nu = \nu_0$. Note that if the hyperboloid is chosen to have the diameter of DNA ($\rho = d_{DNA}/2$) at the pore mouth ($\mu = 0$), as in Figure 2.1.2b, the expression for the access resistance in the presence of a hyperboloid obstruction reduces to:

$$R'^{hyp}_{acc} = \frac{1}{2\sigma\sqrt{d_{pore}^2 - d_{DNA}^2}} = R_{acc}\left(d_{eff}\right). \tag{2.1.8}$$

Remarkably, Equation 2.1.8 is identical to the expression from Kowalczyk *et al*., who equated the obstructed access resistance to the open-state access resistance evaluated with an effective diameter $d_{eff} = \sqrt{d_{pore}^2 - d_{DNA}^2}$, as per Equation 2.1.2. Given that the hyperboloidal obstruction described above has a larger volume than a cylindrical one of the same diameter at μ = 0 (as seen in Figure 2.1.2b), it is evident that Equation 2.1.8 overestimates the current blockage induced by a DNA-like cylindrical obstruction in the access region.

2.1.5 Cylindrical Obstruction of Access Region

We now use the oblate spheroidal coordinate framework outlined above to estimate the impact of an infinitely long cylindrical obstruction on the electrical response of access regions, as to accurately model blockages from biomolecules like DNA. To achieve this, we first partition the access region into an infinite number of oblate spheroidal slices of thickness $d\mu$ for $\mu \in (0, \infty)$

(Figure 2.1.2c). The μ-dependent infinitesimal resistance can be calculated as the ratio of the voltage drop $\delta V(\mu)$ and current $I(\mu)$ across each oblate spheroidal slice, which in turn can be evaluated by assuming that constant-μ surfaces are equipotential surfaces, or equivalently that the electric field is unaltered by the presence of the obstruction (Eq. 2.1.5):

$$dR'(\mu) = \frac{\delta V(\mu)}{I(\mu)} = \frac{E h_\mu d\mu}{\int_0^{2\pi}\int_0^{\nu_{DNA}(\mu)} \sigma E\, h_\nu h_\phi d\phi d\nu} = \frac{\operatorname{sech}\mu\, d\mu}{\pi\sigma d_{pore}\sqrt{1-\frac{d_{DNA}^2}{d_{pore}^2}\operatorname{sech}^2\mu}}. \quad (2.1.9)$$

See Section S2.2.4 of the SI for a more detailed derivation. To obtain the final expression of Eq. 2.1.9, the parametrization of the cylindrical obstruction surface $\nu_{DNA}(\mu)$ was used to delimit the μ-dependent integration bounds $0 < \nu < \nu_{DNA}(\mu)$:

$$\nu_{DNA}(\mu) = \sin^{-1}\left(\sqrt{1-\frac{d_{DNA}^2}{d_{pore}^2}\operatorname{sech}^2\mu}\right). \quad (2.1.10)$$

An expression for the access region resistance in the presence of a cylindrical obstruction of diameter d_{DNA}, $R_{acc}^{\prime cyl}$, can be found by integrating the infinitesimal resistance $dR'(\mu)$ (Eq. 2.1.9) from $\mu = 0$ to $\mu \to \infty$.

$$R_{acc}^{\prime cyl} = \int_{\mu=0}^{\mu=\infty} dR'(\mu) = \frac{K\left(\frac{d_{DNA}}{d_{pore}}\right)}{\pi\sigma d_{pore}} = \frac{1+\frac{1}{4}\left(\frac{d_{DNA}}{d_{pore}}\right)^2+\frac{9}{64}\left(\frac{d_{DNA}}{d_{pore}}\right)^4+\cdots}{2\sigma d_{pore}}. \quad (2.1.11)$$

Here, $K\left(d_{DNA}/d_{pore}\right)$ denotes the complete elliptical integral of the first kind function evaluated at an argument of d_{DNA}/d_{pore} – the first few expansion terms of this function are explicitly written out in Eq. 2.1.11. Details for the derivation can be found in Section S2.2.4 of the SI. Note that the expression for $R_{acc}^{\prime cyl}$ corresponds simply to the sum of the open-state access

resistance, R_{acc}, and of a correction term that depends solely on the dimensionless d_{DNA}/d_{pore} ratio. Furthermore, $R_{acc}^{\prime cyl}$ is equivalent to R_{acc} in the case of $d_{DNA}/d_{pore} \to 0$, and diverges to infinity as $d_{DNA}/d_{pore} \to 1$, as expected. Before inserting Equation 2.1.11 into the resistors-in-series model for finite-length cylindrical pores, as per Equations 2.1.2 and 2.1.3, we begin by discussing and quantifying the differences between the access resistance expressions from the model of Kowalczyk *et al.* and this work.

2.1.6 Hyperboloidal vs Cylindrical Obstruction – 2D Pore Blockage Model comparison

To gain further insight into the nature and predictions of both the model from Kowalczyk *et al.* and the model presented herein (Eq. 2.1.11), we now compare the conductance blockage expected from each model for the case of a pore in a 2D membrane, since such planar membrane geometry omits contributions from R_{pore}, and thus presents an insightful comparison of the changes in the access region. In the limit of $d_{DNA} \ll d_{pore}$, the conductance blockage takes the form:

$$\Delta G_{2D}^{hyp} = \frac{1}{2R_{acc}} - \frac{1}{2R'^{hyp}_{acc}} = \sigma d_{pore} - \sigma d_{pore}\sqrt{1-\left(\frac{d_{DNA}}{d_{pore}}\right)^2} \approx \frac{1}{2}\sigma\frac{d_{DNA}^2}{d_{pore}} \qquad (2.1.12)$$

$$\Delta G_{2D}^{cyl} = \frac{1}{2R_{acc}} - \frac{1}{2R'^{cyl}_{acc}} = \sigma d_{pore} - \frac{\sigma d_{pore}}{1+\frac{1}{4}\left(\frac{d_{DNA}}{d_{pore}}\right)^2 + \cdots} \approx \frac{1}{4}\sigma\frac{d_{DNA}^2}{d_{pore}}. \qquad (2.1.13)$$

The above approximations show that both models predict conductance blockages scaling inversely with d_{pore} however the model by Kowalczyk *et al.*, through its unintended use of a hyperboloidal obstruction to model DNA, predicts 2× the blockage as that of a cylindrical obstruction in this limit. Figure 2.1.2d shows the dependence of the conductance blockage of both models on pore size. As expected, both models converge for $d_{pore} = d_{DNA}$ since the current is fully blocked.

Surprisingly, the discrepancy in access region blockage stabilizes swiftly with respect to pore size, as demonstrated by ΔG_{2D}^{hyp} being 1.96× ΔG_{2D}^{cyl} for a pore size as small as $d_{pore} = 2d_{DNA}$. Section S2.2.5 of the SI discusses in more details how the 2× plateau originates from a balance of the pore-size dependencies of both the electric field distribution and hyperboloid obstruction geometry.

2.1.7 3D Pore Blockage Model – Comparison with Simulated Data

We now attempt to improve the conductance model of a finite-length cylindrical nanopore by introducing the updated access resistance expression (Eq. 2.1.11) into the resistors-in-series model (Eq. 2.1.2). In doing so, we obtain a revised expression for the expected blocked conductance of a nanopore of length L obstructed by a cylindrical polymer model for DNA of diameter d_{DNA}:

$$G'^{cyl}(d_{pore}) = \left(R'_{pore} + 2R'^{cyl}_{acc}\right)^{-1} = \left(\frac{4L}{\sigma\pi\left(d_{pore}^2 - d_{DNA}^2\right)} + \frac{2K\left(\frac{d_{DNA}}{d_{pore}}\right)}{\pi\sigma d_{pore}}\right)^{-1}. \quad (2.1.14)$$

Again, the expected conductance blockage ΔG is obtained by subtracting the blocked-state conductance G'^{cyl} to the open pore conductance G_o (Eq. 2.1.1):

$$\Delta G(d_{pore}) = G_o(d_{pore}) - G'^{cyl}(d_{pore}). \quad (2.1.15)$$

To establish how well Equation 2.1.15 predicts conductance blockages for different pore diameters and lengths, finite element simulations were performed. In these simulations a voltage ΔV was applied across a nanopore in a perfectly insulating membrane both with and without the presence of a cylindrical obstruction of diameter $d_{DNA} = 2.2$ nm. Conductance blockage values were obtained from the simulations (see Methods) and used as benchmarks to assess the accuracy

of the conductance blockage models of Kowalczyk *et al.* and from this work (Eq. 2.1.15) for a corresponding cylindrical nanopore geometry. Figure 2.1.3a plots simulated values of $\Delta G/\sigma$, the conductance blockage normalized by the electrolyte conductivity, for various pore diameters and the corresponding analytical predictions from both models (purple, Kowalczyk *et al.* and green, this work), with different panels corresponding to different membrane thicknesses. Notably, the model by Kowalczyk *et al.* significantly overestimates the conductance blockage for most pore geometries simulated, except in the limit of $d_{pore} = d_{DNA}$, where both models and simulations converge. While the analytical conductance blockage model from this work (Eq. 2.1.15) very slightly overestimates the conductance blockage for all pore dimensions tested, it consistently offers significantly more accurate estimates, especially for thin membranes.

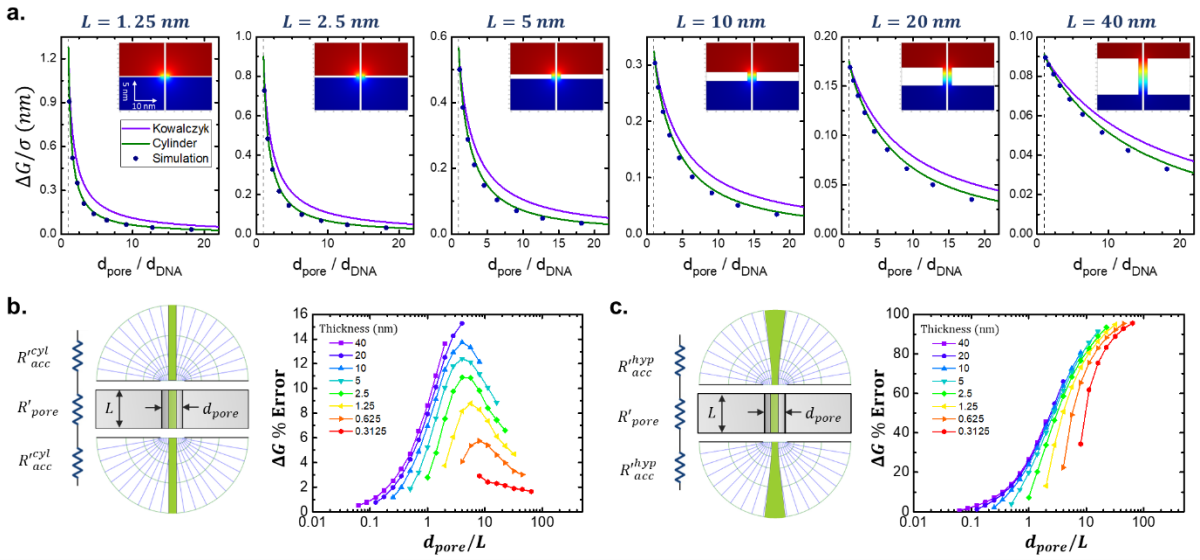

Figure 2.1.3. Simulated vs modeled conductance. Comparison of conductance model predictions with finite element simulations for nanopores obstructed by a 2.2 nm cylinder under various cylindrical pore dimensions. **a)** Dependence of conductance blockage on pore size. Individual graphs plot the normalized conductance blockage $\Delta G/\sigma$ against the normalized pore size d_{pore}/d_{DNA} obtained from simulations (blue scatter), from modeling a hyperboloidal obstruction (purple), and from modeling a cylindrical obstruction (green). **b)** Error percentage calculated between simulations and the predictions from the improved conductance model (Eq. 2.1.15). Each curve corresponds to a different pore length. **c)** Error percentage calculated between simulations and the predictions from the model of Kowalczyk *et al.* (Eq. 2.1.3).

Figures 2.1.3b and 2.1.3c plot the percentage differences between values of $\Delta G/\sigma$ obtained through simulations, and through our improved model (modeling DNA as a cylinder) and that of Kowalczyk *et al.* (modeling DNA as a hyperboloid), respectively. For both cases, the error percentages are plotted against d_{pore}/L, the pore diameter normalized by the pore length, a dimension ratio proportional to the resistance ratio R_{acc}/R_{pore}, i.e. the ratio of access to pore resistance in the open state. Figure 2.1.3b reveals that the percentage error for different membrane thicknesses obtained using our model, Equation 2.1.15, exhibits non-monotonic dependencies on d_{pore}/L. Notably, for all tested pore lengths, the errors from the $\Delta G'^{cyl}$ model appear to approach a negligibly small error in the limits of $d_{pore}/L \to 0$ and $d_{pore}/L \to \infty$, which correspond to regimes where only the pore resistance R_{pore} or the access resistance R_{acc}^{cyl} is dominating, respectively. We consider this observation compelling evidence that both R'_{pore} and R'^{cyl}_{acc} (Eq. 2.1.13) are highly accurate solutions to the respective cases of obstructed long narrow 3D channels ($d_{pore} \ll L$), and 2D membranes ($d_{pore} \gg L$).

For all simulated pore lengths, the $\Delta G'^{cyl}$ model prediction error is maximal in the range $d_{pore}/L = 4 – 6$, the value of which increases monotonically with L. This is expected since it can be shown that the percentage error of ΔG is inversely dependent on its magnitude, which decreases with increasing L. As a reference, the maximum error for a 0.625 nm thick membrane is ~6%, whereas it is ~12.5% for a 5 nm thick membrane. Figure 2.1.3c shows the analogous error percentage of the model from Kowalczyk *et al.* and demonstrates that error percentages for ΔG predictions increase monotonically with d_{pore}/L and appear to converge to 100% in the limit of $d/L \to \infty$. Given that this limit corresponds to 2D membranes, this further validates our earlier

discussion stating that the model by Kowalczyk *et al.* overestimates the access region blockage by a factor of 2 (Figure 2.1.2d). See Section S2.2.6 of the SI for more model-simulation comparisons.

As mentioned, given known dimensions of a cylinder-like obstruction and experimentally measured values of G_o and ΔG (or G'^{cyl}), conductance models can be used to estimate the dimensions, d_{pore} and L, of cylindrical pores. In Section S2.2.7 of the SI, we test and compare the ability of our model (Equation 2.1.15) and that of Kowalczyk *et al.* to extract pore diameters and lengths using open and blocked pore conductance values obtained from simulations. Like Figure 2.1.3, Figures S2.2.4 and S2.2.5 show a significant improvement in determining pore sizes and thicknesses through Equations 2.1.1 and 2.1.15, yet errors can remain important, especially for predicting the thicknesses of thin membranes. We note correspondingly that a web-based pore dimension calculator was made available to perform such calculations.[111]

Although the incorporation of our improved access resistance model has led to very accurate conductance blockage predictions for cylindrical pores with extreme dimensions, i.e. $d_{pore} \ll L$ and $d_{pore} \gg L$, the error for intermediate pore sizes is non-negligible, especially for $d_{pore}/L \approx 5$ (Figure 2.1.3b), as discussed. Such errors result from two inexact model assumptions regarding the potential and electric fields: field lines are assumed to be unimpacted by the presence of insulating obstructions and disks at the pore mouths are assumed to be equipotential surfaces.[88,108,113,114] Section S2.2.8 of the SI further discusses and visualizes the origin of these inexact assumptions. It should be further noted that due to the purely geometric nature of our model, larger errors can be expected when compared to experimental results due to unaccounted electrokinetic and electrohydrodynamic phenomena, to off-axis translocations and to non-cylindrical pore shapes, which are all known to alter conductance blockage amplitudes.[41,42,96,115,116]

In conclusion, in addition to clearly demonstrating why the use of a reduced effective diameter $d_{eff} = \left(d_{pore}^2 - d_{DNA}^2\right)^{1/2}$ overestimates blocked-state access region contributions, we have shown that an oblate spheroidal framework allows for accurate estimates of access resistance for pores of various dimensions in the presence of cylindrical obstructions, especially in the limits of ultra-thin membranes or long and narrow channels where solutions appear to be close to exact. In addition to better ΔG predictions, the proposed conductance model refinement allows for more accurate pore dimension extraction for measured values of G_o and ΔG (see Section S2.2.7 of the SI). A web-application was thus made available for anyone interested in real-time estimating pore dimensions from experimental data.[111] We believe the framework, model and tools[111] presented here can be useful for the rapidly advancing field of nanopores formed in ultra-thin materials, and hope the accompanying discussions serve to inform readers regarding the limitations of different conductance models, including the one introduced in this work.

2.1.8 Methods

Simulations: Finite element simulations were performed with the COMSOL Multiphysics 5.1 software. In its open state, a nanopore was modeled as a channel of diameter d_{pore} in an insulating membrane of thickness L (a.k.a. pore length), centred inside a cylindrical meshing domain of length 10 μm and diameter 5 μm. In its blocked state, a perfectly cylindrical insulating obstruction of diameter $d_{DNA} = 2.2\ nm$ and length 5 μm was added in the center of the system. Solutions to Poisson's equation were found within the finite-resistivity regions of a given geometry, using boundary conditions of 0.2 V and 0 V at the top and bottom surfaces of the meshing domain, respectively. The resulting electric field was calculated in both open and blocked states such that the numerical solver converged as the mesh size was reduced. The electric flux Φ was calculated by integrating the electric field through the plane disk in the middle of the

membrane, i.e. along the reflective symmetry plane of the system. The value of the normalized conductance blockage, $\Delta G/\sigma$, for the simulation parameters were then obtained by dividing the electric flux by the applied voltage since $\Delta G/\sigma = \Phi/\Delta V$, by Ohm's law and the definition of these quantities.

2.2 Supporting Information for Section 2.1

S2.2.1. Potential and Electric Field Solutions for a 2D Membrane

A proper electric field description in the nanopore access region can be described by calculating the field between a planar disk electrode at the pore mouth and a spherical electrode located at infinity, between which is applied a potential difference of amplitude $\Delta V/2$. In 2013, a thorough solution was described by Farahpour *et al.*[87] with the use of an oblate spheroidal coordinate system defined by the coordinate transformation $(\mu, \nu, \phi) \rightarrow (x, y, z)$:

$$\begin{aligned} x &= c \cosh\mu \cos\nu \cos\phi \\ y &= c \cosh\mu \cos\nu \sin\phi \\ z &= c \sinh\mu \sin\nu\,. \end{aligned} \tag{S2.2.1}$$

The Poisson equation can be solved with the assumption that the potential V depends only on μ:

$$0 = \nabla^2 V = \frac{1}{h_\mu h_\nu h_\phi} \frac{\partial}{\partial \mu}\left(\frac{h_\nu h_\phi}{h_\mu}\frac{\partial V}{\partial \mu}\right). \tag{S2.2.2}$$

Here h_μ, h_ν and h_ϕ are scaling factors defined as $h_u = \sqrt{\left(\frac{\partial x}{\partial u}\right)^2 + \left(\frac{\partial y}{\partial u}\right)^2 + \left(\frac{\partial z}{\partial u}\right)^2}$ for $u = \mu, \nu, \phi$:

$$\begin{aligned} h_\mu &= h_\nu = c\sqrt{\sinh^2\mu + \sin^2\nu} \\ h_\phi &= c \cosh\mu \cos\nu\,. \end{aligned} \tag{S2.2.3}$$

Solving the curvilinear Laplacian:

$$\begin{aligned} 0 &= \frac{1}{c^3(\sinh^2\mu + \sin^2\nu)\cosh\mu\cos\nu}\frac{\partial}{\partial\mu}\left(c\cosh\mu\cos\nu\frac{\partial V}{\partial\mu}\right) \\ 0 &= \frac{\partial}{\partial\mu}\left(\cosh\mu\frac{\partial V}{\partial\mu}\right) \\ \mathrm{c}_1 &= \cosh\mu\frac{\partial V}{\partial\mu} \\ V(\mu) &= c_1\int\frac{d\mu}{\cosh\mu} \\ V(\mu) &= c_1\tan^{-1}(\sinh\mu) + c_2, \end{aligned}$$

where c_1 and c_2 are integration constants. Applying boundary conditions: $V(0) = 0 \rightarrow c_2 = 0$, $V(\infty) = \Delta V/2 \rightarrow c_1 = \frac{\Delta V}{\pi}$ leads to:

$$V(\mu) = \frac{\Delta \mathrm{V}}{\pi} \tan^{-1}(\sinh \mu)\,. \tag{S2.2.4}$$

From this, the electric field can be calculated:

$$\vec{E}(\mu, \nu) = -\frac{1}{h_\mu}\frac{dV}{d\mu}\hat{\mu} = -\frac{\Delta V}{\pi c \cosh \mu \sqrt{\sinh^2 \mu + \sin^2 \nu}}\hat{\mu}. \tag{S2.2.5}$$

Note the electric field is directed along $\hat{\mu}$, and depends on both μ and ν, unlike $V(\mu)$. In particular, the electric field in the plane of the pore opening (μ = 0) is predicted to increase in magnitude toward the outside edge of a 2D pore and in fact diverges as $\nu \rightarrow 0$ at the pore boundary. Furthermore, the expected inverse square dependence of the electric field on radial distance,[60,117] is recovered far away from the pore. First note that far away from the pore, $\cosh^2 \mu \approx \sinh^2 \mu \gg 1$, and thus:

$$E(\mu, \nu) \approx \frac{\Delta V}{\pi c \cosh \mu \sinh \mu} \approx \frac{\Delta V}{\pi c \cosh^2 \mu}. \tag{S2.2.6}$$

The radial distance away from the center of the pore mouth r can be expressed as:

$$r^2 = x^2 + y^2 + z^2 \approx c^2 \cosh^2 \mu\,. \tag{S2.2.7}$$

Inserting this into the electric field expression results in the field expected from a radially symmetric point current source, with I_{2D} corresponding to the current through a 2D membrane:

$$E(r \gg 1) = \frac{c\Delta V}{\pi r^2} = \frac{d_{pore}\Delta V}{2\pi r^2} = \frac{\sigma d_{pore}\Delta V}{\sigma(2\pi r^2)} = \frac{\frac{\Delta V}{(2R_{acc})}}{\sigma(2\pi r^2)} = \frac{1}{\sigma}\frac{I_{2D}}{A_{hemis.}(r)} = \frac{j(r)}{\sigma}. \tag{S2.2.8}$$

S2.2.2. Open-Pore Access Resistance Calculation

We can obtain an access resistance expression using Ohm's law, where the current I is calculated by integrating the current density $j = I/A = \sigma E$ over the surface of any oblate spheroid A. A potential difference of $\Delta V/2$ is used to address the resistance of a single access region:

$$\begin{aligned}
\frac{1}{R_{acc}} &= \frac{I}{\frac{\Delta V}{2}} \\
&= \frac{1}{\frac{\Delta V}{2}} \int_0^{2\pi} d\phi \int_0^{\frac{\pi}{2}} \sigma |E|\, h_\nu h_\phi d\nu \\
&= \frac{\sigma}{\frac{\Delta V}{2}} \int_0^{2\pi} d\phi \int_0^{\frac{\pi}{2}} \frac{1}{h_\nu} \frac{dV}{d\mu} h_\nu h_\phi \, d\nu \\
&= \frac{\sigma}{\Delta V/2} \int_0^{2\pi} d\phi \int_0^{\pi/2} \left(\frac{\Delta V}{\pi \cosh \mu}\right) (c \cosh \mu \cos \nu) \, d\nu \\
&= 4\sigma c \int_0^{\pi/2} \cos \nu \, d\nu \\
&= 4\sigma c.
\end{aligned}$$

$$\therefore R_{acc} = \frac{1}{4\sigma c} = \frac{1}{2\sigma d_{pore}}. \tag{S2.2.9}$$

S2.2.3. Access Resistance in Blocked State – Hyperboloidal Obstruction

We can calculate the resistance of the access region obstructed by a hyperboloid as per Section S2.2.2, but limiting the ν integral bounds to $0 < \nu < \nu_o$:

$$\begin{aligned}
\frac{1}{R'^{hyp}_{acc}} &= \frac{I}{\frac{\Delta V}{2}} \\
&= \frac{1}{\frac{\Delta V}{2}} \int_0^{2\pi} d\phi \int_0^{\nu_o} \sigma |E|\, h_\nu h_\phi d\nu \\
&= 4\sigma c \int_0^{\nu_0} \cos \nu \, d\nu \\
&= 4\sigma c \sin \nu_0 \\
R_{acc} &= \left(2\sigma d_{pore} \sin \nu_o\right)^{-1}.
\end{aligned} \tag{S2.2.10}$$

S2.2.4. Access Resistance in Blocked State – Cylindrical Obstruction

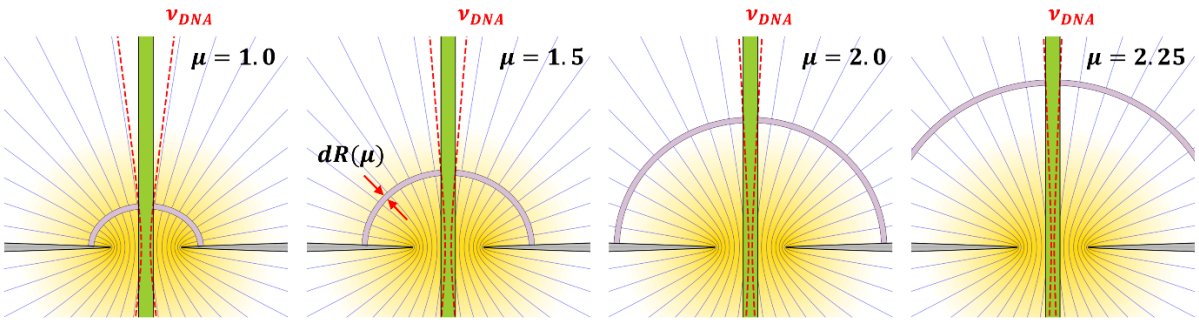

Figure S2.2.1. Oblate spheroidal slice method visualized. Sketch demonstrating the thin slices from which the infinitesimal resistances are calculated at different values of μ. The red dashed lines correspond to the hyperboloid surfaces used to calculate the current $I^{hyp}(\mu)$.

As discussed in the main text, the access resistance in the presence of a cylindrical obstruction can be calculated by summing up the infinitesimal resistances of thin oblate spheroidal slices partitioning the access region from $\mu = 0$ to $\mu \to \infty$:

$$R'^{cyl}_{acc} = \int_0^\infty dR'(\mu)\,. \tag{S2.2.11}$$

The μ-dependent resistance of an oblate spheroid slice can be calculated as the ratio of the potential difference $\delta V(\mu)$ and the current $I(\mu)$ running through it: $dR'(\mu) = \delta V(\mu)/I(\mu)$. Both values can be estimated by using the obstruction-free electric field expression, and thus assuming that oblate spheroid surfaces are equipotential surfaces. Given this assumption, we note that the resistance $dR'(\mu)$ of the thin slice is the same whether it is punctured by a cylindrical obstruction of diameter d_{DNA}, or by a hyperboloid obstruction lying along $\nu_{DNA}(\mu)$ (Figure S2.2.1), defined as:

$$\nu_{DNA}(\mu) = \sin^{-1}\left(\sqrt{1 - \frac{d_{DNA}^2}{d_{pore}^2}\operatorname{sech}^2\mu}\right). \tag{S2.2.12}$$

The resistance of the infinitesimal slice at μ is calculated as:

$$\begin{aligned} dR'(\mu) &= \frac{\delta V(\mu)}{I(\mu)} \\ &= \frac{E(\mu,\nu)h_\mu d\mu}{\int_0^{2\pi} d\phi \int_0^{\nu_{DNA}(\mu)} \sigma E\, h_\nu h_\phi d\nu} \\ &= \frac{\frac{\Delta V}{\pi c \cosh\mu \sqrt{\sinh^2\mu + \sin^2\nu}}\, c\sqrt{\sinh^2\mu + \sin^2\nu}\, d\mu}{2\sigma c \sin\nu_{DNA}(\mu)\, \Delta V} \\ &= \frac{d\mu}{2\pi\sigma c \cosh\mu \sin\nu_{DNA}(\mu)}. \end{aligned}$$

$$\therefore dR'(\mu) = \frac{\operatorname{sech}\mu\, d\mu}{\pi\sigma d_{pore}\sqrt{1 - \frac{d_{DNA}^2}{d_{pore}^2}\operatorname{sech}^2\mu}}. \quad \text{(S2.2.13)}$$

The access resistance can now be calculated by integrating $dR'(\mu)$:

$$R'^{cyl}_{acc} = \frac{1}{\pi\sigma d_{pore}}\int_0^\infty \frac{\operatorname{sech}\mu\, d\mu}{\sqrt{1 - \frac{d_{DNA}^2}{d_{pore}^2}\operatorname{sech}^2\mu}} = \frac{1}{\pi\sigma d_{pore}}\int_0^{\frac{\pi}{2}} \frac{d\theta}{\sqrt{1 - \frac{d_{DNA}^2}{d_{pore}^2}\sin^2\theta}}. \quad \text{(S2.2.14)}$$

The last expression is obtained by the variable change $\theta = \sin^{-1}(\operatorname{sech}\mu)$, such that $\operatorname{sech}\mu = \sin\theta$, and $\operatorname{sech}\mu\, d\mu = -d\theta$. The resulting integral is a well-known function that corresponds to $K(d_{DNA}/d_{pore})$, the complete elliptic integral of the first kind, for which a series expansion is known. The expression for the resistance of an access region obstructed by an infinitely long cylinder is therefore:

$$R'^{cyl}_{acc} = \frac{K\left(\frac{d_{DNA}}{d_{pore}}\right)}{\pi\sigma d_{pore}} = \frac{\frac{\pi}{2}\sum_{n=0}^{\infty}\left(\frac{(2n)!}{2^{2n}(n!)^2}\right)^2\left(\frac{d_{DNA}}{d_{pore}}\right)^{2n}}{\pi\sigma d_{pore}} = \frac{1 + \frac{1}{4}\left(\frac{d_{DNA}}{d_{pore}}\right)^2 + \frac{9}{64}\left(\frac{d_{DNA}}{d_{pore}}\right)^4 + \cdots}{2\sigma d_{pore}}. \quad \text{(S2.2.15)}$$

S2.2.5. Hyperboloidal vs Cylindrical Obstruction – Comparison Details

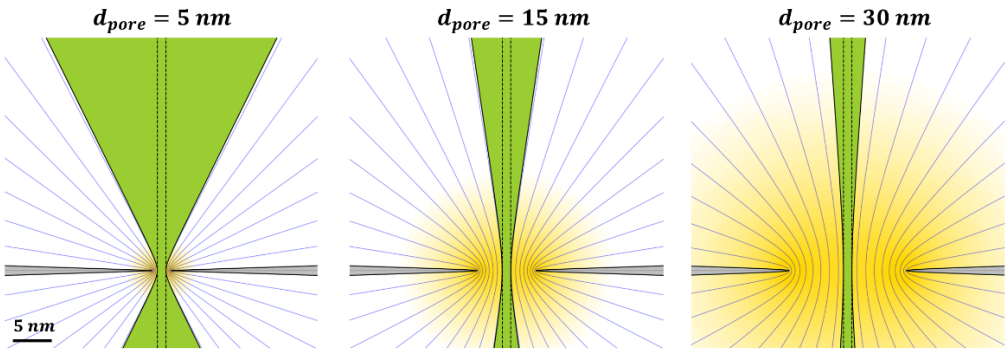

Figure S2.2.2. Hyperboloidal obstruction of fixed waist in different sized pores. Effect of pore size on distribution of electric field and shape of hyperboloid with a fixed waist diameter of d_{DNA} at $\mu = 0$.

To further depict the origin of the discrepancy between the model from Kowalczyk *et al.* and the model from this work, Figure S2.2.2 plots the re-interpretation of the model of Kowalczyk *et al.,* wherein the intended cylindrical DNA obstruction takes the form of a hyperboloid in the access region of different pore sizes. As illustrated in Figure S2.2.2, the shape of the hyperboloid depends significantly on the pore diameter. This is because the oblate spheroidal coordinate system used to parametrize the blocking hyperboloid (of fixed waist diameter d_{DNA} at $\mu = 0$) depends directly on pore size through the focal distance $c = d_{pore}/2$. The hyperboloid thus takes up a larger volume within the access region for smaller pore sizes, whereas its geometry more closely resembles that of a cylinder for larger pore sizes. Although the geometry of cylinders and hyperboloids differ most for smaller pores, the electric field extends less outside the pore in this limit than it does for bigger pores, and this latter effect leads the different geometries of the blocking object to contribute less towards the overall resistance calculation. As shown in Figure 2.2.2e, these two opposing effects balance out as pore size is increased for $d_{pore} > 2d_{DNA}$, resulting in a fixed 2x conductance blockage overestimate by the model of Kowalczyk *et al*.

S2.2.6. Error Percentages of Conductance Models

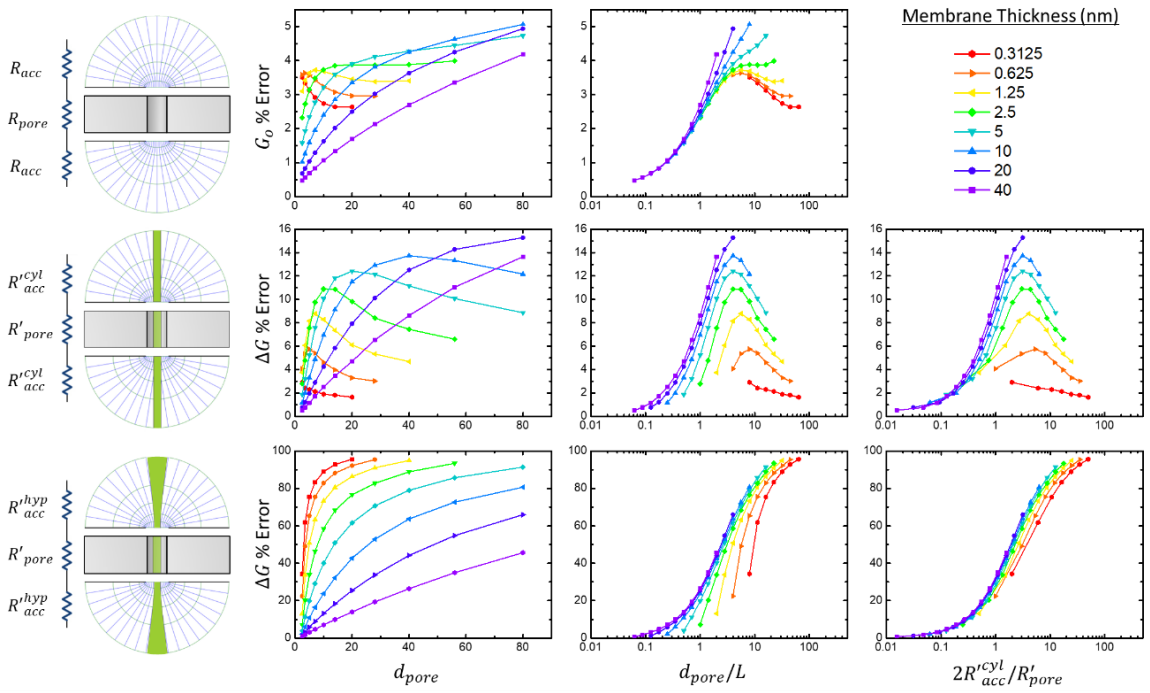

Figure S2.2.3. Conductance model error. Error percentages for the resistors-in-series models for the open pore conductance G (Eq. 2.1.1 in main text), the conductance blockage ΔG due to a cylindrical obstruction (Eq. 2.1.15 in main text), and the conductance blockage ΔG from Kowalczyk *et al.*[41] (Eq. 2.1.3 in main text). In the separate columns, the error percentages are plotted respectively against the pore diameter d_{pore}, the open-pore resistance ratio $2R_{acc}/R_{pore}$, and the blocked state resistance ratio $2R'^{cyl}_{acc}/R'_{pore}$.

S2.2.7. Extracting Pore Dimensions from Open and Blocked Conductance Values

If a cylindrical insulating molecule with a known cross-sectional diameter d_{DNA} goes through a nanopore of unknown dimensions, the pore diameter d_{pore} and length L can be estimated using the open and blockade state conductance expressions presented in the main text (Eq. 2.1.1 and 2.1.14):

$$\frac{G_o}{\sigma} = \left(\frac{4L}{\pi d_{pore}^2} + \frac{1}{d_{pore}}\right)^{-1},$$

$$\frac{G'}{\sigma} = \left(\frac{4L}{\pi\left(d_{pore}^2 - d_{DNA}^2\right)} + \frac{2K\left(\frac{d_{DNA}}{d_{pore}}\right)}{\pi d_{pore}} \right)^{-1}. \quad \text{(S2.2.16)}$$

Given experimental values (G_o, G'), there exists corresponding geometric pair(s) $\left(d_{pore}, L\right)$. From each of the above two equations, we isolate expressions relating L and d_{pore}:

$$L\left(d_{pore}\right) = \frac{\pi}{4} d_{pore}^2 \left(\frac{\sigma}{G_o} - \frac{1}{d_{pore}} \right), \quad \text{(S2.2.17)}$$

$$L'^{(d_{pore})} = \frac{\pi}{4}\left(d_{pore}^2 - d_{DNA}^2\right)\left(\frac{\sigma}{G'} - \frac{2K\left(\frac{d_{DNA}}{d_{pore}}\right)}{\pi d_{pore}} \right). \quad \text{(S2.2.18)}$$

We then find which value of d_{pore} results in $L = L'$:

$$\frac{\pi}{4} d_{pore}^2 \left(\frac{\sigma}{G_o} - \frac{1}{d_{pore}} \right) = \frac{\pi}{4}\left(d_{pore}^2 - d_{DNA}^2\right)\left(\frac{\sigma}{G'} - \frac{2K\left(\frac{d_{DNA}}{d_{pore}}\right)}{\pi d_{pore}} \right). \quad \text{(S2.2.19)}$$

This is equivalent to finding the roots x_o of the following function $f(x)$, which can be done numerically, and then setting $d_{pore} = x_o$:

$$f(x_o) = \left(1 - \frac{d_{DNA}^2}{x_o^2}\right)\left(\frac{\sigma}{G'} - \frac{2K\left(\frac{d_{DNA}}{x_o}\right)}{\pi x_o} \right) - \left(\frac{\sigma}{G_o} - \frac{1}{x_o} \right) = 0. \quad \text{(S2.2.20)}$$

Note that if $d_{DNA} \leq G_o/\sigma$, the function $f(x)$ has two possible zeros, x_1 and x_2. In such case, one of the solutions may result in a negative thickness and is thus unphysical, or, alternatively, two admissible solutions may exist – the latter can occur for ultrathin membranes, i.e. $d_{pore} \gg L$. For the model from Kowalczyk *et al*.,[41] the function for which to find the roots is:

$$f(x_o) = \left(1 - \frac{d_{DNA}^2}{x_o^2}\right)\left(\frac{\sigma}{G'} - \frac{1}{\sqrt{x_o^2 - d_{DNA}^2}}\right) - \left(\frac{\sigma}{G_o} - \frac{1}{x_o}\right) = 0. \qquad \text{(S2.2.21)}$$

Similarly, this function sometimes has two zeros, one of which is unphysical due to resulting in negative thicknesses.

Figures S2.2.4 and S2.2.5 show the pore diameters and thicknesses extracted using the open and blocked pore conductance values from finite element simulations (those of Figure 2.1.3 in the main text). The adjusted conductance equations from this work result in pore diameters at least twice as precise as those extracted from the model from Kowalczyk *et al.* (see Figure S2.2.4). Of particular interest, we note that for the wide range of pore geometries simulated, no extracted pore sized deviated by more than 30% from the simulated pore diameter, with higher errors observed for larger aspect ratio pores $d_{pore} > L$. Although a relative improvement is again observed using the present model for thickness extraction, it should be noted that both models result in very inaccurate values of $L_{extracted}$ for ultrathin membranes, as shown in Figure S2.2.5.

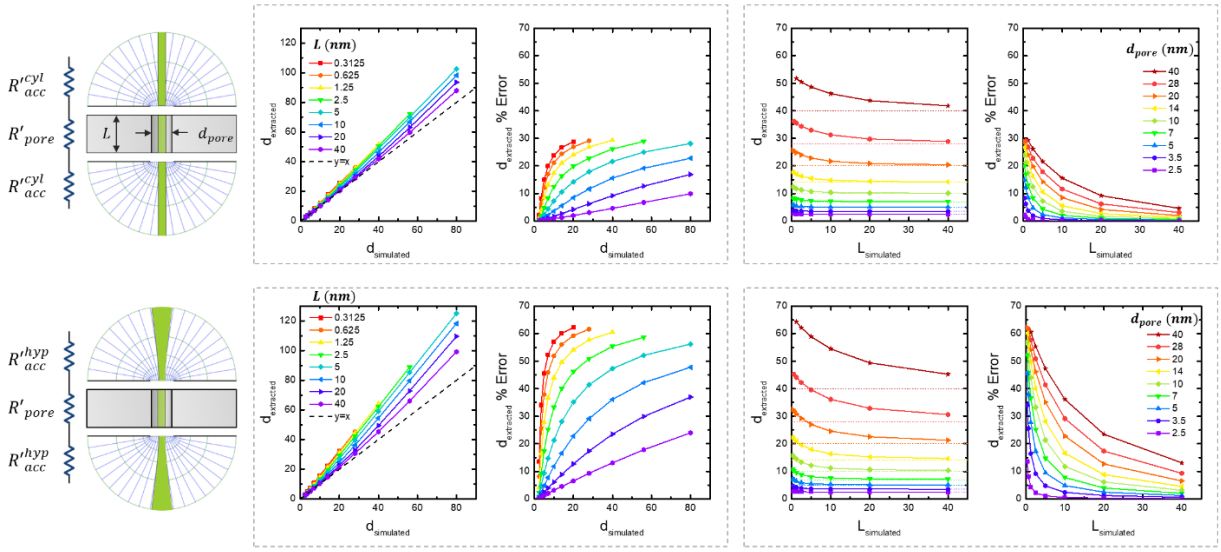

Figure S2.2.4. Pore diameter extraction. Accuracy of conductance-model assisted extraction of pore diameter using a known obstruction diameter of $d_{DNA} = 2.2\ nm$, and open and blocked conductance values from finite element simulations. The cylindrical obstruction model presented in the main text is consistently at least twice as accurate as the model from Kowalczyk *et al.*

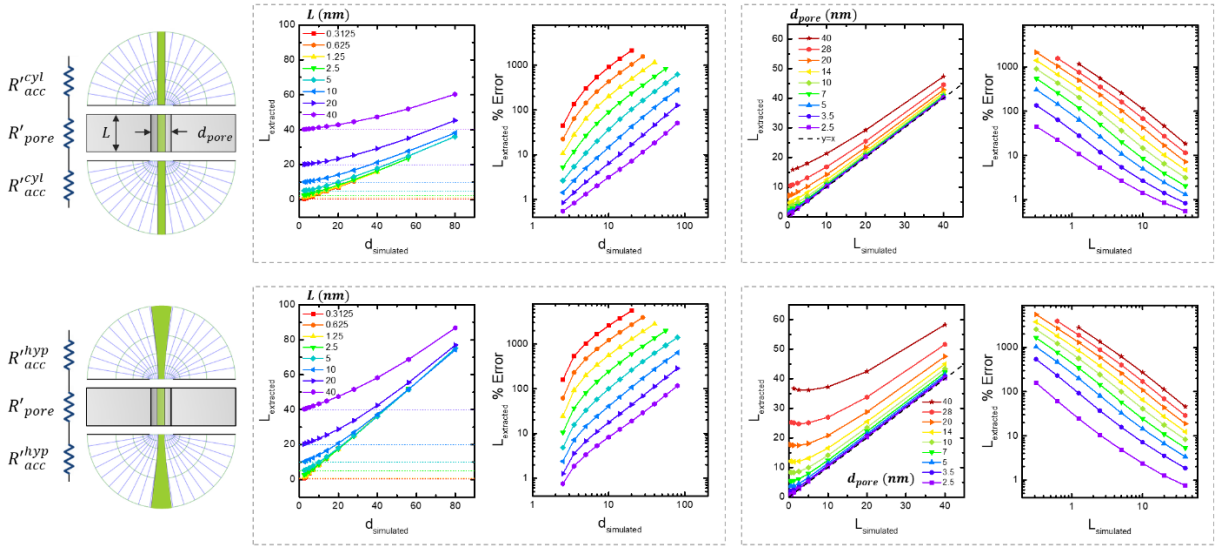

Figure S2.2.5. Pore length extraction. Accuracy of conductance-model assisted extraction of pore thickness L using a known obstruction diameter of $d_{DNA} = 2.2\ nm$, and open and blocked conductance values from finite element simulations. Both models demonstrate a very weak ability of predicting the thicknesses of thin membranes.

S2.2.8. Model Assumptions

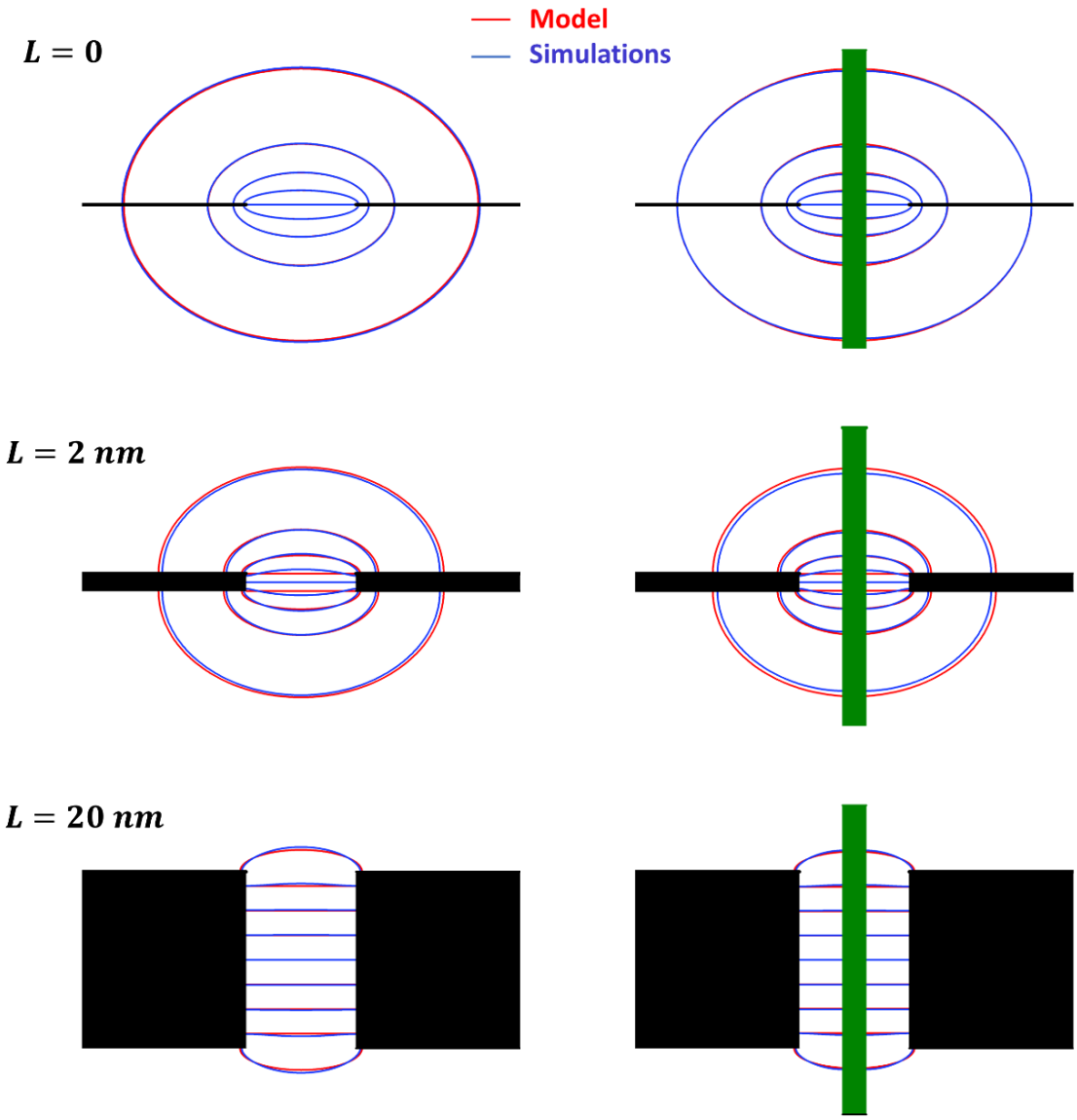

Figure S2.2.6. **Visualization of model assumptions and source of error.** Equipotential lines for 10nm pores with varying membrane thicknesses in the open and blocked states, as estimated by our model (blue) and calculated from simulations (red). A voltage of 200mV is applied across the pore, and the -80, -60, -40, …, 40, 60 and 80 mV equipotential lines are shown, thus delimiting 80% of the voltage drop in the system.

Although the incorporation of our improved access resistance model has led to very accurate conductance blockage predictions for cylindrical pores with extreme dimensions, i.e. $d_{pore} \ll L$ and $d_{pore} \gg L$, the error for intermediate pore sizes is non-negligible, especially for $d_{pore}/L \approx 5$ (Figure S2.2.3), as discussed. Here, we demonstrate how such errors result from inexact field treatments in two distinct modeling steps. First, as discussed in the main article, by treating the nanopore system as three conductive regions in series, our model assumes that equipotential surfaces are represented by oblate spheroids in the access regions and as disks inside the pore, which is only true in the limits of unobstructed 2D membranes and infinitely long channels, respectively.

Figure S2.2.6 further displays this by plotting the equipotential lines expected from our model (red) and corresponding simulations (blue) for a pore of diameter $d_{pore} = 10\,nm$ in membranes with thicknesses of $L = 0, 2, 20$ nm. The simulations show that in a finite length pore, the disks at the pore mouths are not equipotential surfaces. Further confirming the inexact treatment of equipotential surfaces, we note that equipotential disk pore mouths would result in a field discontinuity at the pore mouth, where radially uniform and non-uniform electric fields would be predicted inside ($E = \Delta V_{pore}/L$) and outside the pore (Eq. 2.1.5), respectively. The simulated electric field of an unobstructed pore is shown in Figure S2.2.7, which further shows that the electric field has a radial component inside the pore. The second field mistreatment in our model arises from the assumption that the presence of the obstruction does not alter the field distribution around it. As a result, the constant-μ equipotential lines from our model are not perpendicular to the obstruction's surface, as shown in Figure S2.2.6, as opposed to simulated lines.[88] We note that similar assumptions are made in resistance calculations integrating over infinitesimal conductive

slices, and are known known to underestimate changes in conductance, yet result in accurate calculations.[46]

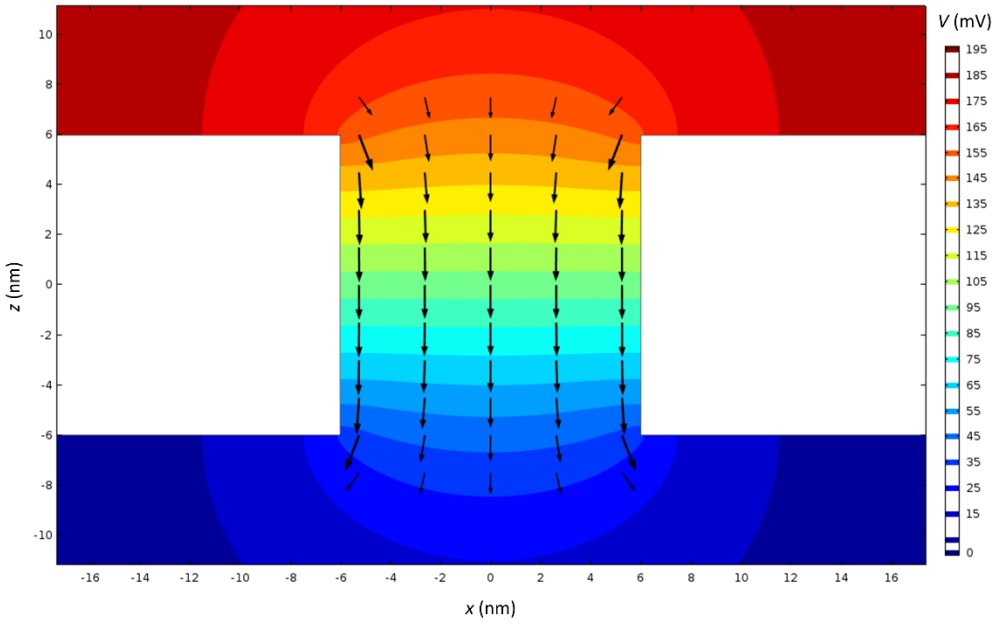

Figure S2.2.7. Finite element simulations of nanopore electric field. Demonstration that the electric field inside a nanopore is not uniform, as assumed in the derivation of in-series conductance models.

2.3 Modeling Access Region Contributions during Resistive Pulse Sensing

Martin Charron, Zachary Roelen, Deekshant Wadhwa, Vincent Tabard-Cossa

Abstract

Resistive pulse sensing has been widely used to characterize and count single particles in solution moving through channels under an electric bias, with nanoscale pores more recently providing enough spatial resolution for nucleic acid sequencing. At its core, this single-molecule technique relies on measuring the drop in ionic current through the pore induced by the passage of a molecule and, through the use of conductance models, mapping the blockage amplitude to molecular dimensions. However, there exists no model considering the resistive contributions of the pore exterior, i.e. access regions, when obstructed by molecules which is becoming increasingly important for low aspect ratio pores, with the advent of 2D materials and ultrathin membranes. In this work, a general method by which to model the resistance of the access regions of pores in the presence of insulating obstructions is presented. Thin oblate spheroidal slices are used to partition access regions and infer their conductance when blocked by differently shaped objects. We show that our model accurately estimates the blocked-state conductance of 2D and finite-length pores as a function of the distance from the pore in the presence of simple obstructions geometries (e.g. cylindrical and spherical objects) or complex structures (i.e. sequence of simple obstruction sub-units). The model is further shown to capture off-axis effects by predicting deeper blockages for obstructions offset from the pore's central axis. A web-based tool was created to predict the electrical signatures of a wide range of molecule geometries translocating through differently shaped pores. The introduced model will help guide experimental designs and thus presents a straightforward way to extend the quantification of the resistive pulse technique at the nanoscale.

2.3.1. Introduction

Resistive pulse sensing is a well-established single-particle detection method that relies on measuring the reduction of current induced by the passage of an object through a fluid-embedded channel across which a potential difference is applied (Figure 2.3.1a).[1,2,26,118–120] Since the current blockage amplitude is closely related to the volume of the current-obstructing object, microchannels have been used to count and size cells, viruses and colloidal particles.[26,118] More recently, nanopores have pushed the resolution of this technique further by sensing single molecules of DNA, and proteins as well as other nanostructures for different sequencing, diagnostics or next-generation information storage applications.[1–4,119,120]

At the heart of nanopore sensing and more generally the resistive pulse method, mathematical models are required to transduce blockage amplitudes into molecular dimensions so as to characterize and identify translocating objects.[40,47] For cylindrical pores whose length L_p is much larger than their diameter d_p, the potential drop ΔV occurs almost entirely inside the channel, and as such the electric field inside the pore is estimated to be constant $E = \Delta V / L_p$. Under these conditions, the interior of the channel can be partitioned into circular slices of thickness dz, and an accurate estimate of the channel resistance can be obtained by summing up the z-dependent resistance $dR(z)$ of each slice:

$$R = \int dR\,(z) = \frac{1}{\sigma} \int_{-\frac{L_p}{2}}^{\frac{L_p}{2}} \frac{dz}{A(z)}\,. \tag{2.3.1}$$

Here, σ and $A(z)$ denote the bulk conductivity and the z-dependent conductive area of each circular slice. Equation 2.3.1 can either be applied to open pores, or to pores blocked by an insulating obstruction. For example, a linear polymer with cylindrical cross-section of radius r_c

passing through a cylindrical pore of radius r_p, $A(z)$ is simply $\pi(r_p^2 - r_c)$. Equation 2.3.1 is generalizable to non-cylindrical obstructions and pores, and has been improved upon for specific use cases.[47] An important result from Eq. 2.3.1 is that the resistance change ΔR upon the introduction a molecule of volume $\mathcal{V}_{mol}$ inside a pore channel of volume $\mathcal{V}_{pore}$ with an open pore resistance of R_o is well approximated by $\Delta R/R_o \approx \Delta G/G_o \approx \mathcal{V}_{obs}/\mathcal{V}_{pore}$ for $\mathcal{V}_{mol} \ll \mathcal{V}_{pore}$, where $G = R^{-1}$ is the corresponding pore conductance. This simple relation has been extensively used for sizing particles from the amplitude of the induced transient resistive pulses.

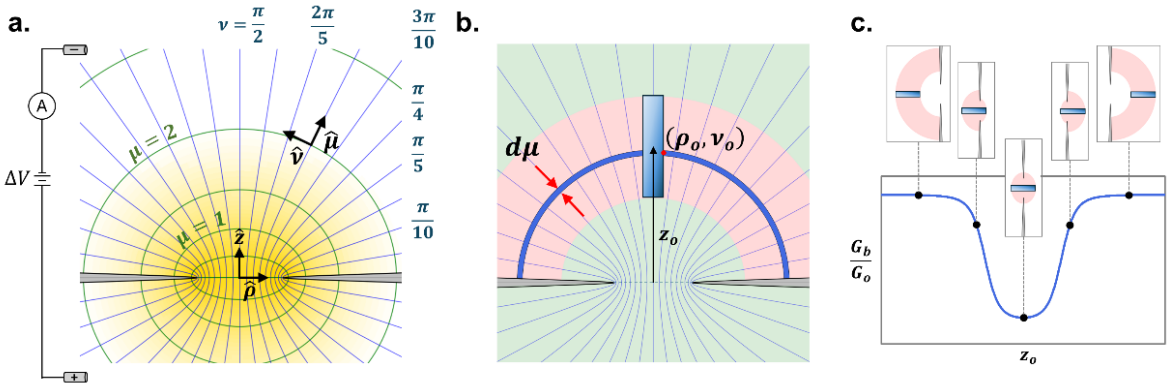

Figure 2.3.1. Oblate spheroidal slice method. a. Oblate spheroidal coordinates used to map the access regions of a 2D pore. Constant-μ and constant-ν surfaces correspond to oblate spheroids and hyperboloid surfaces. Equipotential surfaces can be mapped to constant-μ oblate spheroids. **b.** Access region blocked by a cylindrical obstruction (pale blue) and divided into open (green) and blocked (red) oblate spheroidal segments. Blocked access resistance is obtained by partitioning region into spheroidal slices of thickness $d\mu$ (blue). **c.** Normalized conductance values during different translocation stages for a cylindrical obstruction through a 2D pore, with corresponding partitioning schemes.

This slicing technique (Eq. 2.3.1) is however non-applicable to low aspect ratio pores ($r_p \geq L_p$) for which resistive contributions from outside the pore cannot be ignored due to the significant electric field and voltage drop occurring in this access region. Although some models have addressed specific blockage scenarios,[41,88,90,121–123] there currently exists no generalizable approach akin to Equation 2.3.1 for modeling the conductance of a partially blocked access regions

that would be applicable to ultra-thin pores.[40] Such a model would be highly valuable in predicting electrical signatures from a wide range of translocating molecules, including cases of long obstructions that reside partially in the access regions even when inside the pore, or for obstructions entirely in the access regions, such as molecules approaching a pore.

In this work, we expand on existing modeling methods (e.g. Equation 2.3.1) and introduce a general framework to estimate the conductance of the access region of a channel in the presence of a wide range of insulating blocking objects (i.e. obstructions) by using thin oblate spheroidal slices to partition this access region (Figure 2.3.1b). We first demonstrate how this approach can be used to estimate the conductance of pores in 2D membranes in the presence of insulating obstructions with simple geometries such as cylinders, spheres, truncated cones, and ellipsoids at a distance z_o from a pore (Figure 2.3.1c). These results can be useful for predicting electrical signatures from DNA, proteins and other translocating molecules with simple geometries. To address effects of off-axis passage, we derive numerically solvable expressions describing the radial dependence of cylinders and spheres located away from the pore's central axis. To illustrate the model's practical utility in modeling complex translocation blockades from molecules used in many sensing applications, we then show solutions for the resistance of more complex obstructions assembled from simple geometrical units. Finite-length pores can be modeled by using a combination of oblate spheroidal slices in the access regions, and circular slices inside the pore (Eq. 2.3.1), thus treating the access regions and the pore channel as resistors in series. Importantly, finite element simulations are performed to assess the accuracy and limitations of the method, thus outlining conditions in which the model should be used. Due to the intricacy of most equations shown, a web-based tool is made available to predict the electrical signatures of any user-defined

blocking object, which can be used in turn to optimize the nanopore architecture enhancing the sensing resolution for a particular application.

2.3.2 Oblate Spheroidal Framework for 2D membranes

Following Farahpour *et al.,*[87] we use the oblate spheroidal variables $\mu \in [-\infty, \infty]$, $\nu \in [0, \pi/2]$ and $\phi \in [0, 2\pi]$ to map the access region of a pore, which are defined through the following transformations with cartesian coordinates $(\mu, \nu, \phi) \rightarrow (x, y, z)$:

$$\begin{aligned} x &= r_p \cosh\mu \cos\nu \cos\phi\,, \\ y &= r_p \cosh\mu \cos\nu \sin\phi\,, \\ z &= r_p \sinh\mu \sin\nu. \end{aligned} \tag{2.3.2}$$

Note that the radial distance from the z axis, ρ, can be calculated to be $\rho = r_p \cosh\mu \cos\nu$ (Figure 2.3.1a). Importantly, by defining r_p as the pore radius, this coordinate system naturally maps the access region: constant-μ surfaces form oblate spheroids with semi-axes of $r_p \sinh\mu$ along $\hat{z}$, and of $r_p \cosh\mu$ along $\hat{\rho}$, where the $\mu = 0$ surface corresponds to a disk of radius r_p at the pore mouth, and the $\mu \rightarrow \pm\infty$ surface to infinitely large hemispheres.

To isolate and model the electrical response of access regions, we first study pores in 2D membranes which, by definition, exclude contributions from the pores' interior. For an open pore of radius r_p in a 2D membrane, the Laplace equation $\nabla^2 V = 0$ can be solved under the assumption that the electric potential $V(\mu)$ depends solely on μ, or equivalently that equipotential surfaces form constant-μ oblate spheroids. Using boundary conditions of $V(\mu \rightarrow \pm\infty) = \pm\Delta V/2$ and $V(0) = 0$, which corresponds to the field between a circular electrode at the pore mouth and an infinitely large hemisphere electrode, an expression for the access region electric field is found:

$$\vec{E}_o(\mu,\nu) = -\frac{1}{h_\mu}\frac{dV}{d\mu}\hat{\mu} = \frac{\Delta V}{\pi r_p \cosh\mu\sqrt{\sinh^2\mu + \sin^2\nu}}\hat{\mu}\,. \tag{2.3.3}$$

Here h_μ denotes one of the three scaling factors for oblate spheroidal coordinates, where $h_\mu = h_\nu = r_p\sqrt{\sinh^2\mu + \sin^2\nu}$ and $h_\phi = r_p\cosh\mu\cos\nu$. See Section S2.4.1 of the SI for a full derivation of Eq. 2.3.3.

Expanding on the method of Equation 2.3.1, the resistance of a pore in a 2D membrane can be calculated by first partitioning its access regions into an infinite number of oblate spheroidal slices of thickness $d\mu$.[46] As per Ohm's law, the infinitesimal resistance $dR(\mu)$ of each slice can be obtained by calculating the ratio of the potential difference across the slice, $dV(\mu) = \vec{E}\cdot d\vec{\ell}$, and the current through the slice, $I(\mu) = \int\int_S \sigma\vec{E}\cdot d\vec{S}$, where σ denotes conductivity. A rigorous expression for the access resistance of a pore partially blocked by a translocating molecule requires an exact solution for $\vec{E}$, which in most scenarios is highly arduous or impossible to obtain. To estimate $dR(\mu)$, we thus introduce the assumption that $\vec{E} \approx \vec{E}_o = E_o\hat{\mu}$, i.e. the electric field is well approximated by that of the open pore (Equation 2.3.3). If a current-blocking molecule's surface is delimited by $\nu = \nu_o(\mu,\phi)$ (Figure 2.3.1b), then the infinitesimal resistance is approximated as:

$$dR(\mu) = \frac{\vec{E}\cdot d\vec{\ell}}{\int\int \sigma\vec{E}\cdot d\vec{S}} \approx \frac{E_o h_\mu d\mu}{\int_0^{2\pi}\int_0^{\nu_o(\mu,\phi)} \sigma E_o h_\nu h_\phi\, d\nu d\phi} = \frac{d\mu}{\int_0^{2\pi}\int_0^{\nu_o(\mu,\phi)} \sigma h_\phi\, d\nu d\phi}\,. \tag{2.3.4}$$

Assuming a uniform conductivity and an insulating obstruction that is rotationally symmetric about the *z*-axis, the above expression can be integrated to estimate the resistance between two delimiting oblate spheroid surfaces:

$$R'_{obst}(\mu_1,\mu_2) = \int_{\mu_1}^{\mu_2} dR(\mu) = \frac{1}{2\pi\sigma r_p}\int_{\mu_1}^{\mu_2} \frac{\operatorname{sech}\mu\, d\mu}{\sqrt{1-\frac{\rho_o^2(\mu)}{r_p^2}\operatorname{sech}^2\mu}}. \quad (2.3.5)$$

Note in the above that $\rho_o(\mu)$ denotes the ρ-parametrization of the obstruction's surface, which delimits the region over which the current density σE is integrated (Figure 2.3.1b). The expression for the resistance of an open region delimited by oblate spheroids intersecting $z = z_1$ and z_2 is readily obtained by setting $\rho_0 = 0$ in Eq. 2.3.5:

$$R_{free}(z_1,z_2) = \frac{1}{2\pi\sigma r_p}\left[\tan^{-1}\left(\frac{z_2}{r_p}\right) - \tan^{-1}\left(\frac{z_1}{r_p}\right)\right]. \quad (2.3.6)$$

Note importantly that in the open pore limit, we find $R_o(0,\infty) = 1/4\sigma r_p$ which corresponds to the access resistance expression determined by Hall.[44]

As depicted in Figure 2.3.1b, by separating the access region into different blocked and open oblate spheroidal domains, the conductance of a 2D pore in the presence of an obstruction G_b^{obst} of finite size can be calculated as the inverse of the sum of the resistances of the blocked interval, R'_{obst}, and the open segments above and below the pore

$$G_b^{obst} = R_b^{-1} = \left[R_{free}^{bottom} + R'_{obst} + R_{free}^{top}\right]^{-1}, \quad (2.3.7)$$

and the corresponding conductance blockage is simply $\Delta G = G_o - G_b^{obst}$, where $G_o = 2\sigma r_p$ is the open-pore conductance. Solving Equations 2.3.5-2.3.7 represents a general method by which to calculate the blocked-state conductance of 2D membranes, which requires: i) determining the μ delimitations of blocked and open regions to use as integration bounds of Equations 2.3.5-2.3.6, ii) calculating the ρ-parametrization of the obstruction surface, $\rho_o(\mu)$, to find an expression for the integrand of R'_{obst} (Equation 2.3.5), and iii) analytically or numerically calculating the solution to R'_{obst}, and inserting this result into the blocked-state equation (Equation 2.3.7). The rest of this

work showcases how to evaluate Equations 2.3.5-2.3.7 for channels and translocating objects of various geometries.

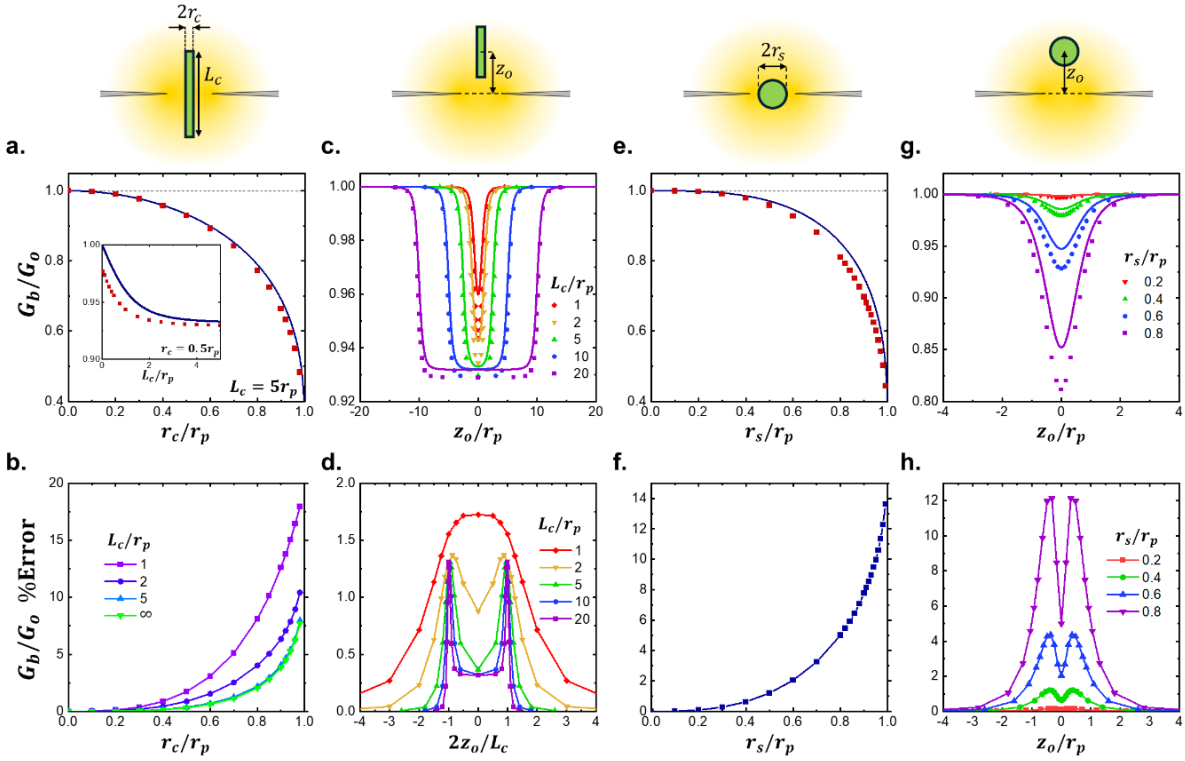

Figure 2.3.2. Cylindrical and spherical obstructions. Dependence of normalized conductance G_b/G_o on obstruction dimensions and distance from a 2D pore. Lines are from model predictions, whereas points are from finite element simulations. A normalized conductance of 1 is when Gb = G0, i.e. the pore is unobstructed, whereas a value of 0 represents a fully blocked access region. **a)** G_b/G_o vs cylindrical obstruction radius r_c. Inset shows dependence of G_b/G_o on cylindrical obstruction length L_c. **b)** Absolute error percentage between modelled and simulated G_b/G_o values from (a). **c)** G_b/G_o vs z_o for cylindrical obstruction of radius $r_c = 0.5r_p$ and different lengths L_p. **d)** Absolute error percentage between modelled and simulated G_b/G_o values from (c). **e)** G_b/G_o vs centered ($z_o = 0$) spherical obstruction radius r_s. **f)** Absolute error percentage between modelled and simulated G_b/G_o values from (e). **g)** G_b/G_o vs z_o for spherical obstructions of different radii. **h)** Absolute error percentage between modelled and simulated G_b/G_o values from (g).

2.3.3. Cylindrical Obstructions

To model the conductance of a 2D pore blocked by a rigid linear polymer like double-stranded DNA, we first consider an insulating cylinder of radius r_c and of finite length L_c and half-

length $\ell_c \equiv L_c/2$ centered inside a 2D pore of radius r_p, as shown above Figure 2.3.2a. Here, the obstructed region is delimited by $\mu_{\pm} = \sinh^{-1}(\pm\ell_c/r_p)$, and the cylinder surface is trivially parametrized by $\rho_o(\mu) = r_c$. Inserting those values into Equation 2.3.5, the resistance of the segment obstructed by a finite-length cylinder R'_{cyl} can be calculated:

$$R'_{cyl}(\ell_c, r_c) = \frac{1}{2\pi\sigma r_p}\int_{\sinh^{-1}\left(\frac{-\ell_c}{r_p}\right)}^{\sinh^{-1}\left(\frac{\ell_c}{r_p}\right)} \frac{\operatorname{sech}\mu\, d\mu}{\sqrt{1-\frac{r_c^2}{r_p^2}\operatorname{sech}^2\mu}}$$

$$= \frac{1}{2\pi\sigma r_p}\int_{\frac{\pi}{2}-\tan^{-1}\left(\frac{-\ell_c}{r_p}\right)}^{\frac{\pi}{2}-\tan^{-1}\left(\frac{\ell_c}{r_p}\right)} \frac{d\theta}{\sqrt{1-\frac{r_c^2}{r_p^2}\sin^2\theta}}$$

$$R'_{cyl}(\ell_c, r_c) = \frac{1}{2\pi\sigma r_p}\left[F\left(\frac{\pi}{2}-\tan^{-1}\left(\frac{-\ell_c}{r_p}\right),\frac{r_c}{r_p}\right) - F\left(\frac{\pi}{2}-\tan^{-1}\left(\frac{\ell_c}{r_p}\right),\frac{r_c}{r_p}\right)\right]. \qquad (2.3.8)$$

Note that Equation 2.3.8 was obtained using the variable substitution $\tanh\mu = \cos\theta$, and that the function $F(\varphi, k)$ denotes the incomplete elliptic integral of the first kind and is defined as $F(\varphi, k) = \int_0^{\varphi}(1-k^2\sin^2\theta)^{-1/2}\,d\theta$. From Equation 2.3.8, a closed-form expression for the blocked state conductance of the 2D system, G_b^{cyl}, normalized by the corresponding open-pore conductance $G_o = 2\sigma r_p$, can be obtained by considering the additional contributions from the unobstructed oblate spheroidal segments (Eq. 2.3.6-2.3.7):

$$\frac{G_b^{cyl}}{G_o}(r_c, \ell_c) = \left[1 - \frac{2}{\pi}\tan^{-1}\left(\frac{\ell_c}{r_p}\right) + \frac{1}{\pi}F\left(\frac{\pi}{2}+\tan^{-1}\left(\frac{\ell_c}{r_p}\right),\frac{r_c}{r_p}\right) - \frac{1}{\pi}F\left(\frac{\pi}{2}-\tan^{-1}\left(\frac{\ell_c}{r_p}\right),\frac{r_c}{r_p}\right)\right]^{-1}. \qquad (2.3.9)$$

Figure 2.3.2a and its inset plot the dependence of G_b^{cyl}/G_o on r_c (for fixed length $L_c = 5r_p$), and of G_b^{cyl}/G_o on L_c (for fixed radius $r_c = 0.5r_p$), respectively. To evaluate the model accuracy, results from finite element simulations performed with identical system dimensions (see Methods) are plotted alongside predictions from Equation 2.3.9. Figure 2.3.2b plots the error

percentage measured between simulations and Equation 2.3.9 and shows that the error monotonically increases as $r_c/r_p \to 1$, and is highest for shorter L_c, but it is typically <5% for the practical cases of dsDNA ($\geq$ 20 bp) through a $\geq$ 3 nm pore.

We note that the normalized conductance blockage $\Delta G_{cyl}/G_o = (G_o - G_b^{cyl})/G_o$ can be calculated from Equation 2.3.9, from which it can be shown that $\Delta G_{cyl}/G_o$ scales proportionally to the ratio r_c^2/r_p^2 in the limit of ultra long and thin cylinders, i.e. $r_c \ll r_p \ll L_c$:

$$\frac{\Delta G_{cyl}}{G_o}\left(r_c \ll r_p \ll \ell_c\right) \approx \frac{1}{4}\frac{r_c^2}{r_p^2} = \frac{1}{3}\frac{2\pi r_c^2 r_p}{\frac{8}{3}\pi r_p^3} = \frac{1}{3}\frac{\mathcal{V}_{cyl}}{\mathcal{V}_{acc}} \,. \tag{2.3.10}$$

The last term of Eq. 2.3.10 shows that just like for very long pores (Eq. 2.3.1), the fractional blockage is related to the volume ratio $\mathcal{V}_{cyl}/\mathcal{V}_{acc}$. Here $\mathcal{V}_{acc}$ denotes the volume of the 2D-pore sensing region, defined as a constant-μ oblate spheroid with dimension r_p along the z axis, and $\mathcal{V}_{cyl}$ denotes the volume of the cylindrical obstruction contained within the sensing region (see Figure S2.4.2 of the SI).

Now, to model the conductance when cylindrically-shaped linear polymers like dsDNA are approaching a 2D pore of radius r_p, we consider an insulating cylinder of radius r_c and of finite length L_C along the pore's central z-axis, with its center located a distance z_o above the pore, as depicted above Figure 2.3.2c. Given the blocked region delimitation of $\mu_{\pm} = \sinh^{-1}\left((z_o \pm \ell_c)/r_p\right)$ and the trivial parametrization of $\rho_o(\mu) = r_c$, a closed-form expression for the conductance of the blocked system can be obtained with similar manipulations to that of Equation 2.3.9 (see Section S2.4.2 of the SI for the full derivation):

$$\frac{G_b^{cyl}}{G_o}(r_c, \ell_c, z_o) = \left[1 + \frac{1}{\pi}\tan^{-1}\left(\frac{z_o - \ell_c}{r_p}\right) - \frac{1}{\pi}\tan^{-1}\left(\frac{z_o + \ell_c}{r_p}\right) + \frac{1}{\pi}F\left(\frac{\pi}{2} + \tan^{-1}\left(\frac{z_o - \ell_c}{r_p}\right), \frac{r_c}{r_p}\right) - \frac{1}{\pi}F\left(\frac{\pi}{2} - \tan^{-1}\left(\frac{z_o + \ell_c}{r_p}\right), \frac{r_c}{r_p}\right)\right]^{-1}. \quad (2.3.11)$$

Figure 2.3.2c plots the z_o-dependence of Equation 2.3.11, where the five plotted curves correspond to cylinder lengths of $L_c/r_p = 1, 2, 5, 10, 20$, and fixed radius of $r_c = 0.5r_p$. Data obtained from finite element simulations in identical conditions are color-matched and plotted as individual points alongside the corresponding model predictions (continuous line). Figure 2.3.2d shows that Equation 2.3.11 is highly accurate, with consistent <2% error measurements.

We note that Equations 2.3.8-2.3.11 treat the cylinder extremities as oblate spheroidal surfaces instead of flat disks. Section S2.4.3 of the SI shows how to properly consider flat extremities, the solution of which even allows solutions for cylinders larger than pores, i.e. $r_c > r_p$, further generalizing the treatment of cylindrical obstructions.

2.3.4. Spherical Obstruction

To model the conductance of pores in the presence of an insulating object well approximated by spheres, such as viruses, nanoparticles, or globular proteins, we now consider a sphere of radius r_s centered inside a 2D pore of radius r_p, as shown above Figure 2.3.2e. As detailed in Section S2.4.4 of the SI, inserting the right boundaries and parametrization in Equations 2.3.5-2.3.7, a closed-form expression for the conductance of the 2D pore blocked by a spherical obstruction, G_b^{sph}, is obtained:

$$\frac{G_b^{sph}}{G_o}(r_s) = \left[1 - \frac{2}{\pi}\tan^{-1}\left(\frac{r_s}{r_p}\right) + \frac{2}{\pi}\frac{r_p}{r_s}\tanh^{-1}\left(\frac{r_s^2}{r_p^2}\right)\right]^{-1}. \quad (2.3.12)$$

Figure 2.3.2e shows the dependence of G_b^{sph}/G_o on r_s from Equation 2.3.12, and plots the corresponding values obtained from finite element simulations. The r_s dependence of G_b^{sph}/G_o is well captured by Equation 2.3.12, as shown in Figure 2.3.2f, which plots the error percentages between simulations and model predictions. Sub-15% error percentages were measured through the range of sphere radii explored ($r_s < 0.99r_p$), notably with errors < 5% observed for spheres with $r_s < 0.8r_p$.

As per long channels and cylindrical obstructions (Eq. 2.3.10), the normalized blockage $\Delta G_{sph}/G_o = \left(G_o - G_b^{sph}\right)/G_o$ can be calculated from Eq. 2.3.12 and related to the volume ratio of the spherical obstruction and the access region volume $\mathcal{V}_{sph}/\mathcal{V}_{acc}$ for spheres with radii much smaller than that of the pore ($r_s \ll r_p$):

$$\frac{\Delta G_{sph}}{G_o}\left(r_s \ll r_p\right) \approx \frac{2}{3\pi}\frac{r_s^3}{r_p^3} = \frac{4}{3\pi}\frac{\frac{4\pi}{3}r_s^3}{\frac{8\pi}{3}r_p^3} = \frac{4}{3\pi}\frac{\mathcal{V}_{sph}}{\mathcal{V}_{acc}}\,. \tag{2.3.13}$$

To model the access conductance as spherical objects approach and traverse 2D pores, we now consider an insulating sphere of radius r_s whose center lies along the z-axis at a distance z_o from a 2D pore of radius r_p (Figure 2.3.2g). Section S2.4.4 details the derivation for the conductance of the obstructed 2D pore system, $G_b^{sph}(z_o, r_s)$:

$$\left(\frac{G_b^{sph}}{G_o}\right)^{-1} = 1 + \frac{1}{\pi}\tan^{-1}\left(\frac{z_o - r_s}{r_p}\right) - \frac{1}{\pi}\tan^{-1}\left(\frac{z_o + r_s}{r_p}\right) + \frac{1}{\pi}\int_{\sinh^{-1}\left(\frac{z_o - r_s}{r_p}\right)}^{\sinh^{-1}\left(\frac{z_o + r_s}{r_p}\right)} \frac{\operatorname{sech}^2\mu\, d\mu}{\sqrt{1 - \frac{r_s^2 + z_o^2}{r_p^2}\operatorname{sech}^2\mu + 2\frac{z_o^2}{r_p^2} - 2\frac{z_o}{r_p}\tanh\mu\sqrt{1 + \frac{z_o^2}{r_p^2} - \frac{r_s^2}{r_p^2}\operatorname{sech}^2\mu}}}. \tag{2.3.14}$$

Although Eq. 2.3.14 presents no closed form solution, it can be numerically integrated. Figure 2.3.2g shows the z_o dependence of G_b^{sph}/G_o for spheres with radii $r_s/r_p = 0.2, 0.4, 0.6, 0.8$ and plots finite-element simulations performed at various z_o values. As in the $z_o = 0$ case, the error percentage calculated between simulations and model predictions is biggest for larger spheres, as shown in Figure 2.3.2h. Moreover, like longer cylindrical obstructions (Figure 2.3.2d), the error is not maximal for $z_o = 0$, but instead between $z_o = 0$ and $z_o = r_p$.

Note that the oblate spheroidal slice method presented in this work is applicable to any rotationally symmetric obstruction whose surface is parametrizable by $\nu_o(\mu)$ or $\rho_o(\mu)$. To demonstrate the generality of the approach, the conductance of 2D pores in the presence of ellipsoidal and conical obstructions centered in the pore ($z_o = 0$) as well as positioned above the pore ($z_o \neq 0$) are derived and illustrated in Section S2.4.5 of the SI. Non-rotationally symmetric scenarios can also be considered, as demonstrated by Section S2.4.6 of the SI which shows the calculation for a wedged cylinder.

2.3.5 Off-Axis Effects

Because of the non-uniform electric field (Eq. 2.3.3) inside the pore, off-axis translocations are known to result in deeper blockades,[28,114–116,124–126] yet other than the computationally demanding three-dimensional finite-element analysis, no mathematical treatment of this phenomenon currently exists, which would be a beneficial tool for properly interpreting individual blockades and predicting blockage distributions of real-world experiments. Here, we consider the off-axis effects of cylindrical and spherical obstructions positioned a distance r_o away from the central axis of the pore.

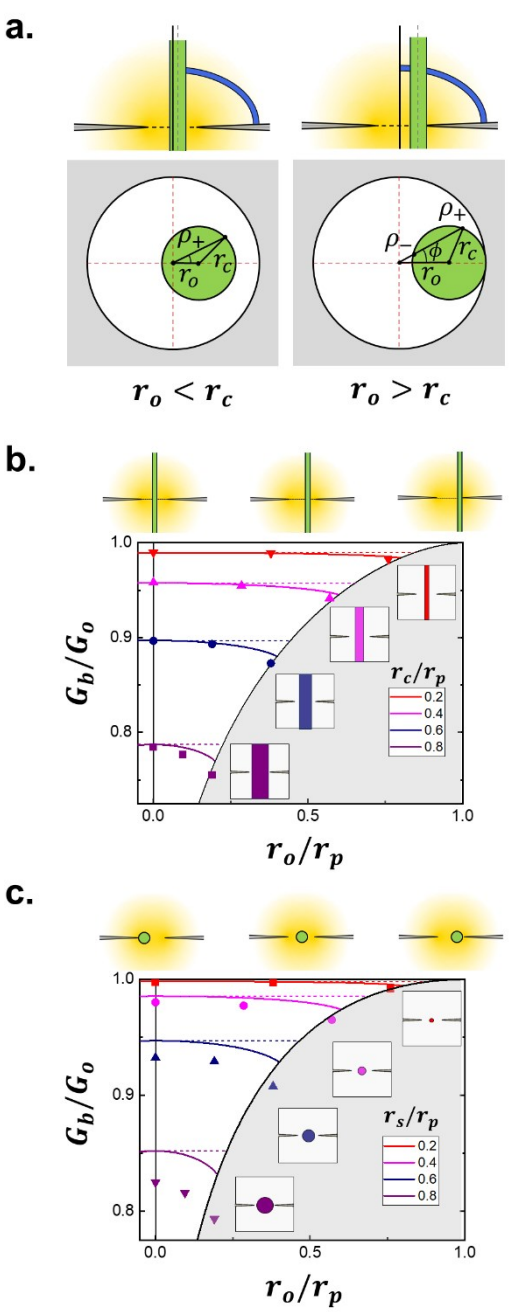

Figure 2.3.3. Off-axis blocked-state conductance. a) Schematic representation of 2D pores in the presence of off-centered obstructions at a distance r_o from the pore center. **b)** Normalized change in a 2D pore conductance blocked state versus normalized distance away from the pore center for four infinitely long cylindrical obstruction with different radii compared to the pore size (20, 40, 60, 80%). $r_o = 0$ corresponds to the centered case, $r_o = r_p - r_c$ corresponds to the pore in contact with the pore wall. **c**) For spherical obstruction. Continuous lines correspond to model predictions and individual points to calculations from finite element simulations. The greyed-out areas correspond to regions in the domain of Eqs. 2.3.15 and S2.4.62 where $r_o > r_p - r_{c,s}$.

To model the off-axis effects for 2D pores in the presence of rigid linear polymers such as dsDNA, we first consider an infinitely long cylindrical obstruction of radius r_c, whose central axis is located at a distance of $\rho = r_o$ away from the pore center (Figure 2.3.3a). The equation for the ϕ-dependent obstruction surface parametrization is shown in Section S2.4.7 of the SI, which demonstrates that the conditions $r_o < r_c$ and $r_o > r_c$ need to be treated separately, since the ν integration domain for $r_o < r_c$ is a single interval, whereas the $r_o > r_c$ scenarios result in two distinct intervals over which to integrate (Figure 2.3.3a):

$$\left(\frac{G_b^{cyl}}{G_o}(r_o)\right)^{-1} = \begin{cases} 2\int_{-\infty}^{\infty} \dfrac{\operatorname{sech}\mu}{\int_0^{2\pi}\sqrt{1-\frac{\rho_+^2}{r_p^2}(\phi)\operatorname{sech}^2\mu}\,d\phi}\,d\mu\,, & \text{for } r_o \le r_c \\ 2\int_{-\infty}^{\infty} \dfrac{\operatorname{sech}\mu}{2\pi + \int_{-\sin^{-1}\left(\frac{r_c}{r_o}\right)}^{\sin^{-1}\left(\frac{r_c}{r_o}\right)}\left[\sqrt{1-\frac{\rho_+^2}{r_p^2}\operatorname{sech}^2\mu} - \sqrt{1-\frac{\rho_-^2}{r_p^2}\operatorname{sech}^2\mu}\right]d\phi}\,d\mu\,, & \text{for } r_o > r_c \end{cases} \tag{2.3.15}$$

Here the ρ_+ and ρ_- are the ϕ-dependent surface parametrizations of the infinitely long cylinders (see Figure 2.3.3a), the expressions of which are found in Equation S2.4.49 of the SI.

Although Equation 2.3.15 presents no closed-form solution, it can be numerically integrated, as displayed in Figure 2.3.3b which plots the dependence of the blocked state conductance G_b^{cyl}/G_o on the radial position r_o away from the pore center for different cylinder radii. Finite element simulations were performed to assess the accuracy of Equation 2.3.15 and are also plotted in Figure 2.3.3b. Equation 2.3.15 captures the off-axis dependence well, with larger r_o values resulting in deeper blockades (lower G_b values) for a given cylinder radius. For example, Eq. 2.3.15 predicts that a dsDNA ($r_c = 1.1\ nm$) inside a pore with $r_p = 5.5\ nm$ could increase its blockage amplitude ΔG by ~50% by going from the pore's center to the pore wall, with smaller

pores seeing smaller blockage fluctuation. A more quantitative comparison between simulations and Eq. 2.3.15 is shown in Section S2.4.7 of the SI.

Off-axis effects of spherical obstructions in 2D pores can also be modelled, though the manipulations are more involved in this case due to the spherical surface parametrization $\rho_o(\mu, \phi)$ depending both on ϕ and μ, unlike for cylinders. Figure 2.3.3c summarizes the results derived in Section S2.4.7 of the SI by plotting blockade state conductance values, G_b^{sph}/G_o, predicted by the model and simulated by finite element analysis for different values of r_o and different sphere sizes. Although the absolute conductance values are less accurate for spheres than for cylinders, as per the $r_o = 0$ case (Figure 2.3.2), the increase in blockage amplitude ΔG with respect to $r_o = 0$ is better captured by the spherical obstruction model, as further discussed in Section S2.4.7 of the SI.

2.3.6. Structured Obstructions

The development of many pore sensing schemes makes use of DNA-protein structures or nanostructured DNA to create more uniquely identifiable signals or molecular barcodes.[34,127–131] Predicting the signals generated by the translocation of these complex molecular structures for a given pore dimension is of high practical importance to successfully guide experimental design. To this end, we now show how to address the conductance of complex obstructions made up of a series of simpler obstruction units, as pictured in Figure 2.3.4a. This is achieved by further partitioning the obstructed oblate segment into multiple smaller segments allowing the treatment of each blocking sub-unit individually (Figure 2.3.4a). For example, if z_o is the vertical distance between the 2D pore of radius r_p and the center of the complex molecule made up of N simpler units and of total length $L_{comp} = 2\ell_{comp}$, then the conductance of the system is simply:

$$\frac{G_b^{comp}}{G_o}(z_o) = \left[1 + \frac{1}{\pi}\tan^{-1}\left(\frac{z_o - \ell_{comp}}{r_p}\right) - \frac{1}{\pi}\tan^{-1}\left(\frac{z_o + \ell_{comp}}{r_p}\right) + \sum_{i=1}^{N} R_i'(\mu_{i\_}, \mu_{i_+})\right]^{-1}. \quad (2.3.16)$$

Here $R_i'(\mu_{i-}, \mu_{i+})$ denotes the resistance of the i^{th} blocked segment delimited by $\mu_{i\_}$ and μ_{i_+}, and other terms of Equation 2.3.18 originate from the open segment above and below the complex obstruction (Eq. 2.3.6). We note particularly that the treatment of complex obstructions made up of cylindrical sub-units of different sizes results in closed form solutions due to Eq. 2.3.11 being an analytic function.

Figures 2.3.4b-d show signals, i.e. G_b^{comp}/G_o vs. z_o traces, produced by the translocation of differently designed blocking structures as calculated from Eq. 2.3.16 (black) and compared to finite element simulations (red). Figure 2.3.4b shows the calculated electrical signature of twenty-three stacked cylinders designed to emulate the signal from a barcoded DNA design, i.e. eleven bit-like cylinders with radii $r_0 = 0.3r_p$ and $r_1 = 0.4r_p$ equally spaced along the backbone of a long cylinder of radius $r_c = 0.2r_p$. Similarly, Figure 2.3.4c shows the conductance signals of a sequence of eight spheres, with two of radius $r_s = 0.85r_p$ and six of $r_s = 0.7r_p$. To show that different sub-unit types can be used to make up complex obstructions, Figure 2.3.4d plots the conductance *z*-mapping of a series of cylinders ($r_c = 0.2r_p$, $L_c = 10r_p$) and spheres ($r_s = 0.5r_p$ and $0.7r_p$). As expected from the discussion surrounding cylindrical and spherical obstructions (Figure 2.3.2), strong agreement is observed between model predictions and simulations for smaller structured objects – predictions with larger structures deviate more significantly from the simulated conductance values (while still capturing well the shape of the expected traces).

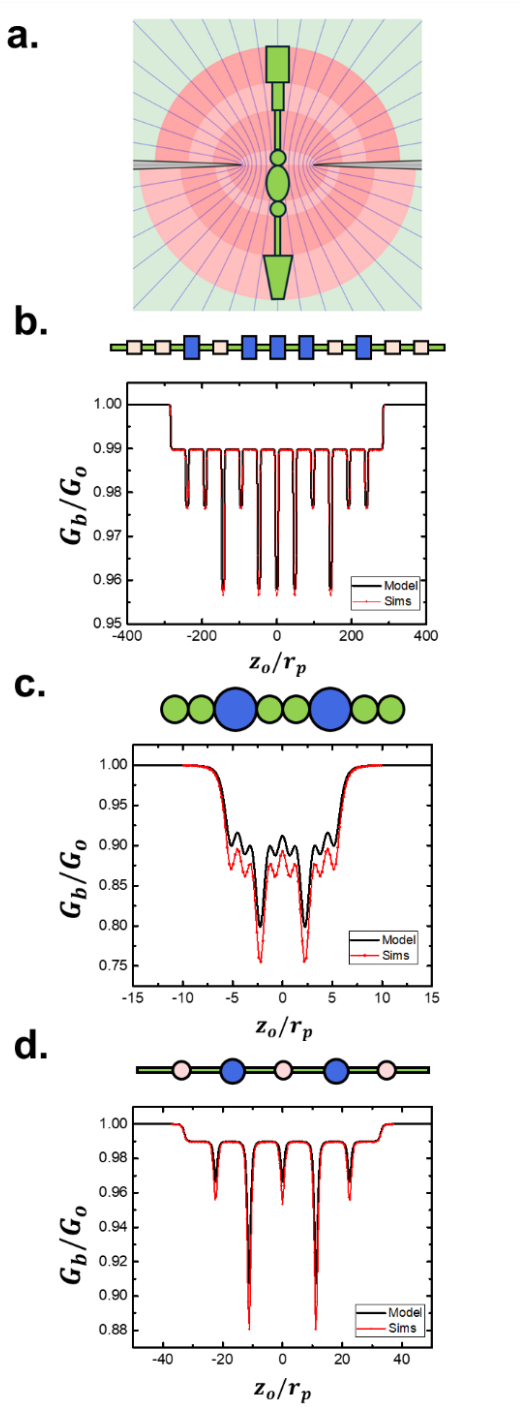

Figure 2.3.4. Structured obstructions. a) Oblate spheroidal partitioning of a structured obstruction made up of multiple simple geometrical units. **b)** z-dependence of G_b/G_o for a sequence of cylinders, with three types of cylinders ($r_c, L_c = r_i, L_i$ for $i = 1,2,3$) mimicking the design of a DNA barcode. **c)** z-dependence of G_b/G_o for a string of beads with $r_s = 0.85r_p$ or $r_s = 0.7r_p$ **d)** z-dependence of G_b/G_o for a complex obstruction made up of cylinders ($r_c = 0.2r_p$, $L_c = 10r_p$) and spheres ($r_s = 0.5r_p$, $r_s = 0.7r_p$).

To demonstrate the generality of Equation 2.3.16, Section S2.4.8 of the SI shows the traces of various complex blocking structures, with different sequences of sub-unit geometries. Notably, we show that by modeling biomolecules as a sequence of simple sub-units in series, G_b^{comp} vs z_o traces can be obtained through Eq. 2.3.16 which, under a constant-velocity assumption, resemble temporal current traces measured in real experiments. We have made a web-based tool implementing Eq. 2.3.16 to predict the conductance signals of any user-defined blocking structure,[132] which we believe can assist in designing structured biomolecules to be efficiently sensed with nanopores, or conversely optimizing pore diameter and shape (discussed below) to better resolve a given molecular design.

2.3.7. Finite-Length Nanopores

In addition to modeling pore conductance in 2D membranes, oblate spheroidal slices can be used to treat the access resistances (R_{acc}^{top} and R_{acc}^{bot}) of finite-length pores, as a natural extension of the circular slices used to calculate the resistance within a cylindrical channel ($R_{channel}$, see Eq. 2.3.1). This is of practical significance since many nanopore devices used in experimental work rely on large ($r_p > 5\,nm$) nanopores fabricated in thin (0.3-20 nm) membranes, resulting in important access resistance contributions.[110,133–139] The general expression modeling the total resistance (access and channel) of a finite pore of length $L_p \equiv 2\ell_p$ with a rotationally symmetric geometry described by a z-dependent radius $r_p(z)$ can thus be approximated by treating the two contributions in series:

$$
\begin{aligned}
R_b &= R_{acc}^{bot} + R_{channel} + R_{acc}^{top} \\
&= \frac{1}{2\pi\sigma r_p(-\ell_p)} \int_{-\infty}^{0} \frac{\operatorname{sech}\mu \, d\mu}{\sqrt{1 - \frac{\rho_o^2(\mu)}{r_p^2} \operatorname{sech}^2 \mu}} + \frac{1}{\pi\sigma} \int_{-\ell_p}^{\ell_p} \frac{dz}{r_p^2(z) - r_o^2(z)} \\
&\quad + \frac{1}{2\pi\sigma r_p(\ell_p)} \int_{0}^{\infty} \frac{\operatorname{sech}\mu \, d\mu}{\sqrt{1 - \frac{\rho_o^2(\mu)}{r_p^2} \operatorname{sech}^2 \mu}} \, .
\end{aligned}
\tag{2.3.17}
$$

Here, $\rho_o(\mu)$ and $r_o(z)$ denote the radial parametrization of the obstruction surface outside and inside the pore respectively, with the trivial case of $\rho_o(\mu) = r_o(z) = r_c$ for cylinders, and $\mu = 0$ corresponds to the membrane surface in the first and third integral term. Solving Equation 2.3.17 for a pore in the presence of an insulating molecule requires segmenting each access and channel region into blocked and open segments, naturally separating solutions of Equation 2.3.17 into a minimum of three regimes, depending on if the obstruction is: i) completely in one access region, ii) partially inside the pore and one of the access regions, or iii) completely inside the pore, if shorter than the pore, or partially in both access regions at once and fully inside the pore if longer than pore. Note that more conditions arise for non-symmetric pores (in z) or obstructions.

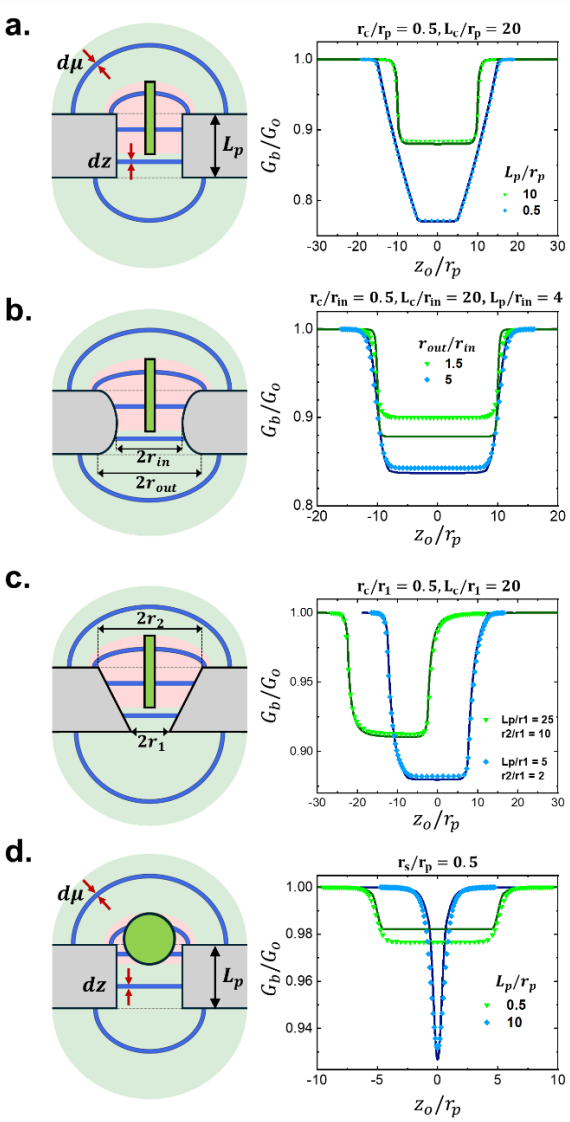

Figure 2.3.5. Finite-length pores. Conductance of finite length pores of various shapes during the translocation of a cylindrical obstruction $(r_c, L_c) = (0.5r_p, 20r_p)$: **a)** cylindrical pores with lengths $L_p = 0.5r_p$ (blue) and $L_p = 10r_p$ (green), showing different aspect ratios; **b)** hyperboloidal pores with $L_p = 4r_p$ and external radii $r_{out} = 5r_{in}$ (blue) and $r_{out} = 1.5r_{in}$ (green), showing different pore tapers; **c)** conical pores with dimensions $(L_p, r_2) = (5r_1, 2r_1)$ in blue, and $(L_p, r_2) = (25r_1, 10r_1)$ in green, emulating conical pores or pipette-like dimensions. **d)** A spherical obstruction $(r_s = 0.5r_p)$ going through cylindrical pores of length $L_p = 10r_p$ (blue) and $L_p = 0.5r_p$ (green), i.e. through membranes thicker and thinner than the sphere.

From Equation 2.3.17 and the corresponding treatment described above, closed-form z_o-mappings, mimicking the electrical signature during translocation, can be obtained for

cylindrical obstructions of length L_c and radius r_c through different rotationally symmetric channels or pores of length L_p. For example, Figure 2.3.5a-c plots z_o-mappings of a cylindrical object ($r_c = 0.5r_p$ and $L_c = 20r_p$) passing through cylindrical, hyperboloidal, and conical shaped pores, the solutions of which are explicitly written out in Section S2.4.9 of the SI. Two mappings are shown per figure panel, corresponding to two different sets of dimensions tested for each pore shape. Corresponding conductance values calculated from finite element simulations are plotted as individual points alongside the z_o-mappings calculated from Equation 2.3.17. Generally, good agreement is found between model predictions and simulation values, although better agreement is found for smaller obstruction volumes and for pore radii that vary smoothly along the z-axis, as is generally expected when working with circular slices (Eq. 2.3.1).[46,47] Additionally, as with 2D membranes, numerical solutions can be obtained for spheres as well as any other obstruction geometry treated in previous sections, as calculated in Section S2.4.9 of the SI and demonstrated in Figure 2.3.5d which shows the numerical solutions to Equation 2.3.17 for a sphere of radius $r_s = 0.5$ passing through cylindrical pores of two different lengths, with one being thinner than the sphere diameter (green) and one longer (blue). Although only simple obstructions are shown in Figure 2.35, complex geometries can also be considered as per Equation 2.3.16 and Figure 2.3.4, which can further help elucidate the effect of pore shape on the conductance signal for a given molecule, and thus a further demonstration of the usefulness of the presented model.

Through the oblate spheroidal treatment of the space outside a pore, we have introduced a general framework by which the resistance of the access regions blocked by an object can be modeled. This approach presents itself as a natural extension to the circular slice method commonly used to model resistances of channel interiors (Eq. 2.3.1).[40] The applicability of the method is exemplified by the various scenarios (obstruction and pore geometries) and physical

phenomena (e.g. off-axis effects) it successfully estimates, as assessed through comparison to finite element analyses. Of particular interest, the modeling of complex molecular structures as a sequence of geometrically simple blocking units (i.e., cylinders, spheres, etc.), allows the calculation of conductance traces as a function of the distance from the pore for predicting the shape of the current traces from actual experiments. However, it should be noted that in addition to inexact field treatment being a source of error, the model is purely geometric in nature and ignores electrokinetic effects that can arise in real experiments, especially in low salt conditions (< 1 M concentrations) or on weakly charged objects.[42] Moreover, except for cylindrical obstructions and centered spheres, many obstructions present no closed-form solutions and must be integrated numerically, the computation of which still represents a significant decrease in complexity compared to 2D or 3D finite element analysis simulations. Nevertheless, the methods presented herein represent a very useful first step towards obtaining more accurate and generally applicable models for blocked access regions, recently described as being in their infancy[40]. With the rapidly advancing micro- and nano-fabrication techniques resulting in thinner membranes with access-resistance dominated sensing conditions, we believe the introduced technique and web-based tool can greatly assist researchers in sizing molecules, for protein fingerprinting and nanoparticle sensing applications, or for optimally designing complex biomolecules for barcoding multiplexing applications.

2.3.8. Methods

Simulations: Finite element simulations were performed with the Electric Currents Module of COMSOL Multiphysics 5.1. In its open state, a nanopore was modeled as a channel of radius r_p in an insulating membrane of either zero or finite thickness L_p (a.k.a. pore length), centred inside a cylindrical meshing domain of length 10 μm and diameter 5 μm. In its blocked state, an insulating region with dimensions matching those of the particular obstruction being modeled was added to the system at the desired coordinates (r_o, z_o). Solutions to Poisson's equation were found within the finite-resistivity regions (defined by constant conductivity σ) of a given geometry, using boundary conditions of 0.2 and 0 V at the top and bottom surfaces of the meshing domain, respectively ($\Delta V = V_{top} - V_{bottom}$). The resulting electrical conductance of the system was evaluated in both open and blocked states such that the numerical solver converged as the mesh size was reduced. The normalized conductance G/σ was calculated by integrating the current density J across the planar top boundary to find the total current I through the system and then dividing this value by the defined transmembrane potential ($G = I/\Delta V$) and conductivity.

2.4 Supporting Information for Section 2.3

S2.4.1. Electric Field in a 2D pore

Oblate spheroidal coordinates (μ, ν, ϕ) are described by the following transformations with cartesian coordinates (x, y, z):

$$\begin{aligned} x &= r_p \cosh\mu \cos\nu \cos\phi\,, \\ y &= r_p \cosh\mu \cos\nu \sin\phi\,, \\ z &= r_p \sinh\mu \sin\nu. \end{aligned} \tag{S2.4.1}$$

As discussed in the main text, the electric potential V between a disk electrode of radius r_p and an infinitely large hemispherical electrode is assumed to depend solely on μ. Under the boundary conditions $V(0) = 0$ and $V(\pm\infty) = \pm\Delta V/2$, and assuming no net charge in the system, a solution for $V(\mu)$ can be found by solving the curvilinear Laplacian equation:

$$\begin{aligned} 0 &= \nabla^2 V \\ 0 &= \frac{1}{h_\mu h_\nu h_\phi}\frac{\partial}{\partial\mu}\left(\frac{h_\nu h_\phi}{h_\mu}\frac{\partial V}{\partial\mu}\right) \\ 0 &= \frac{\partial}{\partial\mu}\left(\cosh\mu\frac{\partial V}{\partial\mu}\right) \\ \mathrm{c}_1 &= \cosh\mu\frac{\partial V(\mu)}{\partial\mu} \\ V(\mu) &= c_1\int\frac{d\mu}{\cosh\mu} \\ V(\mu) &= c_1\tan^{-1}(\sinh\mu) + c_2 \end{aligned}$$

$$V(\mu) = \frac{\Delta V}{\pi}\tan^{-1}(\sinh\mu)\,. \tag{S2.4.2}$$

Note here that c_1 and c_2 are integration constants, and h_μ, h_ν and h_ϕ are scaling factors defined as $h_u = \sqrt{\left(\frac{\partial x}{\partial u}\right)^2 + \left(\frac{\partial y}{\partial u}\right)^2 + \left(\frac{\partial z}{\partial u}\right)^2}$ for $u = \mu, \nu, \phi$, evaluated as:

$$\begin{aligned} h_\mu &= r_p\sqrt{\sinh^2\mu + \sin^2\nu}\,, \\ h_\nu &= r_p\sqrt{\sinh^2\mu + \sin^2\nu}\,, \\ h_\phi &= r_p\cosh\mu\cos\nu. \end{aligned} \tag{S2.4.3}$$

The electric field can be calculated from Equations S2.4.2 and S2.4.3:

$$\vec{E}(\mu,\nu) = -\frac{1}{h_\mu}\frac{\partial V}{\partial \mu}\hat{\mu} = -\frac{\Delta V}{\pi r_p}\frac{\operatorname{sech}\mu}{\sqrt{\sinh^2\mu + \sin^2\nu}}\hat{\mu}\,. \tag{S2.4.4}$$

Note that since $V(\mu)$ depends only on μ, the electric field is directed along $\hat{\mu}$ (See Figure 2.3.1a of main text), and its magnitude $E_o = \left\|\vec{E}\right\|$ depends on both μ and ν, due to the introduction of the h_μ scaling factor.

S2.4.2. Finite Cylindrical Obstruction – z dependence

Consider an insulating cylinder of radius r_c and of finite length $L_c = 2\ell_c$ with its center located a distance z_o away from a 2D pore of radius r_p. Inserting the obstructed region delimitation of $\mu_\pm = \sinh^{-1}\left((z_o \pm \ell_c)/r_p\right)$ and the trivial parametrization of $\rho_o(\mu) = r_c$ into the expression for the obstructed segment (Equation 2.3.5 in main text) results in:

$$\begin{aligned} R'_{cyl}(r_c,\ell_c,z_o) &= \frac{1}{2\pi\sigma r_p}\int_{\sinh^{-1}\left(\frac{z_o-\ell_c}{r_p}\right)}^{\sinh^{-1}\left(\frac{z_o+\ell_c}{r_p}\right)} \frac{\operatorname{sech}\mu}{\sqrt{1-\frac{r_c^2}{r_p^2}\operatorname{sech}^2\mu}}\,d\mu \\ &= \frac{1}{2\pi\sigma r_p}\int_{\frac{\pi}{2}-\tan^{-1}\left(\frac{z_o+\ell_c}{r_p}\right)}^{\frac{\pi}{2}-\tan^{-1}\left(\frac{z_o-\ell_c}{r_p}\right)} \frac{d\theta}{\sqrt{1-\frac{r_c^2}{r_p^2}\sin^2\theta}} \\ &= \frac{1}{2\pi\sigma r_p}\left[F\left(\frac{\pi}{2}-\tan^{-1}\left(\frac{z_o-\ell_c}{r_p}\right),\frac{r_c}{r_p}\right) - F\left(\frac{\pi}{2}-\tan^{-1}\left(\frac{z_o+\ell_c}{r_p}\right),\frac{r_c}{r_p}\right)\right]. \end{aligned} \tag{S2.4.5}$$

Equation S2.4.5 is obtained from the variable substitution $\tanh\mu = \cos\theta$, resulting in $\operatorname{sech}\mu\,d\mu = -d\theta$, and from identities of inverse trigonometric functions:

$$\begin{aligned} \theta|_{\mu=\sinh^{-1}(x)} &= \cos^{-1}(\tanh(\sinh^{-1}(x))) \\ &= \cos^{-1}\left(\frac{x}{\sqrt{1+x^2}}\right) \\ &= \frac{\pi}{2} - \sin^{-1}\left(\frac{x}{\sqrt{1+x^2}}\right) \\ &= \frac{\pi}{2} - \tan^{-1}x\,. \end{aligned} \tag{S2.4.6}$$

As noted in the main text the function $F(\varphi, k)$ is the incomplete elliptic integral of the first kind and is defined as $F(\varphi, k) = \int_0^{\varphi} (1 - k^2 \sin^2 \theta)^{-1/2}\, d\theta$.

The resistance of the unobstructed segments above and under the cylinder can be calculated:

$$\begin{aligned} R_{free}(z_o - \ell_c, z_o + \ell_c) &= R_{free}^{bot} + R_{free}^{top} \\ &= \frac{1}{2\pi\sigma r_p} \int_{-\infty}^{\sinh^{-1}\left(\frac{z_o - \ell_c}{r_p}\right)} \operatorname{sech} \mu \, d\mu + \frac{1}{2\pi\sigma r_p} \int_{\sinh^{-1}\left(\frac{z_o + \ell_c}{r_p}\right)}^{\infty} \operatorname{sech} \mu \, d\mu \\ &= \frac{1}{2\pi\sigma r_p} [\tan^{-1}(\sinh \mu)]_{-\infty}^{\sinh^{-1}\left(\frac{z_o - \ell_c}{r_p}\right)} + \frac{1}{2\pi\sigma r_p} [\tan^{-1}(\sinh \mu)]_{\sinh^{-1}\left(\frac{z_o + \ell_c}{r_p}\right)}^{\infty} \\ &= \frac{1}{2\pi\sigma r_p} \left(\tan^{-1}\left(\frac{z_o - \ell_c}{r_p}\right) + \frac{\pi}{2} \right) + \frac{1}{2\pi\sigma r_p} \left(\frac{\pi}{2} - \tan^{-1}\left(\frac{z_o + \ell_c}{r_p}\right) \right) \\ &= \frac{1}{2\sigma r_p} \left[1 + \frac{1}{\pi} \tan^{-1}\left(\frac{z_o - \ell_c}{r_p}\right) - \frac{1}{\pi} \tan^{-1}\left(\frac{z_o + \ell_c}{r_p}\right) \right]. \end{aligned} \tag{S2.4.7}$$

From Equations S2.4.5 and S2.4.7, an expression for the conductance of the entire 2D pore system in the presence of a cylindrical obstruction of finite length is found:

$$\begin{aligned} \frac{G_b^{cyl}}{G_o}(r_c, \ell_c, z_o) = \Bigg[& 1 + \frac{1}{\pi} \tan^{-1}\left(\frac{z_o - \ell_c}{r_p}\right) - \frac{1}{\pi} \tan^{-1}\left(\frac{z_o + \ell_c}{r_p}\right) \\ & + \frac{1}{\pi} F\left(\frac{\pi}{2} - \tan^{-1}\left(\frac{z_o - \ell_c}{r_p}\right), \frac{r_c}{r_p} \right) - \frac{1}{\pi} F\left(\frac{\pi}{2} - \tan^{-1}\left(\frac{z_o + \ell_c}{r_p}\right), \frac{r_c}{r_p} \right) \Bigg]^{-1}. \end{aligned} \tag{S2.4.8}$$

Here $G_o = 2\sigma r_p$ is the open 2D pore conductance. Figure S2.4.1 plots Equation S2.4.8 against the normalized distance $z_o/(\ell_c + r_p)$, for which a value of ± 1 corresponds the closest extremity of the cylinder being at a distance r_p from the pore mouth. Although each trace corresponds to a different cylinder length, all traces appear to converge near $z_o = \ell_c + r_p$, thus indicating that the dimension of the sensing volume of a 2D pore is on the order of r_p along the z-axis.

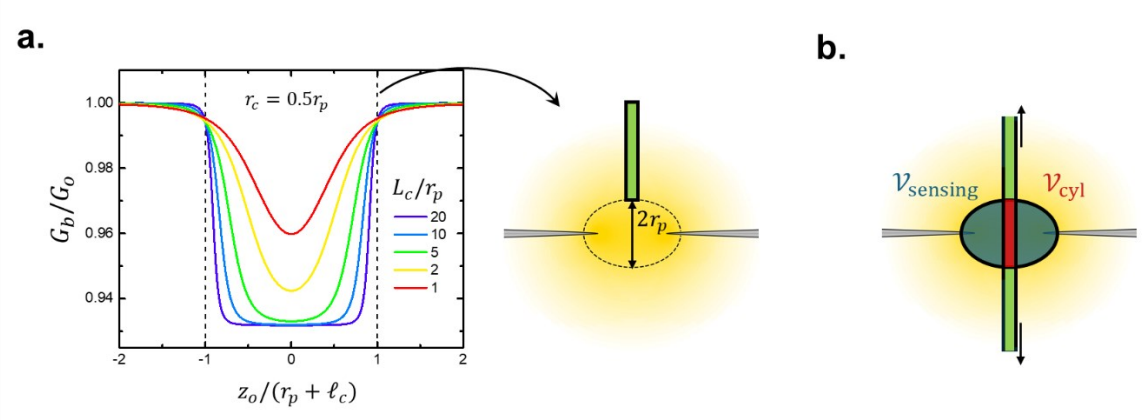

Figure S2.4.1. Conductance of 2D pore blocked by cylindrical obstruction. a) z-dependence of 2D pore conductance in the presence cylindrical obstructions of various lengths L_c, of fixed radius $r_c = 0.5r_p$, with their center at a distance z_o from the pore center. **b)** Sketch demonstrating the interpretations of $\mathcal{V}_{\text{sensing}}$ and $\mathcal{V}_{\text{cyl}}$ as the volumes of the 2D pore sensing volume, and the volume of the cylinder contained with it, respectively.

Additionally, when evaluated for long cylinders ($\ell_c \gg r_p$) centered inside a pore ($z = 0$), Equation S2.4.8 reduces to a simpler form involving the complete elliptic integral of the first kind $K(k)$, related to the incomplete elliptic integral of the first kind through $K(k) = F\left(\frac{\pi}{2}, k\right)$:

$$\begin{aligned}\frac{G_b^{cyl}}{G_o}\left(r_c, \ell_c \gg r_p, z_o = 0\right) &= \left[\frac{1}{\pi}F\left(\pi, \frac{r_c}{r_p}\right)\right]^{-1} \\ &= \left[\frac{2}{\pi}K\left(\frac{r_c}{r_p}\right)\right]^{-1} \\ &= \left[1 + \frac{1}{4}\frac{r_c^2}{r_p^2} + \frac{9}{64}\frac{r_c^4}{r_p^4} + \cdots\right]^{-1} \\ &= 1 - \frac{1}{4}\frac{r_c^2}{r_p^2} - \frac{9}{64}\frac{r_c^4}{r_p^4} + \cdots \end{aligned} \quad \text{(S2.4.9)}$$

The final expression of Equation S2.4.9 used the known relationship $2K(k) = F(\pi, k)$ and the series expansion of $K(k)$ around $k = 0$, the first terms of which are written. For small values of

cylinder radii, $r_c \ll r_p$, Equation S2.4.9 indicates that the fractional conductance blockage $\Delta G/G_o = 1 - G_{cyl}/G_o$ is proportional to r_c^2/r_p^2:

$$\frac{\Delta G_{cyl}}{G_o}\left(r_c \ll r_p \ll \ell_c, z_o = 0\right) \approx \frac{1}{4}\frac{r_c^2}{r_p^2} = \frac{1}{3}\frac{2\pi r_c^2 r_p}{\frac{8}{3}\pi r_p^3} = \frac{1}{3}\frac{\mathcal{V}_{\text{cyl}}}{\mathcal{V}_{\text{sensing}}}. \tag{S2.4.10}$$

Multiplying r_c^2 and r_p^2 by $2\pi r_p/3$, we note interestingly that the fractional blockade $\Delta G/G_o$ is proportional to the ratio of $\mathcal{V}_{\text{cyl}}$ and $\mathcal{V}_{\text{sensing}}$, where $\mathcal{V}_{\text{sensing}}$ is the volume of the oblate spheroid with semi-axis r_p along z (which from now on we designate as the "sensing region"), and $\mathcal{V}_{\text{cyl}}$ is the partial volume of the cylinder contained within the sensing volume.

S2.4.3. Treatment of Flat Cylindrical Obstruction Extremities

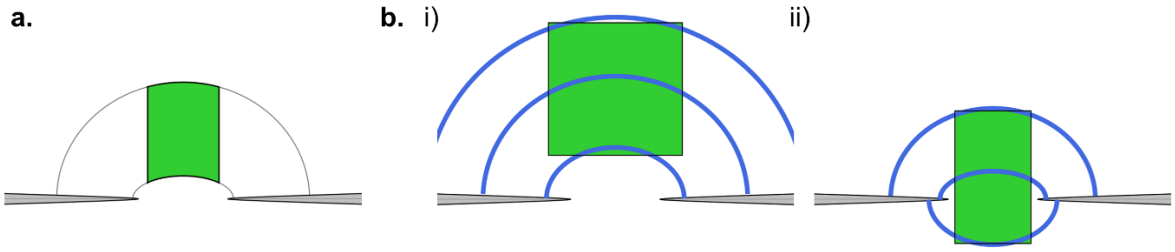

Figure S2.4.2. **Oblate- vs Flat-ended cylindrical obstructions. a)** Sketch showing how cylindrical obstructions are treated as having oblate spheroidal extremities in the main text. **b)** Sketches demonstrating the two independent treatments required to address flat extremities of cylindrical obstructions outside the pore (i) or inside the pore (ii).

The treatment of cylindrical obstructions in the main text inherently assumes cylinder extremities are curved and follow the shape of the oblate spheroidal surface delimiting the obstructed segment, as depicted in Figure S2.4.2a. Cylinders with radii similar in size to that of the pore therefore have their extremities significantly deformed, with the scenario of $r_c > r_p$ even being untreatable. A more thorough treatment of cylindrical obstructions requires segmenting the

access region into more domains, depending on whether constant-μ oblate spheroidal slices intersect with the cylinder's bottom, side, top, or any combination of those, as demonstrated in Figure S2.4.2b. Two different scenarios must be considered: i) the cylinder is completely outside the pore or ii) the cylinder is partially inside the pore.

Outside the pore ($|z_o| > \ell_c$)

When the cylinder is completely outside the pore, as displayed in Figure S2.4.2b-i, the obstructed volume has to be separated into three independently treated oblate spheroidal segments corresponding to resistances R'^{bot}_{obs}, R'^{side}_{obs}, and $R'^{side-top}_{obs}$, in addition to the unobstructed resistive contributions:

$$G_b^{cyl}(r_c, \ell_c, z_o) = \left[R_{free}^{bot} + R'^{bot}_{cyl} + R'^{side}_{cyl} + R'^{side-top}_{cyl} + R_{free}^{top}\right]^{-1}. \quad \text{(S2.4.11)}$$

Before determining expressions for each term in Eq. S2.4.11, let us first determine the values of μ delimiting the different integration domains. Generally, for a cylinder edge located at z, this is achieved by calculating for what value of μ a constant-μ oblate spheroid intersects with a cylinder edge $(\rho, z) = (r_c, z)$:

$$\frac{r_c^2}{\cosh^2 \mu} + \frac{z^2}{\sinh^2 \mu} = r_p^2 \,. \quad \text{(S2.4.12)}$$

Equation S2.4.12 can be rewritten as $0 = r_p^2(\sinh^2 \mu)^2 + \left(r_p^2 - r_c^2 - z^2\right)\sinh^2 \mu - z^2$, which can be solved for $\sinh^2 \mu$ using the quadratic formula:

$$\sinh^2 \mu = \frac{-r_p^2 + r_c^2 + z^2 + \sqrt{\left(r_p^2 - r_c^2 - z^2\right)^2 + 4r_p^2 z^2}}{2r_p^2} \,. \quad \text{(S2.4.13)}$$

An expression for $\mu_{lim}(z)$, the value of μ delimiting the integration domains, is found:

$$\mu_{lim}(z) = \sinh^{-1}\left(\frac{z}{r_p}\sqrt{\frac{1}{2}\left(1 - \frac{r_p^2 - r_c^2}{z^2} + \sqrt{\left(\frac{r_p^2 - r_c^2}{z^2} - 1\right)^2 + 4\frac{r_p^2}{z^2}}\right)}\right) = \sinh^{-1}\left(\frac{z}{r_p}\xi(z)\right). \quad \text{(S2.4.14)}$$

First consider the R'^{bot}_{cyl} contribution, corresponding to the region where oblate spheroids at μ intersect solely with the bottom extremity of the cylindrical obstruction. From the coordinate transformations (Eq. S2.4.1), the fixed-z horizontal bottom extremity is parametrized as:

$$\sin\nu = \frac{z_o - \ell_c}{r_p \sinh\mu}\,. \quad \text{(S2.4.15)}$$

The resistance for the domain accounting for the flat bottom of the cylindrical obstruction is thus:

$$\begin{aligned} R'^{bot}_{cyl} &= \frac{1}{2\sigma\pi r_p}\int_{\sinh^{-1}\left(\frac{z_o-\ell_c}{r_p}\right)}^{\sinh^{-1}\left(\frac{z_o-\ell_c}{r_p}\xi(z_o-\ell_c)\right)} \frac{\operatorname{sech}\mu\, d\mu}{\sin\nu} \\ &= \frac{1}{2\sigma\pi(z_o-\ell_c)}\int_{\sinh^{-1}\left(\frac{z_o-\ell_c}{r_p}\right)}^{\sinh^{-1}\left(\frac{z_o-\ell_c}{r_p}\xi(z_o-\ell_c)\right)} \frac{\sinh\mu\, d\mu}{\cosh\mu} \\ &= \frac{1}{2\sigma\pi(z_o-\ell_c)}\left[\ln(\cosh\mu)\right]_{\sinh^{-1}\left(\frac{z_o-\ell_c}{r_p}\right)}^{\sinh^{-1}\left(\frac{z_o-\ell_c}{r_p}\xi(z_o-\ell_c)\right)} \\ R'^{bot}_{cyl} &= \frac{1}{4\sigma\pi(z_o-\ell_c)}\ln\left(\frac{1+\left(\frac{z_o-\ell_c}{r_p}\xi(z_o-\ell_c)\right)^2}{1+\left(\frac{z_o-\ell_c}{r_p}\right)^2}\right). \end{aligned} \quad \text{(S2.4.16)}$$

Now consider the R'^{side}_{cyl} contribution, corresponding to the region where constant-μ surfaces intersect only with the side of the cylinder, which is trivially parametrized by $\rho_o(\mu) = r_c$, as per the main text, and delimited by $\mu = \sinh^{-1}\left(\frac{z_o-\ell_c}{r_p}\xi(z_o-\ell_c)\right)$ and $\mu = \sinh^{-1}\left(\frac{z_o+\ell_c}{r_p}\right)$:

$$R'^{side}_{cyl} = \frac{1}{2\pi\sigma r_p}\int_{\sinh^{-1}\left(\frac{z_o-\ell_c}{r_p}\xi(z_o-\ell_c)\right)}^{\sinh^{-1}\left(\frac{z_o+\ell_c}{r_p}\right)} \frac{\operatorname{sech}\mu\, d\mu}{\sqrt{1-\frac{r_c^2}{r_p^2}\operatorname{sech}^2\mu}}$$

$$= \frac{1}{2\pi\sigma r_p} \int_{\frac{\pi}{2}-\tan^{-1}\left(\frac{z_o+\ell_c}{r_p}\right)}^{\frac{\pi}{2}-\tan^{-1}\left(\frac{z_o-\ell_c}{r_p}\xi(z_o-\ell_c)\right)} \frac{d\theta}{\sqrt{1-\frac{r_c^2}{r_p^2}\sin^2\theta}}$$

$$= \frac{1}{2\sigma r_p}\left[\frac{1}{\pi}F\left(\frac{\pi}{2}-\tan^{-1}\left(\frac{z_o-\ell_c}{r_p}\xi(z_o-\ell_c)\right),\frac{r_c}{r_p}\right)-\frac{1}{\pi}F\left(\frac{\pi}{2}-\tan^{-1}\left(\frac{z_o+\ell_c}{r_p}\right),\frac{r_c}{r_p}\right)\right]. \quad \text{(S2.4.17)}$$

$R'^{side-top}_{cyl}$, the last obstructed contribution, accounts for the region where oblate spheroidal slices intersect both with the side of the cylinder and its top (Figure S2.4.2). Note, as a result, that the ν integral in the dR calculation thus must be split into two integration domains:

$$R'^{side-top}_{cyl} = \frac{1}{2\pi\sigma r_p}\int_{\sinh^{-1}\left(\frac{z_o+\ell_c}{r_p}\right)}^{\sinh^{-1}\left(\frac{z_o+\ell_c}{r_p}\xi(z_o+\ell_c)\right)} \frac{\operatorname{sech}\mu\, d\mu}{\int_0^{\nu_{side}}\cos\nu\, d\nu+\int_{\nu_{top}}^{\frac{\pi}{2}}\cos\nu\, d\nu}$$

$$= \frac{1}{2\pi\sigma r_p}\int_{\sinh^{-1}\left(\frac{z_o+\ell_c}{r_p}\right)}^{\sinh^{-1}\left(\frac{z_o+\ell_c}{r_p}\xi(z_o+\ell_c)\right)} \frac{\operatorname{sech}\mu\, d\mu}{1-\frac{z_o+\ell_c}{r_p\sinh\mu}+\sqrt{1-\frac{r_c^2}{r_p^2}\operatorname{sech}^2\mu}}. \quad \text{(S2.4.18)}$$

Lastly, the resistance of the unobstructed regions is calculated as:

$$R_{free} = R^{bot}_{free} + R^{top}_{free}$$

$$= \frac{1}{2\pi\sigma r_p}\int_{-\infty}^{\sinh^{-1}\left(\frac{z_o-\ell_c}{r_p}\right)}\operatorname{sech}\mu\, d\mu + \frac{1}{2\pi\sigma r_p}\int_{\sinh^{-1}\left(\frac{z_o+\ell_c}{r_p}\xi(z_o+\ell_c)\right)}^{\infty}\operatorname{sech}\mu\, d\mu$$

$$= \frac{1}{2\pi\sigma r_p}\left(\tan^{-1}\left(\frac{z_o-\ell_c}{r_p}\right)+\frac{\pi}{2}\right)+\frac{1}{2\pi\sigma r_p}\left(\frac{\pi}{2}-\tan^{-1}\left(\frac{z_o+\ell_c}{r_p}\xi(z_o+\ell_c)\right)\right)$$

$$= \frac{1}{2\sigma r_p}\left[1+\frac{1}{\pi}\tan^{-1}\left(\frac{z_o-\ell_c}{r_p}\right)-\frac{1}{\pi}\tan^{-1}\left(\frac{z_o+\ell_c}{r_p}\xi(z_o+\ell_c)\right)\right]. \quad \text{(S2.4.19)}$$

Inside the pore ($|z_o| \le \ell_c$)

Again, as per Figure S2.4.2 and similarly to Equation S2.4.11, the resistances of five separate domains need to be considered when calculating the conductance of flat-ended obstructions bridging across the membrane:

$$G^{b}_{cyl}(r_c, \ell_c, z_o) = \left[R^{bot}_{free} + R'^{bot-side}_{cyl} + R'^{side}_{cyl} + R'^{side-top}_{cyl} + R^{top}_{free}\right]^{-1}. \quad \text{(S2.4.20)}$$

Similarly to the $|z_o| > \ell_c$ case, the resistance of the unobstructed regions is found to be:

$$\begin{aligned} R^{bot}_{free} + R^{top}_{free} &= \frac{1}{2\pi\sigma r_p}\int_{-\infty}^{\sinh^{-1}\left(\frac{z_o-\ell_c}{r_p}\xi(z_o-\ell_c)\right)} \operatorname{sech}\mu\, d\mu \\ &\quad + \frac{1}{2\pi\sigma r_p}\int_{\sinh^{-1}\left(\frac{z_o+\ell_c}{r_p}\xi(z_o+\ell_c)\right)}^{\infty} \operatorname{sech}\mu\, d\mu \\ &= \frac{1}{2\sigma r_p}\left[1 + \frac{1}{\pi}\tan^{-1}\left(\frac{z_o-\ell_c}{r_p}\xi(z_o-\ell_c)\right) - \frac{1}{\pi}\tan^{-1}\left(\frac{z_o+\ell_c}{r_p}\xi(z_o+\ell_c)\right)\right]. \end{aligned} \quad \text{(S2.4.21)}$$

The $R'^{bot-side}_{cyl}$ terms accounts for the segment where oblate spheroidal slices intersect both with the side of the cylinder and its bottom (Figure S2.4.2). As a result, the ν integral in the dR calculation must again be split into two integration domains:

$$\begin{aligned} R'^{bot-side}_{cyl} &= \frac{1}{2\pi\sigma r_p}\int_{\sinh^{-1}\left(\frac{z_o-\ell_c}{r_p}\xi(z_o-\ell_c)\right)}^{\sinh^{-1}\left(\frac{z_o-\ell_c}{r_p}\right)} \frac{\operatorname{sech}\mu\, d\mu}{[\sin\nu]_0^{\nu_{side}} + [\sin\nu]_{\nu_{bot}}^{\frac{\pi}{2}}} \\ &= \frac{1}{2\pi\sigma r_p}\int_{\sinh^{-1}\left(\frac{z_o-\ell_c}{r_p}\xi(z_o-\ell_c)\right)}^{\sinh^{-1}\left(\frac{z_o-\ell_c}{r_p}\right)} \frac{\operatorname{sech}\mu\, d\mu}{1 - \frac{z_o-\ell_c}{r_p\sinh\mu} + \sqrt{1 - \frac{r_c^2}{r_p^2}\operatorname{sech}^2\mu}}. \end{aligned} \quad \text{(S2.4.22)}$$

The R'^{side}_{cyl} terms accounts for the segment where oblate spheroidal slices intersect only with the side of the cylinder (Figure S2.4.2), and is delimited by $\mu_{\pm} = \sinh^{-1}\left(\frac{z_o \pm \ell_c}{r_p}\right)$:

$$\begin{aligned} R'^{side}_{cyl} &= \frac{1}{2\pi\sigma r_p}\int_{\sinh^{-1}\left(\frac{z_o-\ell_c}{r_p}\right)}^{\sinh^{-1}\left(\frac{z_o+\ell_c}{r_p}\right)} \frac{\operatorname{sech}\mu\, d\mu}{\sqrt{1 - \frac{r_c^2}{r_p^2}\operatorname{sech}^2\mu}} \\ &= \frac{1}{2\sigma r_p}\left[\frac{1}{\pi}F\left(\frac{\pi}{2} - \tan^{-1}\left(\frac{z_o-\ell_c}{r_p}\right)\right) - \frac{1}{\pi}F\left(\frac{\pi}{2} - \tan^{-1}\left(\frac{z_o+\ell_c}{r_p}\right)\right)\right]. \end{aligned} \quad \text{(S2.4.23)}$$

The $R'^{side-top}_{cyl}$ terms accounts for the segment where oblate spheroidal slices intersect both with the side of the cylinder and its top (Figure S2.4.2):

$$R'^{side-top}_{cyl} = \frac{1}{2\pi\sigma r_p}\int_{\sinh^{-1}\left(\frac{z_o+\ell_c}{r_p}\right)}^{\sinh^{-1}\left(\frac{z_o+\ell_c}{r_p}\xi(z_o+\ell_c)\right)} \frac{\operatorname{sech}\mu\, d\mu}{[\sin\nu]_0^{\nu_{side}} + [\sin\nu]_{\nu_{top}}^{\frac{\pi}{2}}}$$

$$= \frac{1}{2\pi\sigma r_p}\int_{\sinh^{-1}\left(\frac{z_o+\ell_c}{r_p}\right)}^{\sinh^{-1}\left(\frac{z_o+\ell_c}{r_p}\xi(z_o+\ell_c)\right)} \frac{\operatorname{sech}\mu\, d\mu}{1 - \frac{z_o+\ell_c}{r_p\sinh\mu} + \sqrt{1-\frac{r_c^2}{r_p^2}\operatorname{sech}^2\mu}}\,. \qquad \text{(S2.4.24)}$$

We note that the above equations do not apply for very thin and wide cylinders whose treatment requires the consideration of an oblate spheroidal segment in which constant-μ surfaces intersect both the bottom and top surfaces of the cylinders. Figure S2.4.3 plots Equation S2.4.11 for cylinders of length $L_c = 10r_p$ with radii smaller and larger than the pore radius. For $r_c \geq r_p$, the conductance is zero when $z_o \leq L_c/2$, as expected.

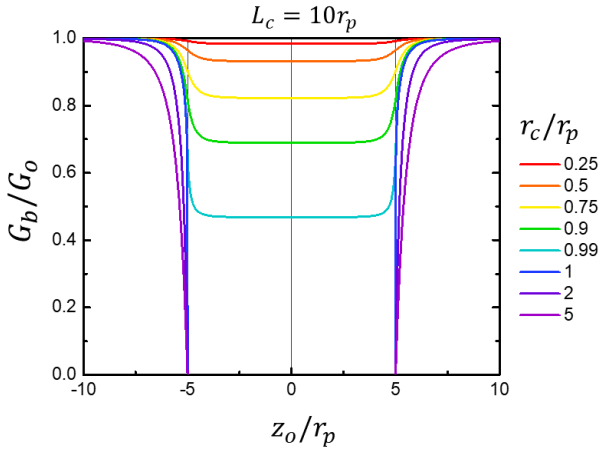

Figure S2.4.3. z-mappings of flat-ended cylindrical obstruction. z-dependence of 2D pore conductance in the presence of cylinders of different radii and fixed length $L_c = 10r_p$.

S2.4.4. Spherical Obstruction

Here the full derivation of a spherical obstruction in a 2D pore is presented.

Centered case ($z_o = 0$)

The equation describing the surface of the spherical obstruction is $r_s^2 = \rho^2 + z^2$, from which an expression for $z^2 = r_s^2 - \rho^2$ is obtained and inserted into the equation of a constant-μ oblate spheroid:

$$1 = \frac{\rho^2}{r_p^2 \cosh^2 \mu} + \frac{r_s^2 - \rho^2}{r_p^2 \sinh^2 \mu} \,. \tag{S2.4.25}$$

Through simple manipulations, an expression for the ρ-parametrization can be obtained:

$$\rho_o^2 = \left(r_s^2 - r_p^2 \sinh^2 \mu\right) \cosh^2 \mu \,. \tag{S2.4.26}$$

The resistance of the oblate spheroidal segment containing the spherical obstruction is thus:

$$\begin{aligned}
R'_{sph}(r_s) &= \frac{1}{2\pi\sigma r_p} \int_{\sinh^{-1}\left(\frac{-r_s}{r_p}\right)}^{\sinh^{-1}\left(\frac{r_s}{r_p}\right)} \frac{\operatorname{sech} \mu \, d\mu}{\sqrt{1 - \frac{r_s^2 - r_p^2 \sinh^2 \mu}{r_p^2}}} \\
&= \frac{1}{\pi\sigma r_p} \int_0^{\sinh^{-1}\left(\frac{r_s}{r_p}\right)} \frac{\operatorname{sech}^2 \mu \, d\mu}{\sqrt{1 - \frac{r_s^2}{r_p^2}} \sqrt{1 + \frac{r_s^2/r_p^2}{1 - \frac{r_s^2}{r_p^2}} \tanh^2 \mu}} \\
&= \frac{1}{\pi\sigma r_s} \left[\sinh^{-1} \left(\frac{r_s/r_p}{\sqrt{1 - r_s^2/r_p^2}} \tanh(\mu) \right) \right]_0^{\sinh^{-1}\left(\frac{r_s}{r_p}\right)} \\
&= \frac{1}{\pi\sigma r_s} \left(\sinh^{-1} \left(\frac{r_s^2/r_p^2}{\sqrt{1 - \left(r_s^2/r_p^2\right)^2}} \right) \right)
\end{aligned}$$

$$\Rightarrow R'_{sph}(r_s) = \frac{1}{\pi\sigma r_s} \tanh^{-1} \left(\frac{r_s^2}{r_p^2} \right) \,. \tag{S2.4.27}$$

By including the contribution from the unobstructed segments (Equation 2.3.6, main text), the conductance of a 2D nanopore in the presence of a centered spherical obstruction is:

$$\frac{G_b^{sph}}{G_o}(r_s) = \left[1 - \frac{2}{\pi}\tan^{-1}\left(\frac{r_s}{r_p}\right) + \frac{2}{\pi}\frac{r_p}{r_s}\tanh^{-1}\left(\frac{r_s^2}{r_p^2}\right)\right]^{-1}. \quad \text{(S2.4.28)}$$

Non-Centered case $(z_o \neq 0)$

The surface of the sphere translated along the z axis by z_o is described by the equation:

$$\rho^2 + (z - z_o)^2 = r_s^2. \quad \text{(S2.4.29)}$$

From Equation S2.4.29, an expression for z^2 can be obtained, and inserted into the constant-μ oblate spheroidal equation:

$$\frac{\rho^2}{r_p^2\cosh^2\mu} + \frac{r_s^2 - \rho^2 + 2z_o\sqrt{r_s^2 - \rho^2} + z_o^2}{r_p^2\sinh^2\mu} = 1. \quad \text{(S2.4.30)}$$

Equation S2.4.30 can be rewritten as a quadratic equation with respect to $\rho^2\,\mathrm{sech}^2\,\mu$:

$$\begin{aligned} 0 = \rho^4\,\mathrm{sech}^4\,\mu - \left(2\left(r_s^2 + z_0^2 - r_p^2\sinh^2\mu\right) - 4z_0^2\cosh^2\mu\right)\rho^2\,\mathrm{sech}^2\,\mu \\ + \left(\left(r_s^2 + z_0^2 - r_p^2\sinh^2\mu\right)^2 - 4z_0^2r_s^2\right). \end{aligned} \quad \text{(S2.4.31)}$$

Inserting the positive quadratic formula solution for $\rho^2\,\mathrm{sech}^2\,\mu$ into Equation 2.3.5 of the main text, i.e. $dR = \left(2\pi\sigma r_p\right)^{-1}/\sqrt{1 - \rho^2\,\mathrm{sech}^2\,\mu\,/r_p^2}$, results in an expression for the resistance of the obstructed oblate spheroidal segment:

$$\frac{R'_{sph}}{R_o}(r_s, z_o) = \frac{1}{\pi}\int_{\sinh^{-1}\left(\frac{z_o - r_s}{r_p}\right)}^{\sinh^{-1}\left(\frac{z_o + r_s}{r_p}\right)} \frac{\mathrm{sech}^2\,\mu\,d\mu}{\sqrt{1 - \frac{r_s^2 + z_o^2}{r_p^2}\mathrm{sech}^2\,\mu + 2\frac{z_o^2}{r_p^2} - 2\frac{z_o}{r_p}\tanh\mu\sqrt{1 + \frac{z_o^2}{r_p^2} - \frac{r_s^2}{r_p^2}\mathrm{sech}^2\,\mu}}}. \quad \text{(S2.4.32)}$$

Here, $R_o = 1/2\sigma r_p$ is the resistance of an open 2D pore. The contributions from the two unobstructed segments can above and below the sphere can also be considered:

$$R_{free}(r_s, z_o) = R_{free}^{bot} + R_{free}^{top}$$
$$= \frac{1}{2\pi\sigma r_p}\int_{-\infty}^{\sinh^{-1}\left(\frac{z_o - r_s}{r_p}\right)} \operatorname{sech}\mu \, d\mu + \frac{1}{2\pi\sigma r_p}\int_{\sinh^{-1}\left(\frac{z_o + r_s}{r_p}\right)}^{\infty} \operatorname{sech}\mu \, d\mu$$
$$= \frac{1}{2\sigma r_p}\left(1 + \frac{1}{\pi}\tan^{-1}\left(\frac{z_o - r_s}{r_p}\right) - \frac{1}{\pi}\tan^{-1}\left(\frac{z_o + r_s}{r_p}\right)\right). \quad \text{(S2.4.33)}$$

The general expression for the conductance of a 2D pore in the presence of a spherical obstruction of radius r_s at a distance z_o from the pore center is thus:

$$\left(\frac{G_b^{sph}}{G_o}\right)^{-1} = 1 + \frac{1}{\pi}\tan^{-1}\left(\frac{z_o - r_s}{r_p}\right) - \frac{1}{\pi}\tan^{-1}\left(\frac{z_o + r_s}{r_p}\right)$$
$$+ \frac{1}{\pi}\int_{\sinh^{-1}\left(\frac{z_o - r_s}{r_p}\right)}^{\sinh^{-1}\left(\frac{z_o + r_s}{r_p}\right)} \frac{\operatorname{sech}^2\mu \, d\mu}{\sqrt{1 - \frac{r_s^2 + z_o^2}{r_p^2}\operatorname{sech}^2\mu + 2\frac{z_o^2}{r_p^2} - 2\frac{z_o}{r_p}\tanh\mu \sqrt{1 + \frac{z_o^2}{r_p^2} - \frac{r_s^2}{r_p^2}\operatorname{sech}^2\mu}}}. \quad \text{(S2.4.34)}$$

Equation S2.4.34 is plotted in Figure 2.3.2c of the main text alongside conductance values from corresponding finite element simulations. Interestingly, we note that unlike with cylinders, no special treatment is required for spheres bigger than the pores, as demonstrated in Figure S2.4.4 which plots examples of Equation S2.4.34 for both $r_s < r_p$ and $r_s \geq r_p$.

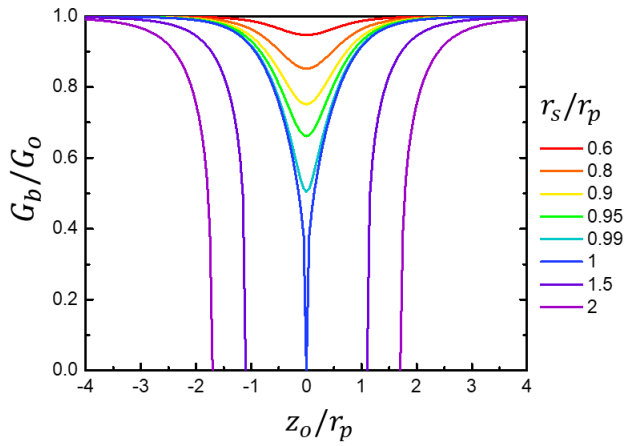

Figure S2.4.4. z-mappings of spherical obstruction. z_o-dependence of the conductance of 2D pores in the presence of spherical obstructions of various radii.

S2.4.5. Rotationally Symmetric Obstructions – More Examples

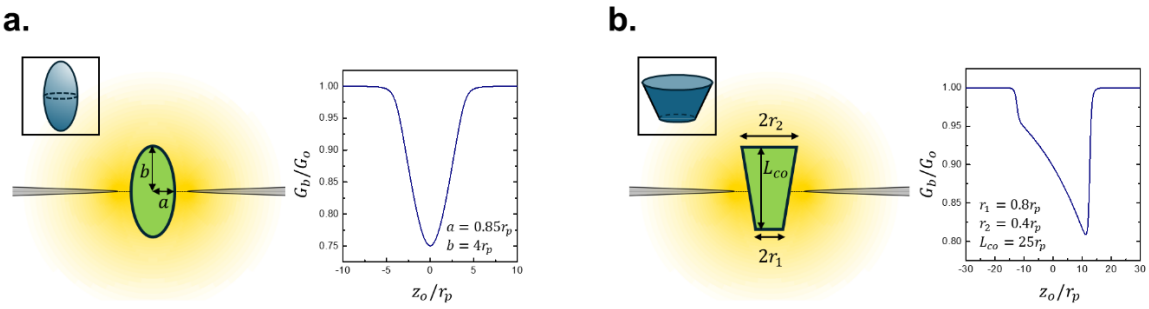

Figure S2.4.5. Conductance of a 2D pore blocked by an obstruction with **(a)** an ellipsoidal geometry and **(b)** with a truncated conical geometry.

Prolate Ellipsoid Centered Inside a 2D Pore

The surface of an ellipsoid at a distance z_o from a 2D pore with dimensions a along the ρ-axis and b along the z-axis is described by the equation:

$$\frac{\rho^2}{a^2} + \frac{(z - z_o)^2}{b^2} = 1\,. \tag{S2.4.35}$$

The $\rho_o(\mu)$ parameterization of the ellipsoid obstruction is found by isolating z^2 in Equation S2.4.35 and inserting the it into the equation of a constant-μ surface, resulting in (for $z_o = 0$):

$$\rho_o^2(\mu) = \frac{\sinh^2\mu - \dfrac{b^2}{r_p^2}}{\sinh^2\mu - \dfrac{b^2}{a^2}\cosh^2\mu}\, r_p^2 \cosh^2\mu\ . \tag{S2.4.36}$$

The corresponding expression for the resistance of the oblate spheroidal segment containing the ellipsoidal obstruction is thus:

$$R'_{ellipse}(a,b) = \frac{1}{2\pi\sigma r_p}\int_{\sinh^{-1}\left(-\frac{b}{r_p}\right)}^{\sinh^{-1}\left(\frac{b}{r_p}\right)} \frac{\operatorname{sech}\mu\, d\mu}{\sqrt{1-\dfrac{\sinh^2\mu - \dfrac{b^2}{r_p^2}}{\sinh^2\mu - \dfrac{b^2}{a^2}\cosh^2\mu}}}$$

$$= \frac{1}{2\pi\sigma r_p}\int_{\sinh^{-1}\left(-\frac{b}{r_p}\right)}^{\sinh^{-1}\left(\frac{b}{r_p}\right)} \frac{\sqrt{1-\dfrac{a^2}{b^2}\tanh^2\mu}}{\sqrt{1-\dfrac{a^2}{r_p^2}\operatorname{sech}^2\mu}}\operatorname{sech}\mu\, d\mu\,. \qquad \text{(S2.4.37)}$$

Equation S2.4.37 presents no closed form solution, however, note that in the two limits of $a = b$ and $b \to \infty$, $R'_{ellipse}(\mu)$ corresponds exactly to the expressions for the spherical obstruction (Equation S2.4.27), and the infinitely long cylindrical obstruction (Equation S2.4.9), respectively. The resistance of a nanopore obstructed by a centered ellipsoid is therefore:

$$\frac{G_b^{ellipse}}{G_o}(a,b) = \left[1 - \frac{2}{\pi}\tan^{-1}\left(\frac{b}{r_p}\right) + \frac{1}{\pi}\int_{\sinh^{-1}\left(-\frac{b}{r_p}\right)}^{\sinh^{-1}\left(\frac{b}{r_p}\right)} \frac{\sqrt{1-\dfrac{a^2}{b^2}\tanh^2\mu}}{\sqrt{1-\dfrac{a^2}{r_p^2}\operatorname{sech}^2\mu}}\operatorname{sech}\mu\, d\mu\right]^{-1}. \qquad \text{(S2.4.38)}$$

Prolate Ellipsoid Centered at distance z_o from a 2D Pore

Let an ellipsoid of semi-axes a and b along the ρ and z dimensions, respectively, have its center be at a distance z_o from a 2D nanopore. Its surface can be parametrized by finding its intersection points with constant-μ ellipses, as was done above. Doing so results in the following simple expression for the resistance of a punctured ellipsoidal slice:

$\frac{R'_{ellipse}}{R_o} = 2\sigma r_p \int dR(\mu)$

$$= \frac{1}{\pi}\int_{\sinh^{-1}\left(\frac{z_o-b}{r_p}\right)}^{\sinh^{-1}\left(\frac{z_o+b}{r_p}\right)} \frac{\operatorname{sech}\mu\, d\mu}{\sqrt{1+\frac{\left(\tanh^2\mu-\frac{b^2}{a^2}\right)\left(\frac{b^2+z_o^2}{r_p^2}-\sinh^2\mu\right)+2\frac{z_o^2b^2}{r_p^2a^2}-\operatorname{sign}(\mu)2\frac{z_ob}{r_pa}\sqrt{\left(\tanh^2\mu-\frac{b^2}{a^2}\right)\left(\frac{b^2+z_o^2}{r_p^2}-\sinh^2\mu\right)+\frac{z_o^2b^2}{r_p^2a^2}+\frac{a^2}{r_p^2}\left(\tanh^2\mu-\frac{b^2}{a^2}\right)^2}}{\left(\tanh^2\mu-\frac{b^2}{a^2}\right)^2}}} \quad \text{(S2.4.39)}$$

The total resistance in the system can be expressed as:

$$R_b^{ellipse}(a,b,z_o) = R_{free}(-\infty, z_o-b) + R'_{ellipse} + R_{free}(z_o+b,\infty). \quad \text{(S2.4.40)}$$

and the normalized blocked-state conductance can be expressed as:

$$\frac{G_b^{ellipse}}{G_o}(a,b,z_o) = \left[1+\frac{1}{\pi}\tan^{-1}\left(\frac{z_o-b}{r_p}\right)-\frac{1}{\pi}\tan^{-1}\left(\frac{z_o+b}{r_p}\right)+\frac{R'_{ellipse}}{R_o}\right]^{-1}. \quad \text{(S2.4.41)}$$

The z dependence of Equation S2.4.41 is plotted in Figure S2.4.5a for an ellipsoid of dimension $a = 0.85r_p$ and $b = 4r_p$.

Truncated Cone

Here we consider a truncated cone of length $L_{co} = 2\ell_{co}$, centered at z_o with one of its faces located at $z = z_o - \ell_c$ having radius r_1 and the other located at $z = z_o + \ell_{co}$ with radius r_2. The surface of the conical section is parametrized by the following equation:

$$\rho_o(z) = \frac{r_2-r_1}{2\ell_{co}}(z-z_o)+\frac{r_1+r_2}{2}. \quad \text{(S2.4.42)}$$

The parametrization of ρ_o with respect to μ can be found by isolating z from the above and inserting this result into the expression of a constant-μ surface, as before. The infinitesimal resistance of an oblate spheroidal slice containing the obstruction can then be found using Equation 2.3.5 in the main text:

$$dR'_{co}(\mu) = \frac{1}{2\pi\sigma r_p}\frac{\operatorname{sech}\mu\, d\mu}{\sqrt{1-\frac{\left(\frac{2\ell_{co}}{r_2-r_1}\left(\ell_{co}\frac{r_2+r_1}{r_2-r_1}-z_o\right)+\operatorname{sign}(\mu(r_2-r_1))\sqrt{\left(\tanh^2\mu+\frac{4\ell_{co}^2}{(r_2-r_1)^2}\right)r_p^2\sinh^2\mu-\tanh^2\mu\left(z_o-\ell_{co}\frac{r_2+r_1}{r_2-r_1}\right)^2}\right)^2}{r_p^2\cosh^2\mu\left(\tanh^2\mu+\frac{4\ell_{co}^2}{(r_2-r_1)^2}\right)^2}}}. \quad \text{(S2.4.43)}$$

The total resistance in the system can be expressed as:

$$R_b^{co}(r_1, r_2, \ell_{co}, z_o) = R_{free}(-\infty, z_o - \ell_{co}) + \int_{\sinh^{-1}\frac{z_o-\ell_{co}}{r_p}}^{\sinh^{-1}\frac{z_o+\ell_{co}}{r_p}} dR'_{co}(\mu) + R_{free}(z_o + \ell_{co}, \infty)\,. \quad \text{(S2.4.44)}$$

and the normalized blocked-state conductance as:

$$\frac{G_b^{co}}{G_o} = \left[1 + \frac{1}{\pi}\tan^{-1}\left(\frac{z_o - \ell_{co}}{r_p}\right) - \frac{1}{\pi}\tan^{-1}\left(\frac{z_o + \ell_{co}}{r_p}\right) + 2\sigma r_p \int_{\sinh^{-1}\frac{z_o-\ell_{co}}{r_p}}^{\sinh^{-1}\frac{z_o+\ell_{co}}{r_p}} dR'_{co}(\mu)\right]^{-1}. \quad \text{(S2.4.45)}$$

The z dependence of Equation S2.4.45 is plotted in Figure S2.4.5b for a truncated cone of dimension $r_1 = 0.8r_p$, $r_2 = 0.4r_p$ and $L_{co} = 2\ell_{co} = 25r_p$.

S2.4.6. Rotationally Asymmetric Obstructions – Wedged Cylinder

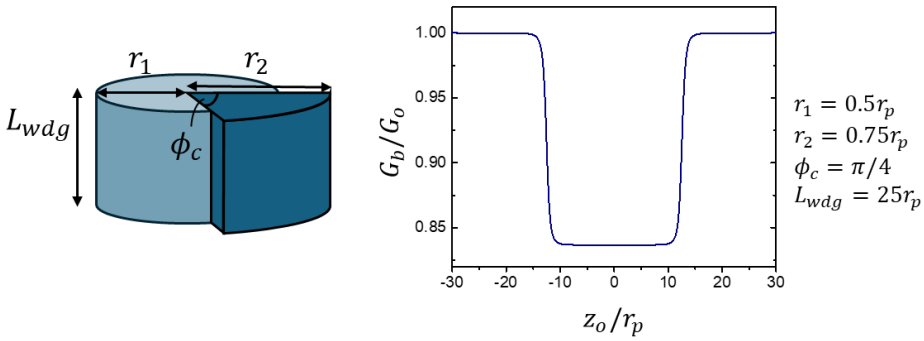

Figure S2.4.6. Conductance of a 2D pore blocked by a wedged cylindrical obstruction.

Consider the simple rotationally asymmetric case of a wedged cylinder of length $L_{wdg} = 2\ell_{wdg}$, whose surface is defined as:

$$\rho_o(\phi) = \begin{cases} r_1, & \text{for } \phi_c/2 < \phi < 2\pi - \phi_c/2 \\ r_2, & \text{for } -\phi_c/2 < \phi < \phi_c/2 \end{cases} \quad \text{(S2.4.46)}$$

The resistance of the punctured oblate spheroidal slice at μ can be calculated as:

$$dR'_{wedge}(\mu) = \frac{1}{\sigma r_p} \frac{\operatorname{sech}\mu}{\int_{\phi_c/2}^{2\pi-\phi_c/2} \sqrt{1-\frac{r_1^2}{r_p^2}\operatorname{sech}^2\mu}\, d\phi + \int_{-\phi_c/2}^{\phi_c/2} \sqrt{1-\frac{r_2^2}{r_p^2}\operatorname{sech}^2\mu}\, d\phi}$$
$$= \frac{1}{2\sigma\pi r_p} \frac{\operatorname{sech}\mu}{\left(1-\frac{\phi_c}{2\pi}\right)\sqrt{1-\frac{r_1^2}{r_p^2}\operatorname{sech}^2\mu} + \frac{\phi_c}{2\pi}\sqrt{1-\frac{r_2^2}{r_p^2}\operatorname{sech}^2\mu}}. \quad \text{(S2.4.47)}$$

The total resistance in the system can be expressed as:

$$R_b^{wedge}(r_1, r_2, \phi_c, \ell_{wdg}, z_o) = R_{free}(-\infty, z_o - \ell_{wdg}) + R'_{wedge} + R_{free}(z_o + \ell_{wdg}, \infty). \quad \text{(S2.4.48)}$$

and the normalized blocked-state conductance can be expressed as:

$$\frac{G_b^{wedge}}{G_o} = \left[1 + \frac{1}{\pi}\tan^{-1}\left(\frac{z_o - \ell_w}{r_p}\right) - \frac{1}{\pi}\tan^{-1}\left(\frac{z_o + \ell_w}{r_p}\right) + 2\sigma r_p \int_{\sinh^{-1}\frac{z_o-\ell_w}{r_p}}^{\sinh^{-1}\frac{z_o+\ell_w}{r_p}} dR'_{wedge}(\mu)\right]^{-1}. \quad \text{(S2.4.49)}$$

S2.4.7. Rotationally Asymmetric Obstructions – Off-Axis Effects

Off-Centered Cylinder

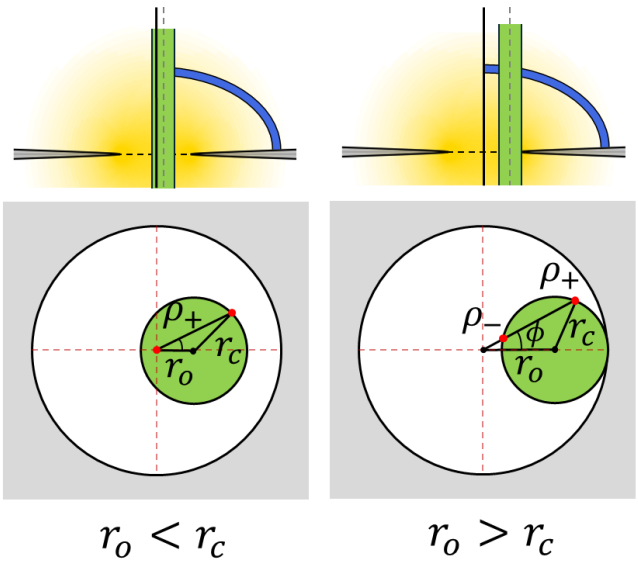

Figure S2.4.7. Geometrical considerations of off-centered cylindrical obstructions. Cross-sectional view of the x-y plane showing the geometrical parameters of a 2D pore in the presence of an infinitely long cylindrical obstruction at a distance r_o from the pore center.

Consider an infinitely long cylindrical obstruction of radius r_c, lying parallel to the z axis, but centred at a distance r_o away from the central pore axis, as per Figure S2.4.7. The parametrization of the obstruction's surface is found by calculating the distance ρ_o at which the constant-ϕ planes and the cylindrical obstruction intersect. As per Figure S2.4.7, this can be achieved using the trigonometry of the system cross-section in the $z = 0$ plane:

$$\rho_{\pm}(\phi) = r_o \cos\phi \pm \sqrt{r_c^2 - r_o^2 \sin^2\phi}\,. \tag{S2.4.50}$$

Note that the scenarios for which $r_o < r_c$ and $r_o > r_c$ need to be treated separately. For $r_o < r_c$, the resistance of the obstructed system is found to be:

$$\begin{aligned} R'_{cyl}(r_o < r_c) &= \frac{1}{\sigma r_p}\int_{-\infty}^{\infty} \frac{\operatorname{sech}\mu\, d\mu}{\int_0^{2\pi}[\sin\nu]_0^{\nu_o(\phi)} d\phi} \\ &= \frac{1}{\sigma r_p}\int_{-\infty}^{\infty} \frac{\operatorname{sech}\mu\, d\mu}{\int_0^{2\pi}\sqrt{1 - \frac{\rho_+^2(\phi)}{r_p^2}\operatorname{sech}^2\mu}\, d\phi} \\ &= \frac{1}{\sigma r_p}\int_{-\infty}^{\infty} \frac{\operatorname{sech}\mu\, d\mu}{\int_0^{2\pi}\sqrt{1 - \left(\frac{r_o}{r_p}\cos\phi + \sqrt{\frac{r_c^2}{r_p^2} - \frac{r_o^2}{r_p^2}\sin^2\phi}\right)^2 \operatorname{sech}^2\mu}\, d\phi}\,. \end{aligned} \tag{S2.4.51}$$

For $r_o > r_c$, the resistance calculation involves integrating over two distinct ν domains, and thereby using both the ρ_+ and ρ_- solutions of Equation S2.4.50. Moreover, not all constant-ϕ planes intersect the cylindrical obstruction, only those within the angles $|\phi| < \phi_c = \sin^{-1}(r_c/r_o)$:

$$\begin{aligned} R'_{cyl}(r_o > r_c) &= \frac{1}{\sigma r_p}\int_{-\infty}^{\infty} \frac{\operatorname{sech}\mu\, d\mu}{\int_{\phi_c}^{2\pi-\phi_c}[\sin\nu]_0^{\frac{\pi}{2}} d\phi + \int_{-\phi_c}^{\phi_c}\left([\sin\nu]_0^{\nu_+(\phi)} + [\sin\nu]_{\nu_-(\phi)}^{\frac{\pi}{2}}\right) d\phi} \\ &= \frac{1}{\sigma r_p}\int_{-\infty}^{\infty} \frac{\operatorname{sech}\mu\, d\mu}{2\pi - 2\phi_c + \int_{-\phi_c}^{\phi_c}\left(\sqrt{1 - \frac{\rho_+^2}{r_p^2}\operatorname{sech}^2\mu} + 1 - \sqrt{1 - \frac{\rho_-^2}{r_p^2}\operatorname{sech}^2\mu}\right) d\phi} \end{aligned}$$

$$= \frac{1}{\sigma r_p}\int_{-\infty}^{\infty} \frac{\operatorname{sech}\mu\, d\mu}{2\pi + \int_{-\sin^{-1}\left(\frac{r_c}{r_o}\right)}^{\sin^{-1}\left(\frac{r_c}{r_o}\right)} \left(\sqrt{1-\frac{\rho_+^2}{r_p^2}\operatorname{sech}^2\mu} - \sqrt{1-\frac{\rho_-^2}{r_p^2}\operatorname{sech}^2\mu}\right) d\phi} \,. \tag{S2.4.52}$$

Equation 2.3.17 of the main text thus denotes the blocked-state conductance, i.e. inverse values of Equations S2.4.51 and S2.4.52 normalized by the open pore conductance $2\sigma r_p$. As in Figure 2.3.3b of the main text, Figure S2.4.8a plots the dependence of the normalized conductance on r_o for different values of r_c/r_p. Figure S2.4.8b plots the extra blockage arising from $r_o > 0$ values, calculated as the percentage of extra conductance in the $r_o = 0$ case compared to $r_o \neq 0$.

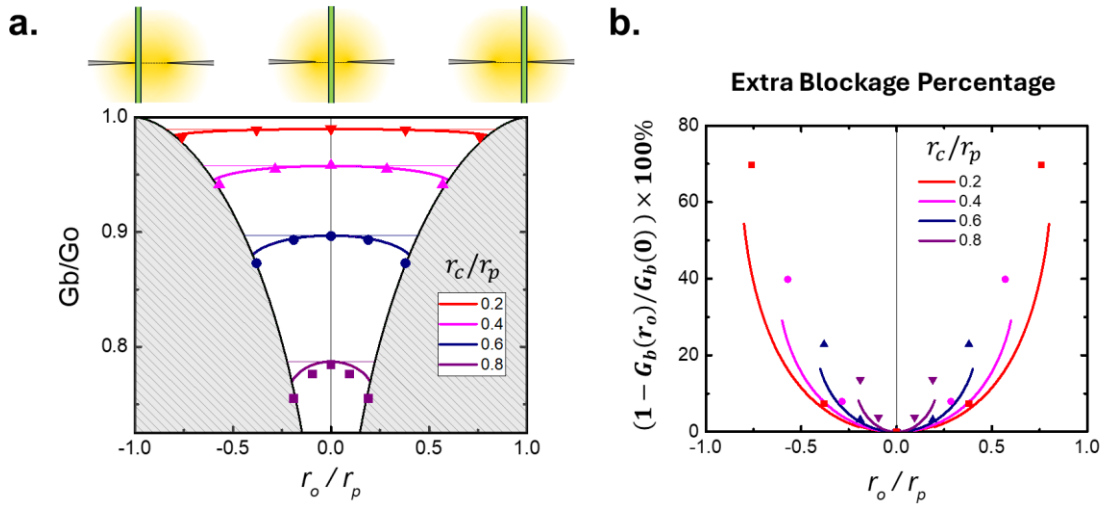

Figure S2.4.8. Off-axis effects for infinitely long cylindrical obstructions. **a)** Dependence of normalized blocked-state conductance G_b^{cyl}/G_o on radial position of cylinder inside pore r_o. **b)** Extra conductance induced by centred cylinder position $r_o = 0$, compared to off-axis $r_o \neq 0$. All individual points are values calculated from finite element simulations, whereas continuous curves are from Equations S2.4.50-51.

Off-Centered Sphere

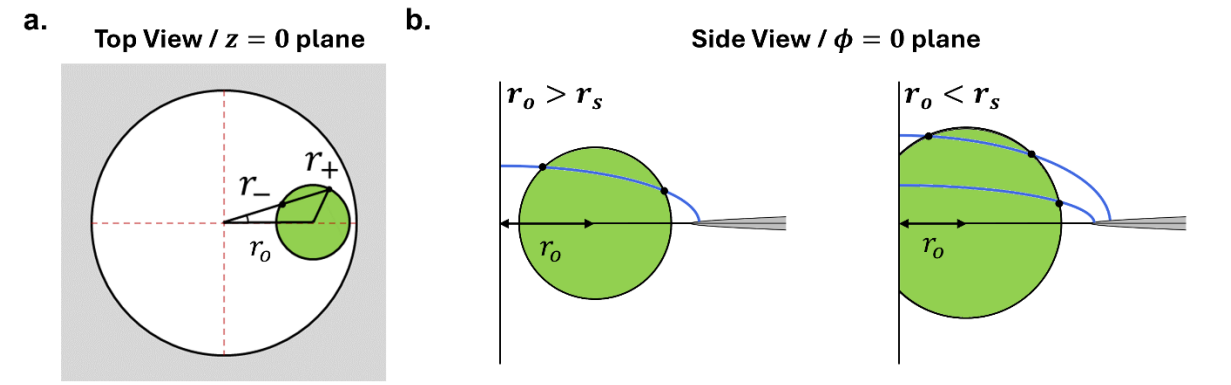

Figure S2.4.9. Geometrical considerations of off-centered sphere obstructions. a) $z = 0$ cross-section sketch showing the simple trigonometry required to characterize the intersection circles resulting from the presence of a spherical obstruction in a 2D pore using $r_{\pm}$. **b)** Sketch depicting the number of intersection points between the surface of a circle and an ellipse.

Unlike infinitely long cylindrical obstructions, the surface parametrization of spherical obstructions is not solely dependent on μ, as is now discussed. First note that the intersection of constant-ϕ planes with the sphere surface is a circle. The intersection of constant-ϕ with constant-μ oblate spheroids is instead an ellipse. Finding the parametrization $\rho_o(\phi, \mu)$ of the spherical surface therefore relies on finding the intersection point(s) between these ϕ-characteristic circles and ellipses.

Let us first characterize the circle resulting from the intersection of the ϕ-plane with the vertically centred ($z_o = 0$) spherical obstruction. As shown in Figure S2.4.9a, the problem is again solved using simple trigonometry while considering the $z = 0$ plane cross-section. We can thus find $r_{\pm}$, defined as the intersection points of the ϕ-plane and the sphere in the $z = 0$ plane:

$$r_{\pm} = r_o \cos\phi \pm \sqrt{r_s^2 - r_o^2 \sin^2\phi}\,. \tag{S2.4.53}$$

The ϕ-dependent radius r_{cs} of the intersection circle as well as its mean radial distance from the pore center r_{co} can be calculated from $r_{\pm}$:

$$r_{cs}(\phi) = \frac{r_+ - r_-}{2} = \sqrt{r_s^2 - r_o^2 \sin^2 \phi}\,, \tag{S2.4.54}$$

$$r_{co}(\phi) = \frac{r_- + r_+}{2} = r_o \cos \phi\,. \tag{S2.4.55}$$

The surface of the intersection circle in the constant-ϕ plane is thus described by:

$$\left(\rho - r_{co}(\phi)\right)^2 + z^2 = r_{cs}^2\,. \tag{S2.4.56}$$

The parametrization $\rho_o(\mu, \phi)$ of the sphere surface is found by isolating z^2 and inserting it into the equation for the surface of a constant-μ oblate spheroid:

$$\rho_\pm(\mu, \phi) = r_{co}(\phi) \cosh^2 \mu \pm \sqrt{\left(r_{co}^2(\phi) - r_p^2\right) \cosh^2 \mu \sinh^2 \mu + r_{cs}^2 \cosh^2 \mu}\,. \tag{S2.4.57}$$

Note that just like cylindrical obstructions, there can be one or two intersections points, as denoted by the positive and negative signs of Equation S2.4.57. Unlike for cylinders however, the number of intersection points to consider is not only dependent on r_o but also on μ, as shown in Figure S2.4.9b. For $r_o > r_s$ there are always two intersection points, i.e. two ν intervals over which to integrate, whereas for $r_o < r_s$, there is a value of $\mu = \mu_l$ that delimits the oblate spheroidal segments with one or two intersection points. Two intersections are considered when both $\rho_\pm$ are positive, and so μ_l is found by setting $\rho_- = 0$:

$$0 = r_o \cos \phi \cosh^2 \mu_l - \sqrt{\left(r_o^2 \cos^2 \phi - r_p^2\right) \cosh^2 \mu_l \sinh^2 \mu_l + (r_s^2 - r_o^2 \sin^2 \phi) \cosh^2 \mu_l}$$

$$0 = r_o \cos \phi \cosh \mu_l - \sqrt{\left(r_o^2 \cos^2 \phi - r_p^2\right) \sinh^2 \mu_l + (r_s^2 - r_o^2 \sin^2 \phi)}$$

$$0 = r_o^2 \cos^2 \phi \cosh^2 \mu_l - r_o^2 \cos^2 \phi \sinh^2 \mu_l + r_p^2 \sinh^2 \mu_l - r_s^2 + r_o^2 \sin^2 \phi$$

$$\sinh^2 \mu_l = \frac{r_s^2 - r_o^2}{r_p^2}.$$

$$\Longrightarrow \mu_l = \sinh^{-1}\left(\sqrt{\frac{r_s^2 - r_o^2}{r_p^2}}\right). \tag{S2.4.58}$$

Note μ_l is independent of ϕ, an important requirement for the slice method to function properly.

Now, we note that the ϕ interval spanned by the obstruction depends both on r_o and on the μ-value of a slice, i.e. $|\phi| < \phi_{max}(r_o, \mu)$. The limiting value $\phi_{max}(r_o, \mu)$ is found by setting $\rho_-(\mu, \phi_{max}) = \rho_+(\mu, \phi_{max})$, which results in:

$$\begin{aligned}
0 &= \sqrt{\left(r_o^2 \cos^2 \phi_{max} - r_p^2\right) \cosh^2 \mu \sinh^2 \mu + \left(r_s^2 - r_o^2 \sin^2 \phi_{max}\right) \cosh^2 \mu} \\
0 &= r_o^2 \cos^2 \phi_{max} \sinh^2 \mu - r_p^2 \sinh^2 \mu + r_s^2 - r_o^2 \sin^2 \phi_{max} \\
0 &= \left(r_o^2 - r_p^2\right) \sinh^2 \mu + r_s^2 - r_o^2 \sin^2 \phi_{max} \cosh^2 \mu \\
\sin^2 \phi_{max} &= \left(1 - \frac{r_p^2}{r_o^2}\right) \tanh^2 \mu + \frac{r_s^2}{r_o^2} \operatorname{sech}^2 \mu.
\end{aligned}$$

$$\Longrightarrow \phi_{max} = \sin^{-1}\left(\sqrt{\left(1 - \frac{r_p^2 + r_s^2}{r_o^2}\right) \tanh^2 \mu + \frac{r_s^2}{r_o^2}}\right). \tag{S2.4.59}$$

Lastly, we find the maximal μ-value containing the sphere, μ_{max}, in order to delimit the obstructed and unobstructed μ-integrals. μ_{max} is found by setting both $\rho_- = \rho_+$ and $\phi = 0$:

$$\mu_{max} = \sinh^{-1}\left(\sqrt{\frac{r_s^2}{r_p^2 - r_o^2}}\right). \tag{S2.4.60}$$

For $r_o > r_s$, the resistance of the obstructed oblate spheroidal segment is therefore:

$$\begin{aligned}
R'_{sph}(r_o > r_s) &= \frac{2}{\sigma r_p} \int_0^{\mu_{max}} \frac{\operatorname{sech} \mu \, d\mu}{\int_{\phi_{max}}^{2\pi - \phi_{max}} [\sin \nu]_0^{\frac{\pi}{2}} d\phi + \int_{-\phi_{max}}^{\phi_{max}} \left([\sin \nu]_0^{\nu_+} + [\sin \nu]_{\nu_-}^{\frac{\pi}{2}}\right) d\phi} \\
&= \frac{2}{\sigma r_p} \int_0^{\sinh^{-1}\left(\frac{r_s}{\sqrt{r_p^2 - r_o^2}}\right)} \frac{\operatorname{sech} \mu \, d\mu}{2\pi + \int_{-\phi_{max}}^{\phi_{max}} \left(\sqrt{1 - \frac{\rho_+^2}{r_p^2} \operatorname{sech}^2 \mu} - \sqrt{1 - \frac{\rho_-^2}{r_p^2} \operatorname{sech}^2 \mu}\right) d\phi}.
\end{aligned} \tag{S2.4.61}$$

And for $r_o < r_s$:

$$R'_{sph}(r_o < r_s) = \frac{2}{\sigma r_p} \int_0^{\sinh^{-1}\left(\frac{\sqrt{r_s^2 - r_o^2}}{r_p}\right)} \frac{\operatorname{sech} \mu \, d\mu}{\int_0^{2\pi} \sqrt{1 - \frac{\rho_+^2}{r_p^2} \operatorname{sech}^2 \mu} \, d\phi}$$

$$+\frac{2}{\sigma r_p}\int_{\sinh^{-1}\left(\frac{\sqrt{r_s^2-r_o^2}}{r_p}\right)}^{\sinh^{-1}\left(\frac{r_s}{\sqrt{r_p^2-r_o^2}}\right)}\frac{\operatorname{sech}\mu\, d\mu}{2\pi+\int_{-\phi_{max}}^{\phi_{max}}\left(\sqrt{1-\frac{\rho_+^2}{r_p^2}\operatorname{sech}^2\mu}-\sqrt{1-\frac{\rho_-^2}{r_p^2}\operatorname{sech}^2\mu}\right)d\phi}. \quad \text{(S2.4.62)}$$

The conductance of the entire system considers the contributions from the unobstructed segments:

$$\frac{G_b^{sph}}{G_o}(r_o,r_s)=\left[1-\frac{2}{\pi}\tan^{-1}\left(\frac{r_s}{\sqrt{r_p^2-r_o^2}}\right)+2\sigma r_p R'_{sph}(r_o,r_s)\right]^{-1}. \quad \text{(S2.4.63)}$$

The dependence of Equation S2.4.63 on r_o/r_p is plotted in Figure S2.4.10a for different sphere radii alongside the corresponding values obtained from finite-element simulations. Figure S2.4.10b further plots the predicted and simulated excess conductance at $r_o = 0$ compared to nonzero r_o values. Interestingly, although the absolute values predicted from Equation S2.4.63 are in worse agreement with the simulations than those of cylinders (Figure S2.4.8a), the relative r_o-dependence compared to a centred obstruction is better captured for spheres than for cylinders, as evidenced by the closer spacing between modelled and simulated values in Figure S2.4.10b (compared to Figure S2.4.8b).

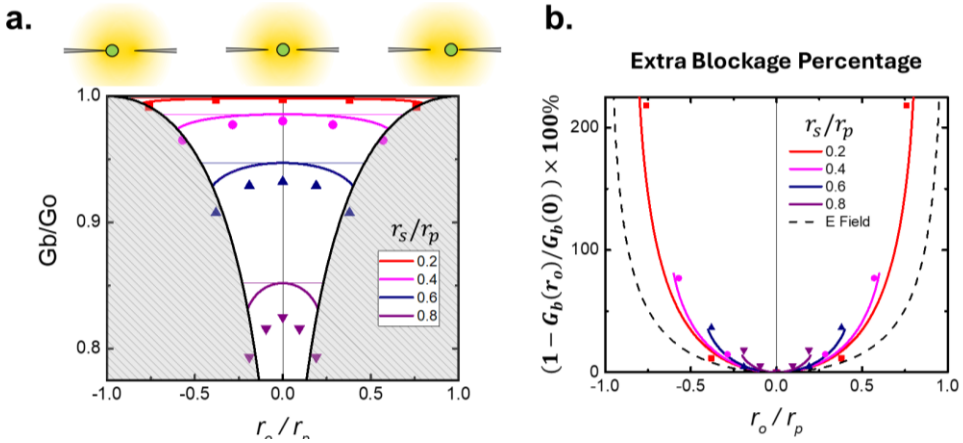

Figure S2.4.10. Off-axis effects for vertically centred spherical obstructions. **a)** Dependence of normalized blocked-state conductance G_b^{sph}/G_o on radial position r_o of the sphere inside the pore. **b)** Extra conductance induced by centred sphere position $r_o = 0$, compared to off-axis $r_o \neq 0$. All individual points are values calculated from finite element simulations, whereas continuous curves are from Equations S2.4.60-S62.

S2.4.8. Complex Obstruction – More Examples

As discussed in the main text (Figure 2.3.4), the presented modeling framework allows for predicting the shape of signals from real-life complex molecules by first modeling them as a sequence of sub-units with simple geometries. Here, we show a few examples to demonstrate how this can be applied to various types of molecule shapes.

Side Chains on Scaffold

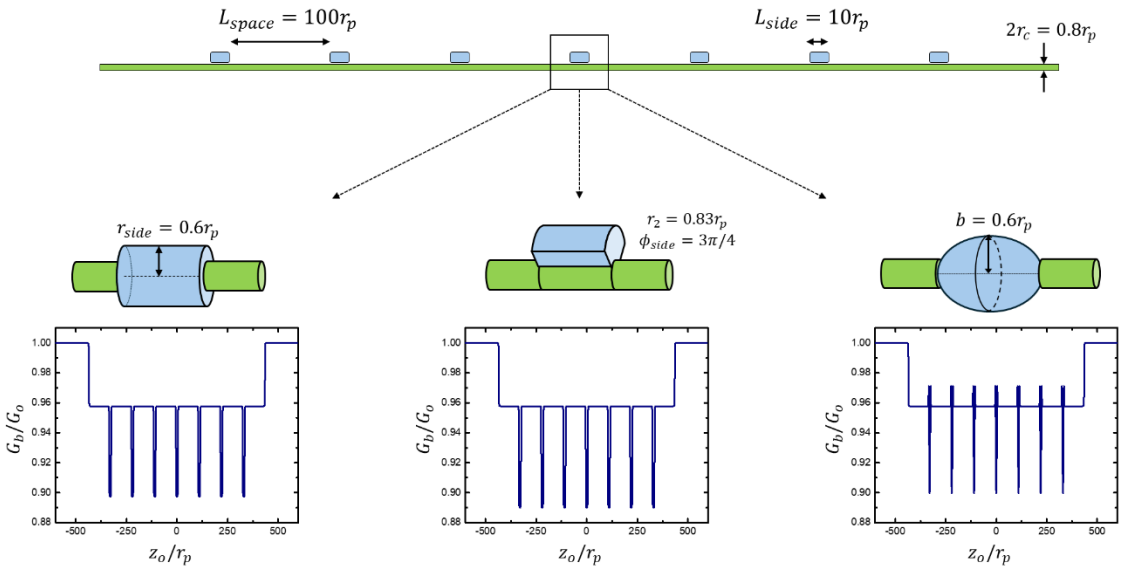

Figure S2.4.11. Different ways of modeling seven sidechains along a cylindrical scaffold: **a)** cylindrical, **b)** wedged cylinder, and **c)** ellipsoidal obstructions. In each case, the modeled conductance blockages G_b are plotted as a function of the distance z_o of the scaffold centre from the 2D pore opening (radius r_p).

We first show how to address modeling the nanopore signals of molecules used in scaffold-assisted sensing, wherein molecules of interest such as RNA, proteins, or biomarkers are bound along an extended double-stranded DNA backbone and produce an additional transient blockage during their passage through the pore. Here, we model the passage of a cylindrical backbone $r_c = 0.4r_p$, with 7 equidistant side chains of length $L_{side} = 10r_p$ separated by $L_{space} = 100r_p$. Figure S2.4.11 shows three different methods to model sidechains: i) as cylinders with radii $r_{side} =$

$0.6r_p$, ii) as wedged cylinders with $r_1 = 0.4r_p$, $r_2 = 0.83r_p$, $\phi_{side} = 3\pi/4$, and iii) as ellipsoids with $a = L_{side}$ and $b = 0.6r_p$. These specific values were chosen so that the maximal cross-sectional area of each type of side chain would be kept constant.

Shooting Stars

Here, we model real-world DNA nanostructures as a series of simple sub-structures and, motivated by the discussion of a constant-velocity approximation surrounding Equation 2.3.16 in the main text, compare their predicted conductance z-mappings to experimentally acquired time traces of corresponding translocation events. Figure S2.4.12 shows the current traces induced by the passage of two DNA nanostructures through a nanopore of diameter $d_p = 2r_p = 13\ nm$ and length $L_p = 12\ nm$, from prior work.[140] The nanostructures are made up of a single 12-arm DNA star attached to double-stranded DNA tails with lengths of 1.8 and 6.2 kilo-base pairs (kbp), and can be modeled as two cylinders of corresponding radii of $r_c^{tail} = 2.2\ \text{nm}$ and $r_c^{star} = \sqrt{6} \times 2.2\ \text{nm} = 5.4\ \text{nm}$ (i.e. same cross-sectional area as six DNA fragments) and lengths $L_{star} = 48\ \text{bp} \times 0.34 \frac{\text{nm}}{\text{bp}} = 16.3\ \text{nm}$ and $L_{tail} = 1.8\ \text{kbp} = 0.61\ \mu\text{m}$ or $6.2\ \text{kbp} = 2.1\ \mu\text{m}$. The closed-form conductance z-mappings calculated for both structures in a 2D pore of size $2r_p = 13\ \text{nm}$ are also shown in Figure S2.4.12 and although the modelled and experimental x scales (position vs. time) and pore geometries (2D vs. 3D) inherently differ in nature, the z-mappings calculated from Eq. 2.3.16 qualitatively capture the overall shape of experimental traces.

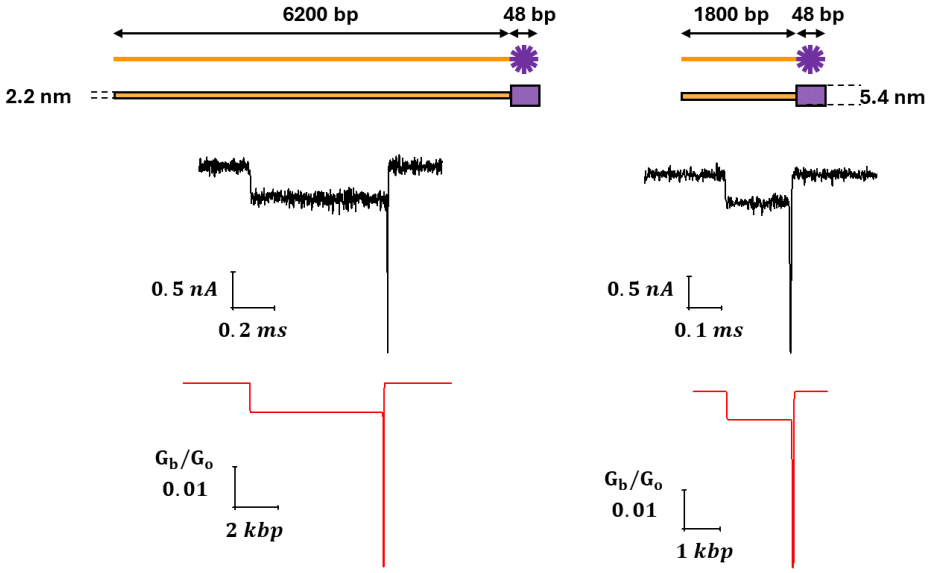

Figure S2.4.12. Modeling shooting star DNA nanostructures to predict their conductance blockages**.** Current traces (conductance blockage vs. time) were obtained from translocations of shooting stars through a nanopore of diameter $d_p = 2r_p = 13$ nm and thickness of $L_p = 12$ nm [140], while z -mappings (conductance blockage vs. position) were calculated through Eq. 2.3.16 in the main text by approximating the nanostructures as two cylinders in series (dimensions $r_c^{tail} = 2.2$ nm, $L_{tail} = 0.61/2.1$ μm and $r_c^{star} = 5.4$ nm, $L_{star} = 16.3$ nm) passing through a 2D pore of diameter $d_p = 13$ nm.

Spatial Resolution Limit for Molecular Design

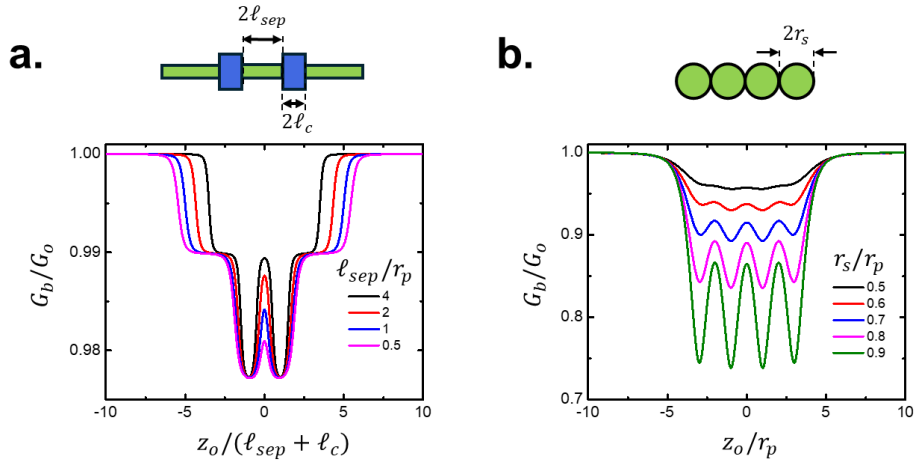

Figure S2.4.13. Demonstration of inherent resolution limit. a) short barcode-like cylinders in series ($r_c^{wide} = 0.3r_p$, $r_c^{narrow} = 0.2r_p$, $\ell_c = 2r_p$), and **b)** spheres in series.

We now comment on the intrinsic z-resolution limit of the components of a complex obstruction, imposed by the non-zero sensing volume of a 2D pore. Figure S2.4.13a shows the conductance trace of a barcode-like obstruction made up of five cylinders in series, with two wider but shorter ($r_c^{wide} = 0.3r_p$, $L_c = 2\ell_c = 4r_p$) sub-units separated by $L_{sep} = 2\ell_{sep}$ along a backbone with $r_c^{narrow} = 0.2r_p$. By changing the value of ℓ_{sep}, Figure S2.4.13a shows the that the larger diameter features are harder to resolve within a z-mapping when they are separated by less than $2r_p$, again implying that the sensing volume of a 2D pore of radius r_p has dimension $2r_p$ in the z direction. Similarly, Figure S2.4.13b shows the conductance z-mappings expected from a series of four identical spheres with radii ranging between $r_s = 0.5r_p$ and $r_s = 0.9r_p$. Although spheres that take up most of the sensing volume ($r_s \approx r_p$) can be identified individually, strings of smaller spheres result in traces without obviously identifiable sub-unit characteristics. The observations from Figure S2.4.13 provide useful insights with regards to designing molecules with information contained in their substructure to be sensed with pores.

Insects Wearing Hats

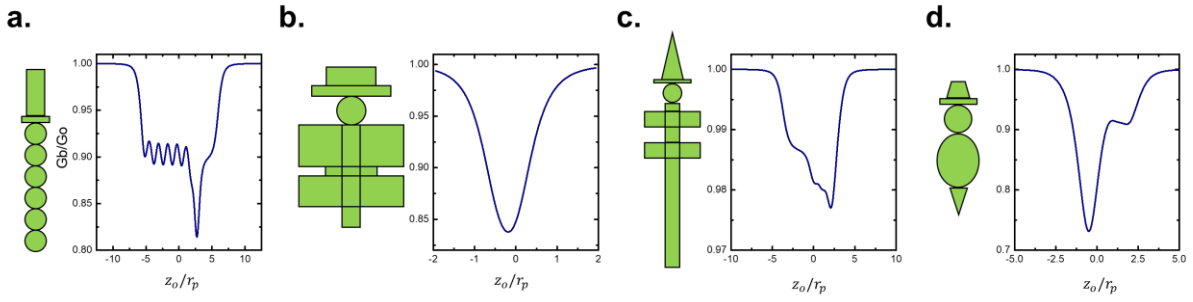

Figure S2.4.14. Blockade predictions for complex obstructions modeled as simple sub-units in series. Conductance expected during the passage through a 2D pore of **a)** Caterpillar wearing a top hat; **b)** Butterfly wearing a boater hat; **c)** Dragonfly wearing a witch hat; **d)** Bee wearing a fedora hat.

S2.4.9. Finite-Length Pore Equations

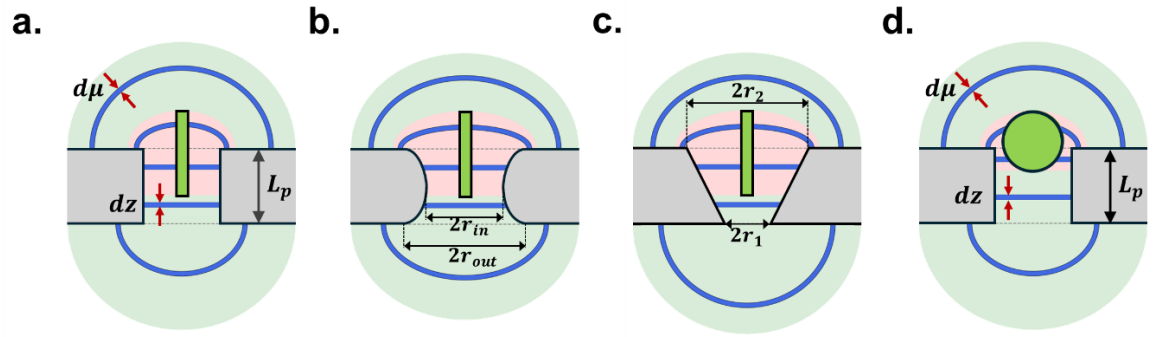

Figure S2.4.15. Method for modeling conductance of finite-length pores: oblate spheroidal slices outside the pore and circular slices inside the pore. **a)** Cylindrical obstruction in a cylindrical pore. **b)** Cylindrical obstruction in a hyperboloidal pore. **c)** Cylindrical obstruction in a conical pore. **d)** Spherical obstruction in a cylindrical pore.

As discussed in the main text, the oblate spheroidal resistive slice method can also be applied to estimate the access resistance of finite-length pores. The total conductance of a pore of radius r_p and length $L_p = 2\ell_p$ is thus calculated by considering the contributions from the two access regions and channel region in series:

$$\begin{aligned} G_b &= \left[R_{acc}^{bot} + R_{pore} + R_{acc}^{top}\right]^{-1} \\ &= \left[\int_{-\infty}^{0} dR_{acc}^{bot}(\mu) + \int_{-\ell_p}^{\ell_p} dR_{pore}(z) + \int_{0}^{\infty} dR_{acc}^{top}(\mu)\right]^{-1}. \end{aligned} \tag{S2.4.64}$$

For the simple scenario of a cylindrical obstruction of radius r_c and length $L_c = 2\ell_c$ at a distance of z_o from a pore with a z-dependent radial profile of $r_p(z)$, and of length $L_p = 2\ell_p$, the terms of Equation S2.4.64 can be further segmented into obstructed and unobstructed regions. For this reason, the resistance calculation needs to be broken down into five scenarios, depending on whether the cylindrical obstruction is: i) completely in the top access region ($z_o > \ell_p + \ell_c$), ii) partially in the pore and the top access region ($|\ell_p - \ell_c| < z_o < \ell_p + \ell_c$), iii) entirely inside the pore ($\ell_c - \ell_p < z_o < \ell_p - \ell_c$ for $\ell_c < \ell_p$) or partially inside the top access region, pore, and bottom access region ($\ell_p - \ell_c < z_o < \ell_c - \ell_p$ for $\ell_c > \ell_p$), iv) partially in the pore and the

bottom access region ($-\ell_p - \ell_c < z_o < -|\ell_p - \ell_c|$), or v) entirely in the bottom access region ($z_o < -\ell_p - \ell_c$). Note that in the case of z-symmetric pore shapes, the number of scenarios to consider drops to three. Let us now consider the solutions for cylindrical obstructions in channels of various rotationally symmetric shapes.

Finite Cylinder in Cylindrical Pore

We first consider a cylindrical pore with a radial profile trivially parametrized as $r_p(z) = r_p$. Note that the access region contributions are identical to Equation 2.3.9 from the main text, only with a translation in z_o of $\pm\ell_p$ due to the presence of the membrane. The infinitesimal resistance of thin obstructed slices inside and outside the pore are thus calculated as:

$$dR'_{pore}(z) = \frac{dz}{\sigma\pi\left(r_p^2 - r_c^2\right)}\,, \tag{S2.4.65}$$

$$dR'_{acc}(\mu) = \frac{\operatorname{sech}\mu\, d\mu}{2\pi\sigma r_p\sqrt{1 - \frac{r_c^2}{r_p^2}\operatorname{sech}^2\mu}}\,. \tag{S2.4.66}$$

Open-Pore

$$R_o = \frac{2\ell_p}{\sigma\pi r_p^2} + \frac{1}{2\sigma r_p} \tag{S2.4.67}$$

Cylinder Outside the pore $\left(\ell_p + \ell_c < |z_o|\right)$:

$$R_b(z) = \frac{2\ell_p}{\sigma\pi r_p^2} + \frac{1}{2\sigma r_p}\left[1 + \frac{1}{\pi}\tan^{-1}\left(\frac{|z_o| - \ell_p - \ell_c}{r_p}\right) - \frac{1}{\pi}\tan^{-1}\left(\frac{|z_o| - \ell_p + \ell_c}{r_p}\right)\right.$$
$$\left. + \frac{1}{\pi}F\left(\frac{\pi}{2} - \tan^{-1}\left(\frac{|z_o| - \ell_p - \ell_c}{r_p}\right), \frac{r_c}{r_p}\right) - \frac{1}{\pi}F\left(\frac{\pi}{2} - \tan^{-1}\left(\frac{|z_o| - \ell_p + \ell_c}{r_p}\right), \frac{r_c}{r_p}\right)\right] \tag{S2.4.68}$$

Cylinder Partially inside the pore $\left(\left|\ell_p - \ell_c\right| < |z_o| < \ell_p + \ell_c\right)$:

$$R_b(z_o) = \frac{\ell_p - |z_o| + \ell_c}{\sigma\pi\left(r_p^2 - r_c^2\right)} + \frac{\ell_p + |z_o| - \ell_c}{\sigma\pi r_p^2} + \frac{1}{2\sigma r_p}\left[1 - \frac{1}{\pi}\tan^{-1}\left(\frac{|z_o| + \ell_c - \ell_p}{r_p}\right) + \frac{1}{\pi}F\left(\frac{\pi}{2}, \frac{r_c}{r_p}\right) - \frac{1}{\pi}F\left(\frac{\pi}{2} - \tan^{-1}\left(\frac{|z_o| + \ell_c - \ell_p}{r_p}\right), \frac{r_c}{r_p}\right)\right] \quad \text{(S2.4.69)}$$

Long cylinder $\left(\ell_c > \ell_p\right)$ inside the pore $\left(0 < |z_o| < \ell_c - \ell_p\right)$:

$$R_b(z_o) = \frac{2\ell_p}{\sigma\pi\left(r_p^2 - r_c^2\right)} + \frac{1}{2\sigma r_p}\left[1 + \frac{1}{\pi}\tan^{-1}\left(\frac{|z_o| - \ell_c + \ell_p}{r_p}\right) - \frac{1}{\pi}\tan^{-1}\left(\frac{|z_o| + \ell_c - \ell_p}{r_p}\right) + \frac{1}{\pi}F\left(\frac{\pi}{2} - \tan^{-1}\left(\frac{|z_o| - \ell_c + \ell_p}{r_p}\right), \frac{r_c}{r_p}\right) - \frac{1}{\pi}F\left(\frac{\pi}{2} - \tan^{-1}\left(\frac{|z_o| + \ell_c - \ell_p}{r_p}\right), \frac{r_c}{r_p}\right)\right] \quad \text{(S2.4.70)}$$

Short cylinder $\left(\ell_c < \ell_p\right)$ inside the pore $\left(0 < |z_o| < \ell_p - \ell_c\right)$:

$$R_b(z_o) = \frac{2\ell_c}{\sigma\pi\left(r_p^2 - r_c^2\right)} + \frac{2\left(\ell_p - \ell_c\right)}{\sigma\pi r_p^2} + \frac{1}{2\sigma r_p} \quad \text{(S2.4.71)}$$

Very long cylinder $\left(\ell_c \gg \ell_p\right)$ centered inside pore:

As it is relevant for semiflexible linear polymers with a persistence length longer than that of the pore, such as for double stranded DNA in a nanoscale pore, we also note the solution for very long cylindrical obstructions ($\ell_c \gg \ell_p$):

$$R_b = \frac{2\ell_p}{\sigma\pi\left(r_p^2 - r_c^2\right)} + \frac{\frac{2}{\pi}K\left(\frac{r_c}{r_p}\right)}{2\sigma r_p}\,. \quad \text{(S2.4.72)}$$

Here $K(k) = F\left(\frac{\pi}{2}, k\right)$ is the complete elliptic integral of the first kind. Equation S2.4.72 and its accuracy in various conditions has been evaluated and discussed extensively in a recent publication.[123]

Finite Cylinder in Hyperboloidal Pore

We now consider a cylindrical obstruction of length $L_c = 2\ell_c$ and radius r_c passing through a hyperboloidal pore of length $L_p = 2\ell_p$ characterized by its inner and outer radii r_{in} and r_{out} (See Figure S2.4.15) described by the following parametrization:

$$r_p^2(z) = r_{in}^2 + \frac{r_{out}^2 - r_{in}^2}{\ell_p^2} z^2 \,. \tag{S2.4.73}$$

The infinitesimal resistance of thin obstructed slices inside and outside the pore are calculated as:

$$dR'_{pore}(z) = \frac{dz}{\sigma\pi\left(r_{in}^2 - r_c^2 + \frac{r_{out}^2 - r_{in}^2}{\ell_p^2} z^2\right)} \,, \tag{S2.4.74}$$

$$dR'_{acc}(\mu) = \frac{\operatorname{sech}\mu \, d\mu}{2\pi\sigma r_{out}\sqrt{1 + \frac{r_c^2}{r_{out}^2}\operatorname{sech}^2\mu}} \,. \tag{S2.4.75}$$

Open-Pore

$$R_o = \frac{2\ell_p}{\sigma\pi r_{in}\sqrt{r_{out}^2 - r_{in}^2}} \tan^{-1}\sqrt{\frac{r_{out}^2}{r_{in}^2} - 1} + \frac{1}{2\sigma r_{out}} \tag{S2.4.76}$$

Cylinder Outside the pore $\left(\ell_p + \ell_c < |z_o|\right)$:

$$\begin{aligned} R_b(z_o) = {} & \frac{2\ell_p}{\sigma\pi r_{in}\sqrt{r_{out}^2 - r_{in}^2}} \tan^{-1}\sqrt{\frac{r_{out}^2}{r_{in}^2} - 1} \\ & + \frac{1}{2\sigma r_{out}}\left[1 + \frac{1}{\pi}\tan^{-1}\left(\frac{|z_o| - \ell_c - \ell_p}{r_{out}}\right) - \frac{1}{\pi}\tan^{-1}\left(\frac{|z_o| + \ell_c - \ell_p}{r_{out}}\right)\right. \\ & \left. + \frac{1}{\pi}F\left(\frac{\pi}{2} - \tan^{-1}\left(\frac{|z_o| - \ell_p - \ell_c}{r_{out}}\right), \frac{r_c}{r_{out}}\right) - \frac{1}{\pi}F\left(\frac{\pi}{2} - \tan^{-1}\left(\frac{|z_o| - \ell_p + \ell_c}{r_{out}}\right), \frac{r_c}{r_{out}}\right)\right] \end{aligned} \tag{S2.4.77}$$

Cylinder Partially inside the pore $\left(\left|\ell_p - \ell_c\right| < |z_o| < \ell_p + \ell_c\right)$:

$$R_b(z_o) = \frac{\ell_p}{\sigma\pi\sqrt{r_{out}^2 - r_{in}^2}}\left[\frac{1}{r_{in}}\tan^{-1}\left(\sqrt{\frac{r_{out}^2}{r_{in}^2} - 1}\left(\frac{|z_o|z_o - \ell_c}{\ell_p}\right)\right) + \frac{1}{r_{in}}\tan^{-1}\left(\sqrt{\frac{r_{out}^2}{r_{in}^2} - 1}\right)\right.$$
$$\left. + \frac{1}{\sqrt{r_{in}^2 - r_c^2}}\tan^{-1}\left(\sqrt{\frac{r_{out}^2 - r_{in}^2}{r_{in}^2 - r_c^2}}\right) - \frac{1}{\sqrt{r_{in}^2 - r_c^2}}\tan^{-1}\left(\sqrt{\frac{r_{out}^2 - r_{in}^2}{r_{in}^2 - r_c^2}}\left(\frac{|z_o| - \ell_c}{\ell_p}\right)\right)\right]$$
$$+ \frac{1}{2\sigma r_{out}}\left[1 - \frac{1}{\pi}\tan^{-1}\left(\frac{|z_o| + \ell_c - \ell_p}{r_{out}}\right) + \frac{1}{\pi}F\left(\frac{\pi}{2}, \frac{r_c}{r_{out}}\right)\right.$$
$$\left. - \frac{1}{\pi}F\left(\frac{\pi}{2} - \tan^{-1}\left(\frac{|z_o| + \ell_c - \ell_p}{r_{out}}\right), \frac{r_c}{r_{out}}\right)\right] \quad \text{(S2.4.78)}$$

Long cylinder $\left(\ell_c > \ell_p\right)$ inside the pore $\left(|z_o| < \ell_c - \ell_p\right)$:

$$R_b(z_o) = \frac{2\ell_p}{\sigma\pi\sqrt{(r_{out}^2 - r_{in}^2)(r_{in}^2 - r_c^2)}}\tan^{-1}\left(\sqrt{\frac{r_{out}^2 - r_{in}^2}{r_{in}^2 - r_c^2}}\right)$$
$$+ \frac{1}{2\sigma r_{out}}\left[1 + \frac{1}{\pi}\tan^{-1}\left(\frac{|z_o| - \ell_c + \ell_p}{r_{out}}\right) - \frac{1}{\pi}\tan^{-1}\left(\frac{|z_o| + \ell_c - \ell_p}{r_{out}}\right)\right.$$
$$+ \frac{1}{\pi}F\left(\frac{\pi}{2} - \tan^{-1}\left(\frac{|z_o| - \ell_c + \ell_p}{r_{out}}\right), \frac{r_c}{r_{out}}\right)$$
$$\left. - \frac{1}{\pi}F\left(\frac{\pi}{2} - \tan^{-1}\left(\frac{|z_o| + \ell_c - \ell_p}{r_{out}}\right), \frac{r_c}{r_{out}}\right)\right] \quad \text{(S2.4.79)}$$

Short cylinder $\left(\ell_c < \ell_p\right)$ inside the pore $\left(|z_o| < \ell_p - \ell_c\right)$:

$$R_b(z_o) = \frac{1}{2\sigma r_{out}} + \frac{L}{\sigma\pi\sqrt{r_{out}^2 - r_{in}^2}}\left[\frac{2}{r_{in}}\tan^{-1}\left(\sqrt{\frac{r_{out}^2 - r_{in}^2}{r_{in}^2}}\right) + \frac{1}{r_{in}}\tan^{-1}\left(\sqrt{\frac{r_{out}^2}{r_{in}^2} - 1}\left(\frac{|z_o| - \ell_c}{\ell_p}\right)\right)\right.$$
$$- \frac{1}{r_{in}}\tan^{-1}\left(\sqrt{\frac{r_{out}^2}{r_{in}^2} - 1}\left(\frac{|z_o| + \ell_c}{\ell_p}\right)\right) - \frac{1}{\sqrt{r_{in}^2 - r_c^2}}\tan^{-1}\left(\sqrt{\frac{r_{out}^2 - r_{in}^2}{r_{in}^2 - r_c^2}}\left(\frac{|z_o| - \ell_c}{\ell_p}\right)\right)$$
$$\left. + \frac{1}{\sqrt{r_{in}^2 - r_c^2}}\tan^{-1}\left(\sqrt{\frac{r_{out}^2 - r_{in}^2}{r_{in}^2 - r_c^2}}\left(\frac{|z_o| + \ell_c}{\ell_p}\right)\right)\right] \quad \text{(S2.4.80)}$$

Very long cylinder $(\ell_c \gg \ell_p)$ centered inside pore:

$$R_b(z_o = 0) = \frac{2\ell_p}{\sigma\pi\sqrt{(r_{out}^2 - r_{in}^2)(r_{in}^2 - r_c^2)}} \tan^{-1}\left(\sqrt{\frac{r_{out}^2 - r_{in}^2}{r_{in}^2 - r_c^2}}\right) + \frac{\frac{2}{\pi}K\left(\frac{r_c}{r_{out}}\right)}{2\sigma r_{out}} \quad \text{(S2.4.81)}$$

Finite Cylinder in Conical Pore

We now consider a cylindrical obstruction of length $L_c = 2\ell_c$ and radius r_c passing through a conical pore of length $L_p = 2\ell_p$ characterized by its lower and upper radii r_1 and r_2 (See Figure S2.4.15) described with the following parametrization:

$$r_p(z) = \frac{r_2 - r_1}{2\ell_p} z + \frac{r_1 + r_2}{2} \quad \text{(S2.4.82)}$$

The infinitesimal resistance of thin obstructed slices inside and outside the pore are calculated as:

$$dR'_{pore}(z) = \frac{dz}{\sigma\pi\left(\left(\frac{r_2 - r_1}{2\ell_p} z + \frac{r_1 + r_2}{2}\right)^2 - r_c^2\right)} \quad \text{(S2.4.83)}$$

$$dR'^{top}_{acc}(\mu) = \frac{\operatorname{sech}\mu \, d\mu}{2\pi\sigma r_2\sqrt{1 + \frac{r_c^2}{r_2^2}\operatorname{sech}^2\mu}} \quad \text{(S2.4.84)}$$

$$dR'^{bot}_{acc}(\mu) = \frac{\operatorname{sech}\mu \, d\mu}{2\pi\sigma r_1\sqrt{1 + \frac{r_c^2}{r_1^2}\operatorname{sech}^2\mu}} \quad \text{(S2.4.85)}$$

Open-Pore

$$R_o = \frac{1}{4\sigma r_1} + \frac{1}{4\sigma r_2} + \frac{2\ell_p}{\pi\sigma r_1 r_2} \quad \text{(S2.4.86)}$$

Cylinder above the pore $\left(\ell_p + \ell_c < z_o\right)$:

$$R_b(z_o) = \frac{1}{4\sigma r_1} + \frac{2\ell_p}{\pi\sigma r_1 r_2} + \frac{1}{4\sigma r_2}\left[1 + \frac{2}{\pi}\tan^{-1}\left(\frac{z_o - \ell_c - \ell_p}{r_2}\right) - \frac{2}{\pi}\tan^{-1}\left(\frac{z_o + \ell_c - \ell_p}{r_2}\right) + \frac{2}{\pi}F\left(\frac{\pi}{2} - \tan^{-1}\left(\frac{z_o - \ell_c - \ell_p}{r_2}\right), \frac{r_c}{r_2}\right) - \frac{2}{\pi}F\left(\frac{\pi}{2} - \tan^{-1}\left(\frac{z_o + \ell_c - \ell_p}{r_2}\right), \frac{r_c}{r_2}\right)\right] \quad \text{(S2.4.87)}$$

Cylinder above and partially inside the pore $\left(\left|\ell_c - \ell_p\right| < z_o < \ell_p + \ell_c\right)$:

$$R_b(z_o) = \frac{1}{4\sigma r_1} + \frac{2\ell_p}{\pi\sigma(r_2 - r_1)}\left[\frac{1}{r_1} - \frac{2}{\frac{r_2 - r_1}{\ell_p}(z_o - \ell_c) + r_1 + r_2} + \frac{1}{2r_c}\ln\left(\frac{(r_2 - r_c)\left(\frac{r_2 - r_1}{\ell_p}(z_o - \ell_c) + r_1 + r_2 + 2r_c\right)}{(r_2 + r_c)\left(\frac{r_2 - r_1}{\ell_p}(z_o - \ell_c) + r_1 + r_2 - 2r_c\right)}\right)\right] + \frac{1}{4\sigma r_2}\left[1 - \frac{2}{\pi}\tan^{-1}\left(\frac{z_o + \ell_c - \ell_p}{r_2}\right) + \frac{2}{\pi}F\left(\frac{\pi}{2}, \frac{r_c}{r_2}\right) - \frac{2}{\pi}F\left(\frac{\pi}{2} - \tan^{-1}\left(\frac{z_o + \ell_c - \ell_p}{r_2}\right), \frac{r_c}{r_2}\right)\right] \quad \text{(S2.4.88)}$$

Long cylinder $\left(\ell_c > \ell_p\right)$ inside the pore $\left(|z_o| < \ell_c - \ell_p\right)$:

$$R_b(z_o) = \frac{1}{4\sigma r_1}\left(1 + \frac{2}{\pi}\tan^{-1}\left(\frac{z_o - \ell_c + \ell_p}{r_1}\right) + \frac{2}{\pi}F\left(\frac{\pi}{2} - \tan^{-1}\left(\frac{z_o - \ell_c + \ell_p}{r_1}\right), \frac{r_c}{r_1}\right) - \frac{2}{\pi}F\left(\frac{\pi}{2}, \frac{r_c}{r_1}\right)\right) + \frac{1}{4\sigma r_2}\left(1 - \frac{2}{\pi}\tan^{-1}\left(\frac{z_o + \ell_c - \ell_p}{r_2}\right) - \frac{2}{\pi}F\left(\frac{\pi}{2} - \tan^{-1}\left(\frac{z_o + \ell_c - \ell_p}{r_2}\right), \frac{r_c}{r_2}\right) + \frac{2}{\pi}F\left(\frac{\pi}{2}, \frac{r_c}{r_2}\right)\right) + \frac{\ell_p}{\pi\sigma r_c(r_2 - r_1)}\ln\left(\frac{(r_2 - r_c)(r_1 + r_c)}{(r_2 + r_c)(r_1 - r_c)}\right) \quad \text{(S2.4.89)}$$

Short cylinder $\left(\ell_c < \ell_p\right)$ inside the pore $\left(|z_o| < \ell_p - \ell_c\right)$:

$$R_b(z_o) = \frac{2\ell_p}{\pi\sigma(r_2 - r_1)}\left[\frac{1}{r_1} - \frac{1}{r_2} + \frac{2}{\frac{r_2 - r_1}{\ell_p}(z_o + \ell_c) + r_1 + r_2} - \frac{2}{\frac{r_2 - r_1}{\ell_p}(z_o - \ell_c) + r_1 + r_2}\right.$$

$$+\frac{1}{2r_c}\ln\left(\frac{\left(\frac{r_2-r_1}{\ell_p}(z_o+\ell_c)+r_1+r_2-2r_c\right)\left(\frac{r_2-r_1}{\ell_p}(z_o-\ell_c)+r_1+r_2+2r_c\right)}{\left(\frac{r_2-r_1}{\ell_p}(z_o+\ell_c)+r_1+r_2+2r_c\right)\left(\frac{r_2-r_1}{\ell_p}(z_o-\ell_c)+r_1+r_2-2r_c\right)}\right)\Bigg]$$
$$+\frac{1}{4\sigma r_1}+\frac{1}{4\sigma r_2} \tag{S2.4.90}$$

<u>Cylinder under and partially inside the pore</u> $\left(-\left|\ell_c-\ell_p\right|>z_o>-\left(\ell_p+\ell_c\right)\right)$:

$$R_b(z_o)=\frac{1}{4\sigma r_2}+\frac{2\ell_p}{\pi\sigma(r_2-r_1)}\Bigg[\frac{2}{\frac{r_2-r_1}{\ell_p}(z_o+\ell_c)+r_1+r_2}-\frac{1}{r_2}$$
$$+\frac{1}{2r_c}\ln\left(\frac{\left(\frac{r_2-r_1}{\ell_p}(z_o+\ell_c)+r_1+r_2-2r_c\right)(r_1+r_c)}{\left(\frac{r_2-r_1}{\ell_p}(z_o+\ell_c)+r_1+r_2+2r_c\right)(r_1-r_c)}\right)\Bigg]$$
$$+\frac{1}{4\sigma r_1}\Bigg[1+\frac{2}{\pi}\tan^{-1}\left(\frac{z_o-\ell_c+\ell_p}{r_1}\right)-\frac{2}{\pi}F\left(\frac{\pi}{2},\frac{r_c}{r_1}\right)$$
$$+\frac{2}{\pi}F\left(\frac{\pi}{2}-\tan^{-1}\left(\frac{z_o-\ell_c+\ell_p}{r_1}\right),\frac{r_c}{r_1}\right)\Bigg] \tag{S2.4.91}$$

<u>Cylinder under the pore</u> $\left(z_o<-\left(\ell_p+\ell_c\right)\right)$:

$$R_b(z_o)=\frac{2\ell_p}{\pi\sigma r_1 r_2}+\frac{1}{4\sigma r_2}$$
$$+\frac{1}{4\sigma r_1}\Bigg[1+\frac{2}{\pi}\tan^{-1}\left(\frac{z_o-\ell_c+\ell_p}{r_1}\right)-\frac{2}{\pi}\tan^{-1}\left(\frac{z_o+\ell_c+\ell_p}{r_1}\right)$$
$$+\frac{2}{\pi}F\left(\frac{\pi}{2}-\tan^{-1}\left(\frac{z_o-\ell_c+\ell_p}{r_1}\right),\frac{r_c}{r_1}\right)-\frac{2}{\pi}F\left(\frac{\pi}{2}-\tan^{-1}\left(\frac{z_o+\ell_c+\ell_p}{r_1}\right),\frac{r_c}{r_1}\right)\Bigg] \tag{S2.4.92}$$

<u>Very long cylinder $\left(\ell_c\gg\ell_p\right)$ centered inside pore:</u>

$$R_b=\frac{K\left(\frac{r_c}{r_1}\right)}{2\pi\sigma r_1}+\frac{K\left(\frac{r_c}{r_2}\right)}{2\pi\sigma r_2}+\frac{\ell_p}{\pi\sigma r_c(r_2-r_1)}\ln\left(\frac{(r_2-r_c)(r_1+r_c)}{(r_2+r_c)(r_1-r_c)}\right) \tag{S2.4.93}$$

Sphere in Cylindrical Pore

As discussed in Section S2.4.4, the infinitesimal resistance of a constant-μ oblate spheroidal slice in the presence of a spherical obstruction (radius r_s) at a distance of z_o from a pore in a 2D membrane is (see Eq. S2.4.32):

$$dR'_{2D}(z_o) = \frac{1}{2\pi\sigma r_p} \frac{\operatorname{sech}^2\mu\, d\mu}{\sqrt{1 - \frac{r_s^2 + z_o^2}{r_p^2}\operatorname{sech}^2\mu + 2\frac{z_o^2}{r_p^2} - 2\frac{z_o}{r_p}\tanh\mu\sqrt{1 + \frac{z_o^2}{r_p^2} - \frac{r_s^2}{r_p^2}\operatorname{sech}^2\mu}}}. \quad \text{(S2.4.94)}$$

When treating oblate spheroidal slices in the access regions of finite-length pores, Equation S2.4.94 can be adapted through a corresponding z-translation:

$$dR'_{acc}(z_o) = dR'_{2D}\left(|z_o| - \ell_p\right). \quad \text{(S2.4.95)}$$

The surface of the spherical obstruction is parametrized with $r_o^2 = r_s^2 - (z - z_o)^2$, and thus the resistance of an obstructed circular slice inside the pore is evaluated as:

$$dR'_{pore}(z_o) = \frac{dz}{\sigma\pi\left(r_p^2 - r_s^2 + (z - z_o)^2\right)} = \frac{1}{\sigma\pi\left(r_p^2 - r_s^2\right)} \frac{dz}{1 + \frac{(z - z_o)^2}{r_p^2 - r_s^2}}. \quad \text{(S2.4.96)}$$

Sphere outside pore $\left(\ell_p + r_s < |z_o|\right)$:

$$R_b(z_o) = \frac{2\ell_p}{\sigma\pi r_p^2} + \int_{\sinh^{-1}\left(\frac{|z_o| - r_s - \ell_p}{r_p}\right)}^{\sinh^{-1}\left(\frac{|z_o| + r_s - \ell_p}{r_p}\right)} dR'_{2D}\left(|z_o| - \ell_p\right) + \frac{1}{2\sigma r_p}\left[1 - \frac{1}{\pi}\tan^{-1}\left(\frac{|z_o| + r_s - \ell_p}{r_p}\right) + \frac{1}{\pi}\tan^{-1}\left(\frac{|z_o| - r_s - \ell_p}{r_p}\right)\right] \quad \text{(S2.4.97)}$$

Sphere partially inside pore $\left(\left|\ell_p - r_s\right| < |z_o| < \ell_p + r_s\right)$:

$$R_b(z_o) = \frac{\ell_p + |z_o| - r_s}{\sigma\pi r_p^2} + \frac{1}{2\sigma r_p}\left(1 - \frac{1}{\pi}\tan^{-1}\left(\frac{|z_o| + r_s - \ell_p}{r_p}\right)\right)$$

$$+\frac{1}{\sigma\pi\sqrt{r_p^2-r_s^2}}\left(\tan^{-1}\left(\frac{\ell_p-|z_o|}{\sqrt{r_p^2-r_s^2}}\right)+\sin^{-1}\left(\frac{r_s}{r_p}\right)\right)$$
$$+\int_0^{\sinh^{-1}\left(\frac{|z_o|+r_s-\ell_p}{r_p}\right)} dR'_{2D}\left(|z_o|-\ell_p\right) \quad \text{(S2.4.98)}$$

Large sphere $\left(r_s > \ell_p\right)$ inside the pore $\left(|z_o| < r_s - \ell_p\right)$:

$$R_b(z_o) = \frac{1}{2\sigma r_p}\left(1+\frac{1}{\pi}\tan^{-1}\left(\frac{z_o-r_s+\ell_p}{r_p}\right)+\frac{1}{\pi}\tan^{-1}\left(\frac{-z_o-r_s+\ell_p}{r_p}\right)\right)$$
$$+\int_0^{\sinh^{-1}\left(\frac{-z_o+r_s-\ell_p}{r_p}\right)} dR'_{2D}\left(-z_o-\ell_p\right)+\int_0^{\sinh^{-1}\left(\frac{z_o+r_s-\ell_p}{r_p}\right)} dR'_{2D}\left(z_o-\ell_p\right)$$
$$+\frac{1}{\sigma\pi\sqrt{r_p^2-r_s^2}}\left(\tan^{-1}\left(\frac{\ell_p-z_o}{\sqrt{r_p^2-r_s^2}}\right)+\tan^{-1}\left(\frac{\ell_p+z_o}{\sqrt{r_p^2-r_s^2}}\right)\right) \quad \text{(S2.4.99)}$$

Small sphere $\left(r_s < \ell_p\right)$ inside the pore $\left(|z_o| < \ell_p - r_s\right)$:

$$R_b(z_o) = \frac{1}{2\sigma r_p}+\frac{2\ell_p-2r_s}{\sigma\pi r_p^2}+\frac{2}{\sigma\pi\sqrt{r_p^2-r_s^2}}\sin^{-1}\left(\frac{r_s}{r_p}\right) \quad \text{(S2.4.100)}$$

2.5 Additional Comment

Here is a concise observation that was not obvious to me when first attempting to model conductance using oblate spheroidal coordinates and that I find interesting enough to note here. As discussed above, a common method to estimate the resistance of various resistive mediums is to divide the volume of interest into infinitely thin slices of thickness $d\ell$ and area A, and the resistive contributions from each of those slices $dR = \sigma^{-1} d\ell / A$. For example, the resistance between two equipotential coaxial cylinders can be found:

$$R_{coaxial}(r_{in}, r_{out}) = \frac{1}{\sigma}\int_{r_{in}}^{r_{out}} \frac{dr}{A(r)} = \frac{1}{\sigma}\int_{r_{in}}^{r_{out}} \frac{dr}{L2\pi r} = \frac{1}{\sigma 2\pi L}\ln\frac{r_{out}}{r_{in}}\,. \tag{2.5.1}$$

The resistance between concentric spherical equipotential shells can be found similarly:

$$R_{shells}(\rho_{in}, \rho_{out}) = \frac{1}{\sigma}\int_{\rho_{in}}^{\rho_{out}} \frac{d\rho}{A(\rho)} = \frac{1}{\sigma}\int_{\rho_{in}}^{\rho_{out}} \frac{d\rho}{4\pi\rho^2} = \frac{1}{4\pi\sigma}\left(\frac{1}{\rho_{in}} - \frac{1}{\rho_{out}}\right). \tag{2.5.2}$$

Note interestingly that Eq. 2.5.2 evaluated with $\rho_{out} \to \infty$ and $\rho_{in} = r_p$ corresponds to the first expression that attempted to model the access resistance of a pore of radius r_p.

The $dR = \sigma^{-1} d\ell / A$ assumption however does not always hold when working with curvilinear coordinates, as is now demonstrated. Consider a curvilinear coordinate system (u, v, w) with scaling factors h_u, h_v and h_w defined as $h_i = \sqrt{\left(\frac{\partial x}{\partial i}\right)^2 + \left(\frac{\partial y}{\partial i}\right)^2 + \left(\frac{\partial z}{\partial i}\right)^2}$ where (x, y, z) are the cartesian coordinates and $i = u, v, w$. Let equipotential surfaces be described by constant-u surfaces, such that the potential $V(u)$ depends solely on u. The resistance of a resistive volume delimited $u \in [u_1, u_2]$, $v \in [v_1, v_2]$ and $w \in [w_1, w_2]$ can be found by partitioning the u-domain into infinitely thin slices and integrating over the corresponding infinitesimal resistances $dR = dV/I$, calculated as follows:

$$
\begin{aligned}
R &= \int_{u_1}^{u_2} \frac{dV(u)}{I(u)} \\
&= \int_{u_1}^{u_2} \frac{\frac{dV}{du}du}{\int_{w_1}^{w_2}\int_{v_1}^{v_2} \sigma|E| h_v h_w \, dvdw} \\
&= \frac{1}{\sigma}\int_{u_1}^{u_2} \frac{\frac{dV}{du}du}{\int_{w_1}^{w_2}\int_{v_1}^{v_2} \frac{1}{h_u}\frac{dV}{du} h_v h_w \, dvdw} \\
R &= \frac{1}{\sigma}\int_{u_1}^{u_2} \frac{du}{\int_{w_1}^{w_2}\int_{v_1}^{v_2} \frac{1}{h_u} h_v h_w \, dvdw} \, . \qquad (2.5.3)
\end{aligned}
$$

Given that $A(u) = \int_{w_1}^{w_2}\int_{v_1}^{v_2} h_v h_w \, dvdw$ corresponds to the u-dependent area of the constant-u surface, Equation 2.5.3 shows that the $dR = \sigma^{-1}du/A(u)$ relation only holds for coordinate systems with unity scaling factors $h_u = 1$, as per cylindrical and spherical coordinates discussed above.

Chapter 3. Nanopore Transport Kinetics in Salt Gradients

This chapter contains an article published in the *Nano Research* scientific journal titled "Elucidating the Dynamics of Polymer Transport through Nanopores using Asymmetric Salt Concentrations" and authored by Martin Charron, Lucas Philipp, Liqun He, Vincent Tabard-Cossa.* The corresponding Supporting Information is provided in Section 3.2.

*Reproduced and adapted from [Charron, M., Philipp, L., He, L. and Tabard-Cossa, V., 2022. Elucidating the dynamics of polymer transport through nanopores using asymmetric salt concentrations. *Nano Research*, *15*(11), pp.9943-9953.] with permission from Springer Nature.

3.1 Elucidating the Dynamics of Polymer Transport through Nanopores using Asymmetric Salt Concentrations

Martin Charron,‡ Lucas Philipp,‡ Liqun He, Vincent Tabard-Cossa

‡M.C. and L.P. contributed equally.

Abstract

While notable progress has been made in recent years both experimentally and theoretically in understanding the highly complex dynamics of polymer capture and transport through nanopores, there remains significant disagreement between experimental observation and theoretical prediction that needs to be resolved. Asymmetric salt concentrations, where the concentrations of ions on each side of the membrane are different, can be used to enhance capture rates and prolong translocation times of electrophoretically driven polymers translocating through a nanopore from the low salt concentration reservoir, which are both attractive features for single-molecule analysis. However, since asymmetric salt concentrations affect the electrophoretic pull inside and outside the pore differently, it also offers a useful control parameter to elucidate the otherwise inseparable physics of the capture and translocation process. In this work, we attempt to paint a complete picture of the dynamics of polymer capture and translocation in both symmetric and asymmetric salt concentration conditions by reporting the dependence of multiple translocation metrics on voltage, polymer length, and salt concentration gradient. Using asymmetric salt concentration conditions, we experimentally observe the predictions of tension propagation theory, and infer the significant impact of the electric field outside the pore in capturing polymers and in altering polymer conformations prior to translocation.

3.1.1. Introduction

Elucidating the physics that govern nanopore transport phenomena is a fertile field of research and is important for increasing our ability to design strategies for controlling molecular passage from which numerous technological applications can be built. On top of the spectacular innovations in DNA sequencing technology,[1,2,141–143] nanopores promise radical advances in the life sciences and medicine with ultra-sensitive, point-of-care diagnosis of disease,[4,34,144–148] identification and sequencing of proteins,[3,124,149–153] and in next-generation information storage with decoding of digital data from sequence-controlled polymers.[129,154,155] To date however, while multiple theories have been developed to describe both the capture[59,62] and translocation[68–70,156–158] processes, only a few experimental studies[30,54,56,63,73,101,139] have attempted to validate the proposed concepts, with varying degrees of agreement. This is in large part due to the complex nature of the translocation dynamics, which occur as a multi-step, highly non-equilibrium process dictated mainly by forces over which experimental control has been challenging or impossible, making verification of theoretical ideas particularly difficult. Only just recently has the first clear experimental confirmation of tension-propagation theory been provided, obtained through the measurement of the two-step, non-constant and non-monotonic velocity profile of nanostructured DNA molecules undergoing translocation.[67] Further experimental work is however needed to provide a more complete picture of the dynamics of polymer transport and to deliver better insights on how to design or improve many sensing and sequencing schemes.

Asymmetric salt concentration (ASC) conditions, in which a nanopore separates two reservoirs of different salt concentrations, offer a flexible method to probe the dynamics of transport through nanopores. Previous publications have shown that ASC conditions provide a simple method by which to decouple capture rate and translocation velocity; Measurements with

molecules in the *cis* side being in a lower salt concentration than the *trans* side ($C_{trans}/C_{cis} > 1$) have revealed both increased capture rates and decreased translocation velocities,[56,91,159–164] whereas these quantities are positively correlated when modulated by other standard means (*e.g.* tuning the voltage, salt concentration,[92,95] pore size[30,95] or temperature [96]).

In this work, we use ASC conditions as a sensitive method to modulate the different forces impacting the capture and translocation of double-stranded DNA fragments through solid-state nanopores in the 5 to 10 nm pore size range, made in ~10 nm thick silicon nitride membranes. For different ASC conditions, we report the dependence on applied voltage, DNA length, and salt concentration ratio of multiple metrics including capture rate, mean and standard deviation of translocation times. In doing so, we reveal that the underlying physics governing the capture and translocation processes under ASC conditions are fundamentally the same as in symmetric salt concentration (SSC) conditions, though the magnitude and balance of forces inside and outside the pore differ due to salt-gradient induced changes in the electric field profile, electrophoretic mobility throughout the system, and to the appearance of diffusioosmotic and diffusiophoretic forces.

Briefly, we find that capture in ASC conditions is described by the same two regimes found in SSC conditions, namely the diffusion- and barrier-limited regimes,[62] but that ASC conditions modulate the voltage and polymer length at which capture transitions from one regime to the other. We then validate that the translocation times scale with voltage and polymer-length as postulated by iso-flux tension propagation formalisms,[70] but reveal different scaling exponents between ASC and SSC conditions. Using higher-order translocation time statistics, we further demonstrate that ASC conditions alter polymer conformations and elongations prior to translocation, which helps explain the different translocation time scalings observed in ASC and SSC conditions. These

results highlight the dual effect of the non-uniform forces outside the pore in first elongating polymers before their arrival at the pore entrance and then compressing them against the nanopore membrane prior to the start of their translocation.[87,165–167] The depth of the data presented provides experimental confirmation of previously proposed theoretical concepts, and delivers new insights to design ways to control the motion and capture of biological or synthetic polymers.

Results and Discussion

Before presenting the main experimental results, we first provide an overview of the different forces present for the experimental conditions used in this work, in which both an electric potential and a salt concentration gradient are used to generate polymer capture and translocation. Here, since all experiments were performed in solutions buffered at pH 8, which is above the isoelectric point of our silicon nitride membranes and of double stranded DNA (dsDNA), we expect both electroosmotic and diffusioosmotic phenomena to be relevant to the polymer transport dynamics.

3.1.2 Electrophoresis & Electroosmosis

In a typical experiment under SSC conditions, the application of a voltage difference between the *cis* and the *trans* side results in most of the electric potential dropping inside the nanopore, i.e. the electric field is highest in the pore. Outside the nanopore, the potential drops as ~1/r, or equivalently the electric field decays as ~$1/r^2$.[60,62,117] The high electric field inside the pore, and the negatively charged pore walls lead to an electroosmotic flow (EOF) in the direction of the field, along the nanopore length, induced by the motion of positive counterions accumulated at the pore wall. Outside the pore, the EOF velocity should decay as ~$1/r^2$, due to fluid flow continuity.[168] Therefore, since dsDNA is also negatively charged, its velocity anywhere in the system has an electrophoretic contribution v_{EP}, due to the electric field's pull on the charged polymer, and an

EOF contribution v_{EO}, due to the convective fluid flow induced by the charged pore surface, with both contributions being in opposite directions (see Figure 3.1.1a). For charged dsDNA and SiN membrane type used here, electrophoresis dominates (i.e. $v_{EP} > v_{EO}$) and dsDNA molecules move in the direction opposite the electric field.

3.1.3. Diffusiophoresis and Diffusioosmosis

Recently, McMullen *et al.*[98] showed that DNA translocation could be achieved under ASC conditions without the need of an applied voltage. Under a salt gradient, the salt-concentration profile should be very similar to that of the electric potential profile under symmetric conditions described above, since to first order the quasi-steady state diffusion equation $\nabla^2 C = 0$ and Poisson equation $\nabla^2 V = 0$ are identical, assuming no convective flow and no charge. For this reason, most of the salt-concentration change is expected to occur inside the nanopore, while concentrations outside the pore to decay as ~1/r to the respective values of the *cis*- and *trans*-side salt concentrations C_{cis} and C_{trans}.[169] Because of the sharp salt-concentration change inside the pore and of the negatively charged walls, a diffusioosmotic flow is expected to form from the high- to the low-concentration reservoir, as experimentally observed in nanochannels by Lee *et al.* [170] Such a convective fluid flow arises when an electrolyte gradient is present along the length of a charged surface, partly due to the different diffusivities of anions and cations inducing an electric field tangent to the pore walls, and due to the osmotic pressure gradient within the double layer.[170,171] Again, because of fluid flow continuity the diffusioosmotic-flow velocity outside the pore is expected decay approximately as ~$1/r^2$. Moreover, since dsDNA is negatively charged and mobile, it feels a diffusiophoretic force opposing the diffusioosmotic solvent force, akin to electrophoresis and electroosmosis. The velocity of dsDNA anywhere in this system therefore has a diffusiophoretic contribution v_{DP}, due to dsDNA probing the non-uniform salt concentration

profile, and a diffusioosmotic flow contribution v_{DO}, due to the convective flow induced by the charged pore surface, with both contributions being in opposite directions, as depicted in Figure 3.1.1b.

Since both electric biases and salt gradients are used to induce DNA capture and translocation in this work, the velocity of DNA at any point in the system is expected to have contributions from electrophoresis, electroosmosis, diffusiophoresis and diffusioosmosis, as discussed above: $\vec{v} = \vec{v}_{EP} + \vec{v}_{EO} + \vec{v}_{DP} + \vec{v}_{DO}$. It should further be noted that salt gradients modulate non-uniformly the electrophoretic mobility and the electric field inside and outside the nanopore system. The former is a direct result of electrophoretic mobility's dependence on ionic concentration, whereas the latter is best understood by modeling the nanopore system as three resistors in series, i.e. one resistor for the cylindrical nanopore R_{pore}, and two for the *cis*- and *trans*-side access regions, and R_{cis} and R_{trans} (Figure 3.1.1c). For example, increasing the salt concentration in the *trans*-reservoir also increases the concentration inside the pore, and therefore reduces the *trans*-side and pore resistances and voltage drops. To conserve the total applied voltage of the system, the voltage and electric field on the *cis* side increase. Lastly, salt gradients are known to induce an electrochemical potential difference between the electrodes in addition to the intended applied bias.[98] To better compare ASC and SSC conditions, this electrochemical bias was compensated before each experiment by applying an offset voltage in order to zero the ionic current. The voltages reported below are therefore measured with respect to this initial potential offset.

3.1.4 Nanopore Capture and Translocation Steps

The capture and translocation of polymers into nanopores is a complex nonequilibrium process resulting from coupled electrohydrodynamic and diffusion processes which occur on a wide variety of timescales spanning both sides of the polymer relaxation time. In SSC conditions, i.e. with no salt gradient, the electric field inside and outside the pore drives most of the directed transport mechanisms.[59,62] In ASC conditions however, additional diffusioosmotic forces are expected to impact the dynamics of capture and translocation. Because of the qualitative similarities between electrophoretic and diffusioosmotic forces outlined above (i.e. forces strongest inside pore, and decaying outside pore), the complete capture and translocation process of a polymer in both SSC and ASC conditions can be described using the five following steps: i) The polymer diffuses from the solution bulk close to the nanopore capture volume, a hemisphere-like volume inside which the force-induced drift (Figure 3.1.1d) is stronger than thermal motion; [56,60,117] ii) The polymer drifts towards the pore, during which it is elongated by the force gradient,[87,165,167] until it arrives at the pore; iii) The polymer at the pore entrance is compressed against the nanopore membrane by the forces until threading begins either by an end or a folded segment of the polymer;[165,167] iv) Due to the high pulling force inside the pore, the polymer undergoes non-equilibrium deformation during translocation. As consecutive segments are pulled inside the pore, the fraction of the polymer still on the *cis*-side is being deformed with a growing mobile segment as the tension propagates along its contour length;[67,68,70–72,158] v) Once the tension reaches the polymer end, the polymer continues translocation but with a shrinking *cis*-side segment fully under tension until the polymer is fully threaded.[67,68,70–72,158]

Note that only the strongly driven translocation regime has been described above, and not the weakly driven regime,[172] in which the translocation steps *iv* and *v* occur on timescales

comparable to or longer than the relaxation time of the polymer. Since the majority of experimental work with solid-state nanopores occurs in the strongly driven regime,[67] we focus our efforts there.

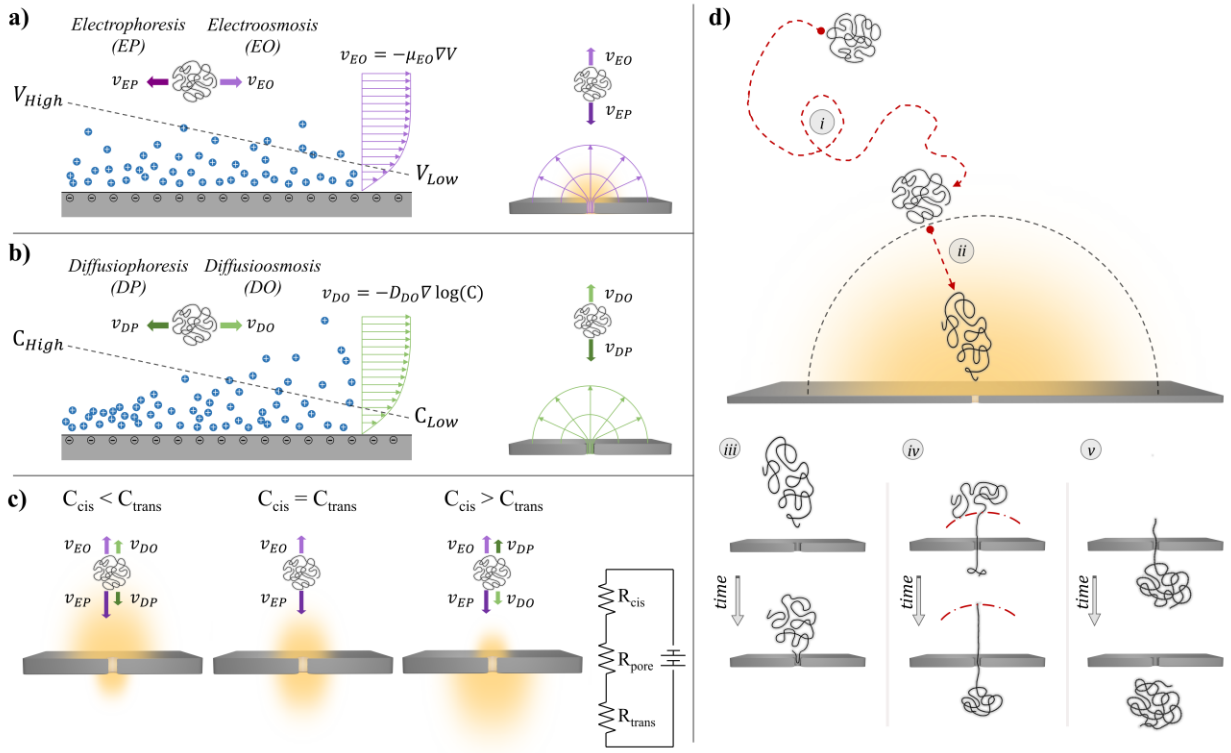

Figure 3.1.1. Capture steps, and forces expected under a potential and salt gradient. a) Schematic of the effect of an applied electric potential difference on a charged polymer near a charged membrane (left), and on a charged polymer outside a nanopore (right). **b)** Schematic of the effect of an electrolyte concentration gradient on a charged polymer near a negatively charged membrane (left), and a charged polymer outside a nanopore (right). **c)** Schematic of the direction of forces present under an applied electric bias and three different salt concentration gradients. The yellow hemispheres are used to depict the modulation of electric field strengths. **d)** Schematic of the capture and translocation steps: (i) Polymer diffuses close to the pore; (ii) Polymer drifts to the pore mouth; (iii) Polymer segment finds and enters the pore, thereby initiating translocation; (iv) Tension propagation: A growing fraction of the polymer is under tension/motion. The tension front is represented by a red dashed line; (v) Post-propagation: All monomers on *cis*-side move towards the pore.

3.1.5. Capture Scaling

In order to investigate how the capture process is affected by different ASC conditions, we first describe the scaling of capture rate with applied voltage (ΔV) and polymer length (N) in both ASC and SSC conditions. As described elsewhere, capture rate in standard SSC conditions is well described by both the barrier-limited regime for short polymers or low voltages, and by the diffusion-limited regime for long polymers or high voltages (also termed drift-limited regime[59,63]), in which the rate-limiting step is the polymer overcoming a largely entropic, free-energy barrier or diffusing into the capture volume, respectively.[59,60,62,173]

$$R \equiv \frac{J}{c} \propto \begin{cases} N^{\gamma} e^{\delta \Delta V}, & N, \Delta V < N^*, \Delta V^* \\ \mu_e \Delta V, & N, \Delta V > N^*, \Delta V^* \end{cases} \tag{3.1.1}$$

Here, R is the normalized capture rate, defined as the ratio of capture rate J and polymer concentration c, μ_e is the electrophoretic mobility of the charged polymer, and γ and δ are scaling coefficients. The regime-transition polymer length and voltage values are denoted by $N^*$and ΔV^*, are interdependent, and both depend strongly on experimental parameters.[59,62] Note that since we use double-stranded DNA (dsDNA) as our model linear polymer, and its electrophoretic mobility is length independent above a few hundred bases,[83] its capture rate is expected to scale as $R \sim N^0 \Delta V^1$ in the diffusion-limited regime.[54,56,63]

To test the validity of the voltage scaling of Equation 3.1.1 for polymer capture in ASC conditions, we performed experiments using 0.25 nM of 10,000 base pairs (bp) dsDNA in a 5.3 nm diameter nanopore, under applied voltages ranging from 50 mV to 600 mV, in three different LiCl salt conditions: SSC (C_{trans}/C_{cis}= 0.45 M/0.45 M = 1); capture-promoting ASC (C_{trans}/C_{cis} = 3.6 M/0.45 M > 1); and capture-opposing ASC (C_{trans}/C_{cis} = 0.45 M/3.2 M < 1). Figures 3.1.2a-c show representative current traces acquired under a bias of 400 mV in SSC, capture-promoting

and capture-opposing ASC conditions, respectively. At each voltage, the inter-event time distribution was extracted, and the corresponding capture rate was determined,[54] as shown in Figure 3.1.2d.

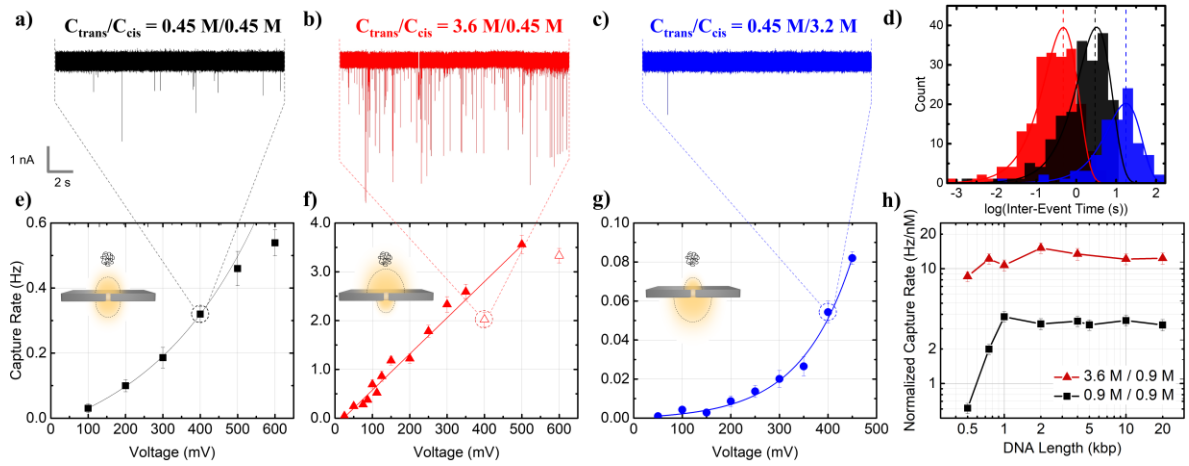

Figure 3.1.2. Capture kinetics in symmetric and asymmetric salt concentration conditions. Representative ionic current traces for 0.25 nM of 10 kbp dsDNA under 400 mV in a 5.3 nm pore in a 10 nm thick SiN membrane under **a)** symmetric salt conditions (0.45 M LiCl); **b)** capture-promoting salt conditions ($C_{trans}/C_{cis} > 1$); **c)** and capture-opposing salt conditions ($C_{trans}/C_{cis} < 1$). Data sampled at 4.17 MHz, analyzed, and displayed at 300 kHz with a low-pass Bessel filter. **d)** Inter-event time distribution fitting for the data at 400 mV shown in a), b) and c) with corresponding colors, where capture rate is extracted by fitting the log-transform of a Poisson distribution. **e)** Voltage dependence of capture rate in SSC conditions (0.45 M LiCl, black squares); **f)** capture-promoting ASC conditions ($C_{trans}/C_{cis} > 1$, red triangles); **g)** and capture-opposing ASC conditions ($C_{trans}/C_{cis} < 1$, blue circles). **h)** Normalized capture rate versus DNA length in an 8.5 nm pore in symmetric 0.9 M LiCl salt conditions (black squares) and 4x capture-promoting ASC conditions (red triangles) under a 400 mV bias. Error bars result from assuming Poisson statistics for capture rate uncertainty and a conservative 10% DNA concentration uncertainty. Note that some intra-pore capture rate variations are present, which we attribute to uncontrolled variability sources.[54] Data deemed as outliers are displayed as hollow, as shown in f), and ignored during fitting.

As a control, Figure 3.1.2e shows the voltage dependence of the capture rate of 10 kbp dsDNA in symmetric 0.45 M LiCl conditions for this 5.3 nm nanopore. A subtle nonlinear trend can be observed for $\Delta V \leq 400$ mV, which fits well to an exponential function. For $\Delta V > 400$ mV, the data does not fit well to an exponential fit and is expected instead to be described by a linear voltage dependence, as supported and discussed in the following section. These trends are expected

from Equation 3.1.1 in SSC conditions,[54,56,60,63] with the change of capture regime from barrier-limited to diffusion-limited occurring around $\Delta V^* \approx$ 400mV.

Figure 3.1.2f shows the voltage dependence of the capture rate in the C_{trans}/C_{cis} = 3.6 M/0.45 M > 1 ASC condition on the same pore. As expected, the measured capture rates are appreciably higher than in SSC conditions (e.g. 3.56 Hz vs. 0.46 Hz at 500 mV). The capture rate in this capture-promoting case clearly exhibits a linear voltage dependence for the entire voltage range, characteristic of the diffusion-limited regime, even at very low voltages ($\Delta V^* <$ 50 mV). Conversely, Figure 3.1.2g shows that when the polymer is located on the high salt concentration side of a comparable salt gradient (C_{trans}/C_{cis} = 0.45 M/3.2 M < 1), the capture rate is drastically reduced and a clear exponential voltage dependence is observed throughout the entire voltage range investigated, characteristic of the barrier-limited regime ($\Delta V^* >$ 500 mV).

Next, we explored the scaling of capture with polymer length, by measuring the capture rates of dsDNA ranging from 500 to 20,000 bp in an 8.5 nm pore under a fixed 400 mV bias in two different LiCl salt conditions. Figure 3.1.2h shows the normalized capture rate J as a function of polymer length N for SSC (C_{trans}/C_{cis} = 0.9 M/0.9 M = 1) and capture-promoting ASC (C_{trans}/C_{cis} = 3.6 M/0.9 M = 4) conditions. In the SSC condition, as previously observed,[54,56,63] the capture rate initially sharply increases with DNA length before exhibiting a length-independent behavior. For the experimental conditions used here, the regime-transition polymer length between the barrier-limited and the diffusion-limited regimes is $N^* \approx$ 1 kbp. In contrast, the 4× ASC condition shows a higher normalized capture rate with no such clear dependence on polymer length for the range studied. Only the shortest length tested, at N = 500 bp, may indicate the onset of a smooth transition towards a length-dependent regime. Although hard to pinpoint, the capture regime

transition appears to be shifted toward shorter polymers in capture-promoting ASC conditions as compared to the SSC conditions.

From the capture rate results presented in Figure 3.1.2, we conclude that the dynamics of capture in ASC conditions are described by the same physical phenomena as in the symmetric case: The barrier-limited and diffusion-limited regimes provide adequate descriptions of the properties of capture under ASC conditions. Moreover, ASC conditions demonstrate modulation of the transition between capture regimes, with capture-opposing gradients ($C_{trans}/C_{cis} < 1$) extending the barrier-limited transition to larger polymers and higher voltages, and capture-promoting gradients ($C_{trans}/C_{cis} > 1$) reducing the transition to shorter polymers and smaller voltages.

3.1.6. Capture Rate Modulation

Characterizing the extent to which capture rate is modulated by ASC conditions is of practical value for precise molecular counting applications. The data in Figure 3.1.2 and ensuing interpretation that salt gradients alter the capture-regime transitions suggest that the observed capture enhancement between different ASC conditions should also be capture-regime dependent.

To investigate this, we used the 10 kbp dsDNA data from Figure 3.1.2e-f to calculate the capture rate enhancement R_{ASC}/R_{SSC} between the capture-promoting ASC (C_{trans}/C_{cis} = 3.6 M/0.45 M >1) and SSC (C_{trans}/C_{cis}= 0.45 M/0.45 M = 1) conditions. Figure 3.1.3a displays the voltage dependence of the capture rate enhancement. Under a 100 mV bias, the capture rate enhancement is measured to be ~20-fold. Capture enhancement decreases with increasing voltages until ≈ 400 mV where it becomes approximately constant. For ≥ 400 mV, the value of the capture enhancement is approximately equivalent to the salt concentration or conductivity ratios of the *trans* and *cis* sides. This enhancement value was observed in previous work and is expected for

the diffusion-limited regime.[56,164] This was attributed to the fact that the electric field far from the pore in ASC conditions is approximately enhanced by a factor of $\sigma_{trans}/\sigma_{cis} \approx C_{trans}/C_{cis}$, when compared to the SSC conditions. Interestingly, the voltage at which R_{ASC}/R_{SSC} plateaus to C_{trans}/C_{cis} coincides well with ΔV^*, the voltage at which capture appears to transition from barrier- to diffusion-limited under the SSC condition (Figure 3.1.2e). Note that in high salt concentration, electrical conductivity is not strictly linearly related to salt concentration.[174] Conductivity measurements across the various LiCl concentrations used here however show that $\sigma_{trans}/\sigma_{cis} \approx C_{trans}/C_{cis}$ is a reasonable approximation (see Section S3.2.1 of the SI).

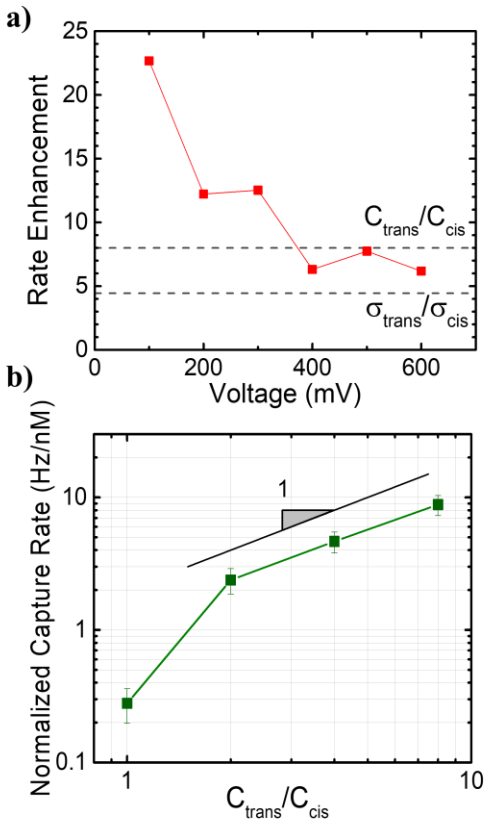

Figure 3.1.3. Regime-dependent capture enhancement. a) Capture rate enhancement (R_{asc}/R_{ssc}) versus voltage using 10 kbp capture data in a 5.3 nm pore from Figure 3.1.2. **b)** Capture rate versus C_{trans}/C_{cis} on a log-log scale, to better show the linear scaling for higher salt concentration ratios. Measurements in a 5.1 nm pore, under a 200 mV bias, using 5 kbp dsDNA with C_{cis} fixed at 0.45 M LiCl.

We next measured the capture rate of 5 kbp dsDNA in a 5.1 nm pore, under a 200 mV bias, with C_{cis} fixed at 0.45 M LiCl and C_{trans} ranging from 0.45 M to 3.6 M LiCl. Figure 3.1.3b shows the normalized capture rate measured for different values of C_{trans}/C_{cis}. As expected from previous publications,[56,164] capture rate grows monotonically with increasing salt-concentration ratios. Interestingly, a linear dependence of capture rate on C_{trans}/C_{cis} is observed for $C_{trans}/C_{cis} \geq 2$, whereas a super-linear trend is observed for smaller salt concentration gradients. As shown in Section S3.2.2 of the SI, the transition from super-linear to linear dependence on C_{trans}/C_{cis} was observed under multiple experimental conditions.[164]

Since increasing the applied voltage or the salt-concentration ratio increases the forces on the *cis*-side, both Figures 3.1.3a and 3.1.3b demonstrate that stronger cis-side forces promote diffusion-limited capture and result in a capture enhancement approximately equal in magnitude to C_{trans}/C_{cis}, whereas weaker forces promote barrier-limited capture and result in enhancements significantly higher than the salt concentration ratio C_{trans}/C_{cis}. We therefore infer that, for the data in Figure 3.1.3b and Section S3.2.2 of the SI, polymers in salt gradients ≥ 2 are in the diffusion-limited capture regime, whereas for smaller salt gradients polymers are in the barrier-limited capture regime.

Interestingly, the concept of regime-dependent capture enhancement appears to be a general feature of transport through nanopores as it also applies to non-linear polymers, such as DNA nanostructures.[175] In Section S3.2.3 of the SI, we show that the scaling of capture rate with C_{trans}/C_{cis} is different for two similar DNA nanostructures with different intrinsic rigidities. Because the nanostructures must deform and bend to pass through the pore, different rigidities result in different free-energy barriers. The more flexible structure, which experiences a lower free-energy barrier, is seen to scale almost linearly with C_{trans}/C_{cis}, indicating diffusion-limited

capture. The more rigid structure, which experiences a higher free-energy barrier, scales super-linearly with the salt concentration ratio, indicating barrier-limited capture.

3.1.7 Translocation Time Scaling

In the second part of this work, in order to gain more insights into the physics of translocation, we investigate the scaling of translocation time τ with applied voltage and polymer length in both ASC and SSC conditions. Translocation dynamics are commonly characterized through the scaling coefficients α and β of translocation time with polymer length and applied voltage, respectively: [156]

$$\tau \sim N^{\alpha} \Delta V^{\beta}. \tag{3.1.2}$$

Tension propagation (TP) models dictate that the length-scaling coefficient α should be bounded by 1 and 1+ν, where ν = 0.588 is the Flory exponent for real self-interacting polymers, with self-exclusion and the voltage-scaling coefficient β should be equal to -1 for free-draining polymers (equivalently, the mean translocation velocity, $\mathcal{v}$, should be linearly dependent on the applied voltage).[68,69,72]

We first investigated the scaling of translocation time with applied voltage $\tau \sim \Delta V^{\beta}$ by using the same data as that of Figure 3.1.2e-g, for 10 kbp dsDNA translocating through a 5.3 nm pore under applied voltages ranging from 50 mV to 600 mV in SSC (C_{trans}/C_{cis} = 0.45 M/0.45 M = 1), capture-promoting ASC (C_{trans}/C_{cis} = 3.6 M/0.45 M > 1), and capture-opposing ASC (C_{trans}/C_{cis} = 0.45 M/3.2 M < 1) conditions. Figure 3.1.4a shows the translocation times measured at various voltages for these three conditions. Interestingly, translocation times measured in both capture-promoting and capture-opposing ASC conditions are longer than in SSC conditions for all applied voltages. As expected from IFTP theory,[69,70,156,158] translocation times in SSC conditions

exhibit an inversely proportional voltage-scaling, as identified by the slope of β = -1.04 ± 0.08 measured on the log-log plot of Figure 3.1.4a. Translocation times from both ASC conditions appear to display a scaling coefficients of -1 at high voltages (here for $\Delta V >$ ~200 mV), but for lower voltages, the coefficients deviate as seen by the non-constant slopes in the log-log plot ($\beta < -1$ for capture-opposing, and $\beta > -1$ for capture-promoting ASC conditions). To explain this behavior, we plotted the translocation velocity ($v = 0.34\ nm \times N/\tau$) as a function of voltage for both ASC conditions (Figure 3.1.4b). Just like SSC conditions, translocation velocity exhibits a linear dependence on voltage, with linear fits of the form $v = a\Delta V + v_0$. An equivalent linear fit for the translocation time versus voltage, $\tau = 0.34 \times N/(a\Delta V + v_0)$, is included in the log-log plot of Figure 3.1.4a and fits remarkably well the data over the entire voltage range. Unlike SSC conditions, translocation velocities in ASC conditions have nonzero intercepts v_0, i.e. nonzero translocation velocities with no voltage applied: Capture-promoting conditions results in an intercept of $v_0 = +1.4 \pm 0.2\ nm/\mu s$, whereas capture-opposing conditions in $v_0 = -1.3 \pm 0.2\ nm/\mu s$.

Note that with no applied voltage, the only forces acting on dsDNA should be solely of diffusioosmotic and diffusiophoretic origin, as discussed above (Figure 3.1.1). The intercepts obtained from the linear fits should therefore correspond to the velocity induced by these forces. Interestingly, the fact that both values are comparable in magnitude but opposite in sign indicates that the salt gradient across the nanopore alone induces a force on DNA pointing from the low-salt-concentration side to the high-salt-concentration side, resulting in a translocation velocity of $v < 2\frac{nm}{\mu s}$. The direction of the force therefore suggests that diffusiophoresis is more important than diffusioosmosis in our experimental configuration (see Figure 3.1.1b). Furthermore, this zero-voltage velocity is in good agreement with the diffusiophoretic translocation velocity values

obtained by McMullen *et al*.[98] under similar experimental conditions. Figures 3.1.4a-b and the corresponding linear fits therefore show that the $\tau \sim \Delta V^{-1}$ scaling is maintained under ASC conditions, albeit with an extra diffusiophoretic force which causes a non-zero translocation velocity under no applied voltage and is responsible for the non-constant slopes observed in log-log plot of Figure 3.1.4a.

Next, to experimentally verify the scaling of translocation time with polymer length $\tau \sim N^{\alpha}$ under ASC condition (C_{trans}/C_{cis} = 3.6 M/0.9 M = 4), we used dsDNA of lengths ranging from 500 bp to 48 kbp translocating through three 8.5 nm ± 1 nm diameter pores under a 400 mV bias and compared it to a SSC (C_{trans}/C_{cis} = 0.9 M/0.9 M = 1) control experiment. The measured translocation times are plotted in Figure 3.1.4c, which shows slower translocations in capture-promoting ASC conditions than in SSC conditions, consistent with Figure 3.1.4a. Fitting the data to power-scaling law functions of the form of Equation 3.1.2 yielded scaling coefficients of α_{SSC} = 1.22 ± 0.02 for SSC and α_{ASC} = 1.10 ± 0.07 for ASC condition (fits shown in Section S3.2.4 of the SI). While the extracted α_{SSC} coefficient is in very good agreement with a handful of values reported in previous experimental studies,[73–75] the scaling coefficient in ASC conditions, α_{ASC}, is significantly smaller than α_{SSC} (P = 0.06, obtained using a Welch t-test). To our knowledge, such a scaling reduction, albeit more drastic, has been only reported when comparing translocation times of DNA entering and exiting a glass nanopipette.[97]

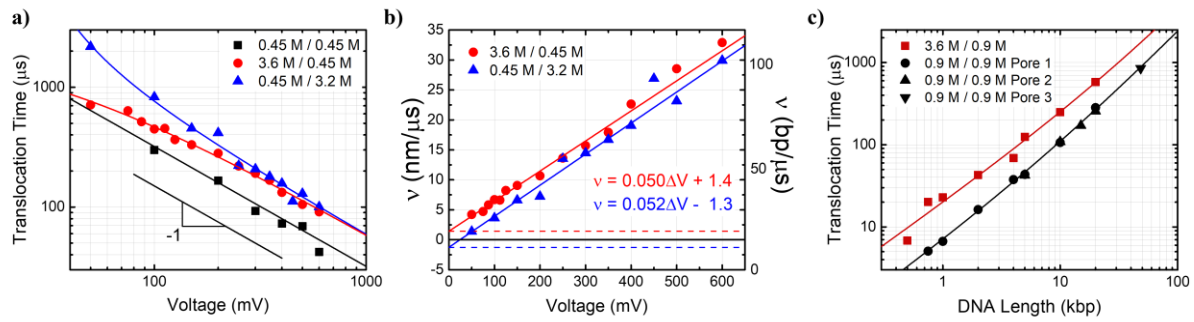

Figure 3.1.4. Translocation kinetics in ASC and SSC conditions. **a)** Log-log plot of translocation time versus voltage in SSC (black squares), capture-promoting (red circles), and capture-opposing (blue triangles) ASC conditions. All data is from 10 kbp dsDNA in the same 5.3 nm pore. Solid lines show the optimal fits to functions of the form $\tau = (a\Delta V + b)^{-1}$. **b)** ASC condition data from (a) replotted to show translocation velocity versus voltage. Solid lines are the same linear fits showed in (a). **c)** Log-log plot of translocation time versus polymer length for symmetric (red squares, C_{trans}/C_{cis} = 0.9 M/0.9 M) and 4x capture-promoting ASC (black circles, triangles C_{trans}/C_{cis} = 3.6 M/0.9 M) conditions, under 400 mV in 8.5 ± 1 nm pores. Red square and black circle data were acquired from the same nanopore. Continuous curves are fits to Equation 3.1.4 (for fits to Equation 3.1.2 see Figure S3.2.4 in the SI). **(b)** *i)* Translocation time versus voltage in SSC, *ii*) capture-promoting ($C_{trans}/C_{cis} > 1$) and *iii*) capture-opposing ($C_{trans}/C_{cis} < 1$) ASC conditions.

Theoretical studies and simulations of tension propagation have shown that a simple power-law expression in the form of Equation 3.1.2 is insufficient to capture the length-dependence of translocation times[70,71,158,176]. To incorporate finite polymer-length effects and pore friction, models such as the Iso-Flux Tension Propagation (IFTP) [70] propose a length-dependence correction of the form

$$\tau = AN^{1+\nu} + BN\,, \tag{3.1.3}$$

where A and B are simple coefficients whose values depend on pore geometry, solution viscosity, and pulling force inside the pore. The first term results from the drag of monomers on the *cis*-side and is expected to dominate for long polymers. The second term results from the polymer-pore interactions and is expected to dominate for short polymers. Note that this two-term scaling is equivalent to having a length-dependent scaling coefficient $\alpha(N)$ in Equation 3.1.2, where translocations dominated by pore friction ($A \ll B$) result in $\alpha \approx 1$, and translocations dominated by

cis-side monomer drag ($A \gg B$) result in α ≈ 1.588. To experimentally verify the validity of Equation 3.1.3, the translocation times of Figure 3.1.4c were fitted using the equivalent but more insightful form

$$\tau = \frac{t_c}{2}\left[\left(\frac{N}{N_c}\right)^{\kappa} + \frac{N}{N_c}\right], \tag{3.1.4}$$

with t_c, N_c and κ as free parameters, allowing the extraction of κ, the scaling coefficient of *cis*-side monomers, and N_c the crossover length at which both the *cis*-monomer friction term and pore-friction term contribute equally to a translocation time of t_c. Note that κ is left as a free parameter in order to verify the IFTP prediction of κ = 1.588.[70] From the optimal fits shown in Figure 3.1.4c, we extracted scaling coefficients of κ_{ssc} = 1.53 ± 0.10 and κ_{asc} = 1.61 ± 1.49, and crossover lengths of N_C^{ssc} = 10 ± 6 kbp and N_C^{asc} = 52 ± 89 kbp in SSC and ASC conditions, respectively. Both κ values correspond within error to the expected theoretical value of κ = 1+ν = 1.588, although with significantly higher uncertainty for κ_{asc}. Moreover, the higher value and higher uncertainty of N_C^{asc} indicate that the fitting of ASC data is insensitive to the first term of Equation 3.1.4, *i.e.* the *cis*-monomer drag term. A broader range of polymer lengths covering both sides of the transition point would be necessary to reduce the uncertainty on this parameter.

Interestingly, a higher N_c value implies that the kinetics of translocation are more dominated by polymer-pore interactions in ASC conditions than in SSC conditions.[70,71,158] This conclusion is consistent with the reduction of the scaling parameter α observed for the simple power-law fits of Equation 3.1.2. Figure 3.1.4c and its corresponding fits therefore show that polymer translocations in ASC and SSC conditions are well described by IFTP, albeit with different relative contributions from *cis*-side and pore-polymer drag forces.

3.1.8 Modulation of Translocation Time Statistics

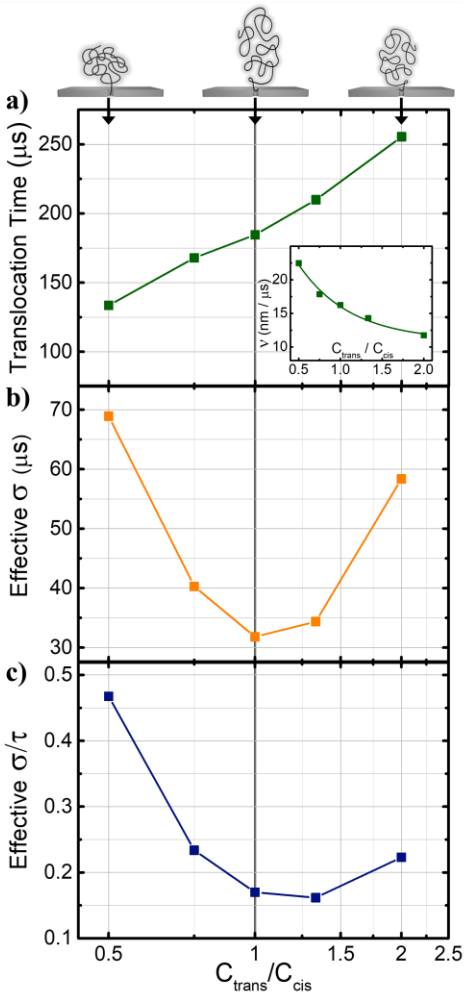

Figure 3.1.5. Translocation Time statistics in ASC conditions. Dependence of 10 kbp translocation time statistics on salt concentration ratios for fixed C_{cis} =1.8M LiCl and varying C_{trans} under 300 mV in a 6.0 nm pore. **a)** Mean Translocation time, **b)** Translocation time standard deviation, and **c)** coefficient of variation versus C_{trans}/C_{cis} on semi-log *x*-scale. The inset of (a) shows the corresponding translocation velocity versus C_{trans}/C_{cis}. Schematics of deduced polymer elongations in different ASC conditions are shown above (a).

We now attempt to gain insights into how ASC conditions alter polymer conformations during steps *ii* and *iii* of capture in Figure 3.1.1b, the steps prior to translocation during which polymers are elongated and compressed by the forces outside the pore, respectively. Since a polymer's conformation directly impacts its translocation time,[177] this section is devoted to

studying the effects of ASC conditions on the distribution of translocation times, i.e. the higher-order statistics of translocation times. To achieve this, we measured the passage times of 10 kbp dsDNA in a 6.0 nm pore, under a 300 mV bias, with C_{cis} fixed at 1.8 M LiCl and C_{trans} ranging from 0.9 M to 3.6 M LiCl.

Figure 3.1.5a and its inset plot the dependence of the mean translocation time τ and velocity $\mathcal{v}$ on the salt concentration ratio C_{trans}/C_{cis}, respectively. For the entire range tested, τ monotonically increases (i.e. $\mathcal{v}$ decreases) with C_{trans}/C_{cis} for both capture-promoting ($C_{trans}/C_{cis} > 1$) and capture-opposing ($C_{trans}/C_{cis} < 1$) ASC conditions, with τ seeing a twofold increase in going from $C_{trans}/C_{cis} = 0.5$ to 2. Velocity and force being proportional, it can be concluded that the pulling force inside the pore, responsible for driving the translocation process, reduces with C_{trans}/C_{cis}.

As discussed earlier (see Figure 3.1.1), the reduction of the pulling force inside the pore with C_{trans}/C_{cis} should be a direct result of diffusiophoretic and electrophoretic force modulations under different salt concentration gradients. Note that translocation velocities reduce by >10 nm/μs in going from $C_{trans}/C_{cis} = 0.5$ to 2 (23 nm/μs vs 12 nm/μs, respectively), as shown in the inset of Figure 3.1.5a. This velocity change is significantly higher than the <2 nm/μs diffusiophoretic contribution estimated in Figure 3.1.4b, but also in the opposite direction: Diffusiophoresis induces DNA motion from the lower to the higher salt concentration reservoir, with higher gradients resulting in higher velocities. Electrophoresis is therefore more likely responsible for slower translocations, and can be altered in two ways by salt gradients: The non-uniform conductivity can modulate the electric field (Figure 3.1.1c), and the local salt concentration inside the pore can alter DNA's mobility during translocation. Due to symmetry, the voltage drop across the pore for a $C_{trans}/C_{cis} = 0.5$ salt gradient should be the same as for a $C_{trans}/C_{cis} = 2$ gradient, and be maximal

for C_{trans}/C_{cis} = 1. The salt-gradient-induced field modulation should therefore contribute non-monotonically to the translocation times, which is inconsistent with observations from Figure 3.1.5a. The most likely primary source of translocation time modulation is therefore the local concentration inside the pore modulating the electrophoretic mobility of dsDNA, for which slower translocations are expected in higher salt concentrations.[92,95] This is further supported by the dependence of translocation time velocity ν on salt gradient C_{trans}/C_{cis} being well described by a decaying exponential (fit shown in Figure 3.1.5a inset), a dependence previously reported by Rivas *et al*.[95]

Since the spread of translocation times is a measure of the conformational entropy of polymers at the onset of translocation,[74,177] we next investigated its dependence on C_{trans}/C_{cis}. To achieve this, we extracted the effective standard deviation σ from the 10 kbp dsDNA translocation time distributions and calculated the effective coefficient of variation σ/τ in different ASC conditions, as shown in Figures 3.1.5b and 3.1.5c. Unlike translocation times, σ exhibits a convex non-monotonic dependence on C_{trans}/C_{cis}, with a minimum located near C_{trans}/C_{cis} = 1. As a result, the σ/τ values are asymmetric around C_{trans}/C_{cis} = 1 with the capture-promoting ASC conditions resulting in significantly smaller σ/τ values than their inverse capture-opposing conditions. Note that since ASC conditions increase the fraction of folded translocations (analysis shown in Section S3.2.5 of SI), the effective spread of translocation times were instead extracted from the population of folded translocations (see Methods and Section S3.2.6 of the SI for description and validation of this method).

Previous studies have shown that polymers stretched prior to translocation display reduced conformational entropy (and σ/τ values) due to their more elongated conformations.[74,178,179] Interpreting σ/τ values as being inversely correlated with the average conformation elongation,

Figure 3.1.5c could therefore show a non-monotonic relationship between elongation and salt concentration ratio C_{trans}/C_{cis}: For a fixed C_{cis} and varying C_{trans}, capture-opposing ASC conditions ($C_{trans}/C_{cis} < 1$) result in less elongated polymer conformations than SSC conditions ($C_{trans}/C_{cis} = 1$), which in turn result in more elongated conformations than capture-promoting ASC conditions ($C_{trans}/C_{cis} > 1$), with the maximal elongation occurring near $C_{trans}/C_{cis} = 1$ (see Figure 3.1.5d). To further validate the increase of σ/τ in capture-promoting ASC conditions and support the proposed elongation interpretation, the dependence of σ and σ/τ on polymer length is shown and analyzed in Section S3.2.7 of the SI, in which a similar σ/τ increase is observed.

3.1.9 Insights from Observations

Multiple observations and claims regarding nanopore capture and translocation dynamics in ASC and SSC conditions were brought forward in the four previous sections, including that capture-promoting ASC conditions promote diffusion-limited capture, whereas capture-opposing ASC conditions promote barrier-limited capture, and that polymers translocating under capture-promoting ASC conditions are slower than in SSC conditions, more dominated by pore friction and are more elongated than under SSC conditions. We now discuss how these observations converge to paint a complete picture of the nanopore transport process, consistent with what was described in Figure 3.1.1.

First, to better assess the change in dynamics when going from SSC to ASC conditions, we address the most plausible mechanisms by which electrophoretically-driven capture and translocation are altered in the presence of salt gradients. Figures 3.1.4 and 3.1.5a showed that salt-gradient-mediated electrophoretic mobility modulation is the main contribution to translocation time variations in ASC conditions. This explains why translocations occurring from the low salt side C_{low} or high salt side C_{high} of a given salt gradient are of similar durations and are both slower

than translocations in SSC conditions (Figure 3.1.4), and why translocation time increases monotonically with C_{trans}/C_{cis} when C_{cis} is kept fixed, i.e. as the average salt concentration inside the pore increases (Figure 3.1.5a). We caution that while this is true of our experimental conditions, for which diffusiophoretic forces are less important than electrophoretic ones (Figure 3.1.4b), this might not be the case for experiments using lower voltages (<100 mV), lower aspect ratio pores (d/L<1), or even in lower salt concentrations (<0.1 M) in which overlapping Debye layers introduce more complex behavior.[91]

Interestingly, the reduction of the pulling force inside the pore in capture-promoting ASC conditions ($C_{trans}/C_{cis} > 1$ Figure 3.1.4 and 3.1.5a) makes it harder for polymers to successfully cross the entropic-based free-energy barrier, and fully translocate the nanopore. Although this appears to be at odds with the observation that ASC conditions promote diffusion-limited capture, a capture regime independent of the energy barrier (Figure 3.1.2), we believe it instead highlights the role that forces outside the pore play on the capture process: Strong attractive forces on the *cis*-side access region make it hard for DNA molecules to diffuse away from the pore and therefore promote successful translocations by virtue of increased time spent near the pore. Since capture-promoting ASC conditions are expected to increase the *cis*-side forces mainly due to increased electrophoretic pull (Figure 3.1.1c), we therefore suggest that salt-gradient-modulated electric fields outside the pore are directly responsible for ASC conditions promoting diffusion-limited ($C_{trans}/C_{cis} > 1$) or barrier-limited ($C_{trans}/C_{cis} < 1$) capture regimes.

In order to better understand the non-monotonic trend of translocation time spread vs C_{trans}/C_{cis} (Figure 3.1.5c), and to support the interpretation that polymer conformations in ASC conditions are less elongated than in SSC conditions, we next discuss how the force modulations in ASC conditions are expected to impact the polymer conformations prior to successfully entering

and threading through the pore, i.e. during steps *ii* and *iii* of Figure 3.1.1d. As per the above discussion, the monotonic increase of capture rate with salt gradient (Figure 3.1.3b) shows that forces outside the pore increase monotonically with C_{trans}/C_{cis}. Due to the forces being non-uniform and strongest near the pore, polymers are radially elongated as they approach the pore, i.e. during step *ii* of Figure 3.1.1d. Since stronger forces can result in stronger stretching, we expect the elongation of polymers throughout step *ii* to increase monotonically with C_{trans}/C_{cis}. Subsequently, once the polymer reaches the pore mouth and attempts to initiate translocation by surmounting the free-energy barrier, i.e. during step *iii* of Figure 3.1.1d, it is actively being compressed against the membrane by the forces outside the pore. The duration of step *iii*, and therefore the amount of time during which a polymer is compressed, is closely related to the magnitude of the pulling force inside the pore. A strong pulling force, for example, should facilitate crossing the free-energy barrier and therefore reduce the time required for a polymer to initiate translocation. As a result, a weaker force should promote polymer compression, as it provides more time for forces outside the pore to compress the polymer, whereas the opposite is true for strong pulling forces. Since Figure 3.1.5a showed that the pulling force inside the pore reduces monotonically with C_{trans}/C_{cis} for fixed C_{cis}, we conclude that increasing C_{trans}/C_{cis} has two confounding effects on polymer conformations: it promotes elongation during step *ii*, and promotes compression during step *iii*.

We believe that these elongation and compression phenomena explain the non-monotonic translocation time σ/τ values shown in Figures 3.1.5b,c: For $C_{trans}/C_{cis} \gg 1$, although polymers arrive at the pore with highly elongated conformations due to strong forces outside the pore, they have time to be significantly compressed prior to threading due to the same strong outside forces and the weak forces inside the pore. For $C_{trans}/C_{cis} < 1$, polymers are not significantly elongated when arriving at the pore, nor are they significantly compressed due to the weaker *cis*-side forces

and stronger forces inside the pore. Note that there exists a value of C_{trans}/C_{cis} that naturally results in maximal elongation during translocation, by optimally balancing pre-stretching and compression. For the current experimental conditions, this value empirically occurs at a salt ratio slightly higher than 1, as demonstrated by the minimal σ/τ value of Figure 3.1.5c. This minimum in translocation time spread, surprisingly close to $C_{trans}/C_{cis} = 1$, corresponds to the optimized experimental condition under which molecules can be characterized and separated.

Finally, the concept of ASC conditions inducing less-elongated conformations is consistent with the observations from Figure 3.1.4a, where in fitting translocation times to Equations 3.1.2 and 3.1.4, we concluded that translocations in ASC conditions (C_{trans}/C_{cis} = 3.6 M / 0.9 M) were more pore-friction dominated than in SSC conditions (C_{trans}/C_{cis} = 0.9 M / 0.9 M), or equivalently that *cis*-side monomer friction was less dominant than in SSC. More elongated conformations are indeed expected to result in more significant *cis*-side monomer friction throughout the translocation steps *iv* and *v*.[70,177] This is simply due to more elongated conformations having more monomers under tension and in motion soon after translocation begins, with the limiting case being a completely stretched-out polymer with end monomers moving almost instantly as translocation begins. We therefore believe that the scaling coefficient reduction observed in ASC conditions is a direct consequence of polymers being less elongated prior to translocation.

3.1.10 Conclusion

We presented an extensive description of DNA capture and translocation dynamics through characterization of the dependence of capture rate, translocation time statistics, and folding kinetics (shown in Section S3.2.5 of the SI), on voltage, polymer length, and salt concentration gradient.

We showed that the underlying physics describing the transport process in asymmetric salt concentration (ASC) conditions is the same as in symmetric salt concentrations (SSC). The barrier- and diffusion-limited capture regimes combined with tension propagation principles fully describe the capture and translocation process. The promotions of diffusion- or barrier-limited regimes in capture-promoting or –opposing ASC conditions respectively demonstrated that the *cis*-side electric field plays a crucial role in determining capture kinetics. The higher order statistics of translocation time distributions further confirmed experimentally that non uniform forces outside the pore are responsible for elongating and compressing polymers before and after reaching the pore mouth, respectively.

This work confirmed the previously published conclusions[56,91,159–164] that detecting molecules from the low salt-concentration side of a salt gradient increases capture rate, slows down translocation, and increases the signal-to-noise ratio through deeper blockage depths (latter not shown). Although these are ideal features for nanopore sensing, we also observed an increase in the spread of the translocation times (Figure 3.1.5a), an increase in the percentage of folded translocations (Figure S3.2.5 of the SI), and significantly more frequent pore clogs when working in capture-promoting ASC conditions. The increased folding and translocation time spread can be undesirable for applications requiring single-file passage, such as DNA-carrier-based bioassays and data storage applications which require mapping with the highest precision objects bound to linear polymers. The biggest drawback however to ASC conditions may probably be the likelihood of permanent pore clogs, occurring more frequently than in symmetric conditions, and therefore significantly reducing the lifespan and usability of nanopores. For asymmetric salt concentration conditions to be of practical use in different applications, this issue should be addressed, possibly

by employing different coating strategies and types of surface chemistries[180,181] to control polymer-pore interactions.

Finally, we hope that our results will provide motivation for further theoretical work on the capture and translocation processes. We believe that consideration of the electric field outside the pore and its role in elongating and compressing polymers should help bridge theoretical and experimental efforts. Namely, elucidating the impact of field-induced polymer conformations on the translocation time scaling with polymer length will help develop a thorough understanding of the nanopore transport process, which will be essential in guiding development of nanopore-based applications in numerous critical fields.

3.1.11. Methods

Nanopore Fabrication. Nanopores were fabricated in 10 nm thick SiN membranes purchased from Norcada Inc. (NBPX5004Z-60O-Hi RES) using controlled breakdown, following the protocols and procedures outlined in detail in Waugh *et al* [22]. Concisely, pores were fabricated in 1 M KCl pH 8 using a linear voltage ramp, followed by conditioning to enlarge using 3 second 3 V pulses in 3.6 M LiCl pH 8, until the desired pore size was reached [38].

DNA Translocation Experiments. Ionic current traces were sampled using a Chimera VC100 at 4.167 MHz. After establishing a difference in salt concentration across the nanopore, a minimum of 30 minutes was allowed to elapse before applying a voltage and recording translocation events, to ensure a time-independent I-V curve (see Section S3.2.9 of the SI), which we attribute to the ζ-potential of the pore walls and the ion distribution inside the pore reaching a steady state.[182,183] For all measurements, the voltage was adjusted in order to zero the current, therein nulling the effects of Nernst potentials, and of diffusio-osmosis[98] induced by a salinity gradient. The current signal is

recorded for 10-15 minutes depending on the observed capture rate with the aim of collecting at least 300 events. During the experiment, a zapping function was enabled which inverted the bias polarity for 3 seconds if the open pore conductance decreased by > 5% its original value indicating undesired clogging of the pore. Data acquired during zapping was ignored for analysis. DNA concentrations were ascertained using a spectrophotometer (Biotek Epoch 2). For experiments on a single pore, for which multiple voltages or DNA lengths were sampled, the experiment order was randomized as to not have time-dependent pore characteristics (e.g. growth) be responsible for changes in capture and translocation kinetics, instead of the varying voltage or DNA length. It should also be noted that only pores with stable conductance baselines (±5% change within experiments) were used.

Data Analysis. Current trace data is analyzed using a custom implementation of the CUSUM+ and adept2state algorithms (see https://github.com/shadowk29/CUSUM)[184]. Since capture inherently obeys Poisson process statistics, capture rates are extracted by fitting the histogram of the logarithm of inter-event times to the log-transform of the Poisson distribution function. A detailed description of the accuracy of this capture rate fitting method and other similar methods in different experimental conditions is provided in our previous work[54]. The mean translocation time of unfolded DNA and its standard deviation are extracted from experimental data in one of two ways: 1) Since unfolded translocation times are sufficiently well described by a log-normal distribution, a Gaussian fit is applied to the histogram of the logarithm of the translocation times, provided enough unfolded translocations are observed. The mean and standard deviation of translocation times are then calculated using well-known lognormal properties; 2) Since asymmetric salts significantly promotes folded translocations (see Figure S3.2.5 in the SI), large sample sizes of unfolded events can be difficult to obtain. In such cases, we define the effective

translocation time τ_{eff} to be the ratio of the equivalent charge deficit (ECD) and the single dsDNA blockage level. Here, ECD denotes the integral of the ionic blockage with respect to the open-pore baseline. This approach mathematically unravels the blockage trace and can be used to faithfully increase the sample size of the mean unfolded translocation time. Section S3.2.6 of the SI validates this second method by demonstrating that both methods quantitatively agree on the standard deviation of the translocation time distribution of a highly populated data set.

3.2 Supporting Information for Section 3.1

S3.2.1. Non-linearity of Salt-concentration and Conductivity

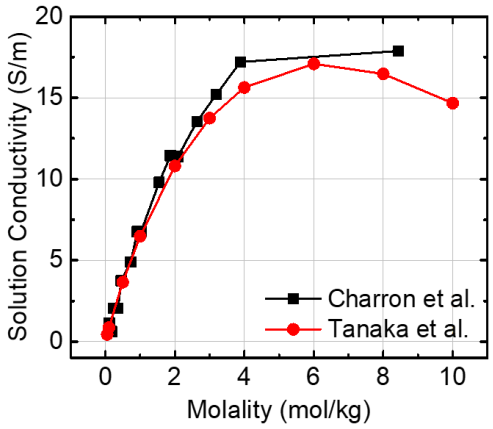

Figure S3.2.1. **LiCl conductivity as a function of molality** (i.e. moles of solute / kg of solvent). The 10 mM HEPES buffer present was neglected in the molality calculation. Material densities are $\rho_{LiCl} = 2.07\ g/cm^3$, $\rho_{H_2O} = 1\ g/cm^3$ at room temperature.

In the main text, we presumed that $\sigma_{trans}/\sigma_{cis} \approx C_{trans}/C_{cis}$, i.e. that salt concentration and conductivity are linearly related. We know from previous studies however that this only holds for low salt concentrations, where ion-ion interactions are negligible. To establish that conductivity-concentration linearity is a fair approximation for the experimental conditions used in this work, we measured the electrical conductivity of different concentrations of LiCl solutions buffered at pH 8 using 10 mM HEPES. Figure S3.2.1 shows the resulting conductivity measurements for concentrations (molality) ranging from 0.1125 M LiCl to 7.2 M LiCl, overlayed with previous measurements obtained by Tanaka *et al*.[174] The conductivity is seen to increase monotonically for concentrations up to 3.6 M LiCl. The conductivity measurements level off for C > 3.6 M LiCl. Our data replicates the same non-linear and non-monotonic trend at higher salt concentrations as observed by Tanaka *et al*. Given that 3.6 M LiCl corresponds to 3.89 mol/kg, and that most experiments were conducted in concentrations at most of 3.6 M LiCl, the data from Figure S3.1.1 suggest that the linear approximation of σ and C is good enough for LiCl concentrations used in

this work. From this, we imply that using either $\sigma_{trans}/\sigma_{cis}$ or C_{trans}/C_{cis} as a metric should not change the conclusion of the experiments shown.

S3.2.2. Regime-Dependent Capture Enhancement – Salt Concentration Ratio Dependence

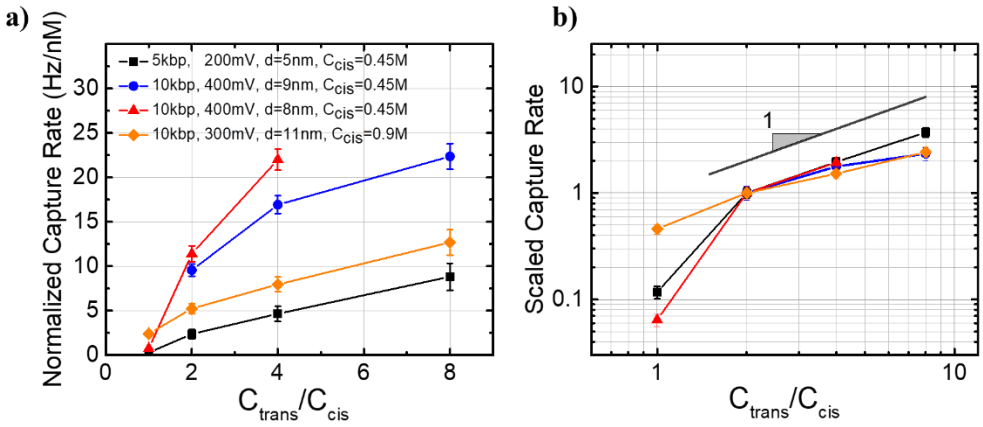

Figure S3.2.2. Modulation of capture rate in ASC conditions. **a)** Normalized capture rate vs salt concentration ratio for different experimental conditions (see legend). **b)** Same capture rates data as a) on log-log scales, and scaled such that the C_{trans}/C_{cis} = 2 measurements of each curve be 1.

In Figure 3.1.3b of the main article, we show that capture rate increases super-linearly with C_{trans}/C_{cis} for smaller salt concentration ratios and linear for larger ratios. To further support this, we show the dependence of capture rate on salt concentration ratio C_{trans}/C_{cis} acquired on four different pores, in four different experimental conditions: Pore 1 (d = 5 nm, N = 5 kbp, ΔV = 200 mV, C_{cis} = 0.45 M), Pore 2 (d = 8 nm, N = 10 kbp, ΔV = 400 mV, C_{cis} = 0.45 M), Pore 3 (d = 9 nm, N = 10 kbp, ΔV = 400 mV, C_{cis} = 0.45 M) and Pore 4 (d = 11 nm, N = 10 kbp, ΔV = 300 mV, C_{cis} = 0.9 M). For each experiment, the capture rates for different C_{trans}/C_{cis} values were obtained by fixing C_{cis} and varying C_{trans}.

Figure S3.2.2a shows the capture rates measured for different C_{trans}/C_{cis} values, of the four different pores. The capture rates vary significantly from one experiment to another due to capture being highly sensitive to experimental conditions.[54] To remove these confounding effects, Figure S3.2.2b plots instead the scaled capture rates, where the data from each pore was scaled by its $C_{trans}/C_{cis} = 2$ measurement, so as to collapse the four different curves. Again, for high salt gradients ($C_{trans}/C_{cis} \geq 2$), a slope of ≈ 1 is observed, indicating a linear dependence of capture rate on salt gradient ($R \propto C_{trans}/C_{cis}$), whereas for smaller salt gradients, super-linear trends are observed, with slopes differing between differing experiments. It is worth noting that the orange diamond data was acquired from 10 kbp dsDNA translocating through a 11 nm pore, two conditions (longer polymer, larger pore diameter) promoting the diffusion-limited capture regime, and that it has the less steep capture enhancement in going from $C_{trans}/C_{cis} = 1$ to 2. The slope for $C_{trans}/C_{cis} < 2$ therefore probably depends on how closely an experiment is to the barrier-diffusion regime transition. More data would be required however to confirm this.

S3.2.3. Regime-Dependent Capture Enhancement - DNA Nanostructures

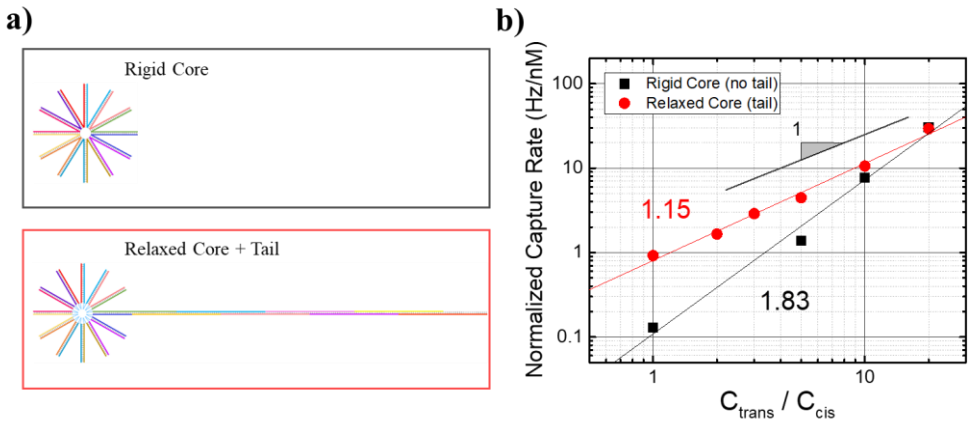

Figure S3.2.3. **Salt-gradient dependence of DNA nanostructure capture. a)** Schematics of the DNA nanostructures. **b)** Capture rate of DNA nanostructures in ASC conditions. The relaxed core DNA nanostructure with no tail experiences diffusion-limited capture (exponent ~ 1) while the non-relaxed core DNA nanostructure with a tail experiences barrier-limited capture (exponent > 1).

In the main text, we discuss that the capture rate enhancement due to asymmetric salt concentrations is regime-dependent, wherein the diffusion-limited capture regime results in linear capture enhancements and the barrier-limited capture regime results in super-linear enhancements. Here, to further support regime-dependent enhancement, we measure the capture rate of two DNA nanostructures in various salt gradients. To probe the two capture regimes, we rely on having two similar nanostructures with different intrinsic rigidities.

A complete description of the DNA nanostructures, including sequence information and assembly protocols based on Wang *et al.*[185] can be found in our previous work.[175] The important common feature to both types of nanostructures is that they are both star-shaped with twelve 25 nt long dsDNA arms, each pair of adjacent arms share the same 50 nt oligo.[175] The first type of DNA nanostructure has twelve 25bp dsDNA arms connected by semi-flexible dsDNA hairpins, partially hybridized to the adjacent arms on either side. Due to the semi-flexible nature of the connections,

we will refer to this structure as the rigid core structure. The second type of DNA nanostructure is also hybridized by twelve 50 nt oligos, but each with an additional flexible internal hexa-ethyleneglycol spacer. Additionally, the nanostructure also has a 175 bp dsDNA extension (tail) built onto one of the arms as shown in Figure S3.2.3a. Due to its flexible connections, we will refer to this structure as the relaxed-core structure.

Figure S3.2.3b plots the capture rate of both structures measured in salt concentration ratios ranging from C_{trans}/C_{cis} = 1 to 20, measured on a 9.0 nm pore, under a 200 mV bias, with a fixed C_{trans} = 3.6M LiCl and varying C_{cis}. As expected, both capture rates increase monotonically with salt gradients, however their enhancement rate differ significantly. Both data sets are well described by power scalings of capture rate and salt gradient, as demonstrated by the linear trends observed on the logarithmic plots. The rigid-core structure demonstrates a super-linear dependence on salt gradients, with $J_{rigid} \sim (C_{trans}/C_{cis})^{1.83 \pm 0.43}$, whereas the relaxed core shows $J_{relaxed} \sim (C_{trans}/C_{cis})^{1.15 \pm 0.12}$, a scaling closer to linear, as expected from diffusion-limited capture. Due to the relaxed-core structure having a more flexible core and an elongated tail, we would expect the height of its energy-barrier to be lower than the one for the rigid-core structure. Since reduction of the free energy barrier is expected to promote diffusion-limited regime, we believe this again demonstrates that capture enhancement is regime dependent, where the rigid-structure is in the barrier-limited regime, and the relaxed-core is in the diffusion-limited regime.

S3.2.4. Translocation Time vs DNA Length Fits

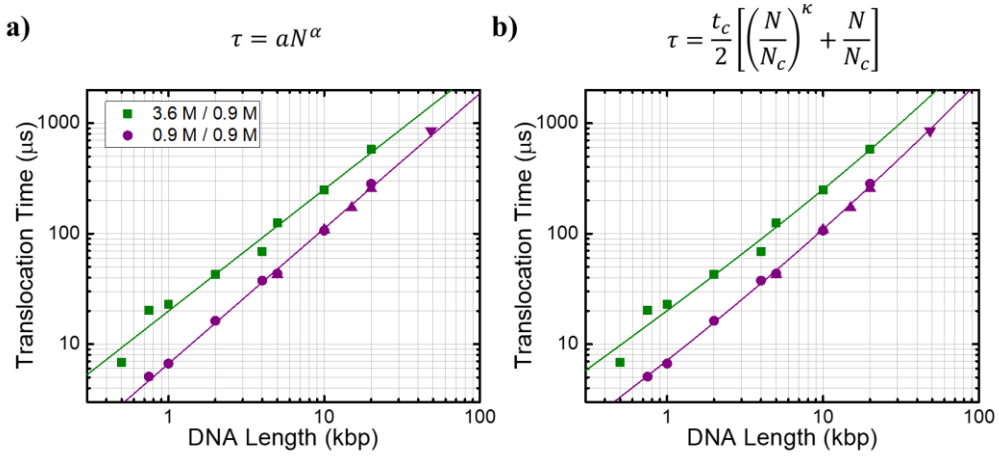

Figure S3.2.4. Fits of translocation time vs DNA length using **a)** a power scaling (Equation 3.1.2 from main text) and **b)** Iso-Flux Tension Propagation (IFTP) dual scaling (Equation 3.1.4 from main text).

S3.2.5. Folding Probability in ASC conditions

To extensively describe translocation dynamics in ASC conditions, we now report the dependence of the folding probability on the salt concentration ratio C_{trans}/C_{cis}, DNA length and applied voltage. The folding probability here is simply calculated as the ratio of the number of folded events to the total number of events, i.e. N_{fold}/N_{tot}. A translocation event is deemed a folded event if any of its fitted blockage levels corresponds to a multiple of the current blockage expected from single-file translocations. Note that the measurement uncertainties were calculated by using error propagation and assuming Poisson errors on individual counts, i.e. $\delta N_{fold} = \sqrt{N_{fold}}$.

To determine the dependence of the folded fraction on salt concentration ratio in asymmetric salt conditions, we used the data acquired for Figure 3.1.5 of the main article in which 10 kbp dsDNA passed through a 6 nm pore under a 300 mV bias, with a fixed *cis*-side concentration of 1.8 M LiCl and a *trans*-side concentration varying from 0.9 M to 3.6 M LiCl. Figure S3.2.5a plots the folded fraction of the different concentration gradients, from which it can be seen that the folded fraction grows monotonically with the salt gradient, in a sigmoidal-like fashion.

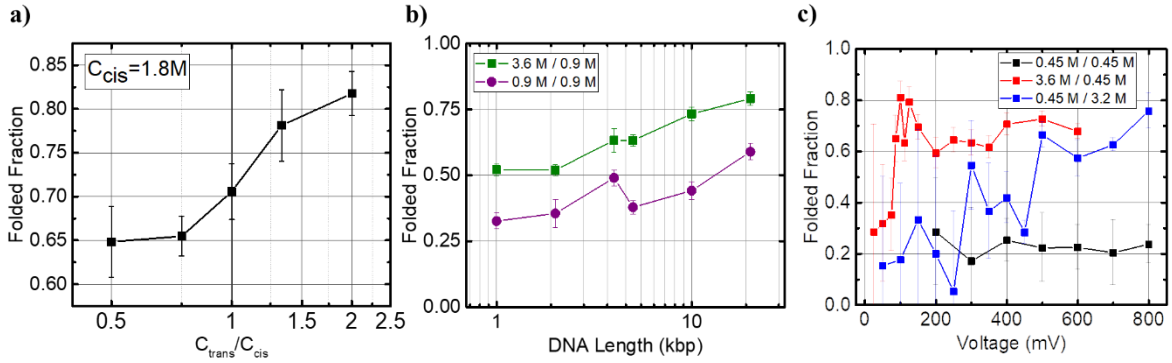

Figure S3.2.5. Folding Kinetics in ASC conditions. a) Fraction of unfolded events observed as a function of salt concentration ratios C_{trans}/C_{cis},with varying C_{trans} and fixed C_{cis} = 1.8 M. d_{pore} = 6.0 nm, ΔV = 300 mV, N = 10 kbp. **b)** Fraction of folded translocation events as a function of DNA length for SSC conditions (0.9 M LiCl, purple), and 4x capture-promoting ASC conditions (3.6 M / 0.9 M, green). d_{pore} = 8.5, ΔV = 400mV. **c)** Fraction of folded 10 kbp dsDNA translocation events as a function of applied voltage in a 5.3 nm pore for SSC (0.45 M LiCl, black), capture-promoting ASC (3.6 M / 0.45 M LiCl, red), and capture opposing ASC (0.45 M / 3.2 M LiCl, blue) conditions.

To determine the dependence of the folded fraction on the DNA length in ASC conditions, we used the data acquired for Figures 3.1.2h and 3.1.4c of the main article, in which a 8.5 nm pore was used to translocate different lengths (500 bp – 48 kbp) of dsDNA under a 400 mV bias in SSC (C_{trans}/C_{cis} = 0.9 M / 0.9 M) and capture-promoting ASC (C_{trans}/C_{cis} = 3.6 M / 0.9 M) conditions. Figure S3.2.5b plots the folded fraction measured for different lengths of dsDNA for both ASC (green) and SSC (purple) conditions. Both salt conditions demonstrate the same qualitative trend

in which the folded fraction increases monotonically with DNA length, as expected. Interestingly, the folded fractions measured in capture-promoting asymmetric conditions are consistently larger than symmetric conditions, by an amount of ~20-25%, consistent with Figure S3.2.5a.

Finally, to investigate the folding dependence on voltage, we used the data acquired for Figures 3.1.2e-g and 3.1.4a-b of the main article, for which 10 kbp dsDNA was run through a 5.3 nm pore in capture-promoting ASC (C_{trans}/C_{cis} = 3.6 M / 0.45 M), capture-opposing ASC (C_{trans}/C_{cis} = 0.45 M / 3.2 M) and SSC (C_{trans}/C_{cis} = 0.45 M / 0.45 M) conditions with applied voltages ranging from 50 mV – 600 mV. Figure S3.2.5c shows the measured folded fraction of the three salt conditions for all measured voltages. The capture-promoting ASC conditions (red) show a monotonically increasing folded fraction for voltages smaller than 150 mV, and a constant folded fraction of ≈ 0.7 for higher voltages. The capture-opposing ASC conditions (blue) shows an increasing folding fraction with increasing voltage for the entire range investigated. SSC conditions (black) shows a constant folded fraction of ≈ 0.2 for the entire voltage range studied. Interestingly, the folded fractions in capture-promoting or capture-opposing conditions are both larger than in symmetric conditions for $\Delta V > 300$ mV.

One should note that the observations shown here regarding the folded translocation fraction are qualitatively of the same nature as those shown for the translocation time. Both translocation time and folded fraction increase monotonically with salt gradient when keeping C_{cis} fixed, whereas both translocation time and folded fraction are highest when DNA is being captured from either side of ASC conditions, when compared to the SSC conditions. Because the SSC condition used here is achieved using 0.45 M LiCl, the lowest salt concentration of a salt gradient, we believe that Figures S3.2.5a-c indicate that the different folding fraction in ASC conditions are most likely a result of the local salt concentration in the vicinity of the pore changing the

persistence length of DNA, and therefore changing its bending energy. Higher effective salt concentrations result in smaller persistence lengths and therefore could be expected to increase folding, consistent with Figures S3.2.5a-c.

S3.2.6. Comparing Translocation Time Standard Deviation Measurements

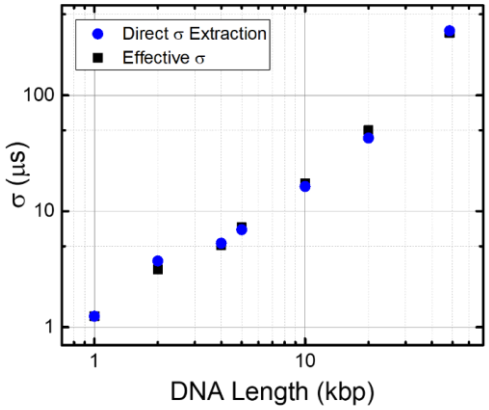

Figure S3.2.6. Comparison of translocation time statistics extraction methods. Blue circles and black squares show the translocation time standard deviations extracted using only the single-file translocations, and using Equation S3.2.1, respectively.

Since asymmetric salt conditions promote folded translocations, not all data collected contained a sufficiently high number of unfolded translocations, required for fitting lognormal functions to translocation time distributions in order to extract the expected translocation time and standard deviations. To overcome this issue, we instead used both the folded and unfolded events and defined an effective translocation time to be the ratio of the ECD, i.e. the integral of the current trace with respect to the baseline, and the blockage depth of a single dsDNA strand, ΔI_1:

$$\tau_{eff} = \frac{ECD}{\Delta I_1} \,. \tag{S3.2.1}$$

To determine whether this is a decent approximation of an unfolded event's translocation time τ or not, we compared the standard deviations σ extracted directly from unfolded events or

using the effective method described above. For a good comparison, we used a data set containing many unfolded events from which we can confidently extract σ using the direct method. Figure S3.2.6 shows the σ values extracted from the direct and effective methods, for the data presented in Figure S3.2.6, for which a range of dsDNA lengths (1 kbp – 48 kbp) ran through an 8.5 nm pore, under a bias of 400 mV in SSC 0.9 M LiCl conditions. As Figure S3.2.6 shows, both methods result in almost identical values of σ. It should be noted that whenever this effective extraction method is used instead of the direct method involving unfolded events, we make sure to label graph axes as "Effective σ" or "Effective τ".

S3.2.7. Higher Order Translocation Time Statistics in ASC Conditions

In the main text, we show that ASC conditions increase the translocation time distributions' standard deviation σ and coefficient of variation σ/τ for both capture-opposing and capture-promoting asymmetric conditions. Here, to complement these observations, we report length-dependence of both σ and σ/τ using the data from presented in 4a of the main article. The experiments were run in a 8.5 nm pore, under a bias of 400 mV in SSC conditions (C_{trans}/C_{cis} = 0.9 M/0.9 M) and capture-promoting ASC conditions (C_{trans}/C_{cis} = 3.6 M/0.9 M).

Figure S3.2.7b shows the extracted values of σ for different dsDNA lengths ranging from 500 bp to 48 kbp. The translocation time standard deviation of each condition monotonically increases with polymer length, with the ASC measurements being consistently ≈ 3-fold higher than SSC conditions. Since standard deviation is expected to be higher for longer translocation times, the fact that both longer polymers and asymmetric conditions result in longer variance comes as no surprise.

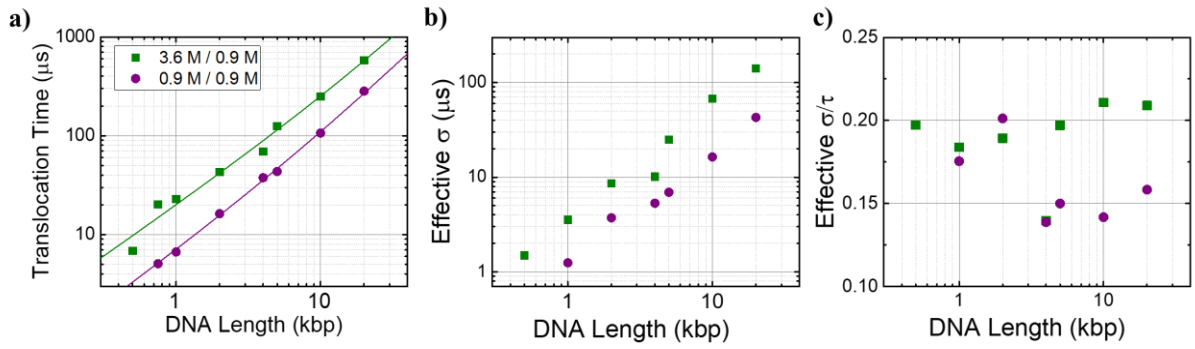

Figure S3.2.7. **Translocation time distribution statistics.** Translocation time statistics of 4x capture-promoting ASC conditions (green) vs SSC conditions (purple) measured for different dsDNA lengths: **a)** Mean translocation time; **b)** Translocation time standard deviation; **c)** Coefficient of variation, σ/τ.

The more interesting metric is then the σ/τ , which normalizes out translocation times, as shown in Figure S3.2.7c. Note first that the measured values of σ/τ are consistent with those measured in Figure 3.1.5c of the main article for both conditions. Interestingly, for longer strands (N $\geq$ 4 kbp) σ/τ values measured in ASC conditions are consistently higher than in SSC conditions. For shorter strands (N < 4 kbp), Figure S3.2.7c shows that smaller DNA strands (N $\leq$ 4kbp) have similar σ/τ values measured in ASC and SSC conditions. This observation is in line with the conclusion outlined in the main article, stating that ASC conditions promote less elongated polymer conformation. Indeed, we expect modulations in conformational entropy to affect longer strands more significantly than shorter ones, due to limited conformations inflicted by their short size.

S3.2.8. I-V Stabilization in ASC conditions

Although only low-noise nanopores demonstrating linear current-voltage (I-V) curves in symmetric 3.6 M LiCl were used for experiments, it was observed that the I-V response was changing over time when changing the salt concentrations from symmetric to asymmetric, sometimes demonstrating significant rectification. Without extensively characterizing the

phenomena, we wanted to roughly determine how long one should wait after changing salt conditions to initiate a current recording in order for the results to be reproducible.

Figure S3.2.8 shows the I-V responses of a 12 nm nanopore initially immersed in symmetric 3.6 M LiCl, upon introducing a 0.45 M LiCl solution on the grounded fluid side. I-V curves were repeatedly measured every three minutes and were stopped once I-V measurement were unchanging with time. In the initial symmetric 3.6 M LiCl measurement, the I-V measurement shows no rectification, whereas I-V responses show significant rectification in asymmetric conditions. pore showed in Figure S3.2.8 took 30 minutes to stabilize. Similar experiments were performed with different initial and final salt conditions (see Table S3.2.1).

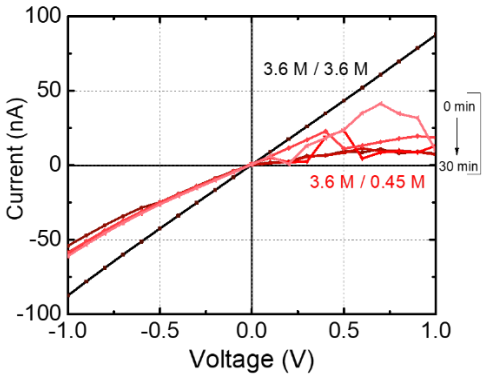

Figure S3.2.8. **IV stabilization after changing salt concentrations.** I-V curves were measured every 3 min for $C_{applied}$ /C_{ground} = 8 using a $d = 12 \pm 1$ nm pore. After 30 mins the I-V curve was rectifying and stable. Then, the asymmetric salt condition was replaced with 3.6 M symmetric LiCl and the I-V curve was observed to be immediately stable and non-rectifying.

Using the same pore, we measured the stabilization times when transitioning from different salt conditions, as summarized in Table S3.2.1. Generally, transitioning from symmetric salt to asymmetric salt took significant time before the I-V curve became stable, with the maximum stabilization time being 30 minutes from 3.6 M / 3.6 M to 0.45 M / 3.6 M LiCl. In contrast, I-V stabilization was instantaneous when the final salt condition was symmetric 3.6 M LiCl. From

these simple results, we determined that we would wait 30 minutes before recording DNA translocation data in salt asymmetry. The stability of the baseline current was also verified before any experiment, in order to confirm the I-V stabilization.

Table S3.2.1: **Transient Response Times for Various Salt Conditions**

Initial Salt Condition (C_{ground} [M]/$C_{applied}$ [M])	**Final Salt Condition (C_{ground} [M]/$C_{applied}$ [M])**	**Approximate I-V Stabilization Time [min]**
3.6/3.6	0.45/3.6	30
0.45/3.6	3.6/3.6	0
3.6/3.6	0.225/3.6	10
0.225/3.6	3.6/3.6	0
3.6/3.6	0.113/3.6	10
0.113/3.6	3.6/3.6	0
3.6/3.6	0.056/3.6	10
0.056/3.6	3.6/3.6	0

3.3 Additional Comment: Modeling Pore Conductance under Salt Gradients

The work of this chapter focused on the dynamics of nanopore capture and translocation, and as such the subject of nanopore conductance under salt asymmetry was not addressed. This is mainly due to the completion of this project occurring prior to the development of the conductance modeling technique of Chapter 2. Although not pursued thoroughly due to time limitations, I now describe preliminary ideas demonstrating that the conductance of pores under asymmetric salt conditions can be well estimated by the oblate spheroidal modeling technique of Chapter 2.

Consider a 2D pore separating two reservoirs with different salt concentrations c_{cis} and c_{trans}. For infinitely large reservoirs, a steady state is achieved wherein the local salt concentration smoothly varies between one reservoir to the other. Under no applied voltage, an expression for the concentration profile c can be found by solving the steady-state diffusion equation:

$$\nabla^2 c = 0\,. \tag{3.3.1}$$

Because of symmetry, the concentration at the pore disk and at the infinitely large hemispheres are expected to be uniform, as such oblate spheroidal coordinates are good candidates to solve Equation 3.3.1, resulting in:

$$c(\mu) = \frac{c_{cis} - c_{trans}}{\pi}\tan^{-1}(\sinh\mu) + \frac{c_{trans} + c_{cis}}{2} = \frac{\Delta V}{\pi}\tan^{-1}(\sinh\mu) + \bar{c}\,. \tag{3.3.2}$$

To find the resistance of the 2D pore under salt gradients, two assumptions are required. First, the concentration profile is assumed to be unaffected by the applied voltage, which is a reasonable approximation for smaller applied voltages. Moreover, the local solution conductivity $\sigma(\mu)$ is assumed to be proportional to the local salt concentration $c(\mu)$, i.e. $\sigma(\mu) = \Sigma c(\mu)$, which typically holds for salt concentrations low enough to avoid inter-molecular ionic mobilities.

Following the oblate spheroidal modeling technique of Chapter 2, the resistance of a 2D pore of radius r_p under salt gradients in its open state is found to be:

$$\begin{aligned} R_{2D} &= \frac{1}{2\pi r_p}\int_{-\infty}^{\infty}\frac{d\mu}{\sigma(\mu)\cosh\mu} \\ &= \frac{1}{2\pi\Sigma r_p}\int_{-\infty}^{\infty}\frac{1}{\cosh\mu}\frac{d\mu}{\frac{\Delta c}{\pi}\tan^{-1}(\sinh\mu)+\bar{c}} \\ &= \frac{1}{2\pi\Sigma r_p}\left[\frac{\pi}{\Delta c}\ln\left(\frac{\Delta c}{\pi}\tan^{-1}(\sinh\mu)+\bar{c}\right)\right]_{-\infty}^{\infty} \\ R_{2D} &= \frac{1}{2\sigma_{cis} r_p}\frac{\ln\frac{c_{trans}}{c_{cis}}}{\frac{c_{trans}}{c_{cis}}-1}\,. \end{aligned} \tag{3.3.3}$$

When blocked by an infinitely long cylinder of radius r_c, the resistance of a 2D pore of radius r_p under salt gradients is found to be:

$$\begin{aligned} R_{2D}^{b} &= \frac{1}{2\pi r_p}\int_{-\infty}^{\infty}\frac{\operatorname{sech}\mu\, d\mu}{\sigma(\mu)\sqrt{1-\frac{r_c^2}{r_p^2}\operatorname{sech}^2\mu}} \\ &= \frac{1}{2\pi\Sigma r_p}\int_{-\infty}^{\infty}\frac{\operatorname{sech}\mu\, d\mu}{\left(\frac{\Delta c}{\pi}\tan^{-1}(\sinh\mu)+\bar{c}\right)\sqrt{1-\frac{r_c^2}{r_p^2}\frac{1}{\cosh^2\mu}}} \\ R_{2D}^{b} &= \frac{1}{2\pi s c_{cis} r_p}\int_{0}^{\pi}\frac{d\theta}{\left(1-\frac{\Delta c}{c_{cis}\pi}\theta\right)\sqrt{1-\frac{r_c^2}{r_p^2}\sin^2\theta}}\,. \end{aligned} \tag{3.3.4}$$

The final expression of Equation 3.3.4 was obtained through a variable substitution, $\tanh\mu = \cos\theta$, and presents no closed form solution; however, an expression can be found for the limiting conditions of small concentration gradients, $\Delta c/\pi c_{cis} \ll 1$, and small cylinders, $r_c \ll r_p$:

$$R_{2D}^{b} \approx \frac{1}{2s c_{cis} r_p}\left(1+\frac{1}{4}\frac{r_c^2}{r_p^2}\right)\left(1+\frac{1}{2}\frac{\Delta c}{c_{cis}}\right)\,. \tag{3.3.5}$$

Interestingly, given the similarities between concentration c and electric potential V profiles, this framework can be extended to finite length pores, where the access regions and the pore region are considered separately. Conductance expressions can be achieved by assuming that the relative potential drops across the pore and access regions are equal to those of the concentration profile, i.e. $\Delta V_{acc}/\Delta V = \Delta c_{acc}/\Delta c$ and $\Delta V_{pore}/\Delta V = \Delta c_{pore}/\Delta c$. Although the solutions are not shown here, the manipulations are only slightly more involved than Equations 3.3.1-3.3.5 and result in closed form solutions for the open-pore state.

Chapter 4. Translocation Velocity Measurements

This chapter contains a submitted manuscript titled “Velocity fluctuation and force scaling during driven polymer transport through a nanopore” and authored by Martin Charron, Breeana Elliott, Nada Kerrouri, Liqun He and Vincent Tabard-Cossa.* The corresponding Supporting Information is provided in Section 4.2.

* Reprinted from [Charron, M., Elliott, B., Kerrouri, N., He, L. and Tabard-Cossa, V., 2024. Velocity fluctuation and force scaling during driven polymer transport through a nanopore. *arXiv preprint arXiv:2411.04261*.].

4.1 Investigation of Forces Governing Polymer Transport through Nanopores using patterned DNA structures

Martin Charron, Breeana Elliott, Nada Kerrouri, Liqun He, Vincent Tabard-Cossa

Abstract

Inspired by its central role in many biological processes, the transport of biopolymers across nanoscale pores is at the heart of a single-molecule sensing technology aimed at nucleic acid and protein sequencing, as well as biomarker detection. When electrophoretically driven through a pore by an electric potential gradient, a translocating polymer hinders the flow of ions, and thus can be detected by a transient current blockade, the characteristics of which can be mapped to physicochemical properties of the polymer. Although investigated theoretically and by simulations, few experimental studies have attempted to validate the predicted transport properties, mainly due to the complex nature of the non-equilibrium translocation process. Here, we elucidate these fundamental concepts by constructing a patterned DNA nanostructure whose current signatures allow estimating the instantaneous velocity throughout the translocation process. With simple physical insights from polymer and fluid dynamics, we show how the resulting molecular velocity profiles can be used to investigate the nanoscale forces at play and their dependence on experimental parameters such as polymer length, pore size and voltage. The results presented allow at last testing of theoretical models and outline their limitations. In addition to bridging experiment and theory, this work aims to clearly characterize and describe velocity fluctuations during passage to assist researchers in designing nanopore experiments with optimized sensing performance.

4.1.1. Introduction

The passage of polymers through pores is a ubiquitous process observed in cellular systems, often driven by salinity or osmotic pressure gradients. When driven by an electric potential gradient, the electrophoretic passage of polymers can be identified and characterized by monitoring transient ionic current blockages due to the polymers impeding the flow of ions through the channel.[4] This principle is at the core of many highly successful applications and exciting research endeavors including nucleic acid sequencing, biomarker detection, and more recently protein fingerprinting and synthetic polymer decoding.[1–3] Although studied theoretically and through simulations,[68–72,87,165,166,186] the physics of driven polymer translocations has yet to be extensively characterized experimentally, mostly due to its highly non-equilibrium nature: Under voltages commonly used for sensing (50 – 1000 mV), translocation times of DNA have been consistently reported to be significantly smaller than their corresponding relaxation times.[67] At any instant during the process, the polymer is thus in a conformation that differs significantly from ones adopted when relaxed in the bulk solution.

Thus far, the kinetics of electrophoretically driven polymer passages through nanopores have been studied experimentally by reporting the dependence of polymer translocation durations on the applied voltage, polymer length, pore dimension, and other experimental parameters such as bulk salt concentration and viscosity.[30,73,92,96,187–189] Additionally, electrohydrodynamic forces in nanopore systems have been measured through the use of optical tweezers inserting and stalling DNA inside nanopores under an applied voltage.[101–105] Although rich in information, such measurements of the total translocation durations and forces under fixed polymer conformations fail to elucidate the time-dependent forces and velocities expected from the non-equilibrium process described by theory and simulations.[68–72,87,165,166,186] To this end, recent experimental

works have made use of nanostructured DNA molecules to estimate the instantaneous velocity throughout the translocation process.[67,97,100] In particular, Chen *et al*. showed that driven polymer translocations are a two-step process, wherein polymers initially slow down before accelerating towards the end of their passage,[67] in qualitative agreement with the principles of Tension Propagation introduced by Saito and Sakaue[68].

In this work, we go beyond the qualitative observation of the translocation velocity profiles of previous experimental studies,[67,97,100] and provide a detailed quantitative report on the dependence on experimental parameters, including polymer length L, pore diameter d_{pore} and applied voltage ΔV, of high practical value for the operation of many sensing schemes. These measurements employ DNA nanostructures with interspaced domains of different cross-sectional areas, allowing precise experimental estimates of the instantaneous translocation velocity. In addition to demonstrating the origin of scalings between translocation time and L, d_{pore} and ΔV, our results characterize the underlying time-dependent forces imparted on translocating polymers. Comparison of our experimentally observed trends with predictions from Tension Propagation and fluid mechanics show good agreement, while also outlining shortcomings and limitations of these theoretical concepts. In parallel to bridging theory and experiment, by characterizing different metrics of velocity profiles we are able to provide answers to simple practical questions such as: How much does velocity fluctuate during translocation? Which polymer segment is inside the pore when the velocity is minimal? This knowledge provides great insights for anyone designing nanopore experiments with optimized sensing performance, whether to select the optimal pore dimensions, or for the architecture of a molecular probe or carrier. Finally, we also report a non-intuitive finding that translocation times increase in larger pores.

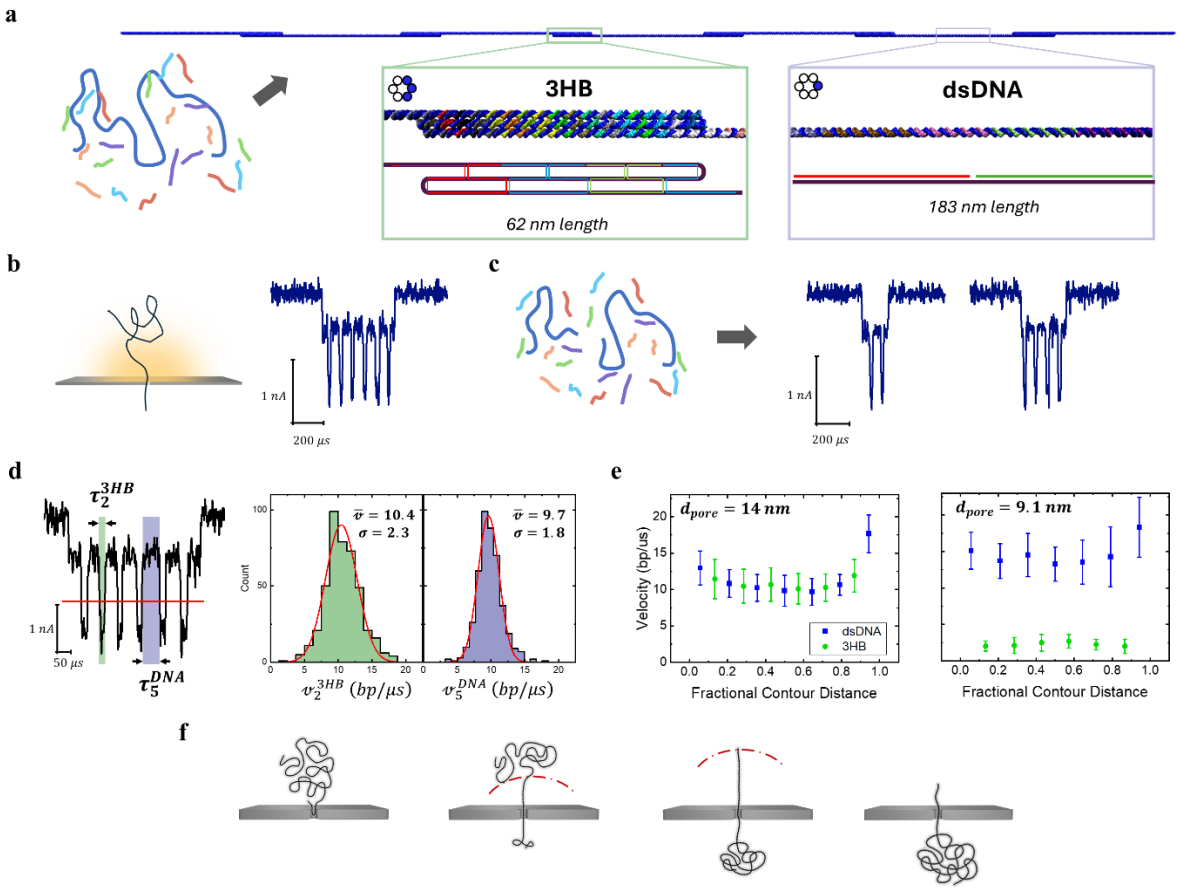

Figure 4.1.1. VPM assembly and analysis. a) Design for the Velocity Profiling Nanostructure (VPN), consisting of six 3-Helix Bundle (3HB) segments interspaced by seven dsDNA segments **b)** Signals of single-file passage of fully assembled VPN **c)** Signals of single-file translocations of partially assembled VPN. **d)** Demonstration of threshold-crossing algorithm used to obtain segment duration and velocity statistics. Velocity distributions of a 3HB and DNA segment are shown with corresponding gaussian fits, obtained from passages through a 14 nm pore. **e)** Translocation velocity profiles obtained from a 14 nm pore, and a 9.1 nm pore. Error bars correspond to the standard deviation of the fitted velocity distributions. **e)** Sketch of Tension Propagation (TP) occurring during translocation.

4.1.2. Nanostructure Design and Velocity Measurements

A patterned DNA nanostructure was designed with two differently sized repeating segments such that the current trace resulting from its passage through a nanopore would allow the estimation of the polymer's instantaneous translocation velocity. The Velocity Profiling Molecule (VPM) was assembled by mixing a 7292 nucleotide (nt) long single-stranded DNA

(ssDNA) scaffold (m13 phage) with 171 short ssDNA staples, resulting in a linear structure with thirteen interspaced domains: seven double-stranded (dsDNA) segments and six three-Helix Bundles (3HB) segments, the latter corresponding to the scaffold folded twice on itself, and thus to three dsDNA segments in parallel.[86,190] See Methods and Section S4.2.1 of the SI for more details on the assembly protocol, sequences, and exact segment dimensions. Due to their different cross-sectional areas and thus different induced current blockages, the passage of individual segments can be identified in the current trace produced by the single-file passage of a VPM through a nanopore (Figure 4.1.1b). As expected, the blockage amplitudes from 3HB segments ΔI_{3HB} are consistently observed to be three times deeper than those from the dsDNA spacers ΔI_{DNA}. The end-to-end length of VPMs was designed to be nearly exactly that of 5 kbp dsDNA. As such, 5 kbp dsDNA was passed through pores before VPMs as a control to ensure similar total translocation durations, thus confirming that the presence of 3HB segments did not appreciably affect the translocation dynamics. Note that we took advantage of the presence of fragmented m13 scaffolds in the assembly mixture resulting in VPMs of different lengths (Figure 4.1.1c) to study velocity profiles versus polymer length on the same pore. We also note that only single-file VPM translocations were analyzed for this work, although events where the polymer entered the pore not by an extremity but instead by bending somewhere along its contour length and folding inside, were commonly observed.[48]

To infer translocation velocities from individual event traces, a simple threshold-crossing algorithm was used, wherein a blockage threshold was set to a value between $2\Delta I_{DNA}$ and $3\Delta I_{DNA}$ away from the baseline, and times at which the current trace crosses the threshold either upwards or downwards were noted (Figure 4.1.1d). The passage duration τ_i of the i^{th} segment of a VPM could then be determined as the time interval between corresponding threshold crossing times of

the i^{th} sub-level in the current trace, with the event start and end times of the entire event used to delimit the first and last segments, respectively. Given the known length ℓ_i of the i^{th} segment, its translocation velocity was calculated as $v_i = \ell_i/\tau_i$, with units of $bp/\mu s$. Figure 4.1.1d shows the histogram of the velocities measured from multiple individual VPM translocations for the second 3HB and fifth dsDNA segments, v_2^{3HB} and v_5^{DNA}, measured in a 14 nm nanopore in 3.6 M LiCl under an applied voltage of 200 mV. By fitting each segment's velocity distribution to a Gaussian function, the mean velocity $\overline{v_i}$ and the standard deviation σ_i of the i^{th} segment velocity can be extracted. Figure 4.1.1e plots the mean translocation velocities calculated for each segment versus the segment center's location relative to the VPM's contour for a 14 nm and a 9 nm diameter nanopore ($\pm 1\,nm$). The magnitude of the velocity error bars corresponds to the segments' extracted σ values. Section S4.2.2 of the SI discusses the robustness of the analysis approach through its sensitivity to fitting parameters and methods.

Qualitatively, Figure 4.1.1e shows that the calculated velocity profiles are non-uniform, non-monotonic, and are consistent with prior experimental work:[67] After translocation begins from the *cis* side, the polymer decelerates until roughly its contour midpoint, after which it speeds up until fully exiting the pore on the *trans* side. Such velocity profiles are expected from tension propagation principles[68–72,186] stating that a polymer is not in equilibrium throughout its translocation process, and as such only monomers under tension are in motion and impart a hydrodynamic drag opposing the electrophoretic pulling force. Initially, as translocation progresses, the number of monomers under motion increases as the tension front progresses along the polymer contour. Once the tension front has reached the back end of the polymer however, its tail-end starts retracting towards the pore, and as such the number of monomers in motion starts to reduce over time.

The velocity profile for the 9 nm pore (Figure 4.1.1e) reveals the importance of pore-polymer interactions, and the quasi-static nature of the translocation process by showing 3HB segments moving significantly slower than dsDNA segments. This is not surprising, since their different cross-sectional areas results in 3HB segments interacting more strongly with the pore walls than the smaller DNA segments, and pores with similar diameters to translocating polymers are known to significantly slow down translocations times due to steric interactions.[30] Most pores used in this work are larger than 9.1 nm, and show similar velocity profiles for 3HB and dsDNA segments, as expected since both polymers were previously measured to have similar electrophoretic mobilities.[190] For readability, most velocity profiles plotted throughout this text do not include error bars (see Section S4.2.3 of the SI for profiles with error bars).

4.1.3. Polymer Length Dependence

We now describe the effects of polymer length on translocation velocity profiles measured using single-file translocations of VPMs of different lengths. Figure 4.1.2a shows current traces of VPM translocations through a 14 nm pore under a 200 mV bias in a 3.6M LiCl solution, wherein individual translocation events were classified according to the number of 3HB segments n_{3HB} detected per current trace. Figure 4.1.2b plots the normalized distributions of translocation times for each VPM population. Distributions were fit to log-normal functions from which the mean translocation time $\bar{\tau}_n$ of each population was obtained. Figure 4.1.2c shows the dependence of mean translocation time $\bar{\tau}_n$ on the effective polymer length L_n of each length of VPMs, which were calculated by assuming a single scaffold fragmentation occurred with equal probability along the scaffold contour, and thus along the dsDNA segments. For example, the average VPM length for n_{3HB} 3HB segments is thus:

$$L_n = (n_{3HB} + 0.5)L_{dsDNA} + n_{3HB}L_{3HB} \,. \tag{4.1.1}$$

where lengths L_{DNA} and L_{3HB}, are the lengths of the dsDNA and 3HB segments, respectively. The data of Figure 4.1.2c is well fitted by a power scaling function: $\bar{\tau}_n \propto L_n^{\alpha}$ with a power scaling coefficient of $\alpha = 1.21 \pm 0.01$. Such power scalings are commonly observed with dsDNA translocations through nanopores, with experimental coefficients ranging in value between 1.19 to 1.4.[54,73,75,188,189] We note that the 1.21 coefficient from VPMs is identical to the coefficients reported in prior publications for dsDNA measured on SiN nanopores fabricated by the control breakdown method.[54,74,188] This supports our hypothesis that these structured VPMs are adequate proxy molecules to study the effect of polymer lengths on translocation dynamics of dsDNA polymers.

Figure 4.1.2d plots the velocity profiles for each VPM length. All profiles share a similar two-step non-monotonic shape, as in Figure 4.1.1e. Interestingly, the initial and final velocities, v_{ini} and v_{end}, appear to be independent of polymer length as they are consistently measured to be $v_{ini} = 13.3\ bp/\mu s \pm 0.6\ bp/\mu s$ and $v_{end} = 17.6\ bp/\mu s \pm 0.2\ bp/\mu s$. The velocity profiles of the different VPM lengths however differ in how much they fluctuate throughout the passage: The minimal velocity achieved v_{min} is consistently measured to be lower for longer polymers. Moreover, the fractional location where the minimal velocity occurs, x_{min}, is consistently lower for shorter polymers. Without employing any physical insights yet, Figure 4.1.2d empirically demonstrates why the dependence of translocation time on polymer length shows a super-linear power scaling, ($\tau \sim L^{1.21}$ in this work). Although translocations of different polymer lengths begin and end at the same velocity, longer polymers simply slow down more importantly throughout the process than shorter ones. This is in contrast with a linear dependence, $\tau \sim L$, which would result in length-independent velocity profiles with identical v_{in}, v_{min} and v_{end}.

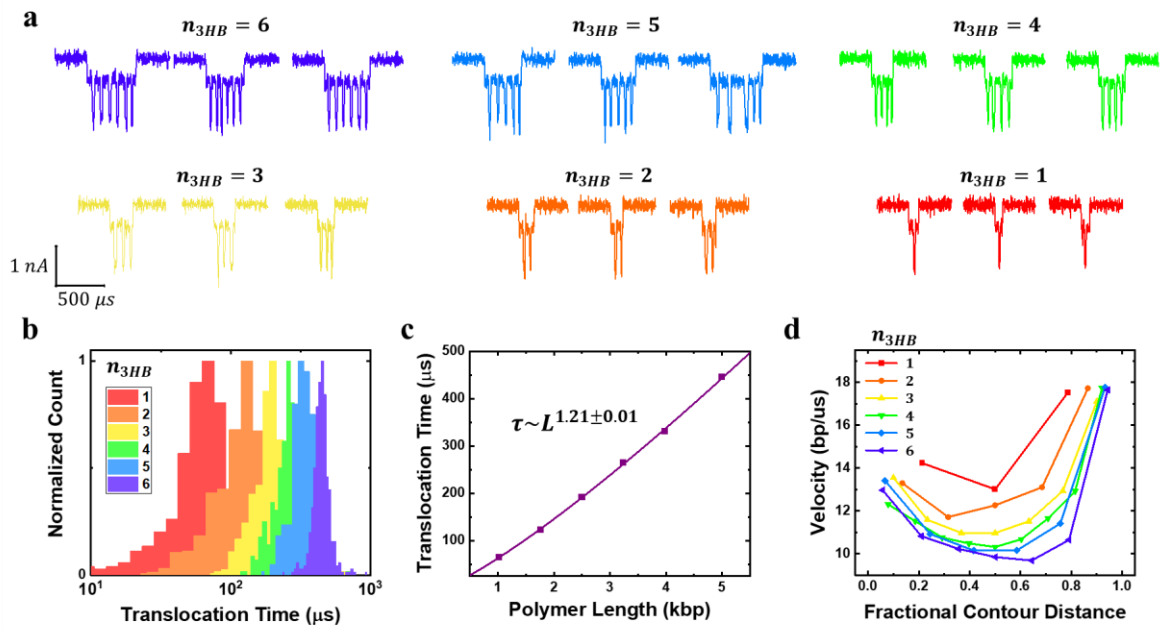

Figure 4.1.2. Effect of polymer length on translocation. a) Current traces of six different VPM lengths through a 14 nm SiN pore under a 200 mV bias in 3.6 M LiCl, 10 mM HEPES pH 8. Traces are classified by n_{3HB}, i.e. the number of detected 3HB segments. **b)** Translocation time distributions of VPMs of different lengths. **c)** Dependence of mean translocation time on VPM length L_n (Eq. 4.1.1). **d)** Extracted mean velocity profiles. Bump velocities are included for $n_{3HB} \leq 4$ for better spatial resolution.

4.1.4. Pore Size Dependence

We now describe the effects of pore size on translocation velocity profiles. Figure 4.1.3a shows current traces obtained from the passage of VPMs in nanopores of diameters ranging between 9 nm and 36 nm, measured under a 200 mV electrical bias and in a 3.6 M LiCl solution. Figure 4.1.3b shows the extracted mean translocation velocity profiles. Velocity profiles in Figure 4.1.3b show a clear dependence on pore size: the velocities across the profile consistently are reduced with increasing pore size. This is further illustrated in Figure 4.1.3c which plots the dependence of the final velocity v_{end} on pore diameter. Moreover, with the spatial resolution provided by the design of the VPM, the contour location of the minimal velocity x_{min} appears to be independent of pore size.

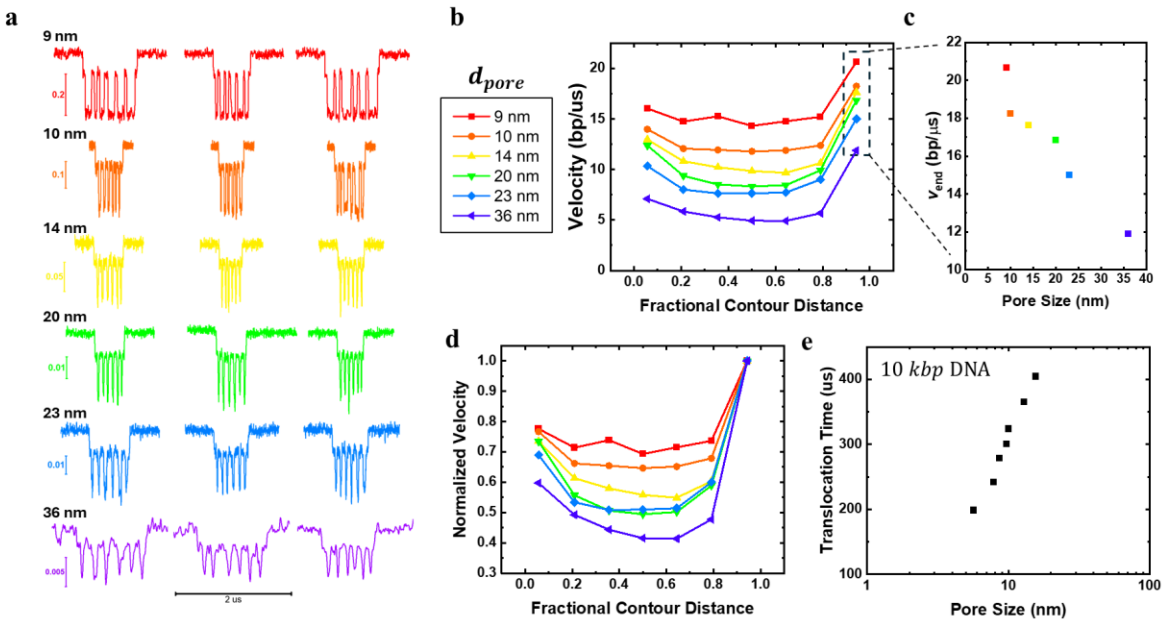

Figure 4.1.3. Effect of pore size on translocation dynamics. a) Current traces of VPM translocations in six different nanopore diameters under a 200 mV bias in 3.6 M LiCl, 10 mM HEPES pH 8.. **b)** VPM velocity profiles for different pore sizes. **c)** Dependence of v_{end} on pore size. **d)** VPM velocity profiles normalized by v_{end}. **e)** Translocation times of 10 kbp dsDNA measured in different pore sizes, in 1M LiCl under a 300 mV applied bias.

Interestingly, across all the velocity profiles shown in Figure 4.1.3b, the differences between the final segment velocity v_{end} and the minimal velocity v_{min} appear to be similar across the different pore diameters with $v_{end} - v_{min}$ values ranging between 6.3 $bp/\mu s$ and 8.5 $bp/\mu s$. Given the consistently lower velocities measured for larger pores, velocity fluctuations are thus more pronounced for larger pores than for smaller ones. For example, the velocity difference $v_{end} - v_{min} = 7.0\ bp/\mu s$ measured in a 36 nm pore corresponds to 59% of v_{end}, whereas the difference of 6.3 $bp/\mu s$ in a 9.1 nm pore represents 30% of v_{end}. Figure 4.1.3d further exemplifies this by plotting the velocity profiles normalized by the end velocity $\bar{v}_i/v_{end}$, where the normalized value v_{min}/v_{end} is shown to reduce monotonically with increasing pore size. We note the qualitative similarity between Figures 4.1.2d and 4.1.3d: Increasing pore size or

polymer length monotonically reduces the value of v_{min}/v_{end}, or equivalently increases the relative velocity fluctuations observed during translocation events.

Before quantifying and expanding on the dependence of v_{min}/v_{end} on pore size and polymer length, we comment on the unexpected result from Figure 4.1.3 showing longer translocation times for large pores (i.e. slower velocities for large pores). To our knowledge, except for Figure S2 in the SI of Garaj *et al.*[137] , the translocation times have always been reported as getting faster with increasing pore size until reaching a plateau due to reduced pore-polymer steric interactions.[30,95,189] Here, for small pores, slower translocation times are indeed observed with increasing pore size, as shown by 3HB segments in smaller pores (Figures 4.1.1e and 4.1.3a), and by figures in Section S4.2.4 of the SI. However, for large pores, translocation times are increasing with d_{pore}. Supporting further this observation for VPMs, Figure 4.1.3e plots the translocation time of 10 kbp dsDNA for different pore diameters, and exhibiting a dependence well described by a logarithmic function.

4.1.5. Velocity Fluctuations Toy Model

With insights from Figures 4.1.2 and 4.1.3, we now quantitatively study the velocity fluctuations observed during the translocation process. Namely, through the help of a toy model, we use experimental velocity fluctuations to study the origin and scalings of the time-dependent forces at play during the electrophoretically driven pore transport process. To model the forces imparted on translocating polymers, we first separate them into two broadly defined classes: forces arising inside and outside the pore, as sketched in Figure 4.1.4a. Importantly, given that the electric field in finite-length pores extends outside the channel, we loosely define the interior (exterior) of the pore as the space where forces arising from the electric field and electrokinetic effects are significant (insignificant).

Inside the pore, as per the stalled DNA measurements,[101] we consider the electric pulling force resulting from the electric field pulling on the charged DNA backbone $-F_e$, and the hydrodynamic drag imparted by the electroosmotic flow resulting from the motion of counterions shielding both the charged pore surface and polymer F_{eo}. Additionally, we consider the hydrodynamic drag resulting from the polymer moving at a velocity v through the pore interior as $\gamma_{in}v$, where γ_{in} is the corresponding internal drag coefficient, which is time-independent throughout translocation. Outside the pore, following tension propagation insights,[68–72,186] we consider the hydrodynamic drag force resulting from the motion of a segment of length ℓ under tension and moving at the same velocity v as segments inside the pore $\gamma_{out}(\ell)v$. Here $\gamma_{out}(\ell)$ denotes the corresponding external drag coefficient and is expected to scale linearly with the length of the polymer in motion, i.e. $\gamma_{out}(\ell)\sim\ell$, which according to tension propagation is dependent on time. Note the directions of the forces arise from the assumption of negatively charged polymer and pore walls, and a *trans* to *cis* pointing electric field, as shown in Figure 4.1.4a. For a polymer segment of length ℓ under tension, the translocation velocity can be simply written:

$$v(\ell) = \frac{F_e - F_{eo}}{\gamma_{in} + \gamma_{out}(\ell)} = v_{end}\left(1 + \frac{\gamma_{out}(\ell)}{\gamma_{in}}\right)^{-1}. \tag{4.1.2}$$

The final expression of Equation 4.1.2 is obtained by recognizing that the end velocity simply corresponds to the case where $\ell = 0$, i.e. $v_{end} = (F_e - F_{eo})/\gamma_{in}$.

According to Equation 4.1.2, the toy model suggests that at any instant during the translocation process, the normalized velocity v/v_{end} depends solely on the ratio of internal and external drag coefficients $\gamma_{out}(\ell)/\gamma_{in}$. We suggest this explains why Figure 4.1.2d (velocity profile versus polymer length) and Figure 4.1.3d (velocity profile versus pore size) look alike: Longer polymers result in larger segments under tension outside the pore on average, thereby

increasing ℓ and $\gamma_{out}(\ell)$, and larger pores result in weaker confinement of the translocating polymer and thus reduce the internal drag, γ_{in}. Both longer polymers and larger pores therefore result in increased values of $\gamma_{out}(\ell)/\gamma_{in}$ throughout the translocation process, and thus in overall slower translocations. Moreover, experimental conditions wherein the time-independent internal drag γ_{in} dominates over the external time-varying drag γ_{out}, i.e. in the case of small pores and short DNA, should result in flatter profiles with less fluctuations, whereas the opposite is true for conditions where the time-dependent γ_{out} dominates over the time-independent γ_{in}, i.e. the case of long polymers and large pores.

To quantitatively analyze the velocity profiles, we further note that the minimal velocity v_{min} corresponds to the point during translocation where the segment under tension is maximal, i.e. $v_{min} = v(\ell_{max})$. Defining the maximal external drag coefficient as $\gamma_{out}^{max} \equiv \gamma_{out}(\ell_{max})$, it can be shown that:

$$\frac{\gamma_{out}^{max}}{\gamma_{in}} = \frac{v_{end}}{v_{min}} - 1. \tag{4.1.3}$$

Equation 4.1.3 shows that the experimentally obtained values of v_{end}/v_{min} from Figures 4.1.2 and 4.1.3 can be used to quantify the maximal external and internal drag coefficient ratio $\gamma_{out}^{max}/\gamma_{in}$. Figure 4.1.4d plots the values of $v_{end}/v_{min} - 1$ calculated from the different polymer lengths L_n shown in Figure 4.1.2d and shows that $\gamma_{out}^{max}/\gamma_{in}$ increases with polymer length. Namely, the data is well-fitted by a power scaling function of the form $L_n^{0.55\pm0.04}$. Since the internal drag γ_{in} is independent of polymer length, and the maximal external drag γ_{out}^{max} is proportional to ℓ_{max}, we can further infer from our experiments that ℓ_{max} scales with polymer length as $\ell_{max} \sim L^{0.55\pm0.04}$. From tension propagation principles, under strong pulling forces, ℓ_{max} should be closely related to the polymer's radius (Figure 4.1.1), which in bulk solution should scale as

$R_{ee} \sim L^{\nu}$ with $\nu = 0.588$ being Flory's coefficient.[191] Great agreement is thus found between our experimental results and predictions from Tension Propagation.

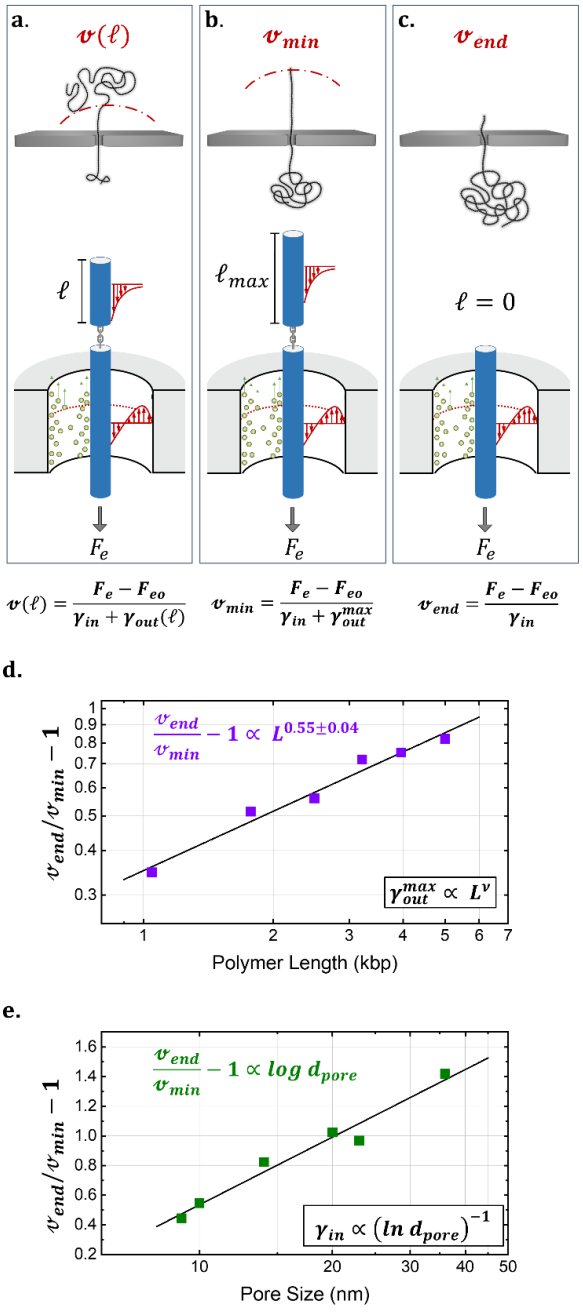

Figure 4.1.4. Toy model and scalings of velocity fluctuations (Eq. 4.1.2). **a-c)** Depiction of forces considered for different translocation steps. **d)** Dependance of $v_{end}/v_{min} - 1$ on polymer length L_n calculated from Eq. 4.1.1. The solid line is a power scaling fit resulting in a scaling coefficient of $\gamma_{out}^{max}/\gamma_{in} \sim L^{0.55\pm0.04}$. **e)** Dependance of $v_{end}/v_{min} - 1$ on pore diameter. The solid line is a log fit of the form $\gamma_{out}^{max}/\gamma_{in} = 0.66 \ln(d_{pore}) - 0.98$. Data taken from Figures 4.1.2d and 4.1.3d.

Figure 4.1.4e plots the calculated values of $v_{end}/v_{min} - 1$ obtained from Figure 4.1.3d against corresponding pore diameters and shows once again that $v_{end}/v_{min} - 1$ and thus $\gamma_{out}^{max}/\gamma_{in}$ increases with pore sizes. The dependence of $\gamma_{out}^{max}/\gamma_{in}$ on pore size appears to be logarithmic, as supported by the data being well fitted by a function of the form $\gamma_{out}^{max}/\gamma_{in} = A\ln(d_{pore}) - B$, where A and B are constant. By assuming the external coefficient γ_{out}^{max} is independent of pore size, we can further infer from our experiments that the internal drag coefficient scales as $\gamma_{in}^{-1} \sim \ln(d_{pore})$. Interestingly, this inverse logarithmic pore size dependence arises when calculating the drag coefficient of an infinitely long cylindrical object moving through an infinitely long cylindrical channel (Section S4.2.5 of the SI). Although no analytical solution exists for the internal drag coefficient γ_{in} of a finite-length nanopore, our translocation velocity experiments suggest that the pore size scaling appears to be maintained, at least to first order.

4.1.6. Polymer Conformations

We now discuss the effects of polymer conformation on velocity profiles. We begin by demonstrating how the fractional location of the segment with minimal velocity x_{min} along the VPM contour can be predicted reasonably well using insights from Tension Propagation. As discussed above, minimal velocity occurs when the segment under tension has reached its maximal length ℓ_{max}. In the extreme limiting case of ultra-fast translocations, polymer segments are frozen in space until they are under tension and move toward the pore. The maximal length ℓ_{max} therefore corresponds to the distance between the pore's entrance and the polymer segment farthest away from the pore, R_{max}, as shown in Figure 4.1.5a. A reasonable expression for x_{min} is therefore:

$$x_{min} = \frac{L_n - \ell_{max} - \ell_{end}}{L_n} = 1 - \frac{R_{max} + \ell_{end}}{L_n}. \quad (4.1.4)$$

Here, ℓ_{end} simply corresponds to the length of segments not yet under tension when the farthest segment becomes under tension, i.e. once the translocation velocity is minimal. Note that Figure 4.1.4 depicts a scenario wherein $\ell_{end} = 0$, as opposed to Figure 4.15a.

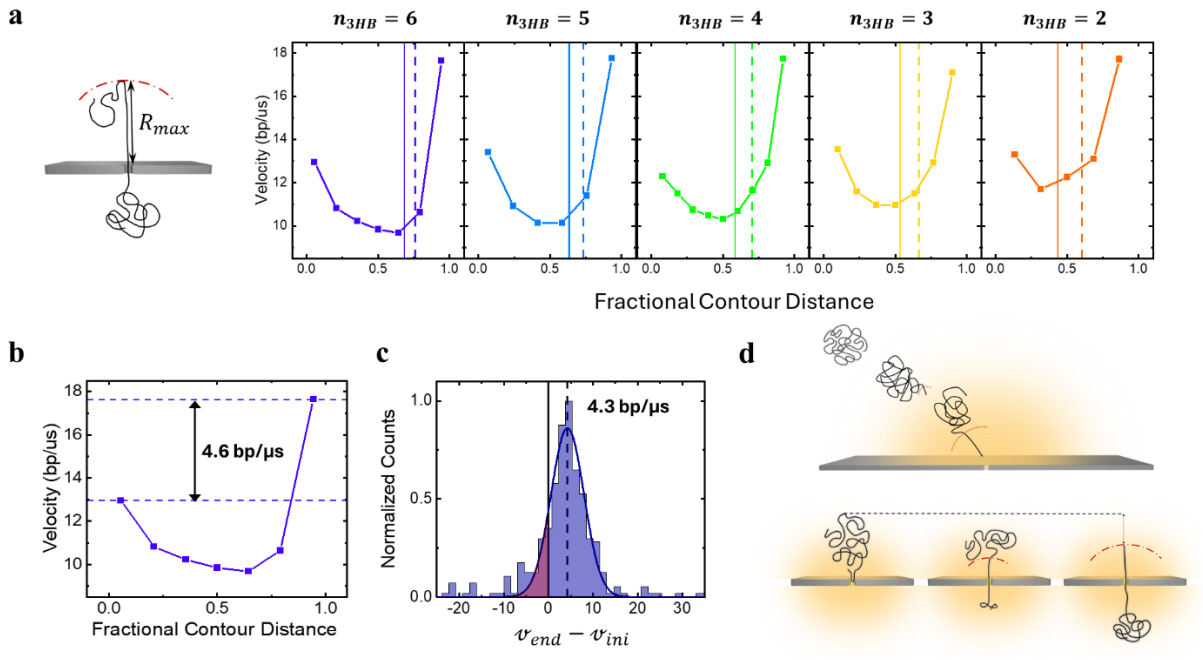

Figure 4.1.5. Effects of polymer conformations on velocity profiles. a) Translocation Velocity Profiles of different VPM lengths. Vertical lines represent x_{min} predictions calculating using $x_{min} = 1 - R_{ee}/L_n$ (dashed) and using most probable x_{min}value extracted from 5000 simulated discrete worm-like chains. **b)** Difference of average start and end velocities. **c)** Distribution of $v_{end} - v_{in}$ values measured for 439 individual events. **d)** Interpretation of the effect of electric field on polymer conformations, as described in the text.

The simplest attempt to solve Equation 4.1.4 is to assume that the length of polymer on the *cis*-side when $v = v_{min}$ is equivalent to the polymer's relaxed end-to-end distance: $R_{ee} = R_{max} + \ell_{end}$. Using wormlike chains statistics, R_{ee} values were calculated for different VPM lengths L_n using a persistence length of 150 bp. Figure 4.1.5a shows the individual translocation velocity profiles for the different VPM lengths (data from Figure 4.1.2) and includes the $x_{min} = 1 - R_{ee}/L_n$ predictions plotted as dashed vertical lines, which consistently overestimates the

location of v_{min}. To better quantify $R_{max} + \ell_{end}$ for the calculation of x_{min}, we generated 5000 discrete wormlike chains (DWLC) with one end tethered to a non-penetrable surface, as detailed in section S4.2.6 of the SI.[192] By identifying the furthest monomer from the pore (tethering point), statistics on $R_{max} + \ell_{end}$ and x_{min} (Eq. 4.1.4) were obtained. Figure 4.1.5a plots the most probable simulated x_{min} values as solid vertical lines, which line up well with local velocity minima, thus establishing that the location of minimum velocity is closely correlated to the relaxed conformation of a polymer with one end inside the pore.

For all velocity profiles obtained and shown in this work, the average initial translocation velocities, $\bar{v}_{ini}$, were consistently smaller than the average end velocities, $\bar{v}_{end}$. This is revealed in Figures 4.1.5b-c which show the difference $\bar{v}_{end} - \bar{v}_{ini}$ and the distribution of $v_{end} - v_{ini}$ with 88% of events with $v_{end} > v_{ini}$. The toy model introduced above suggests that if $v_{end} > v_{ini}$, the segments of the polymer closest to the pore are already under tension when translocation begins. This is consistent with previous research that showed polymers are not in equilibrium during their approach, as they are stretched and elongated by the non-uniform electric field outside the pore.[87,165–167] As a result, we suggest that tension propagation begins prior to entering the pore, thus resulting in $\bar{v}_{end} > \bar{v}_{in}$. This conclusion might appear contradictory with that of Figure 4.1.5a, wherein x_{min} is well predicted by relaxed polymer conformations. However, after a polymer enters a pore, the electric field keeps acting on the external polymer segments, attracting them closer to the pore while tension propagation progresses. The good x_{min} predictions thus suggest that although polymers arrive elongated, they compress down to a size comparable to the corresponding full-length relaxed conformations by the time the tension front reaches the polymer back end. These proposed different polymer conformations as a function of the translocation

process are illustrated in Figure 4.1.5d. Section S4.2.7 of the SI further expands on the role of polymer conformation on velocity profiles by quantifying the inter-segment velocity correlations.

4.1.7. Conclusion

The translocation velocity profiles experimentally obtained in this work as a function of pore size and polymer length allowed us to elucidate the forces at play inside and outside the nanoscale confinement of a nanopore during the polymer translocation process. The use of the nanostructured velocity profile molecules (VMPs) removed the need for complex instrumentation and avoided neglecting the time-dependence resulting from the non-equilibrium nature of strongly driven translocations which were limitations of previous studies.[101,102] The proposed physical toy model allowed us to experimentally validate theoretical concepts from Tension Propagation regarding the dependence of velocity profiles on polymer length and pore sizes which, despite being hinted at by simulations, had eluted thorough experimental validation for a decade. Section S4.2.8 of the SI deepens this analysis by reporting the dependence of profiles on the applied voltage ΔV. Our experiments also displayed the importance of considering external field effects on polymers prior to translocation, as often omitted. Although this work does not allow for exact predictions of translocation velocity profiles, this new knowledge about velocity profile dependence on pore size and polymer length can be used to optimize operating conditions for a wide range of biosensing applications, including DNA nanostructure barcodes for multiplexed biomarker detection or digital information storage.[131,193]

4.1.8. Methods

Linearized Scaffold Preparation – M13mp18 circular single-stranded DNA (New England Biolabs, N4040S) were linearized to create a 7249 nt long single-stranded DNA. First, primers were attached to the circular scaffold by mixing them with 10 μg of M13mp18 at a ratio of 10:1 in 1x NEB 3.1 buffer, heating the sample to 95 ^{o}C, and slowly cooling down to room temperature in a MiniAmp Plus Thermal Cycler (ThermoFisher Scientific, #A37835). To linearize the scaffolds, a mixture of circular scaffold (with primer attached), and 10 units of HincII restriction enzyme (New England Biolabs, R0103S) in a total reaction volume of 50 μL in 1x NEB 3.1 buffer were incubated at 37 ^{o}C for 3 hours, then heat-inactivated at 65 ^{o}C for 20 minutes in the thermal cycler.

Nanostructure Assembly – For the assembly of the VPMs, the linearized scaffold was mixed with 171 staple strands at a molar ratio of 1:10 in assembly buffer (40 mM Tris, 20 mM acetic acid, 2 mM EDTA, and 16 mM $MgCl_2$, pH 8). The product was heated to 95 ^{o}C for 5 minutes, then cooled to 90 ^{o}C, ramped from 90 ^{o}C to 60 ^{o}C at a rate of 0.4 ^{o}C per minute, then from 60 ^{o}C to 26 ^{o}C at a rate of 0.03 ^{o}C, and snap cooled to 4 ^{o}C using a minicamp Plus Thermal Cycler. After assembly, nanostructures purified using 100 kDa Amicon Ultra-0.5 Centrifugal Filter Unit (Millipore Sigma, UFC500396). Three washes with the assembly buffer were performed to completely remove excess staple strands present in the solution. The assembled products were visualized on 0.5% agarose gel in 1x TAE buffer, as shown in Section S4.2.1 of the SI.

Nanopore Fabrication – Nanopores were fabricated in 12 nm thick free-standing SiN_x membranes (Norcada, NBPX5004Z) using the controlled breakdown (CBD) method. Pores were fabricated in 1 M KCl at pH 8 and slowly grown to desired sizes with AC voltages pulses of small

amplitudes in 3.6 M LiCl, as described by Waugh *et al*.[22] Prior to fabrication, membranes were painted with a layer of PDMS to reduce high-frequency noise.[49]

Nanopore Sensing – A volume of 1-2 μL of the VPM samples were added to $50 - 80\ \mu L$ of 3.6 M LiCl solution with pH 8 for nanopore sensing. Prior to all VPM experiments, 5 kbp dsDNA (ThermoFisher Scientific, SM1731) was run as a control experiment. The ionic current recordings were either performed using the VC100 current amplifier (Chimera Instruments) with a bandwidth of 1 MHz for nanopores with baseline currents smaller than 20 nA, or using the Axopatch 200B amplifier with a bandwidth of 200 kHz for larger pores.

Data Analysis – Translocation events in the recorded current traces were located and fitted using a custom implementation of the CUSUM+ algorithm.[184] A digital low-pass filter was applied prior to event detection and fitting. The value of the cutoff frequency was chosen on a per-experiment basis, so as to maximize temporal resolution whilst maintaining good signal to noise ratio. The fitted translocation events were plotted and further analyzed using Nanolyzer (v0.1.41) from Northern Nanopore Instruments

4.2 Supporting Information for Section 4.1

S4.2.1. DNA structure design and sequences

Scaffold preparation and sequence

The linearized M13 single-stranded DNA scaffolds were prepared as described in the Methods Section in the main text, using M13mp18 circular single-stranded DNA (New England Biolabs, N4040S). A primer strand was added in a mixture with 10 μg M13mp18 circular single-stranded DNA at a ratio of 10:1 in 1x NEB 3.1 buffer, the mixture was heated to 95 ^{o}C and slowly cooled down to room temperature in a thermal cycler. A mixture of prepared circular scaffold (with primer attached), and 10 units of HincII restriction enzyme (New England Biolabs, R0103S) in a total reaction volume of 50 μL in 1x NEB 3.1 buffer were incubated at 37 ^{o}C for 3 hours, then heat inactivated at 65 ^{o}C for 20 minutes in a thermal cycler. The sequence of the M13mp18 scaffold is shown below, showing linearization by HincII (New England Biolabs, R0103S). The underlined sequence represents the region where the primer strand is attached, and the red sequences are the recognition site for HincII restriction enzyme.

GACCTGCAGGCATGCAAGCTTGGCACTGGCCGTCGTTTTACAACGTCGTGACTGGGAAAACCCTGGCGTTACCCAACTTAATCGCCTTG
CAGCACATCCCCCTTTCGCCAGCTGGCGTAATAGCGAAGAGGCCCGCACCGATCGCCCTTCCCAACAGTTGCGCAGCCTGAATGGCG
AATGGCGCTTTGCCTGGTTTCCGGCACCAGAAGCGGTGCCGGAAAGCTGGCTGGAGTGCGATCTTCCTGAGGCCGATACTGTCGTCGTC
CCCTCAAACTGGCAGATGCACGGTTACGATGCGCCCATCTACACCAACGTGACCTATCCCATTACGGTCAATCCGCCGTTTGTTCCCACG
GAGAATCCGACGGGTTGTTACTCGCTCACATTTAATGTTGATGAAAGCTGGCTACAGGAAGGCCAGACGCGAATTATTTTTGATGGCGTTCC
TATTGGTTAAAAAATGAGCTGATTTAACAAAAATTTAATGCGAATTTTAACAAAATATTAACGTTTACAATTTAAATATTTGCTTATACAATCTTCCTG
TTTTTGGGGCTTTTCTGATTATCAACCGGGGTACATATGATTGACATGCTAGTTTTACGATTACCGTTCATCGATTCTCTTGTTTGCTCCAGACTC
TCAGGCAATGACCTGATAGCCTTTGTAGATCTCTCAAAAATAGCTACCCTCTCCGGCATTAATTTATCAGCTAGAACGGTTGAATATCATATTGA
TGGTGATTTGACTGTCTCCGGCCTTTCTCACCCTTTTGAATCTTTACCTACACATTACTCAGGCATTGCATTTAAAATATATGAGGGTTCTAAAAA
TTTTTATCCTTGCGTTGAAATAAAGGCTTCTCCCGCAAAAGTATTACAGGGTCATAATGTTTTTGGTACAACCGATTTAGCTTTATGCTCTGAGG
CTTTATTGCTTAATTTTGCTAATTCTTTGCCTTGCCTGTATGATTTATTGGATGTTAATGCTACTACTATTAGTAGAATTGATGCCACCTTTTCAGCT
CGCGCCCCAAATGAAAATATAGCTAAACAGGTTATTGACCATTTGCGAAATGTATCTAATGGTCAAACTAAATCTACTCGTTCGCAGAATTGG
GAATCAACTGTTATATGGAATGAAACTTCCAGACACCGTACTTTAGTTGCATATTTAAAACATGTTGAGCTACAGCATTATATTCAGCAATTAAGC
TCTAAGCCATCCGCAAAAATGACCTCTTATCAAAAGGAGCAATTAAAGGTACTCTCTAATCCTGACCTGTTGGAGTTTGCTTCCGGTCTGGTT
CGCTTTGAAGCTCGAATTAAAACGCGATATTTGAAGTCTTTCGGGCTTCCTCTTAATCTTTTTGATGCAATCCGCTTTGCTTCTGACTATAATAGT
CAGGGTAAAGACCTGATTTTTGATTTATGGTCATTCTCGTTTTCTGAACTGTTTAAAGCATTTGAGGGGGATTCAATGAATATTTATGACGATTCC
GCAGTATTGGACGCTATCCAGTCTAAACATTTTACTATTACCCCCTCTGGCAAAACTTCTTTTGCAAAAGCCTCTCGCTATTTTGGTTTTTATCG
TCGTCTGGTAAACGAGGGTTATGATAGTGTTGCTCTTACTATGCCTCGTAATTCCTTTTGGCGTTATGTATCTGCATTAGTTGAATGTGGTATTCC
TAAATCTCAACTGATGAATCTTTCTACCTGTAATAATGTTGTTCCGTTAGTTCGTTTTATTAACGTAGATTTTTCTTCCCAACGTCCTGACTGGTATA
ATGAGCCAGTTCTTAAAATCGCATAAGGTAATTCACAATGATTAAAGTTGAAATTAAACCATCTCAAGCCCAATTTACTACTCGTTCTGGTGTTT
CTCGTCAGGGCAAGCCTTATTCACTGAATGAGCAGCTTTGTTACGTTGATTTGGGTAATGAATATCCGGTTCTTGTCAAGATTACTCTTGATGAA
GGTCAGCCAGCCTATGCGCCTGGTCTGTACACCGTTCATCTGTCCTCTTTCAAAGTTGGTCAGTTCGGTTCCCTTATGATTGACCGTCTGCG
CCTCGTTCCGGCTAAGTAACATGGAGCAGGTCGCGGATTTCGACACAATTTATCAGGCGATGATACAAATCTCCGTTGTACTTTGTTTCGCG
CTTGGTATAATCGCTGGGGGTCAAAGATGAGTGTTTTAGTGTATTCTTTTGCCTCTTTCGTTTTAGGTTGGTGCCTTCGTAGTGGCATTACGTATT
TTACCCGTTTAATGGAAACTTCCTCATGAAAAAGTCTTTAGTCCTCAAAGCCTCTGTAGCCGTTGCTACCCTCGTTCCGATGCTGTCTTTCGC
TGCTGAGGGTGACGATCCCGCAAAAGCGGCCTTTAACTCCCTGCAAGCCTCAGCGACCGAATATATCGGTTATGCGTGGGCGATGGTTGT

TGTCATTGTCGGCGCAACTATCGGTATCAAGCTGTTTAAGAAATTCACCTCGAAAGCAAGCTGATAAACCGATACAATTAAAGGCTCCTTTTG
GAGCCTTTTTTTTGGAGATTTTCAACGTGAAAAAATTATTATTCGCAATTCCTTTAGTTGTTCCTTTCTATTCTCACTCCGCTGAAACTGTTGAAAG
TTGTTTAGCAAAATCCCATACAGAAAATTCATTTACTAACGTCTGGAAAGACGACAAAACTTTAGATCGTTACGCTAACTATGAGGGCTGTCTG
TGGAATGCTACAGGCGTTGTAGTTTGTACTGGTGACGAAACTCAGTGTTACGGTACATGGGTTCCTATTGGGCTTGCTATCCCTGAAAATGAG
GGTGGTGGCTCTGAGGGTGGCGGTTCTGAGGGTGGCGGTTCTGAGGGTGGCGGTACTAAACCTCCTGAGTACGGTGATACACCTATTCC
GGGCTATACTTATATCAACCCTCTCGACGGCACTTATCCGCCTGGTACTGAGCAAAACCCCGCTAATCCTAATCCTTCTCTTGAGGAGTCTC
AGCCTCTTAATACTTTCATGTTTCAGAATAATAGGTTCCGAAATAGGCAGGGGGCATTAACTGTTTATACGGGCACTGTTACTCAAGGCACTG
ACCCCGTTAAAACTTATTACCAGTACACTCCTGTATCATCAAAAGCCATGTATGACGCTTACTGGAACGGTAAATTCAGAGACTGCGCTTTCC
ATTCTGGCTTTAATGAGGATTTATTTGTTTGTGAATATCAAGGCCAATCGTCTGACCTGCCTCAACCTCCTGTCAATGCTGGCGGCGGCTCTG
GTGGTGGTTCTGGTGGCGGCTCTGAGGGTGGTGGCTCTGAGGGTGGCGGTTCTGAGGGTGGCGGCTCTGAGGGAGGCGGTTCCGGTG
GTGGCTCTGGTTCCGGTGATTTTGATTATGAAAAGATGGCAAACGCTAATAAGGGGGCTATGACCGAAAATGCCGATGAAAACGCGCTACA
GTCTGACGCTAAAGGCAAACTTGATTCTGTCGCTACTGATTACGGTGCTGCTATCGATGGTTTCATTGGTGACGTTTCCGGCCTTGCTAATGG
TAATGGTGCTACTGGTGATTTTGCTGGCTCTAATTCCCAAATGGCTCAAGTCGGTGACGGTGATAATTCACCTTTAATGAATAATTTCCGTCAAT
ATTTACCTTCCCTCCCTCAATCGGTTGAATGTCGCCCTTTTGTCTTTGGCGCTGGTAAACCATATGAATTTTCTATTGATTGTGACAAAATAAAC
TTATTCCGTGGTGTCTTTGCGTTTCTTTTATATGTTGCCACCTTTATGTATGTATTTTCTACGTTTGCTAACATACTGCGTAATAAGGAGTCTTAATC
ATGCCAGTTCTTTTGGGTATTCCGTTATTATTGCGTTTCCTCGGTTTCCTTCTGGTAACTTTGTTCGGCTATCTGCTTACTTTTCTTAAAAAGGGC
TTCGGTAAGATAGCTATTGCTATTTCATTGTTTCTTGCTCTTATTATTGGGCTTAACTCAATTCTTGTGGGTTATCTCTCTGATATTAGCGCTCAATT
ACCCTCTGACTTTGTTCAGGGTGTTCAGTTAATTCTCCCGTCTAATGCGCTTCCCTGTTTTTATGTTATTCTCTCTGTAAAGGCTGCTATTTTCATT
TTTGACGTTAAACAAAAAATCGTTTCTTATTTGGATTGGGATAAATAATATGGCTGTTTATTTTGTAACTGGCAAATTAGGCTCTGGAAAGACGCT
CGTTAGCGTTGGTAAGATTCAGGATAAAATTGTAGCTGGGTGCAAAATAGCAACTAATCTTGATTTAAGGCTTCAAAACCTCCCGCAAGTCGG
GAGGTTCGCTAAAACGCCTCGCGTTCTTAGAATACCGGATAAGCCTTCTATATCTGATTTGCTTGCTATTGGGCGCGGTAATGATTCCTACGA
TGAAAATAAAAACGGCTTGCTTGTTCTCGATGAGTGCGGTACTTGGTTTAATACCCGTTCTTGGAATGATAAGGAAAGACAGCCGATTATTGAT
TGGTTTCTACATGCTCGTAAATTAGGATGGGATATTATTTTTCTTGTTCAGGACTTATCTATTGTTGATAAACAGGCGCGTTCTGCATTAGCTGAA
CATGTTGTTTATTGTCGTCGTCTGGACAGAATTACTTTACCTTTTGTCGGTACTTTATATTCTCTTATTACTGGCTCGAAAATGCCTCTGCCTAAAT
TACATGTTGGCGTTGTTAAATATGGCGATTCTCAATTAAGCCCTACTGTTGAGCGTTGGCTTTATACTGGTAAGAATTTGTATAACGCATATGATA
CTAAACAGGCTTTTTCTAGTAATTATGATTCCGGTGTTTATTCTTATTTAACGCCTTATTTATCACACGGTCGGTATTTCAAACCATTAAATTTAGGT
CAGAAGATGAAATTAACTAAAATATATTTGAAAAAGTTTTCTCGCGTTCTTTGTCTTGCGATTGGATTTGCATCAGCATTTACATATAGTTATATAAC
CCAACCTAAGCCGGAGGTTAAAAAGGTAGTCTCTCAGACCTATGATTTTGATAAATTCACTATTGACTCTTCTCAGCGTCTTAATCTAAGCTATC
GCTATGTTTTCAAGGATTCTAAGGGAAAATTAATTAATAGCGACGATTTACAGAAGCAAGGTTATTCACTCACATATATTGATTTATGTACTGTTTC
CATTAAAAAAGGTAATTCAAATGAAATTGTTAAATGTAATTAATTTTGTTTTCTTGATGTTTGTTTCATCATCTTCTTTTGCTCAGGTAATTGAAATGAA
TAATTCGCCTCTGCGCGATTTTGTAACTTGGTATTCAAAGCAATCAGGCGAATCCGTTATTGTTTCTCCCGATGTAAAAGGTACTGTTACTGTAT
ATTCATCTGACGTTAAACCTGAAAATCTACGCAATTTCTTTATTTCTGTTTTACGTGCAAATAATTTTGATATGGTAGGTTCTAACCCTTCCATTATT
CAGAAGTATAATCCAAACAATCAGGATTATATTGATGAATTGCCATCATCTGATAATCAGGAATATGATGATAATTCCGCTCCTTCTGGTGGTTTC
TTTGTTCCGCAAAATGATAATGTTACTCAAACTTTTAAAATTAATAACGTTCGGGCAAAGGATTTAATACGAGTTGTCGAATTGTTTGTAAAGTCTA
ATACTTCTAAATCCTCAAATGTATTATCTATTGACGGCTCTAATCTATTAGTTGTTAGTGCTCCTAAAGATATTTTAGATAACCTTCCTCAATTCCTTT
CAACTGTTGATTTGCCAACTGACCAGATATTGATTGAGGGTTTGATATTTGAGGTTCAGCAAGGTGATGCTTTAGATTTTTCATTTGCTGCTGGC
TCTCAGCGTGGCACTGTTGCAGGCGGTGTTAATACTGACCGCCTCACCTCTGTTTTATCTTCTGCTGGTGGTTCGTTCGGTATTTTTAATGGC
GATGTTTTAGGGCTATCAGTTCGCGCATTAAAGACTAATAGCCATTCAAAAATATTGTCTGTGCCACGTATTCTTACGCTTTCAGGTCAGAAGG
GTTCTATCTCTGTTGGCCAGAATGTCCCTTTTATTACTGGTCGTGTGACTGGTGAATCTGCCAATGTAAATAATCCATTTCAGACGATTGAGCGT
CAAAATGTAGGTATTTCCATGAGCGTTTTTCCTGTTGCAATGGCTGGCGGTAATATTGTTCTGGATATTACCAGCAAGGCCGATAGTTTGAGTT
CTTCTACTCAGGCAAGTGATGTTATTACTAATCAAAGAAGTATTGCTACAACGGTTAATTTGCGTGATGGACAGACTCTTTTACTCGGTGGCCT
CACTGATTATAAAAACACTTCTCAGGATTCTGGCGTACCGTTCCTGTCTAAAATCCCTTTAATCGGCCTCCTGTTTAGCTCCCGCTCTGATTCT
AACGAGGAAAGCACGTTATACGTGCTCGTCAAAGCAACCATAGTACGCGCCCTGTAGCGGCGCATTAAGCGCGGCGGGTGTGGTGGTTA
CGCGCAGCGTGACCGCTACACTTGCCAGCGCCCTAGCGCCCGCTCCTTTCGCTTTCTTCCCTTCCTTTCTCGCCACGTTCGCCGGCTTT
CCCCGTCAAGCTCTAAATCGGGGGCTCCCTTTAGGGTTCCGATTTAGTGCTTTACGGCACCTCGACCCCAAAAAACTTGATTTGGGTGATG
GTTCACGTAGTGGGCCATCGCCCTGATAGACGGTTTTTCGCCCTTTGACGTTGGAGTCCACGTTCTTTAATAGTGGACTCTTGTTCCAAACTG
GAACAACACTCAACCCTATCTCGGGCTATTCTTTTGATTTATAAGGGATTTTGCCGATTTCGGAACCACCATCAAACAGGATTTTCGCCTGCT
GGGGCAAACCAGCGTGGACCGCTTGCTGCAACTCTCTCAGGGCCAGGCGGTGAAGGGCAATCAGCTGTTGCCCGTCTCACTGGTGAA
AAGAAAAACCACCCTGGCGCCCAATACGCAAACCGCCTCTCCCCGCGCGTTGGCCGATTCATTAATGCAGCTGGCACGACAGGTTTCC
CGACTGGAAAGCGGGCAGTGAGCGCAACGCAATTAATGTGAGTTAGCTCACTCATTAGGCACCCCAGGCTTTACACTTTATGCTTCCGGC
TCGTATGTTGTGTGGAATTGTGAGCGGATAACAATTTCACACAGGAAACAGCTATGACCATGATTACGAATTCGAGCTCGGTACCCGGGGAT
CCTCTAGAGTC

Structure design

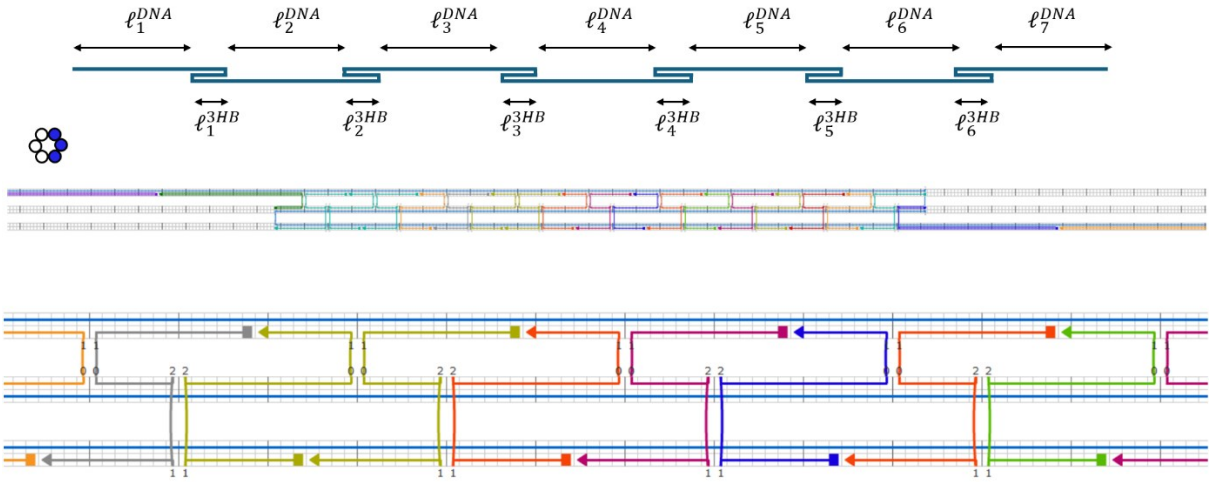

Figure S4.2.1. VPM structure design. caDNAno[86] design of VPM on a honey-comb lattice, using linearized M13mp18 scaffold and 171 staple strands. The long blue strand represents the M13mp18 scaffold, and the short, coloured arrows are the staple strands, with the arrow side being the 3' end.

Segment	Length (bp)
ℓ_1^{DNA}	568
ℓ_1^{3HB}	196
ℓ_2^{DNA}	567
ℓ_2^{3HB}	182
ℓ_3^{DNA}	535
ℓ_3^{3HB}	186
ℓ_4^{DNA}	535
ℓ_4^{3HB}	182
ℓ_5^{DNA}	536
ℓ_5^{3HB}	185
ℓ_6^{DNA}	567
ℓ_6^{3HB}	193
ℓ_7^{DNA}	568
Total	5000

Table S4.2.1. **Lengths of the different segments of the VPM assembly.** Segments near extremities were designed slightly longer in anticipation of faster translocation velocities in those areas.

Nanostructure assembly

Oligo	Sequence	Length
1	TATAGTCAGAAGCAAAGCGGATTGCATCAAAAAGATTAAGAGGAAGCCCGAAAGAC	56
2	AAAGATTCATCAGTTGAGATTTAGGAATACCACATTCAACTAATGCAGA	49
3	ACATACGAGCCGGAAGCATAAAGTGTAAAGCCTGGGGTGCCTAATGAGT	49
4	AAGGAATTGCGAATAATAATTTTTTCACGTTGAAAATCTCCAAAAAAAAGGCTCCA	56
5	GCTTAATTGAGAATCGCCATATTTAACAACGCCAACATGTAATTTAGGCAGAGGCA	56
6	GGAGCACTAACAACTAATAGATTAGAGCCGTCAATAGATAATACATTTGAGGATTT	56
7	CGTTAATAAAACGCAGACGGTCGAAATCCGCGACCTGCTCCATGTT	46
8	TAATTTCATCTTCTGACCTAAATTTAATGGTTTGAAATACCGACCGTGTGATAAAT	56
9	TCGCTATTAAACAATTTCATTTGAATCCTGAT	32
10	CCGATATATTCGGTCGCTGAGGCTTGCAGGGAGTTAAAGGCCGCTTTTGCGGGATC	56
11	CGGTAATCGTCCTCAGAGCATAAAAATTCTAC	32
12	GGCTTAGGTTCGGATTCGCCTGATTACAGTAACAGTACCTTTTACATCGG	50
13	TGCCAGTTTGAGGGGACGACGACAGTATCGGCCTCAGGAAGATCGCACTCCAGCCA	56
14	ATTTTCGGTCATAGCCCCCTTATTAGCGTTTGCCATCTTTTCATAATCAAAATCAC	56
15	TTATAAATCAAAAGAATAGCCCGAGATAGGGTTGAGTGTTGTTCCAGTTTGGAACA	56
16	CCCTAAAGGGTTTTATAATCAGTGATCACTTG	32
17	AAAATTCATATGGTTTACCAGCGCCAAAGACAAAAGGGCGACATTCAACCGATTGA	56
18	AGCTACAATGCCGAACAAAGTTACCAGAAGGAAACCGAGGAAACG	45
19	AGAGTCCACTATTAAAGAACGTGGACTCCAACGTCAAAGGGCGAAAAACCGTCTAT	56
20	TAACCCTCGTTTACCAGACGACGATAAAAACCAAAATAGCGAGAGGCTT	49
21	CGTCAGATGAATATGCTTTGTTTTAACCTCC	31
22	GCAAACAAGACGGTTGTACCAAAAGCGAGCTG	32
23	GCATTAGACGGGAGAATTAACTGAACAGAGAATCGTTTTTATTT	44
24	AACCACCACAGTACTATGGTTGCTCTGAAATG	32
25	TTGCGGATGGCTTAGAGCTTAATTGCTGAATATAATGCTGTAGCTCAACATGTTTT	56
26	ATTCATCAATATAATTACCTTCTGTAAATCG	31
27	GACGCTCAATCGTTTGACGAACGCTGCGCGT	31
28	TGACCGTAATGGGATAGGTCACGTTGGTGTAGATGGGCGCATCGTAACCGTGCATC	56
29	ACAGCTTGATACCGATAGTTGCGCCGACAATGACAACAACCATCGCCCACGCATAA	56
30	TAATGGAAGGGTTATCAAGATGAAAACATAG	31
31	CAATAATAACGGAATACCCAAAAGAACTGGCATGATTAAGACTCCTTAT	49
32	TGGGCTTGAGATGCTTGACAAGAGGCAAAAG	31
33	TCATCGTAGGAGCAGCCTTTACAGACCCTGAA	32
34	AATACACTAATCATCAAGAGTAATGTTTAATT	32
35	GTAAAACAGAAATTTCATTTCAATAGTGAAT	31
36	TCATGGAAATACCCTTTCCTGCGCTGGCAAG	31
37	ACTTAGCCGGAACGAGGCGAACTAACGGAACAACATTATTACAGGTAG	48
38	TTATCAAAATGCAGAGGCGAATTAAAAGAAAT	32
39	TGTAGCGGTCGCACGTATAACGTGTACATTTT	32
40	CGATAGCTTAATGATGAAACAAACAGAACCTA	32
41	CAACAGGTCAGGATTAGAGAGTACCTTTAATTGCTCCTTTTGATAAGAGGTCATTT	56
42	TTAGAATCCTAAACAAAATTAATTCTTCTGAA	32
43	TATCGGCCTTGCTAACGGTACGGGGAAAGCC	31
44	TAAAATTCGCATTAAATTTTTGTTAAATCAGCTCATTTTTTAACCAATA	49
45	AGAACCACCACCAAGTGCCCGCCCGGAATAG	31
46	TTGCAAAAGAAGTTTTGCCAGAGGGGGTAATAGTAAAATGTTTAGACTGGATAGCG	56
47	CTAAAACGAAAGAACCGGATATTCTAGTAAAT	32
48	AAGGCAAAGAATTGTACCCCGGTTGATAATCAGAAAAGCCCCAAAAAC	48
49	AACAATAGATAAGTCCTGAACAAGAAAAATAATATCCCATCCTAATTTACGAGCAT	56
50	TCCAGACGACGACAATAAACAACATGTTCAGCTAATGCAGAACGCGCCTGTTTATC	56
51	AATATATGTGAGTGAATAACCTTGCTTTTTTAATGGAAACTGATGGCA	48
52	GAGCTAACTCACATTAATTGCGTTGCGCTCACTGCCCGCTTTCCAGTCG	49
53	CCACAAGAATTGACCCAATCGCTTATCCGGT	31
54	AGTCTCTGAATTTACCCCAGAATGGAAAGCGC	32
55	TTGCCCCAGCAGGCGAAAATCCTGTTTGATGGTGGTTCCGAAATCGGCAAAATCCC	56
56	CAAAGTCAGAGGGTGAAAATAATCATTACCG	31
57	ATTCTAAGAAGCCATATTATTTATGTTAAGCC	32
58	GCTTTCCGGCACCGCTTCTGGTGCCGGAAACCAGGCAAAGCGCCATTCGCCATTCA	56
59	AACCGCCACCGATGATACAGGAGTGATTGGCC	32
60	GCCAGCATTGACAGGGGTCAGTACTCAGGAG	31
61	TTCAAATATCGCGTTTTAATTCGAGCTTCAAAGCGAACCAGACCGGAAGCAAACTC	56
62	TGCCACTACGAAATCAACGTAACAGACGAGAA	32
63	CCAGAACAATATTATTAAAGGCGAGAAAGGA	31
64	TGGCCAACAGAGATAGAACCCTTCTGACCTGAAAGCGTAAGAATACGTGGCACAGA	56
65	AAAGGAGCCTTTAATTGTATCGGTTTATCAGCTTGCTTTCGAGGTGAATTTCTTAA	56
66	GATTATTTACATTAGGGCGCCCCGCCGCGCTTAATG	36
67	ACACCAGAACGAGATTACCCAAGGCACCAAC	31
68	TAATAGTAGTAGCAATAAAGAAAACTAGCAT	31
69	CAAGAGAAGGATTAGGAGAGGCTGAGACTCCT	32
70	TACATAACGCCAAAAGGAATTACGAGGCATAGTAAGAGCAACACTATCA	49

71	CGTTATTAATTTTAAAAGTTTGAGTAACATTATCATTTTGCGGAACAAAGAAACCA	56
72	CAGTTGGCAAATCAACAGTTGAAAGGAATTGAGGAAGGTTATCTAAAATATCTTTA	56
73	CGCCGCTACGGCAGATTCACCAGTCACACGACCAGTAATAAAAGGGACATTC	52
74	TTCAGGGATAGCAAGCCCAATAGGAACCCATGTACCGTAACACTGAGTTTCGTCAC	56
75	ATCTAAAGCATCACCTTGCTGAACCTCAAATATCAAACCCTCAATCAATATCTGGT	56
76	CAGTACAAACTACAACGCCTGTAGCATTCCACAGACAGCCCTCATAGTTAGCGTAA	56
77	ATCAATATGATGCCTGAGTAATGTTATAACAG	32
78	GGCGAACGTGGGATTTTAGACAGGGGTAATAT	32
79	CCTGAGTAGAAGAGAAGTGTAGCCCCCGATT	31
80	AAATATGCAACTAAAGTACGGTGTCTGGAAGTTTCATTCCAGTAGGTAGTCAAATCACC	59
81	CAATAATAAGAGCATAAACACGCGAGGCGTT	31
82	TAGAGCTTGACGCCAGAATCCTGAACTCAAAC	32
83	AGGAAGATTGTATAAGCAAATATTTAAATTGTAAACGTTAATATTTTGT	49
84	CTGGCTCATTATAAGAGGACCAAAGTACAAC	31
85	AGGCAGGTCAGACGTACTGGGCCACCCTCAG	31
86	ACCACCCTCAGAGTGCCCCCGAGAGGGTTGA	31
87	TTAGCGAACCTTGCCAGTTACAAAAAGAAACA	32
88	CCATATCAAAATTAAAGAAGGATTAAGACGC	31
89	AGGGAAGAAATAAACAGGAGGCCGACCGCCAG	32
90	GGAGATTTGTTGACCAACTTTGAACCAGTCAG	32
91	TATAAGTATAGTATAAACAGTTAACCGCCACC	32
92	TGAGAAGAGTCAATTACCTGAGCAATTTGCAC	32
93	GATTAGTAATAACAGGCCACCTAAATCGGAA	31
94	CGCTAATATCAGATTTTTTGCAAGCAAATCA	31
95	CCGTAAAGCACGAGTAAAAGAGTCACTTCTTT	32
96	GAGTAGATTTAGTTTAGAACAAATTAATGCC	31
97	ATGAAATAGCAATGCCTAATTCCCGACTTGC	31
98	TTTTCGAGCCAGTAATAAGAGAATATAAAGTACCGACAAAAGGTAAAGTAATTCTG	56
99	GTATCATATGCGTTATACAAATTCTTACCAGTATAAAGCCAACGCTCAACAGTAGG	56
100	AAGGCGTTAAATAAGAATAAACACCGGAATCATAATTACTAGAAAAAGCCTGTTTA	56
101	ACCGACTTGAGCCATTTGGGAATTAGAGCCAGCAAAATCACCAGTAGCACCATTAC	56
102	ATATAAAAGAAACGCAAAGACACCACGGAATAAGTTTATTTTGTCACAATCAATAG	56
103	GGAAACCTGTCGTGCCAGCTGCATTAATGAATCGGCCAACGCGCGGGGAGAGGCGG	56
104	GACGTTGGGAAGAACCGAACATCATCGCCTG	31
105	GGAACGCCATCAAAAATAATTCGCGTCTGGCCTTCCTGTAGCCAGCTTTCATCAAC	56
106	ATTAAATGTGAGCGAGTAACAACCCGTCGGATTCTCCGTGGGAACAAACGGCGGAT	56
107	TGTTTGGATTATAACATTTATTAATTTTCCC	31
108	ATAAATTGTGTCAATCATAAGGGAAAAATCTA	32
109	AAGTAAGCAGATATTTATCCTTGCTATTTTGCACCC	36
110	CGCCATTAAAAATACCGAACGAACCACCAGCAGAAGATAAAACAGAGGTGAGGCGG	56
111	GACTCTAGAGGATCCCCGGGTACCGAGCTCGAATTCGTAATCATGG	46
112	TAACCGTTGTAGCAATTGTCCATGGGTCGAGGTG	34
113	CCAGAAGGAGCGGAATTATCATCATATTCCTGATTATCAGAAGTACATAAATC	53
114	GGGAGGGAAGGTAAATATTGACGGAAATTATTCATTAAAGGTGAATTATCACCGTC	56
115	GGCTGCGCAACTGTTGGGAAGGGCGATCGGTGCGGGCCTCTTCGCTATTACGCCAG	56
116	TTGATATTCACAAGGCTTTTCTCAGAACCGC	31
117	TCAAGATTAGTGAATCTTACCAACTTTAAGAA	32
118	CAATATTTTTGAATGGCTATTAGTCTTTAATGCGCGAACTGATAGCCCTAAAACAT	56
119	TACCGAAGCCCTTGCTAACGGAAGCCTTAAA	31
120	GTGTATCACCGTGCCTTGAGTAACGAGCCGCC	32
121	TCAGTATTAACACCGCCTGCAACAGTGCCACGCTGAGAGCCAGCAGCAAATGAAAA	56
122	TACCTTATGCGATCAGACCAGCGATTATACC	31
123	TCAACTTTAATCACTGACCTAACACTCATCT	31
124	CCATTGCAACAGGCGGGAGCGCGAAAGGAGC	31
125	CAATCGCAAGACAAAGAACGCGAGAAAACTTTTTCAAATATATTTTAGT	49
126	TTGACCCCCAGGCGCATAGGCTGGTTGTGAAT	32
127	GGGCGCTAGGCGTTAGAATCAGAGAAAAACGC	32
128	GTCACCCTCAGCAGCGAAAGACAGCATCGGAACGAGGGTAGCAACGGCTACAGAGG	56
129	GAGAAACAATAAGGGTTATATAACTATATGTAAATGCTGATGCAAATC	48
130	CACCCTCAGATAAGCGTCATACATACAAATAA	32
131	TCATAGCTGTTTCCTGTGTGAAATTGTTATCCGCTCACAATTCCACACA	49
132	CAATAACCTGTTTTTTGCGGAAGGCTATCAG	31
133	GATATAGAAGCAAATAAGAAACGAGAGATAAC	32
134	CTGGCGAAAGGGGGATGTGCTGCAAGGCGATTAAGTTGGGTAACGCCAGGGTTTTC	56
135	AAGCGCGAAAAGATGAACGGTGTATTTAAGAA	32
136	GTCATTGCCTGACCCTGTAATACTAGCTATAT	32
137	GGAGAGGGTAAAGGATAAAAATTTTTGACCAT	32
138	GGGAGGTTTTAGCGTCTTTCCAGAAGCTATCT	32
139	CCAGTCACGACGTTGTAAAACGACGGCCAGTGCCAAGCTTGCATGCCTGCAGGTC	55
140	TTTCATTTGGGGCACATTATGAGAGTCTGGA	31
141	TGCGTAGATTTTCAAATCGCCATAGGTCTGA	31
142	AAAAGGTGGCATCGCTAAATGAATCGATGAA	31
143	GGTTTTGCTCAGTTTCTGAAACATGAACCACCCTC	35
144	TACGCAGTATGTTAGCAAACGTAGAAAATACATACATAAAGGTGGCAAC	49
145	GTAGAAACCAATCAATAATCGGCTGTCTTTCCTTATCATTCCAAGAACGGGTATTA	56

146	CAGGGCGATGGCCCACTACGTGAACCATCACCCAAATCAAGTTTTTTGCACGCAAAT	57
147	CATTAGCAAGGCCGGAAACGTCACCAATGAAACCATCGATAGCAGCACCGTAATCA	56
148	GTAGCGACAGAATCAAGTTTGCCTTTAGCGTCAGACTGTAGCGCGTTTTCATCGGC	56
149	TGATTGCCCTTCACCGCCTGGCCCTGAGAGAGTTGCAGCAAGCGGTCCACGCTGGT	56
150	GTCAATCATATAGCAAAATTAAGCATTAACATCCAATAAATCATACAGGC	50
151	TTTTGCTAAACAACTTTCAACAGTTTCAGCGGAGTGAGAATAGAAAGGAACAACTA	56
152	GAATAAGGCTTGCCCTAAGCTGCAAAATACGTAA	34
153	AAGTGCCGTCTGCCTATTTCGGAATCAGAGCC	32
154	AGAACCGCCACCCCCTATTAACCAGGCGGAT	31
155	CGATCTAAAGTTTTGTCGTCTTTCCAGACGTTAGTAAATGAATTTTCTGTATGGGA	56
156	CTTTGAGGACTAAAGACTTTTTCATGAGGAAGTTTCCATTAAACGGGTTCATTCAGT	57
157	GTTTAGTACCTAATAAGTTTTAACGGAGGTTG	32
158	TCCAATACTGCGGAATCGTCATAAATATTCATTGAATCCCCCTCAAATGCTTTAAA	56
159	CAGTTCAGAAAACGAGAATGACCATAAATCAAAAATCAGGTCTTTACCCTGACTAT	56
160	GAGATCTACAGAGAAGCCTTTATTCAAATGGT	32
161	TCTAGCTGATCCTCATATATTTTACTGCGAAC	32
162	TTGATTCCCAATTAATGCAATATTCAACCGT	31
163	ATCCTCATTAAAGGTTCCAGGCCACCACCCTCATT	35
164	AGAAGTATTAGACTTTACAAACAATTCGACAACTCGTATTAAATCCTTTGCCCGAA	56
165	GAGACTACCTAATACCAAGTTACAAGGTTTAA	32
166	CGGAACCAGAGCCACCACCGGAACCGCCTCCCTCAGAGCCGAGTATTAATTAGCGG	56
167	TTTGCGTATTGGGCGCCAGGGTGGTTTTTCTTTTCACCAGTGAGACGGGCAACAGC	56
168	TAGATACATTTCGTCAACGCGCTATTTTTGA	31
169	CGCCCAATAGTTTAACGTCAAAAATAATTGAG	32
170	AACCAAGTACCGCACTCATCGAGAACAAGCAAGCAACATAAAAACAGGGAAGC	53
171	AGAAAGGCCGGAGACAAAGATTCAAAAGGGTG	32

Table S4.2.2. Sequences of oligos used for the VPM assembly.

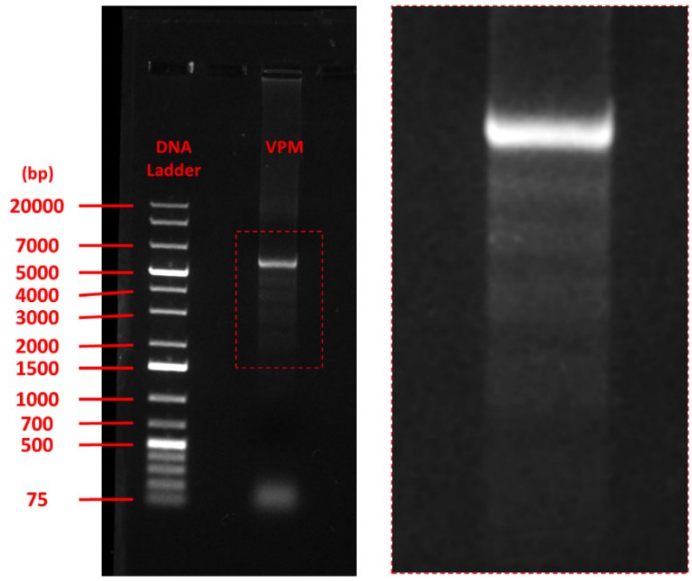

Figure S4.2.2. Gel Electrophoresis prior to filtering the VPM assembly. Left image shows VPM assemblies and a 1kbp+ DNA ladder. Right image shows a zoomed in image of the VPM lane, showing a quantized streak of shorter assemblies, which are attributed to partial VPM assemblies with a randomly cut scaffold.

Figure S4.2.2 shows the migration through a 1% agarose gel of VPMs after the assembly process, and prior to the filtering and washing steps (See Methods section). A clear band can be

observed slightly higher than the 5kbp reference, which we assign to fully assembled VPMs. Underneath the VPM band, quantized bands can also be observed ranging from down to 1.5 kbp DNA reference length. We assign these subpopulations to the partial VPM assemblies which, as discussed, correspond to broken scaffolds undergoing the assembly process. Lastly, a band corresponding to excess staple strands can be observed around the 75 bp DNA reference length, which is consistently removed by the three wash steps after assembly.

S4.2.2. Velocity Profile Extraction Robustness

In this section we aim to show the sensitivity of the threshold-crossing algorithm to analysis parameters and velocity-extraction methods in order to validate the results shown in the main text and the interpretations drawn from them. This is achieved by comparing different methods of velocity extraction, by varying threshold and hysteresis values, and by reporting the effect of temporal resolution on velocity profiles.

As described and showed in Figure 4.1.1 of the main text, the standard analysis method used for all figures in the main text relies on defining a threshold value away from the open-pore baseline and noting the times at which the current crosses the established threshold. When the threshold is set between the blockage states of the 3HB and dsDNA segment blockages, the threshold-crossing times can be used to temporally delimit the passages of the different VPM segments. Knowing the length ℓ_i and the measured duration τ_i of each segment, the mean velocity $\bar{v}_i$ is calculated by fitting the distribution of ℓ_i/τ_i to a normal function, from which the standard deviation σ_v can also be extracted.

We first compare two methods of calculating segment velocities. Namely, the standard method described above is compared to the one used by Chen *et al.*,[67] wherein the centers of each 3HB segments are used as reference for temporal and spatial calculations, as depicted in Figure S4.2.3a. The time corresponding to the center of 3HB segments was found by using the middle-point between that segment's threshold crossings. Two translocation velocity profiles are shown in Figure S4.2.3a, that of a 9 nm pore, and a 20 nm pore under an applied 200 mV voltage. For larger pores, this technique does not have much of an effect on the absolute velocity values. However, for smaller pores, the 3HB segments interact strongly with the pore walls and as a result the absolute velocity values are significantly smaller for velocities extracted from 3HB-centers.

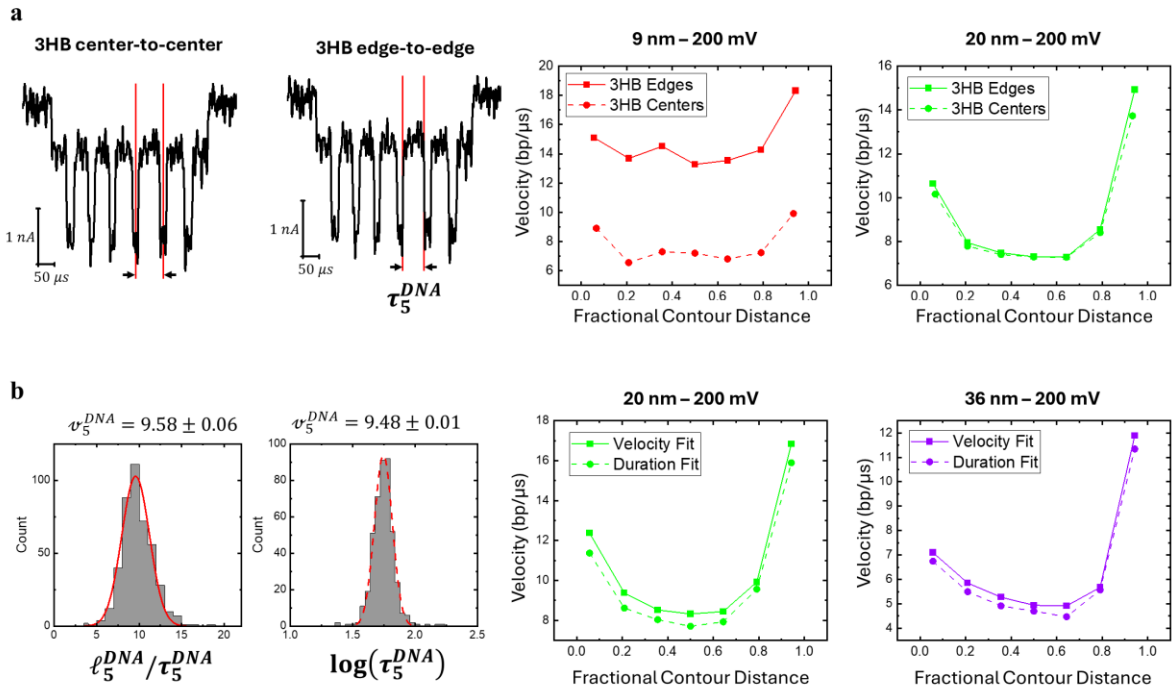

Figure S4.2.3. Different translocation velocity extraction techniques a) Sketches displaying the workings of each method, i.e. the bump-center to bump-center technique, the bump edged velocities, or the bump edged durations. **b)** translocation velocity profiles extracted using the three techniques. **c)** Effect of pore size on end velocity, measured using different techniques.

Empirically, translocation time distributions are well described by log-normal distributions. Using segment edges as reference, we now compare extracting mean segment velocities $\bar{v}_i$ from normally fitting segment velocities $\langle \ell_i/\tau_i \rangle$ or log-normally fitting segment durations τ_i, extracting the mean segment duration $\bar{\tau}_i$, then calculating the mean velocity as $\bar{v}_i = \ell_i/\bar{\tau}_i$. Figure S4.2.3b displays the methods described and plots translocation velocity profiles calculated with both extraction methods for a 20 nm and a 36 nm pore. Velocities extracted from both methods are very similar, although the velocities extracted from duration fits are consistently slightly smaller. Given that both fittings are empirical in nature, we chose to use the velocity fitting method, since unlike log-normal functions, it results in reasonable standard deviation values to be used as error bars.

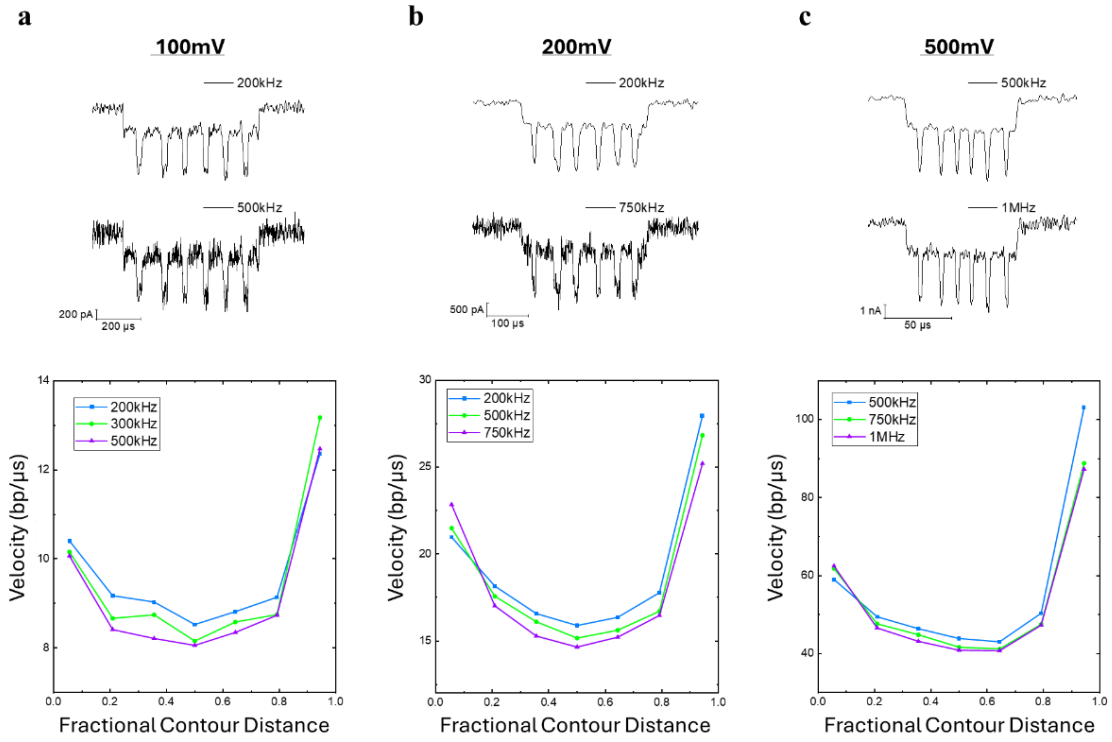

Figure S4.2.4. Effect of cutoff frequency on velocity extraction for a 10 nm pore. Each figure shows the trace of a VPM event and the extracted velocity profiles for a) a voltage of 100 mV, and cutoff frequencies of 200, 300 and 500 kHz, b) a voltage of 200 mV, and cutoff frequencies of 200, 500 and 750 kHz, and c) a voltage of 500 mV, and cutoff frequencies of 500, 750 and 1,000 kHz.

As the durations of VPM segments get close to the temporal resolution imposed by the signal bandwidth, it is well known and understood that transient signals become attenuated and deformed. To this end, we now investigate the effects of a signals' temporal resolution on velocity profiles' absolute values and overall shape. As shown in Figure S4.2.4, velocity profiles from VPMs passing through an 11 nm pore under voltages of 100, 200 and 500 mV were obtained after filtering current recordings with a Bessel low pass filter with three different cutoff frequency values. Higher cutoff frequencies mostly result in smaller translocation velocities, although values remain within 10% across the different bandwidths explored. Moreover, the shape of the profiles is not affected significantly.

We finally test the sensitivity velocity analysis on threshold parameters, achieved simply by analyzing the same dataset with two different threshold settings. The first is the standard method introduced above, wherein the threshold is used to detect the start of 3HB segments, and the hysteresis is used to detect its end. The second method does not use a hysteresis, and as such only the threshold is used to determine the beginning and end of each 3HB, as depicted in Figures S4.2.5a-b. Figures S4.2.5a-b show the velocity profiles from translocations through an 11 nm pore under voltages of 100 and 500 mV, the values of which were extracted with (green) and without (purple) a hysteresis. We note that to analyze events with no hysteresis, a good signal to noise ratio is required as noise from a DNA blockage state could otherwise easily trigger the threshold and be detected as a 3HB segment instead. As such, cutoff filters of 300kHz were used for the analysis of VPM translocations under 100 mV to minimize the events containing false-positive threshold crossings induced by current fluctuations. While increasing temporal resolution would certainly result in more accurate velocity measurements, the 100 mV and 500 mV datasets from Figures S4.2.4b and S4.2.4d show that the profiles remain mostly unaffected. Note by choosing to evaluate

the velocity profiles under two significantly different voltage biases, we tested the limited temporal resolution of higher voltage and the worse signal to noise ratios from lower voltages, thus ensuring the robustness of the velocity measurements to threshold parameters.

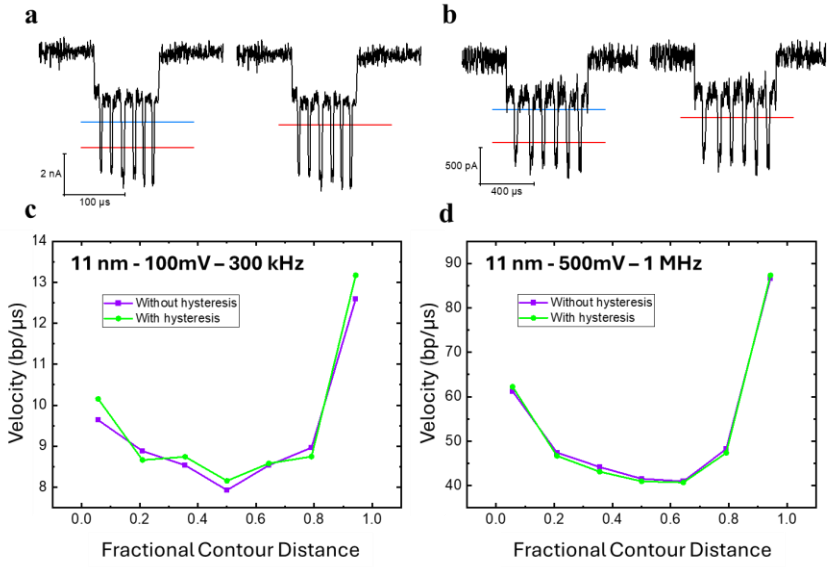

Figure S4.2.5. Effect of threshold and hysteresis on velocity extraction. **a-b)** Sketch demonstrating the placements of thresholds (red) and hysteresis (blue) for the two different analyses parameters tested. **c-d)** Translocation velocities measured with zero (purple) and non-zero (green) hysteresis for VPM translocations in a 11 nm pore, under a 100 mV voltage (c) and under a 500 mV voltage (d). Cutoff frequencies used to filter the signals are denoted in the figures.

To concisely conclude this section, although not perfect, we conclude from these simple tests that the analysis method used throughout this work constitutes a reliable way to characterize translocation velocity profiles. Namely, if the segment durations are significantly longer than the system's rise time, we suggest velocity profiles do not strongly depend on the analysis parameters.

S4.2.3. Velocity Profiles

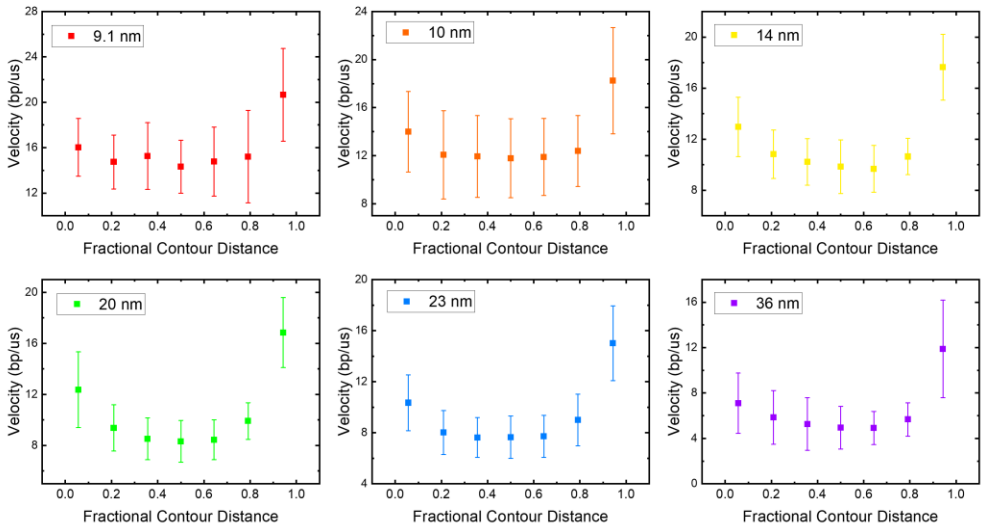

Figure S4.2.6. Velocity Profiles obtained for different pore sizes, denoted in the legends. Error bars are the standard deviations of the extracted velocities.

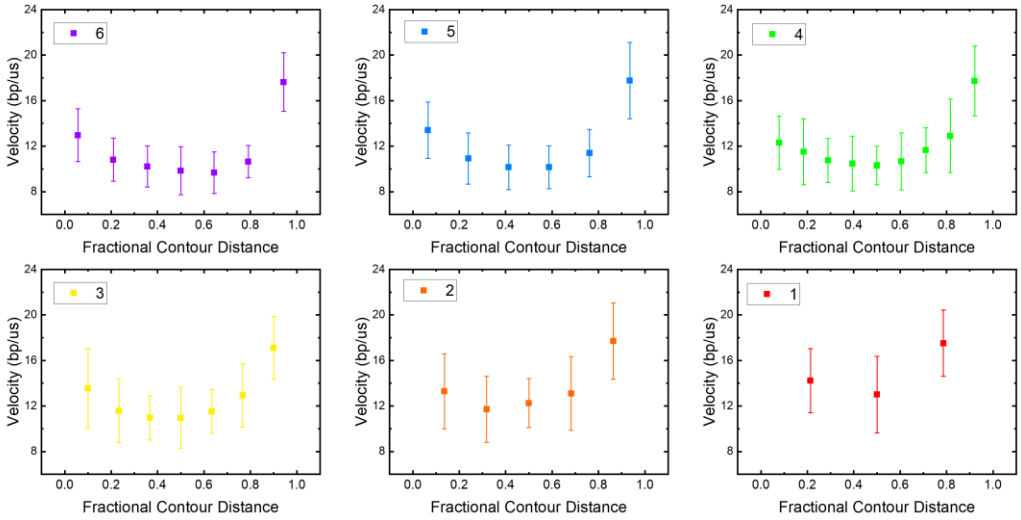

Figure S4.2.7. Velocity Profiles obtained for different partial VMP assemblies. Legend indicates number of 3HB segments 3HB segment velocities were used for partial VPMS with $n_{3HB} < 5$ to increase spatial resolution. Error bars are the standard deviations of the extracted velocities.

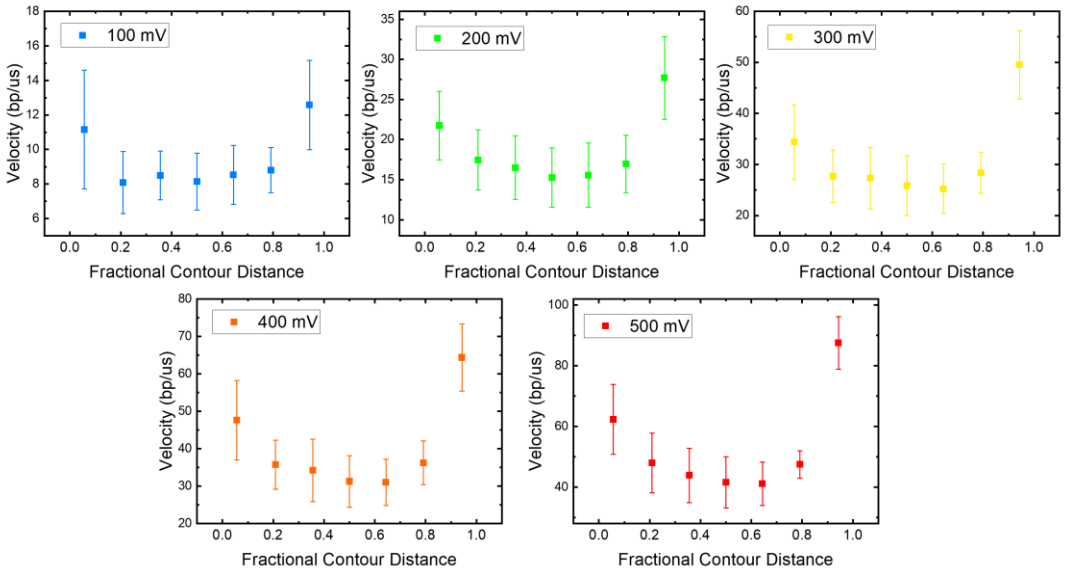

Figure S4.2.8. Velocity Profiles obtained under different applied voltages. Error bars are the standard deviations of the extracted velocities.

S4.2.4. Translocation Time vs Pore Size

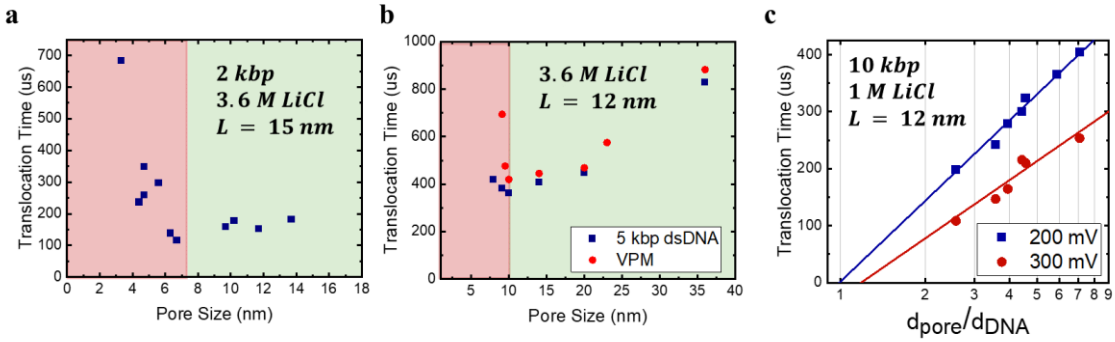

Figure S4.2.9. Translocation vs pore sizes in different conditions. **a)** 2 kbp dsDNA in 3.6 M LiCl with 15 nm thick membranes. **b)** 5 kbp dsDNA and VPM in 3.6 M LiCl in 12 nm thick membranes. **c)** 10 kbp dsDNA in 1M LiCl with 12 nm thick membranes.

S4.2.5. Expanding on the Toy Model

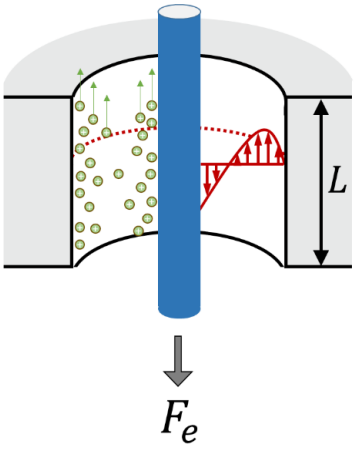

Figure S4.2.10. Developing the toy model. Depiction of internal forces involved when pulling a charged cylinder through a charged cylindrical channel.

In the main text, a toy model is used to experimentally characterize the forces in nanopore systems. This was achieved through Equation 4.1.3, which required no explicit derivation of individual terms for forces considered in the model. Such derivations can however be achieved for the internal forces under the assumption of working with very long pores, i.e. ignoring end effects and forces outside the pore. The resulting expressions provide useful insights for interpreting translocation velocity results of the main text, as shown here.

As per Figure S4.2.10, let a solid cylinder of radius r_{DNA} move through a hollow cylindrical channel of radius r_{pore} at a velocity $\vec{v}_{DNA} \equiv v_{DNA}\hat{z}$ in response to a uniform electrical field $\vec{E} = E\hat{z}$. Furthermore, let the pore walls and moving cylinder have non-zero surface charge densities with corresponding surface potentials of $\phi(r_{pore}) \equiv \phi_{pore}$ and $\phi(r_{DNA}) \equiv \phi_{DNA}$, respectively. Note that cylindrical coordinates are used here, such that r is the radial distance from the pore central axis. The radial dependence of the charge density $\rho(r)$ of counterions between the two charged surfaces is described by the Poisson equation as:

$$\nabla^2\phi(r) = -\frac{\rho(r)}{\varepsilon}\,. \tag{S4.2.1}$$

Here, z-independence is assumed, and ε is the bulk's permittivity. Similarly, the radial dependence of the fluid velocity $\vec{v}(r) = v\hat{z}$ between both cylinder's surface is described by the Navier-Stokes equation under an electric field:

$$\eta\nabla^2 v = -\rho(r)E\,. \tag{S4.2.2}$$

Here, we consider the no-slip boundary conditions $v(r_{DNA}) = v_{DNA}$ and $v(r_1) = 0$. Combining both differential equations, $\nabla^2 v = \frac{\epsilon E}{\eta}\nabla^2\phi$, a general expression can be found for the radial fluid velocity profile $v(r)$:

$$v(r) = \frac{\epsilon E}{\eta}\phi(r) + c_1 \ln r + c_2\,. \tag{S4.2.3}$$

Applying the boundary conditions, the final expression for $v(r)$ is found to be:

$$v(r) = \frac{\varepsilon E}{\eta}\left(\phi(r) - \phi_{pore}\right) + \left[v_{DNA} - \frac{\varepsilon E}{\eta}\left(\phi_{DNA} - \phi_{pore}\right)\right]\frac{\ln\frac{r}{r_{pore}}}{\ln\frac{r_{DNA}}{r_{pore}}}\,. \tag{S4.2.4}$$

The drag force imparted by the fluid on the moving cylinder of length L_{DNA} can thus be calculated by integrating the viscous stress tensor over moving cylinder's surface, i.e.:

$$\begin{aligned} F_{drag} &= 2\pi r_{DNA} L_{DNA}\eta\left.\frac{dv}{dr}\right|_{r_{DNA}} \\ F_{drag} &= -Q_{DNA}E + \frac{\varepsilon E}{\eta}\left(\phi_{DNA} - \phi_{pore}\right)\frac{2\pi L_{DNA}\eta}{\ln\frac{r_{pore}}{r_{DNA}}} - \frac{2\pi L_{DNA}\eta}{\ln\frac{r_{pore}}{r_{DNA}}}v_{DNA}\,. \end{aligned} \tag{S4.2.5}$$

Note that Q_{DNA} corresponds to the total charge of the moving cylinder and arises from Gauss' law, i.e. $Q = \varepsilon 2\pi r_{DNA} L_{DNA}(-d\phi(r_{DNA})/dr)$.

In Equation S4.2.5, the first term simply corresponds to the drag force exerted on the charged cylinder under an applied electric field in free solution (i.e. $r_{pore} \to \infty$), perfectly

balancing the driving electric force $Q_{DNA}E$ in the opposite direction as expected. Similarly, the first and second term, when combined, correspond to the drag force expected from a stationary charged cylinder ($v_{DNA} = 0$) stalled inside a charged cylindrical channel, as determined and tested experimentally.[101] Finally, the last term corresponds to the hydrodynamic drag imparted by an uncharged cylinder moving through an uncharged cylindrical channel , i.e. $\phi_{DNA} = \phi_{pore} = 0$. Equation S4.2.5 thus shows that drag forces are superimposed and could be rewritten as $F_{drag} = F_{EO} + \gamma_{in} v_{DNA}$, where

$$\gamma_{in} = \frac{2\pi L_{DNA}\eta}{\ln \frac{r_{pore}}{r_{DNA}}} \propto \left(\ln \frac{d_{pore}}{d_{DNA}}\right)^{-1} . \tag{S4.2.6}$$

An expression for v_{DNA} can be found by balancing the electric pulling force $F_e = Q_{DNA}E$ and the drag forces of Equation 4.2.6, $F_e + F_{drag} = 0$:

$$v_{DNA} = \frac{\varepsilon E}{\eta}\left(\phi_{DNA} - \phi_{pore}\right) = (\mu_{EP} - \mu_{EO})E . \tag{S4.2.7}$$

Interestingly, due to the common inverse log dependence of the $(F_e - F_{eo})$ and γ_{in} terms, Equation S4.2.7 predicts that the steady-state velocity of a charged cylinder moving through a charged cylindrical channel is independent of pore size, unlike the experimental results presented in Figure 4.1.3 of the main article and Figure S4.2.9. As such, the expected velocity v_{DNA} simply corresponds to the difference between its bulk electrophoretic velocity $\mu_{EP}E$ and the electroosmotic flow velocity due to the charged pore surface $\mu_{EO}E$.

Because of the superimposed nature of the drag force (Eq. S4.2.5), a generic term can be considered for the drag imparted on the segment of length ℓ_{ext} under tension outside the pore, i.e. F_{ext}, as discussed in the main text:

$$F_{ext} = \gamma_{ext}(\ell) v_{DNA} = -2\pi C' \eta \ell_{ext} v_{DNA} . \tag{S4.2.8}$$

Here the C' coefficient is an undefined shape factor on the order of unity, and the 2π factor is pre-emptively used to simplify the derivation of an expression for the steady-state velocity v_{DNA}. If we assume that the electric field is completely inside the pore, then we can replace L_{DNA} with the pore length L_{pore} in Equation S4.2.5, such that:

$$F_{drag} = -Q_{DNA}E + \frac{\varepsilon E}{\eta}\left(\phi_{DNA} - \phi_{pore}\right)\frac{2\pi L_{pore}\eta}{\ln\frac{r_{pore}}{r_{DNA}}} - \frac{2\pi L_{pore}\eta}{\ln\frac{r_{pore}}{r_{DNA}}}v_{DNA} - 2\pi C'\eta\ell_{ext}v_{DNA} \quad \text{(S4.2.9)}$$

The steady state velocity $v_{DNA}(\ell_{ext})$ can thus be found by balancing forces:

$$v_{DNA}(\ell_{ext}) = \frac{\frac{\varepsilon E}{\eta}\left(\phi_{DNA} - \phi_{pore}\right)}{1 + C'\ln\left(\frac{r_{pore}}{r_{DNA}}\right)\frac{\ell_{ext}}{L_{pore}}}\,. \quad \text{(S4.2.10)}$$

Unlike Eq. S4.2.7, Equation S4.2.10 shows that the instantaneous velocity depends on pore size, as expected from experimental results (Figure 4.1.3). Let $s \in [0, L_{DNA}]$ denote the position of the polymer segment inside the pore throughout translocation. Translocation durations can be calculated by integrating $d\tau = ds/\left|v_{DNA}\left(\ell_{ext}(s)\right)\right|$:

$$\begin{aligned}\tau &= \int_0^{L_{DNA}} \frac{ds}{|v_{DNA}(s)|} \\ &= \frac{1}{\frac{\varepsilon E}{\eta}\left|\phi_{DNA} - \phi_{pore}\right|}\left(L_{DNA} + C'\ln\left(\frac{r_{pore}}{r_{DNA}}\right)\frac{1}{L_{pore}}\int_0^{L_{DNA}}\ell_{ext}(s)ds\right) \\ \tau &= \frac{1}{\frac{\varepsilon E}{\eta}\left|\phi_{DNA} - \phi_{pore}\right|}\left(L_{DNA} + C'\ln\left(\frac{r_{pore}}{r_{DNA}}\right)\frac{\bar{\ell}L_{DNA}}{L_{pore}}\right)\,. \quad \text{(S4.2.11)}\end{aligned}$$

In the final expression of Eq. S4.2.11, we introduced $\bar{\ell} \equiv L_{DNA}^{-1}\int_0^{L_{DNA}}\ell_{ext}(s)ds$, the average length of the polymer segment under tension throughout the translocation process. Under the reasonable assumption that $\bar{\ell}$ scales with the polymer radius, $\bar{\ell} \propto R_g \propto L_{DNA}^{\nu}$, we can further write:

$$\tau(L_{DNA}) \approx \frac{1}{\frac{\varepsilon E}{\eta}\left|\phi_{DNA} - \phi_{pore}\right|}\left(L_{DNA} + \frac{C \ln\left(\frac{r_{pore}}{r_{DNA}}\right)}{L_{pore}} L_{DNA}^{1+\nu}\right). \quad \text{(S4.2.12)}$$

Equation S4.2.12 shares identical dependence on polymer length L_{DNA} as predicted by iso-flux tension propagation principles:[71] $\tau = AL_{DNA} + BL_{DNA}^{1+\nu}$, which shows that the coefficient α measured experimentally ($\tau \sim L_{DNA}^{\alpha}$) depends on whether the A or B coefficient dominates for the experimental conditions used. Eq. S4.2.12 shows that longer or narrower pores result in weaker $L_{DNA}^{1+\nu}$ coefficients, thus resulting in smaller α coefficients with values closer to 1. This is expected since the time-independent internal drag forces dominate the process, thus promoting a flatter velocity profile, consistent with arguments presented in the main text.

Additionally, Equations S4.2.10 and S4.2.12 predict that velocity and translocation times should reduce and increase logarithmically with pore size, respectively, which partly explain the results of Section S4.2.4. However, both equations fail to predict why the uniform monotonic reduction with increasing pore size observed in Figure 4.1.3. Equation S4.2.10 instead predicts that the end velocity should be pore-size independent, while only $\ell_{ext} \neq 0$ measurements from middle segments should be pore-size dependent. These inaccuracies most likely arise from ignoring the end-effects of the channel. For instance, the potential drop does not occur solely inside the pore, but instead also extends into the access regions, an effect which is more important in larger pores. This is also true of the electroosmotic flow, which is also present outside the pore. The first term $\left(\frac{\varepsilon E}{\eta}\left|\phi_{DNA} - \phi_{pore}\right|\right)^{-1}$ of Eq. S4.2.12 is thus expected to oversimply the analysis and could potentially provide another source of pore size dependence when calculated properly.

S4.2.6. Simulated Polymer Conformations

Following Tree *et al.*,[192] conformations of Discrete Worm-Like Chains (DWLC) tethered to a pore, i.e. with 10 bp inserted into a pore, were randomly generated in an attempt to predict the minimal velocity location x_{min}. For a polymer with a length of N base pairs (bp), this was achieved by generating N steps of length $\ell_s = 1\ bp$. To represent polymer conformations prior to single-file translocations, the first 10 steps were imposed to be directed along the axis of the pore. After the first 10, the rest of the steps were randomly generated and followed the discrete statistics imposed by wormlike chains. For a chain with a persistence length of ℓ_p, the angle between two consecutive steps is known to follow the following probability distribution:

$$P(\theta) = \frac{\frac{\ell_p}{\ell_s}}{2\sinh\frac{\ell_p}{\ell_s}} e^{\frac{\ell_p}{\ell_s}\cos\theta} \sin\theta \ . \tag{S4.2.13}$$

This probability can be integrated and inverted to be sampled from, with the sampling function being:

$$\theta(r) = \cos^{-1}\left(1 + \frac{\ell_s}{\ell_p} ln\left(1 - r\left(1 - e^{-2\frac{\ell_p}{\ell_s}}\right)\right)\right). \tag{S4.2.14}$$

Here, the value $r \in U(0,1)$ is numerically sampled from the uniform distribution and corresponds to randomly sampling the cumulative distribution function, $r = \int_0^\theta P(\theta)d\theta$.

Figure S4.2.11a shows a few of the polymer conformations generated with the above method and with $\ell_p = 150\ bp$. For each generated polymer, the furthest monomer is located, and its distance from the pore center R_{max} is calculated. By then calculating the contour length between the furthest and extremity monomers ℓ_{end}, the predicted fractional location of the velocity minima was then calculated, as per Equation 4.1.4 of the main text, rewritten here:

$$x_{min} = 1 - \frac{R_{max} + \ell_{end}}{L} \,. \qquad \text{(S4.2.15)}$$

Figure S4.2.11b shows the distributions of x_{min} values calculated for 5000 simulated polymer conformations. The location of the most probable values from each distribution were noted down, and then used to compare to the experimental velocity profiles in Figure 4.1.5 of the main article, showing good agreement between experimental and simulated x_{min} values.

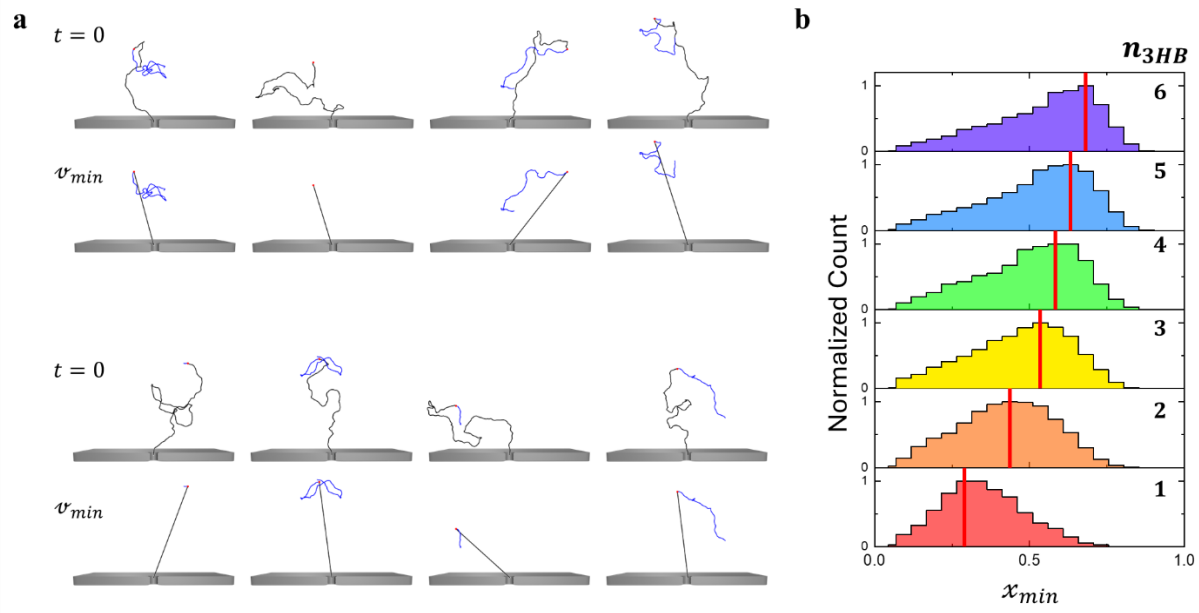

Figure S4.2.11. Simulated x_{min} values. a) Simulated polymer conformations shown at two instances: at the onset of translocation, and when the velocity is minimal, i.e. when the tension front reaches the furthest polymer segment. Only segments on the *cis* side are depicted. **B)** Distributions of x_{min} calculated for different polymer lengths.

S4.2.7. Segment Duration Correlations

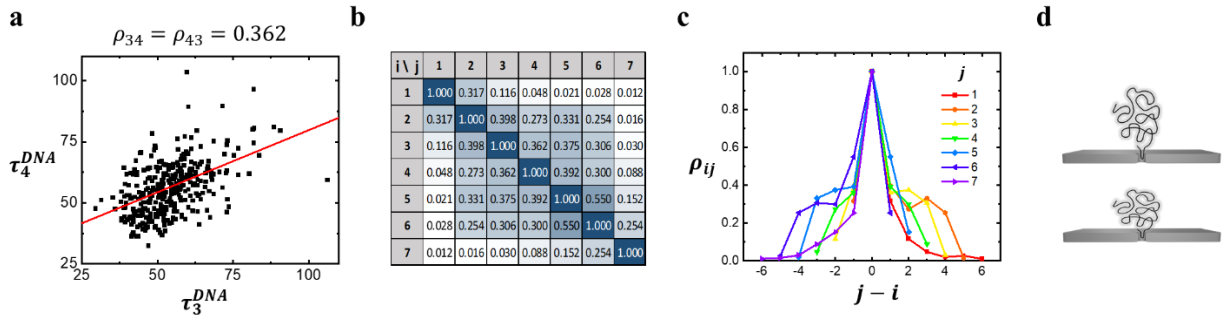

i \ j	1	2	3	4	5	6	7
1	1.000	0.317	0.116	0.048	0.021	0.028	0.012
2	0.317	1.000	0.398	0.273	0.331	0.254	0.016
3	0.116	0.398	1.000	0.362	0.375	0.306	0.030
4	0.048	0.273	0.362	1.000	0.392	0.300	0.088
5	0.021	0.331	0.375	0.392	1.000	0.550	0.152
6	0.028	0.254	0.306	0.300	0.550	1.000	0.254
7	0.012	0.016	0.030	0.088	0.152	0.254	1.000

Figure S4.2.12. Correlations of segment durations for VPM translocations. **a)** Correlation of τ_3^{DNA} and τ_4^{DNA}, resulting in the extraction of $\rho_{43} = \rho_{34}$. **b)** Tabulation of ρ_{ij} with cell color intensities mapped to the value of ρ_{ij}. **c)** Plot of ρ_{ij} vs $j - i$. Each color corresponds to a fixed value of j. **d)** Initial polymer conformations possibly explain long range correlations observed for middle segments undergoing tension propagation.

Following Chen *et al*,[67] we measured the correlation between segment durations within single translocation events. As shown in Figure S4.2.12a, this was achieved by calculating the Pearson correlation coefficient ρ_{ij} between τ_i^{DNA} and τ_j^{DNA}, i.e. the durations of the i^{th} and j^{th} dsDNA segment. Figure S4.2.12b displays all the ρ_{ij} values calculated for VPM translocations in a 14 nm pore in a table, where the color intensity of each cell is mapped to the corresponding ρ_{ij} value. As demonstrated by higher values near the table diagonal, the correlation from adjacent segments is strongest than ones further separated. This is expected from neighboring segments reacting to a monomer undergoing an impulse. These interactions are short-range in nature, as the force dissipates throughout the polymer, i.e. a sudden velocity change of one extremity segment will not affect the velocity state of the other extremity of a long polymer.

For better visualization, Figure S4.2.12 c shows the correlation values ρ_{ij} plotted against the segment separation $j - i$, where each color corresponds to fixed j value, and varying i values. In both figures the correlation between extremity segments, i.e. $j = 1$ and $j = 7$, is consistently weaker than a non-extremity segment with its neighboring segments, as observed by the faster

decay of ρ_{i1} and ρ_{i7} away from $j - i = 0$ in Figure S4.2.12c. This behavior is consistent across the data acquired for this work. We suggest that the higher correlations between non-extremity segments arise from long-range interactions provided by polymer conformations at the onset of translocation, as previously suggested by Lu *et al*.[177] According to Tension Propagation principles, strongly supported by the experiments of this work, a polymer that arrives at the pore in an elongated conformation will have most of its segment farther to the pore than a polymer arriving with a more compressed conformation (Figure S4.2.12d). In addition to short range correlations, largely separated segments are expected be correlated through that polymer's conformation at the onset of translocation.

S4.2.8. Voltage Dependence of Velocity Profiles

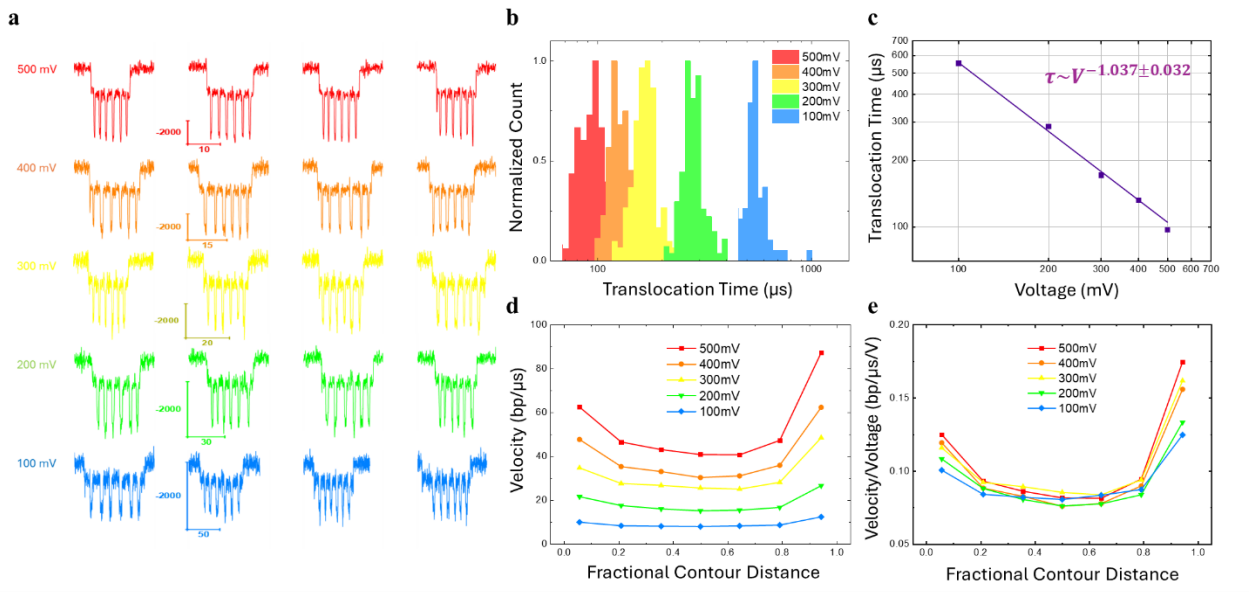

Figure S4.2.13. Effect of voltage on translocation velocity. a) Traces of VPM translocations under voltages ranging from 100 mV to 500 mV measured in a 10 nm pore. **b)** Distribution of VPM translocation times in different voltages. **c)** Plot of mean translocation time vs voltage fitted to a power-scaling law $\tau \sim V^{-\beta}$ with $\beta = 1.04 \pm 0.03$. **d)** Translocation velocity profiles normalized by the applied voltage.

Here, we characterize the effect of applied voltage ΔV on translocation velocity profiles. To this end, VPM passages through a 10 nm nanopore were recorded under voltages of 100, 200, 300, 400 and 500 mV. Traces of each voltage measurements are shown in Figure S4.2.13a. Figure S4.2.13b shows the distribution of VPM translocation times τ, the mean values of which are plotted in Figure S4.2.13c against corresponding ΔV. The mean duration data was fit to a power scaling law of the form $\bar{\tau} \sim \Delta V^{-\beta}$, with a scaling coefficient of $\beta = -1.04 \pm 0.03$ measured. This inverse dependence of $\bar{\tau}$ on voltage agrees with previously published experimental results for dsDNA, which suggests again that VPM translocations should be a good representation of dsDNA translocation kinetics.

Figure S4.2.13d plots the translocation velocity profiles measured for the different voltages. To normalize the effect of voltage resulting in velocities increasing five-fold in between the 100 and 500 mV measurements, Figure S4.2.13e instead plots the translocation velocities divided by the corresponding voltage. As a result, the velocities of the five non-extremity segments essentially overlap, as expected from a perfectly inverse voltage dependence. Interestingly, however, both the first and last DNA segment velocities show voltage dependence, with higher voltages resulting in higher velocities. At the moment of writing, it is unclear whether this observation arises from a physical phenomenon not fully understood yet, or simply due to the limitations of our analysis technique and its sensitivity to temporal resolution, as discussed in section S4.2.2 above. Regarding the latter, we note that the five-fold temporal difference between the 100 mV and 500 mV translocations is much larger than that of the pore-size and polymer length signals, which at maximum show a 2-fold change in velocity in going from a 9 nm to a 36 nm pore.

Chapter 5. Role of Rigidity in Folded Kinetics

This chapter contains an article published in the *Nanoscale* scientific journal titled "DNA origami characterized *via* a solid-state nanopore: insights into nanostructure dimensions, rigidity and yield" and is authored by Liqun He[+], Martin Charron[+], Philipp Mensing, Kyle Briggs, Jonathan Adams, Hendrick de Haan and Vincent Tabard-Cossa.* The corresponding Supporting Information is provided in Section 5.2.

* Reproduced and adapted with permission from [He, L., Charron, M., Mensing, P., Briggs, K., Adams, J., de Haan, H. and Tabard-Cossa, V., 2023. DNA origami characterized via a solid-state nanopore: insights into nanostructure dimensions, rigidity and yield. *Nanoscale*, *15*(34), pp.14043-14054.]

5.1 DNA origami characterized *via* a solid-state nanopore: insights into nanostructure dimensions, rigidity and yield

Liqun He,‡ Martin Charron,‡ Philipp Karau, Kyle Briggs, Jonathan Adams, Hendrick de Haan, Vincent Tabard-Cossa

‡These authors contributed equally

Abstract

Due to their programmability via specific base pairing, self-assembled DNA origami structures have proven to be useful for a wide variety of applications, including diagnostics, molecular computation, drug delivery, and therapeutics. Measuring and characterizing these structures is therefore of great interest and an important part of quality control. Here, we show the extent to which DNA nanostructures can be characterized by a solid-state nanopore; a non-destructive, label-free, single-molecule sensor capable of electrically detecting and characterizing charged biomolecules. We demonstrate that in addition to geometrical dimensions, nanopore sensing can provide information on the mechanical properties, assembly yield, and stability of DNA nanostructures. For this work, we use a model structure consisting of a 3 helix-bundle (3HB), *i.e.* three interconnected DNA double helices using a M13 scaffold folded twice on itself by short DNA staple strands, and translocate it through solid-state nanopores fabricated by controlled breakdown. We present detailed analysis of the passage characteristics of 3HB structures through nanopores under different experimental conditions which suggest that segments of locally higher flexibility are present along the nanostructure contour that allow for the otherwise rigid 3HB to fold inside nanopores. By characterizing partially melted 3HB structures, we find that locally flexible segments are likely due to short staple oligomers missing from the fully assembled structure. The 3HB used herein is a prototypical example to establish nanopores as a sensitive, non-destructive, and label-free alternative to conventional techniques such as gel electrophoresis with which to characterize DNA nanostructures.

5.1.1 Introduction

Significant advances have been made in the field of DNA nanotechnology since its introduction.[85,194–198] The fabrication of nanoscale objects using DNA oligomers as building blocks is attracting a growing number of scientists from different disciplines looking to create a variety of 2-dimensional (2D) and 3-dimensional (3D) DNA nanostructures for diagnostics, therapeutics, and single-molecule biophysics applications.[199–206] While the programmable self-assembly process of DNA is highly efficient, it is also a highly complex thermodynamic process and the end product must usually be characterized to ascertain yield and structural consistency with the desired DNA nanostructure.[207]

DNA origami structures are characterized using a variety of techniques such as gel electrophoresis, transmission electron microscopy (TEM), atomic force microscopy (AFM), or Förster resonance energy transfer (FRET) microscopy.[207] Gel electrophoresis has been the gold standard for the characterization of DNA nanostructures given its simplicity and low cost. It provides rapid bulk estimation on the yield and purity of the assembly process but does not provide information about the correct assembly of the entire structure. Despite these shortcomings, gel electrophoresis remains a staple technique due to its non-destructive nature and is a popular tool for purification of assembled structures. Microscopy techniques, on the other hand, provide high resolution imaging of the sample at the single-molecule level and give information about the correctness of the assembly of 2D and 3D nanostructures. However, the sample preparation and experimental procedures of these techniques are invasive and can disrupt the structural integrity of the assembled products.[195,208–214]

Over the last few years, several studies have involved the characterization of DNA nanostructures using solid-state nanopores,[107,175,215–217] primarily for the development of

biosensing,[34,148,218–222] and next-generation molecular data storage applications.[129,131,223] In a typical nanopore experiment, a membrane containing a nanometer-sized pore is placed between two electrolyte-filled compartments. When a voltage is applied across the membrane, ionic current flows through the nanopore. As individual nanostructures translocate through the pore, a modulation in ionic currents is observed. The extracted blockage depth, duration, frequency, and temporal structure of translocation events reveals structural information (size, conformation, shape) about the molecular structures of interest and their abundance. The nanopore approach has distinct advantages as a characterization tool for DNA nanostructures, as recently shown by Confederat *et al.* [217]: It allows for the detection from bulk solution which preserves the structural features of the sample as opposed to immobilizing it on a surface and drying it; detection is performed label-free without the use of optical dyes, which can affect mechanical properties and functions;[224,225] given their single-molecule sensitivity, nanopores consume low amount of materials, with most current fluidic cells requiring low volumes (~1-10 μL) and as little as 1 ng or on the order of femtomoles of sample to operate in the high pM to low nM range for a single nanopore to collect a 100-1000 events in minutes.

Here, we demonstrate how solid-state nanopore sensing can be used as an analytical platform to characterize DNA nanostructure properties beyond geometry and yield. As a prototypical example, we characterize the electrophoretic capture and translocation characteristics of a 3 helix-bundle (3HB) nanostructure in various experimental conditions (salt, voltage, and pore size), and show through identification and characterization of nanopore translocation events that we are able to extract information about geometry, local mechanical properties, and assembly yield. Notably, we demonstrate that statistics of folded translocations can yield information regarding the local rigidity of molecules folding inside nanopores. Our results and interpretation

of the folding kinetics of 3HB nanostructures in pores suggest that structures folding through pores have a non-uniform rigidity. By degrading 3HB samples using heat, we further show that such heterogeneous rigidity can arise from defects such as missing staple oligomers. The data presented here therefore demonstrate the extent by which solid-state nanopores can be used to characterize DNA nanostructures, shed light on the kinetics of folded nanopore transport, and show how local missing oligomers arising from thermodynamic effects can affect structural properties of DNA nanostructures that may otherwise pass other quality-control metrics.

5.1.2 3HB assembly and Nanopore Characterization

In this work, we used a three-helix DNA bundle (3HB) as our model DNA nanostructure, which consists of three parallel dsDNA double-helices bound together. More precisely, 191 short single-stranded DNA (ssDNA) oligomers hybridize to different locations of a 7249 nucleotide-long linearized single-stranded m13mp18 DNA, resulting in the scaffold folding twice on itself, as sketched in Figure 5.1.1a. The resulting structure is therefore expected to have a contour length of ~820 nm, a cross-sectional area at any point along its contour corresponding to three times that of double-stranded DNA (dsDNA), and have side-to-side distance of ~6 nm, due to the hexagonal pattern used to build the structure (Figure 5.1.1b).[86] The protocols employed, the design and the sequences of the structures are described in the Methods Section and in Supplementary Sections S5.2.1 and S5.2.2, respectively. Once assembled, the structures were characterized by gel electrophoresis, through which assembly quality was verified by confirming the presence of only one band, as shown in Figure 5.1.1c.

For all experiments shown here, 3HB structures were electrophoretically driven through nanopores (Figure 5.1.1d) fabricated by the controlled breakdown method.[15,22] Experiments were performed with pores (n = 11) of different sizes (9 – 15 nm), in different salt concentrations (0.45

– 3.6 M LiCl), and under a wide range of voltages (100 - 900 mV). As an example, Figure 5.1.1e shows concatenated current traces of current blockages induced by 3HB structures in a 13.2 nm pore, under a 200 mV bias in 1.2 M LiCl salt. The current trace from each detected blockade event is then fitted (See Methods) to extract metrics useful for characterization, such as maximum conductance blockage depth reached during a blockade event ΔG_{max}, and the total translocation time τ, as shown in Figure 5.1.1e. A typical example of nanopore data visualization is displayed in Figure 5.1.1f, which shows a scatterplot of ΔG_{max} *versus* τ, for 486 single molecule events. As will be discussed in the following sections, the information contained in such data is diverse and can be related to the nanostructure geometry, structure, or to the different ways a molecule can enter a pore.

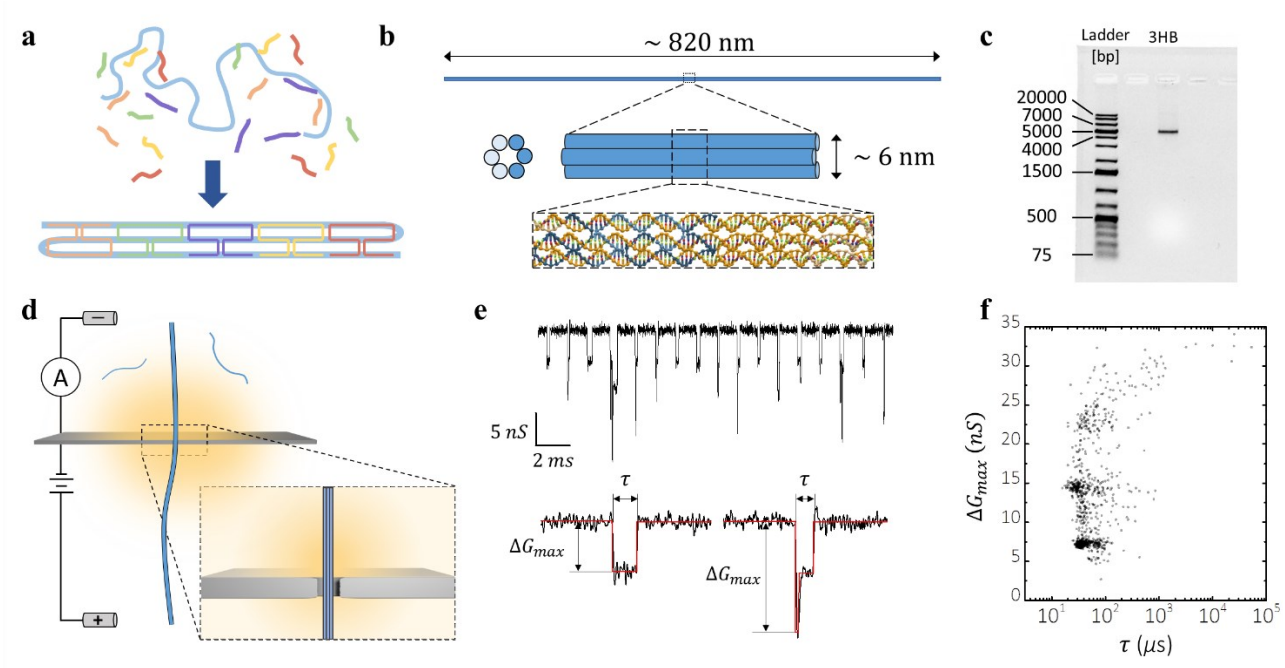

Figure 5.1.1. DNA nanostructure assembly and characterization with nanopore. a) Schematic of DNA helix bundle hybridization: thermal annealing of 7249 nt M13mp13 with 191 short "staple" strands. **b)** Expected dimensions, and structure of 3-Helix bundle assembly. c) 1% agarose gel electrophoresis showing a ladder of various DNA lengths in one lane and fully assembled 3HB structures in the other. **d)** Setup for nanopore sensing of 3HB structures. Yellow hue depicts the electric field strength. **e)** Concatenated current traces of transient ionic blockades induced by the presence of 3HB in 1.2M LiCl

under 200 mV in a 13.2nm pore (top). Individual blockade events fit to extract variables such as maximum conductance blockage, and translocation time (bottom). f) Scatterplot of maximum conductance blockage *versus* translocation time in the same experimental conditions as in (e), N = 846 single-molecule events.

5.1.3 3HB Dimensions

To better interpret Figure 5.1.1f, Figure 5.1.2a replots the same data, *i.e.* 3HB in 1.2 M LiCl in a 13.2 nm pore under a 200 mV bias, with blockages normalized by ΔG_{DNA}, the blockage level of single-file dsDNA. Here, $\Delta G_{DNA} = 1.54\ nS$, and is obtained from the average maximum conductance blockage value measured from the translocations of 2 kbp dsDNA fragments inside the same pore. Figure 5.1.2a also plots a histogram of $\Delta G_{max}/\Delta G_{DNA}$, from which three peaks can easily be identifiable. Fitting those three peaks to normal distributions we find each peak to have mean and standard deviation values of:

$$\begin{aligned} \Delta G_1 \pm \sigma_1 &= (3.1 \pm 0.2) \times \Delta G_{DNA} \\ \Delta G_2 \pm \sigma_2 &= (6.2 \pm 0.4) \times \Delta G_{DNA} \\ \Delta G_3 \pm \sigma_3 &= (9.9 \pm 0.6) \times \Delta G_{DNA}. \end{aligned} \tag{5.1.1}$$

The shallowest population has a mean blockage ΔG_1 equal to $3.1 \times \Delta G_{DNA}$, which corresponds precisely to the blockage expected from single-file translocation of properly assembled 3HB structures, whose cross-sectional area should be three times that of dsDNA, and therefore block current three times as much when inside the pore. Interestingly, the two other populations appear to be quantized and show $\Delta G_2 \approx 2 \times \Delta G_1$, and $\Delta G_3 \approx 3 \times \Delta G_1$. Such quantized blockages are commonly observed for dsDNA translocations[48] and correspond to folded passages, *i.e.* translocations for which multiple segments of an individual molecule are inside the pore at once. These folded translocations can occur for example if a polymer enters a pore not by one of its ends, but by bending somewhere along its contour. For 3HB experiments, quantized

blockages were observed in all pores and under most voltages tested, as observed in Figure 5.1.2b, which shows $\Delta G_{max}/\Delta G_{DNA}$ histograms for a 9.3 nm pore in 0.9 M LiCl as a function of voltage.

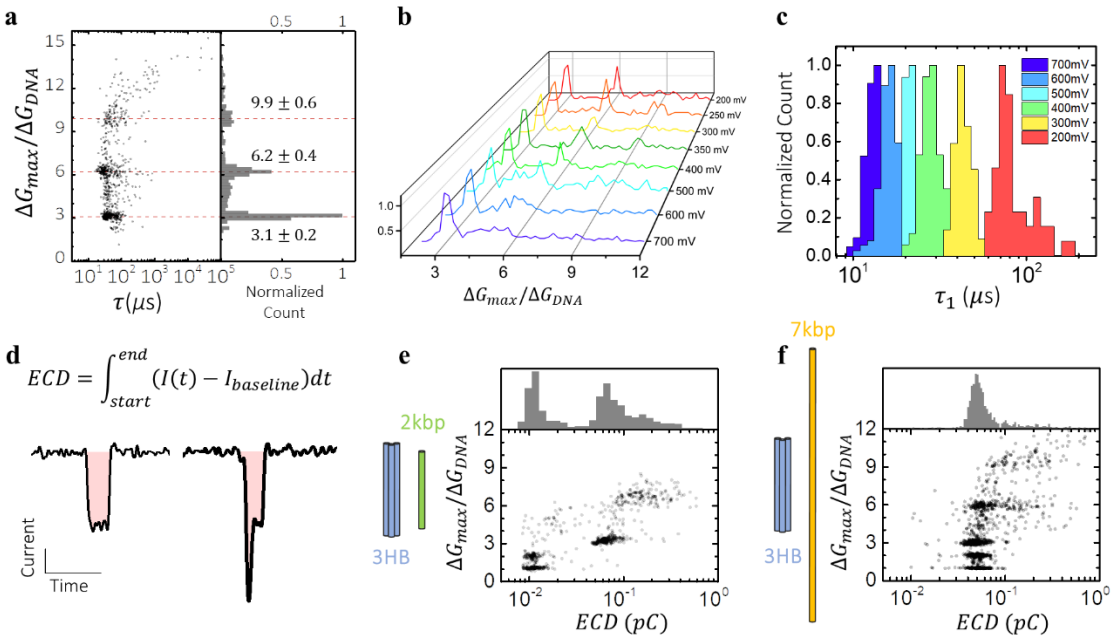

Figure 5.1.2. 3HB dimensions. a) Scatter plot of maximum conductance blockage *versus* translocation time for 3HB in 1.2 M LiCl at 200 mV in a 13.2 nm pore (left), N = 846 single-molecule events. The maximum conductance blockage of 3HB blockades is normalized by ΔG_{DNA}, *i.e.* the maximum conductance blockage for 2 kbp dsDNA measured in the same nanopore. Distribution of normalized blockages (right). **b)** Distributions of maximum 3HB blockages measured under different voltages on a 9.3 nm pore in 0.9 M LiCl. **c)** Translocation time distributions measured under different voltages for the same pore as in b). Only the durations of single-file translocations, $2 < \Delta G_{max}/\Delta G_{DNA} < 4$, are considered for statistics. **d)** Definition and visual representation of Equivalent Charge Deficit (ECD), *i.e.* the area in pink. **e)** ECD comparison of 3HB and 2 kbp dsDNA (similar length) in a 13.3 nm pore in 0.9 M LiCl under a 200 mV bias, N = 630 single-molecule events. **f)** ECD comparison of 3HB and 7 kbp dsDNA (similar # of bp) in an 11.2 nm pore in 0.9 M LiCl under a 200 mV bias, N = 1189 single-molecule events.

To clarify the nature of the various blockades, we analyzed each ΔG_{max} sub-population, starting with the events from the ΔG_1 subpopulation. Figure 5.1.2c plots the normalized distributions of blockade durations τ_1 observed under different voltages for events from Figure 5.1.2b with blockages corresponding to $2 < \Delta G_{max}/\Delta G_{DNA} < 4$. Figure 5.1.2c shows a monotonic reduction of τ_1 with voltage. This is expected from full translocations from one side of the pore to

the other as opposed to collisions, where molecules interact with the pore but remain on the same side of the membrane. Indeed, the blockage duration of molecules entering and fully traversing nanopores reduces under higher voltages due to increasing drift velocities, whereas the blockage duration arising from collisions with a pore increases with voltage due to the increased pulling force making it harder for molecules to diffuse away.[153,215] A voltage sweep obtained under a different salt concentration and pore size is shown in Supplementary Figure S5.2.4, and shows a similar monotonic voltage trend. Additionally, we characterized ΔG_1 events by measuring the dependence of translocation time on salt concentration and determined that similarly to dsDNA translocations,[42] 3HB structures translocate faster in lower salt concentrations (see Figure S5.2.4 of Supplementary Information).[92]

We further analyzed 3HB translocations by calculating their equivalent charge deficit (ECD), calculated as the time-integral of the difference between the current during the blockade event and the open-pore current (Figure 5.1.2d), which corresponds to the amount of charge that would have traversed the nanopore had the translocating molecule not blocked it.[220] For large nanopores with minimal molecular interactions with the pore wall, ECD values of folded and single-file translocations are nearly identical. ECD is therefore primarily related the volume of the translocating molecular structure, in addition to its mobility. Figures 5.1.2e-f show scatter plots of the maximum blockage $\Delta G_{max}/\Delta G_{DNA}$ *versus* ECD for a mixture of 3HB and 2 kbp dsDNA, two molecules of similar contour lengths ($L_{3HB} = 820\ nm$, $L_{2kbp} = 680\ nm$), and a mixture of 3HB and 7 kbp dsDNA, two molecules of similar number of base pairs and thus volumes. These two experiments were done in nanopores of 13.3 nm (Figure 5.1.2e) and 11.2 nm (Figure 5.1.2f), in 0.9 M LiCl under a bias of 200 mV. The normalized ECD distribution of each mixture is shown above the corresponding scatterplot in Figures 5.1.2e-f. The ECD distribution of 2 kbp dsDNA is

significantly smaller than 3HB, whereas the ECD distributions of 7 kbp dsDNA and 3HB overlap. This is expected since 3HB structures are assembled by hybridizing staple strands to a 7249 nt ssDNA scaffold, resulting in a volume similar to that of a 7 kbp dsDNA. Figure S5.2.5 in the Supplementary Information further demonstrates the sensitivity of such comparisons by showing that the ECD distributions of 3HB and 10 kbp dsDNA are separable.

From the combined observations obtained from Figure 5.1.2, we conclude that blockade events from ΔG_1, *i.e.* the sub-population centered around $\Delta G_{max}/\Delta G_{DNA} \approx 3$, result from translocations of molecules with cross-sectional areas three times that of dsDNA, and volumes similar to 7 kbp dsDNA. These dimensions correspond exactly to those expected from properly assembled 3HB structures passing through nanopores in a single-file manner. Note that ECD values from ΔG_2 and ΔG_3 3HB populations in Figures 5.1.2e-f are slightly larger than those of ΔG_1 or 7 kbp dsDNA. This either points to increased pore-polymer interactions, or at more complex dynamics.

5.1.4 3HB Folding – Metastable State

After establishing that events from the ΔG_1 population result from single-file translocations of properly assembled 3HB nanostructures, we next investigated the blockade events from the ΔG_2 sub-population: events with maximum blockages corresponding to six times that of dsDNA, *i.e.* $\Delta G_{max} \approx 6 \times \Delta G_{DNA}$, or equivalently to twice that of single-file 3HB translocations. Figure 5.1.3a plots the normalized maximum blockage level $\Delta G_{max}/\Delta G_{DNA}$ of individual 3HB translocations *versus* the corresponding translocation times for a 13.3 nm pore in 0.9 M LiCl under 200, 300 and 400 mV. Consistent with Figure 5.1.2a, different populations can be identified based on maximum

level blockage alone. The ΔG_2 sub-population ($5 < \Delta G_{max}/\Delta G_{DNA} < 7.5$) is highlighted in Figure 5.1.3a to better visualize its response to different voltages.

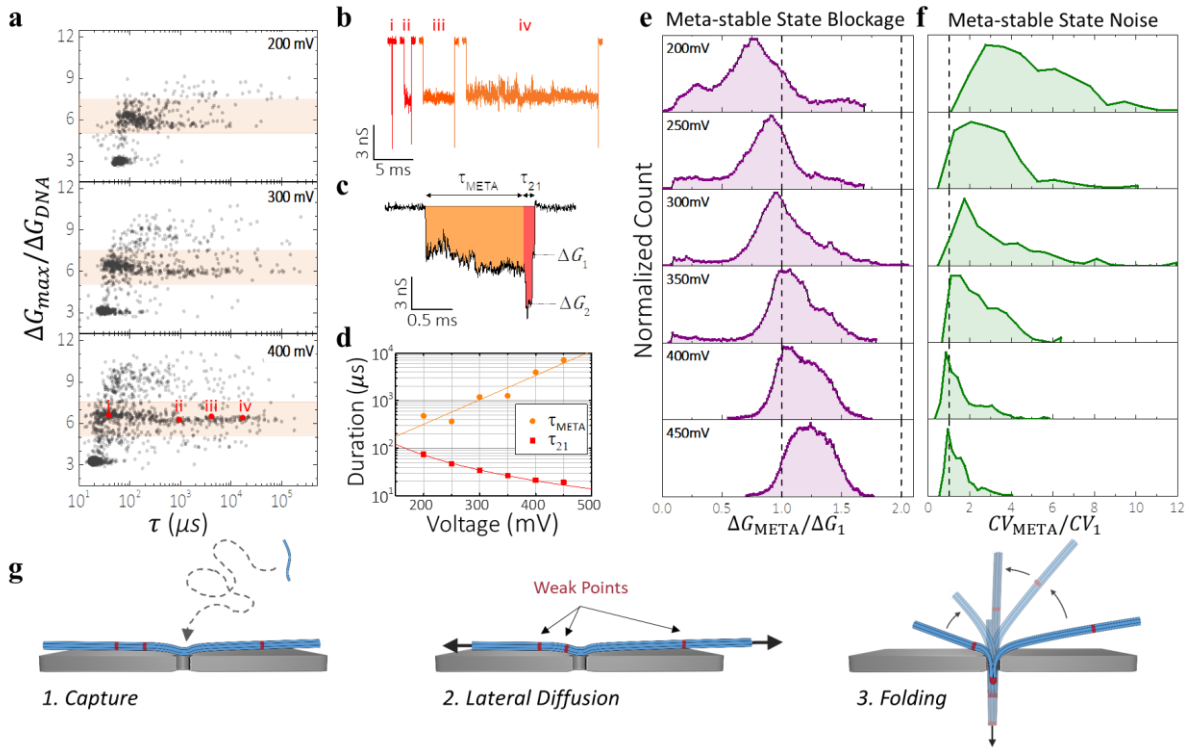

Figure 5.1.3. Folding statistics of 3HB translocations in a 13.3 nm pore in 0.9 M LiCl. **a)** Scatter plots of maximum blockage level *versus* translocation time measured at 200 mV, 300 mV, and 400 mV, with N = 615, 903, and 1333 single-molecule events, respectively. Red dots and roman numerals identify which events are shown in b). **b)** Current traces of four events with $\Delta G_{max} = 2\Delta G_{3HB} \approx 6\Delta G_{DNA}$ of various durations. Events are from the 400 mV data set shown in a). **c)** Representative current trace of a folded 3HB translocation event preceded by a meta-stable state. Orange portion represents the meta-stable state, which is followed by a folded state and single-file state shown in red. **d)** Duration of meta-stable (orange dots) and folded translocation states (red squares) as a function of applied voltage. **e)** Histograms of meta-stable state blockage level, normalized by single-file 3HB translocation blockage ΔG_{3HB} for 200, 250, 300, 350, 400, and 450 mV. The histograms were obtained by averaging the area-normalized conductance histograms of each individual event. **f)** Histograms of the coefficient of variation (CV) of the nanopore conductance during the metastable states, CV_{META}. Values are normalized by the CV measured during single-file 3HB translocations, CV_{3HB}. Measurements under 200, 250, 300, 350, 400, and 450 mV are shown. **g)** Illustrations of the proposed translocation process of folded 3HB.

The three different voltages displayed in Figure 5.1.3a show that events in the ΔG_2 population behave differently than single-file translocations: Whereas the blockage duration of

some translocations gets shorter with increasing voltage, as expected from full translocations (Figure 5.1.2c), the blockage duration of other events increases with voltage, as expected from collision-like events. Under a bias of 400 mV, some events have translocation times up to 2-3 orders of magnitude longer than 200 mV events. These two confounding behaviors result in a spread of τ that significantly increases with voltage, as seen in Figure 5.1.3a. This behavior was observed in other high-voltage nanopore experiments and is not unique to this single-data set.

Insight into the nature of this sub-population of 3HB with $\Delta G_2 \approx 6 \times \Delta G_{DNA}$ blockage level is gained by examining the current signature of individual blockade events. Figure 5.1.3b displays the traces of four events which span the entire range of translocation times (selected events are highlighted in red in Figure 5.1.3a). Interestingly, these events begin with a shallow blockage state, followed by a deeper one. In fact, more than 90 % of events from the ΔG_2 sub-population can be divided into three consecutive blockage states, as depicted in Figure 5.1.3c: an initial metastable state with a blockage depth (ΔG_{META}) which can be noisy and very long (up to $10^5\ \mu s$), followed by an intermediate blockage of depth ΔG_2 and a final blockage state of depth ΔG_1. These latter two states are expected of a folded translocation in which a 3HB molecule entered a pore not by an end, but by bending a segment along its contour inside the pore.[48,75] We therefore attribute these events in the ΔG_2 sub-population as folded 3HB translocations preceded by a metastable state. Indeed, Figure 5.1.3d plots the voltage dependence of metastable state durations τ_{META} and of the final two states $\tau_{21} = \tau - \tau_{META}$ (as also defined in Figure 5.1.3c), showing that τ_{21} monotonically reduces with voltages, and is well described by a power scaling law of the form $\tau_{21} \sim \Delta V^{(-1.8 \pm 0.1)}$, whereas τ_{META} monotonically increases with voltage, and is well described by an exponential function $\tau_{META} \sim e^{\Delta V/(85 \pm 10)mV}$. Just as for single-file translocations, the fact that τ_{21} reduces with voltage supports the interpretation that the two final blockage states correspond

to a 3HB traversing the nanopore in a folded conformation. Conversely, because of its increasing duration with increasing voltage, the metastable state is collision-like, and is hypothesized to result from the 3HB nanostructure lying across the pore opening. At high voltages, the metastable state dominates the event duration and is therefore responsible for the wide spread of translocation times observed in Figure 5.1.3a (see Figure S5.2.5 of Supplementary Information).

To better understand the nature and origin of the metastable state, we further investigated the properties of the current blockage observed during the metastable state. Figure 5.1.3e displays histograms of the metastable state conductance blockage ΔG_{META} measured under different voltages, normalized by ΔG_1 to reduce inter-measurement variability. Figure 5.1.3e shows that ΔG_{META} gets deeper for larger voltages, as shown by its most probable value increasing monotonically with voltage: At 200 mV, the most probable metastable state blockage value is $\Delta G_{META}/\Delta G_1 \approx 0.77$, whereas it is ≈ 1.21 at 450 mV. At lower voltages therefore, a 3HB nanostructure presumably lying above the pore blocks less current than if it were fully inserted into the nanopore (as for single-file translocations), whereas the opposite is true for higher voltages.

Figure 5.1.3f shows the histogram of the metastable state blockage noise measured at different voltages. Here the noise is quantified using the coefficient of variation $CV_{META} = \sigma_{META}/\mu_{META}$, *i.e.* the ratio of the metastable state standard deviation $\sigma_{META}^2 = \langle(\Delta G_{META} - \mu_{META})^2\rangle$ and mean $\mu_{META} = \langle\Delta G_{META}\rangle$ values. CV_{META} values are normalized by the average noise of single-file translocations CV_1, calculated in the same way. The relative metastable state noise is observed to reduce with increasing voltage. Interestingly, for higher voltages the noise reduces to the same values as for single-file 3HB translocations. In Supplementary Figure S5.2.8,

it is further shown that the current blockage during the metastable state displays voltage-independent 1/*f* noise.

The voltage trends identified in Figure 5.1.3 help form a complete picture of the mechanism by which 3HB nanostructures fold inside nanopores: The bending and folding of 3HB inside nanopores is identified by the last two blockage states (Figure 5.1.3c), and is preceded by a collision-like metastable state which lasts longer (Figure 5.1.3d), blocks more current (Figure 5.1.3e), and gets less noisy (Figure 5.1.3f) with increasing voltage. Based on these observations, we unravel the folding steps of 3HB as follows: 1) When a 3HB does not approach the nanopore by an end, it gets pulled down across the pore opening by the electric field at some intermediate position along its contour; 2) Due to its high local rigidity (persistence length $\ell_{3HB} > \ell_{DNA} > d_{pore}$), it does not bend inside the pore; It instead diffuses laterally, the action of which is hindered by the electric field in the vicinity of the pore, which acts to pin nanostructures against the pore mouth and membrane; 3) Through lateral diffusion, a segment of weaker local rigidity along the 3HB eventually finds the nanopore, which facilitates bending and entry inside the nanopore. A folded translocation subsequently occurs, wherein two 3HB segments are in the pore at once (folded state ΔG_2), followed by a single segment (unfolded state ΔG_1). See Figure 5.1.3g for a depiction of the proposed folding mechanism.

Similar docking phenomena have been previously described for dsDNA,[226] observed for DNA nanostructures and for stiff filamentous viruses.[18,99,153,221,227] In this work, docking and diffusion prior to translocation helps explain the observations of Figures 5.1.3e and 5.1.3f: increasing voltage enhances the electrophoretic pull in the pore vicinity, and pins 3HB nanostructures more strongly to the pore mouth, which increases blockage, and reduces the amplitude of the thermal motion that contributes to the additional noise in the metastable state.

Supplementary Information Section S5.2.8 provides additional discussion and experimental results under different experimental conditions to support this interpretation.

Proposing 3HB molecules with a spatially varying rigidity helps explaining the observation from Figure 5.1.3d in which τ_{META} increases with voltage. Consider a heterogeneous linear polymer with segments too rigid to instantly bend inside nanopores, separated by a random distribution of more flexible segments which, when in contact with the nanopore, rapidly bend and enter. Unlike a uniformly rigid structure, the time required for the molecule of non-uniform rigidity to bend inside a nanopore is not determined by the characteristic time it takes for the molecule to overcome the bending energy barrier, but is instead determined by how long it takes for a flexible segment to find the pore through lateral diffusion. At higher voltages, 3HB molecules should be pinned closer to the pore (Figure 5.1.3e), and the increased membrane-polymer interactions (friction) should hinder lateral diffusion, therefore resulting in longer times required for flexible segments to find the pore.

Lateral diffusion prior to translocation is further supported by a number of events displaying the metastable state followed only by a single-file blockage state instead of a folded-translocation sequence. Such events were presumably docked onto the pore near their ends, diffused laterally until their ends entered the pore, resulting therefore in a single-file translocation, as characterized, and displayed in Section S5.2.8 of the Supplementary Information. Furthermore, although the metastable state was observed in almost all experimental conditions tested, it was notably more prominent under high voltages and in low salt concentrations (See Figures S5.2.11 and S5.2.12 of the Supplementary Information), two conditions that increase the electrophoretic pull on the 3HB molecules and therefore pin it more against the pore.

5.1.5 Complex Folding of Degraded Nanostructures

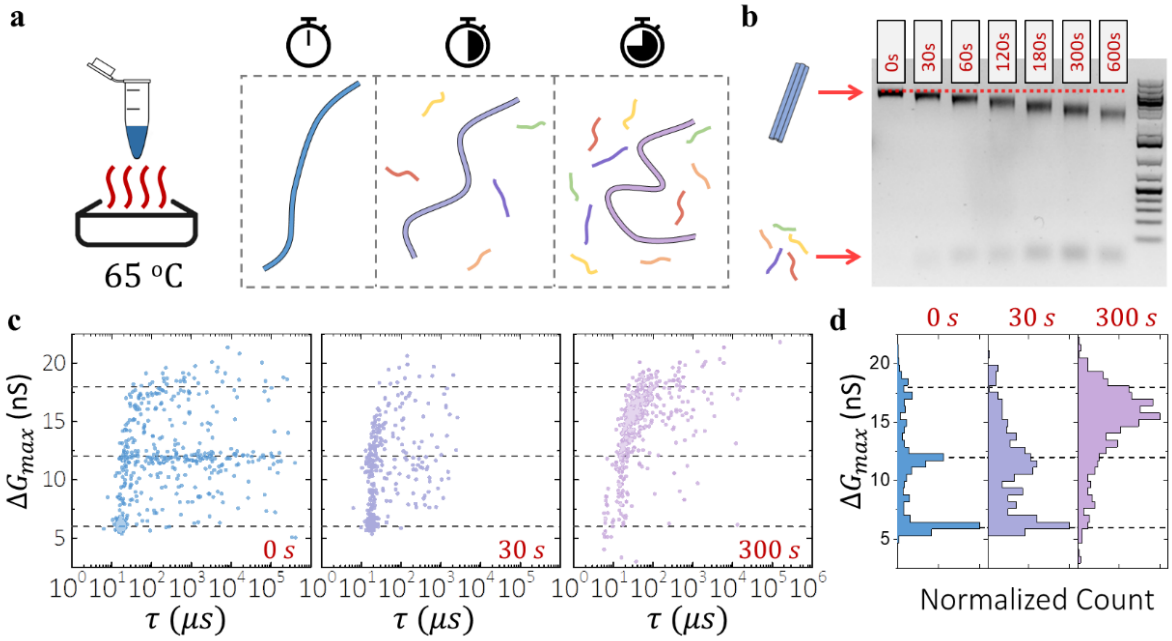

Figure 5.1.4. Nanopore characterization of heat-shocked 3HB. **a)** Sketch of 3HB structures heated at $65°C$, gradually loosing staples. **b)** Gel electrophoresis of 3HB nanostructures thermally degraded for $0, 30, 60, 120, 180, 300,$ and 600 seconds and snap cooled to $4°C$. 1 % Agarose gel in 1xTAE buffer (40 mM Tris, 20 mM acetic acid, and 2 mM EDTA) with an applied voltage of 70 V. Right lane: Generuler 1 kb plus DNA Ladder (ThermoFisher Scientific, SM1331). **c)** Scatter plots of Maximum conductance blockage level *versus* translocation time of 3HB structures heated at $65°C$ for 0, 30, and 300 seconds for a 11.4 nm nanopore in 0.9 M LiCl with an applied bias of 400 mV, with N = 650, 325, and 547 single-molecule events. Single-file 3HB events produce a blockage level of $\sim 6\ nS$. Dash line are integers of the single-file level. **d)** Distributions of maximum conductance blockages from c).

The previous section proposed that the 3HB molecules have a heterogeneous rigidity, *i.e.* flexible segments scattered along the more rigid contour 3HB, to explain the mechanism by which 3HB folds inside nanopores. The experimental data of Figures 5.1.2 and 5.1.3 however offer no insight into the origin nor into the characteristics of such flexible segments. One possibility is that added flexibility arises from missing oligomer staples at different location along the length of the nanostructure. Unfortunately, individual missing oligomers cannot be mapped from the nanopore ionic current signal at this time due to the relatively fast translocations.

Here, to study the effect of missing oligomer staples on 3HB translocations, and the resulting of a non-homogeneously rigidity along 3HB contour, we purposefully induced partial melting of the staples by briefly heating the 3HB structures. Using a thermal cycler, samples of the same 3HB assembly batch were heated to a temperature of $65°C$ for durations of $\Delta t = 0$, 30, 60, 120, 180, and 300 seconds. A temperature of $65°C$ was chosen since it is slightly above the melting temperature of individual staple strands. By heating the 3HB samples for different durations, an increasing fraction of staples are removed, and the structures gradually degrade (Figure 5.1.4a). Following the heat shock, the samples were snap-cooled to $4^{o}C$ to preserve the degraded state, and immediately characterized by gel electrophoresis and nanopore translocation. Figure 5.1.4b shows a 1% agarose gel electrophoresis experiment where each lane contains 3HB nanostructures heated for different amounts of time. Structures heated for longer times have higher gel mobility, and contain fast migrating bands, which can be attributed to staples released from the 3HB structure. This confirmed that heat shocks controllably and gradually remove a random subset of staples from 3HB.

Figure 5.1.4c shows the corresponding nanopore data, with ΔG_{max} *versus* τ scatter plots for the 3HB nanostructures heat-shocked for $\Delta t = 0$, 30 and 300 seconds, and passing through a 11.4 nm nanopore, in 0.9 M LiCl, under a 400 mV applied voltage. See Supplementary Information Section S5.2.11 for the scatter plots of samples degraded for all times tested. The blockades of 3HB structures before heat shocks ($\Delta t = 0\ s$) show blockages and translocation times consistent with that of Figure 5.1.3a: a well-defined single-file population, and a folded population approximately twice as deep displaying a wide τ distribution covering 4 orders of magnitude, indicative of the metastable state. In addition, a few events have maximum blockages centered

around $\sim 3 \times \Delta G_1$, corresponding to more complex folded passages, *i.e.* translocation events which at some point during translocation had three segments inside the nanopore at once.

Figure 5.1.4c and the corresponding ΔG_{max} histograms shown in Figure 5.1.4d reveal that distinct features in the translocation profiles can be observed as the nanostructures are heated. First, the peaks within the ΔG_{max} distributions broaden (making distinct population less easily distinguishable) yet remain consistently centered around the same values. Second, 3HB nanostructures heated for longer periods of time result in more events populating the folded states and consequently less the single-file state. Eventually barely any single-file 3HB events are detected, and mostly complex folding ($> 2 \times \Delta G_1$) is observed, as shown in Figures 5.1.4c-d for $\Delta t = 300$ seconds. Lastly, as samples are heat shocked for longer times, translocation events display shorter metastable states: When only heated for 30 seconds, the metastable state is present at the start of many events, yet is significantly shorter than the intact structures, as revealed by the much narrower τ distribution of folded events. For longer heating durations, metastable states become shorter and eventually become undetectable.

This gradual degradation of nanostructures shows that 3HB structures with missing staples have an increased propensity for complex folded translocations. Under controlled experimental conditions, the fraction of translocation events showing complex folding states should give a qualitative insight into the fraction of nanostructures with missing short staple oligomers. Moreover, the reduction and eventual disappearance of metastable states for more degraded samples supports the hypothesis of a heterogeneous rigidity used to explain 3HB folding. By intentionally removing a subset of staple strands, more segments of increased local flexibility should be introduced along the structure. As a result, the average contour distance between the initial docking site and the closest flexible segment should be reduced, in turn reducing the time

required for a flexible segment to find the pore through lateral diffusion, and therefore the metastable state duration τ_{META}. Note that although intentionally removing staples supports the idea that heterogeneous rigidity is responsible for 3HB folding, it does not necessarily imply that missing staples are the cause of weaker spots for fully assembled structures. For example, smaller defects such as nicks (*i.e.* the space between where two neighboring staples end), could be at the root the proposed heterogeneity.[228,229] The nanoscopic distinction between such minute features remain inaccessible to the analysis shown here.

5.1.6 Folded Fraction

Figures 5.1.3 and 5.1.4 and the corresponding discussions have addressed the potential mechanism and origin of folded 3HB translocations. We now attempt to give insight into the complementary subject of the fraction of folded events (*i.e.* folded fraction) to understand how often 3HB translocates in a single-file or folded fashion. Figure 5.1.5a plots the normalized ΔG_{max} histograms for 2 kbp dsDNA and 3HB passing through a 13.3 nm nanopore, in 0.9 M LiCl, under an applied voltage of 200 mV. Recall that these two molecules have similar contour lengths ($L_{3HB} = 820\ nm$, $L_{2kbp} = 680\ nm$). For better visualization, ΔG_{max} values were normalized by the single-file blockage of DNA translocations ΔG_{DNA}. Fitting both histograms to bimodal distributions and comparing the amplitudes of single-file and folded populations, we found that 60% of 3HB translocations, and 36% of 2 kbp translocations were folded. Under the same experimental conditions, 3HB structures therefore translocated in a folded conformation roughly 66% more than 2 kbp. Note that this folded fraction increase was observed for all experiments obtained for this work in which both 3HB and 2 kbp dsDNA were run on the same pore, consistently resulting in 3HB folding 60-80% more than 2 kbp.

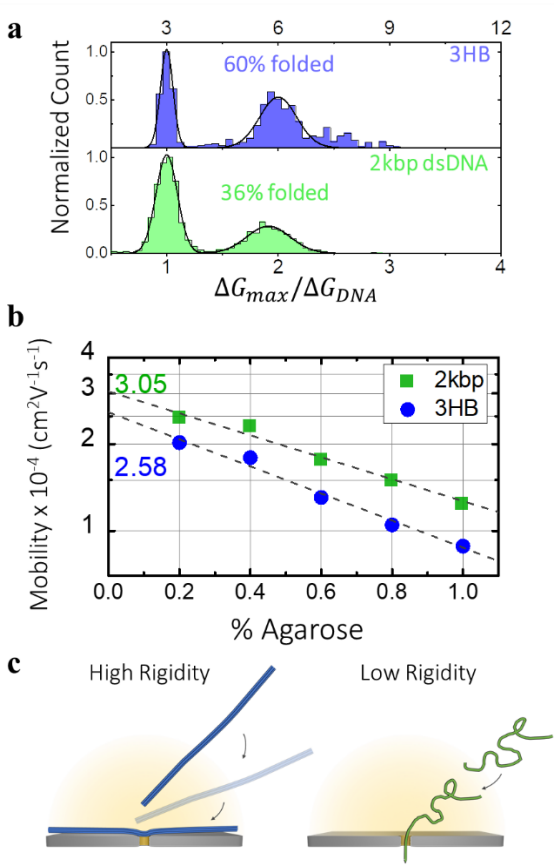

Figure 5.1.5. Insights into the fraction of folded 3HB translocations. **a)** Normalized maximum conductance blockage histograms for 3HB (top) and 2 kbp dsDNA (bottom) in a 13.3 nm pore in 0.9 M LiCl under a 200 mV voltage. The distributions are fit to a bimodal distribution to estimate the fraction of folded events. **b)** Extrapolation of 3HB and 2 kbp dsDNA free-solution mobility using 0.2 – 1 % Agarose gels. **c)** Sketch demonstrating the effects of rigidity and on the conformations expected when a slightly misaligned molecule comes into proximity to a pore.

As previously stated, folded translocations occur when a molecule enters the nanopore not by its end, but instead by bending a segment along its contour. Understanding the folded fraction of a molecule is therefore equivalent to understanding what factors impact whether a molecule gets captured by an end or not. Here, in order to explain the increased folding fraction observed with 3HB nanostructures, we briefly give insight into the role that polymer rigidity and that non-

uniform electric field play in determining a polymer's capture location, *i.e.* where along its contour a polymer first comes into contact with a nanopore.

We first consider the role played by the electric field emanating from the nanopore on the conformation of approaching charged polymers. When a voltage is applied across an insulating membrane containing a nanopore, a strong electric field forms within the nanopore and its vicinity. The electric field is strongest inside the pore, and decays as it extends outward radially. The electric field gradient outside of the nanopore can cause both dsDNA and 3HB to approach the pore by an end: For dsDNA, the field gradient stretches out and "unwraps" the polymer as it approaches since the field pulls on the parts of dsDNA that are closer to the pore significantly more than those that are distant.[87,165,166,188,230] For the rigid 3HB molecules, the gradient results in a torque that aligns the 3HB with the field lines.[227,231,232] Similar effects have been seen for rigid molecules in other nanofluidic devices.[233] For sufficiently strong fields, both molecules are therefore expected to approach the pore by an end in the majority of cases. Generally, however, molecules with higher electrophoretic mobility should respond more strongly to the non-uniform electric-field and align with the pore better than molecules of lower mobility, resulting in less folding.

To test whether different electrophoretic mobilities are at the root of 3HB structures consistently folding more than 2 kbp dsDNA, we estimated the free solution mobilities of 3HB and 2 kbp dsDNA molecules by calculating their electrophoretic mobilities μ in agarose gels of different concentrations. For each agarose gel percentages, the distance travelled by the 3HB δx under an applied voltage ΔV was used to estimate the gel-percentage-dependent mobility μ calculated as

$$\mu = \frac{\delta x}{\delta t}\frac{L}{\Delta V}. \tag{5.1.2}$$

Here, L is the distance between the electrodes applying voltage for a duration of δt. The different mobility measurements were used to extrapolate the 0% gel mobility, *i.e.* the free solution mobility, as shown in Figure 5.1.5b. The extrapolation was achieved by fitting the data to an exponential decay function, since electrophoresis for lower gel concentrations is well described by Ogston sieving.[234] The free solution mobility of 3HB structures was extracted to be 2.6×10^{-4} $cm^2V^{-1}s^{-1}$, whereas 2 kbp dsDNA yielded a higher free-solution mobility of 3.1×10^{-4} $cm^2V^{-1}s^{-1}$. These values are in a reasonable agreement with accepted dsDNA mobility values of 3.7×10^{-4} $cm^2V^{-1}s^{-1}$.[83] We therefore estimate the mobility of 3HB structures to be roughly 15% smaller than that of 2 kbp dsDNA.

Since the mobility of 3HB is marginally smaller than that of 2 kbp dsDNA, we instead suggest that, somewhat counter intuitively, the overall increased rigidity of 3HB is responsible for the 60 - 80% increase in folded translocation fraction. Although both molecules are more likely to approach a nanopore end-first, as discussed, approaching by an end does not guarantee threading by an end. Thermal noise can kick the proximal end of the polymer/nanostructure off track such that it misses the pore. Due to its relative flexibility, dsDNA can still fold and thread through by – or at least very near – an end even if the initial attempt failed. This is however not possible for the more rigid 3HB molecules. Instead, if the end misses, the molecule's center of mass will continue to approach the pore, eventually resulting in it being pinned against the pore, thereby initiating the metastable state described above. This behavior has been observed in studies of the translocation of rigid filaments through nanopores where even events in which the polymer approached the pore by an end could yield a docked state with the molecules lying against the surface of the membrane on the *cis* side.[227] In accord with this tip deflection scenario, this result was measured to be more likely if the polymer approached the pore at an angle that was oblique relative to the axis of the

pore. Through this mechanism, the overall rigidity of 3HB means that even events in which the molecule approaches the pore by an end can result in folded events and thus the more rigid 3HB yields more folded events than 2 kbp dsDNA of similar length.

5.1.7 Conclusion

By thoroughly classifying and analyzing the different types of current signatures for 3-helix bundle (3HB) structures translocating under various conditions, we showed the extent to which DNA nanostructures can be characterized by solid-state nanopores. From the blockage depth and the equivalent charge deficit of single-file translocations, we calculated the volume and the cross-sectional area of 3HB. This substantiated the proper assembly and anticipated dimensions of the nanostructures. Through analysis and the understanding of the 3HB structure folding mechanism, we further revealed that nanopores can give information on the structural rigidity of a DNA nanostructure, which in turn reflects the quality of the assembly. We proposed that 3HB have a heterogeneous rigidity along their contour due to missing a subset of staple strands, allowing for 3HB to fold for nanopore entry. We verified our hypothesis by purposefully removing oligomers from 3HB structures, which resulted in more complex folded translocations (defined as having maximum blockage levels $> 2 \times \Delta G_1$), and facilitated entrance of 3HB into nanopores. Both the metastable state durations and fraction of events showing complex folding sequences are therefore related to the density of missing oligomers along the 3HB structure, or equivalently to the yield of fully assembled structures.

In addition to giving insights on physical characteristics of the 3HB nanostructure, the results shown in this work outline the role of rigidity in the nanopore capture and translocation

process. Our results suggest that docked polymers, when incapable of bending and entering a nanopore, can diffuse laterally along their contour while remaining atop the pore due to the strong electrophoretic pull. Under these circumstances, the contour of the rigid polymer is scanned by the nanopore until a segment and conformation are found that favors translocation, either by an end or by folding. Therefore, in addition to conformational entropy,[75] rigidity should accentuate the energetic contributions required for initiating the translocation process, and as a result should alter the statistics of where along its contour a polymer folds when entering a nanopore.

We note that similar docking behavior has been observed recently by Shi *et al.*[99] who showed that 6-helix bundle structures could dock on top of solid-state nanopores, and undergo rotary motion due to the competing effects of electrophoresis and electroosmosis under the presence of a potential gradient, or of diffusiophoresis and diffusioosmosis in the presence of a salt concentration gradient. In addition to lateral diffusion, rotational motion could indeed occur during the outlined metastable state, however evidence of such behavior could not be detected when looking only at ionic current signatures due to the cylindrical symmetry of the nanopore.

Finally, we hope that our results show how the plurality of signals obtained by nanopore translocations contain rich information about the dimensions of an analyte and its rigidity and will further motivate their use for characterizing more complex DNA origami nanostructures.

5.1.8 Methods

Scaffold Preparation - The linearized M13 single-stranded DNA scaffolds were prepared from M13mp18 circular single-stranded DNA (New England Biolabs, N4040S). To attach the primer, primer strand was added in a mixture with 10 μg M13mp18 circular single-stranded DNA at a ratio of 10:1 in 1x NEB 3.1 buffer, the mixture was heated to 95 ^{o}C, and slowly cooled down to room temperature in a MiniAmp Plus Thermal Cycler (ThermoFisher Scientific, #A37835). A mixture of prepared circular scaffold (with primer attached), and 10 units of HincII restriction enzyme (New England Biolabs, R0103S) in a total reaction volume of 50 μL in 1x NEB 3.1 buffer were incubated at 37 ^{o}C for 3 hours, then heat-inactivated at 65 ^{o}C for 20 minutes in the thermal cycler.[220] The linearized products were characterized by denaturing agarose gel electrophoresis at 1% in 1x TAE buffer (40 mM Tris, 20 mM acetic acid, and 2 mM EDTA, pH 10.5). Upon completion, the agarose gel was submerged in 1xTAE buffer (40 mM Tris, 20 mM acetic acid, and 2 mM EDTA) at pH 8 and incubated on incubator at 60 RPM for an hour to bring gel pH back to 8. The gel was then submerged in 2x gel volume de-ionized water with 1x GelRed (Biotium, #41003) for 45 minutes on incubator then store at 4 ^{o}C overnight to post stain. As shown in Supplementary Figure S5.2.1, linear single-stranded M13 migrate faster than circular single-stranded M13 molecules, the disappearance of circular band is an indication of complete cut. The sequence of the linearized M13 scaffold is provided in Supplementary Information Section S5.2.1.

Nanostructure Assembly - For the assembly of the 3HB molecules, the scaffold (linearized M13mp18 from New England Biolabs, N4040S) was mixed with 191 staple strands at a molar ratio of 1:10 in assembly buffer (at final 40 mM Tris, 20 mM acetic acid, 2 mM EDTA, and 16 mM $MgCl_2$, pH 8). The product is heated to 95 ^{o}C for 5 minutes, cooled to 90 ^{o}C, ramped from 90 ^{o}C to 60 ^{o}C at a rate of 0.4 ^{o}C per minute, then from 60 ^{o}C to 26 ^{o}C at a rate of 0.03 ^{o}C, and snap

cooled to 4 ^{o}C using minicamp Plus Thermal Cycler (ThermoFisher Scientific, #A37835).[218,235] After the assembly, the nanostructures were spun down using 100 kDa Amicon Ultra-0.5 Centrifugal Filter Unit (Millipore Sigma, UFC500396), three washes with the assembly buffer were performed to completely remove excess staple strands present in the solution. The assembled products were visualized on 1% agarose gel in 1x TAE buffer (40 mM Tris, 20 mM acetic acid, and 2 mM EDTA, pH 8), as shown in Supplementary Section 5.2.1. Generuler 1 kb plus DNA Ladder (ThermoFisher Scientific, SM1331) was used as a reference guide for nanostructure migration. GelRed (Biotium, #41003) was used for visualization of the DNA bands.

Nanopore Fabrication - Nanopores were fabricated in 12 nm thick free-standing SiN_x membranes (Norcada, NBPX5004Z) using the controlled breakdown (CBD) method.[15,22,39,236] CBD was performed in 1 M KCl buffered with 10 mM HEPES at pH 8 and pores were grown to 9–15 nm in 3.6 M LiCl buffered with 10 mM HEPES at pH 8 using moderate voltage conditioning, using Spark-E2 instruments and flow cells similar to products from Northern Nanopore Instruments (NNi) as described in Waugh *et al*.[22] The uncertainties of pore diameters are calculated to be 0.5 nm, or smaller, for every pore used in this work, using NNi online calculator (https://www.solidstatenanopore.com/nanopore-calculator). Prior to fabrication, the chips were cleaned using air plasma for 70 s and painted with PDMS to reduce high-frequency noise.

Nanopore Sensing - The DNA nanostructures in 1x assembly buffer were added to a LiCl solution of 0.45 M to 3.6 M for nanopore sensing, typically 5 μL of the nanostructure solution was added to 35 μL LiCl buffered with 10 mM HEPES at pH 8. Linear 2 kbp (ThermoFisher Scientific, SM1701) and 7 kbp (ThermoFisher Scientific, SM1741) NoLimits DNA fragments were always run prior to nanostructures or in a mixture to normalize pore geometry variations. Samples were introduced to the *cis* side of the chip and a negative voltage was applied to the *cis* side with the

trans side grounded. The ionic current recordings were performed in MATLAB 2013a (32-bit) using the VC100 current amplifier (Chimera Instruments) with sampling frequency of 4.17 MHz and a bandwidth of 1 MHz and were subsequently software low-pass Bessel filtered as needed.

Data Analysis - Translocation events in the recorded current traces were located and fitted using a custom implementation of the CUSUM+ algorithm.[237] A digital low-pass filter of 200 kHz was applied for the analysis. The fitted translocation events were plotted and further analyzed using Nanolyzer (v0.1.41) from Northern Nanopore Instruments and Origin 2016 from OriginLab.

5.2 Supporting Information for Section 5.1

S5.2.1. M13mp18 Scaffold Preparation and Characterization

Scaffold preparation

The linearized M13 single-stranded DNA scaffolds were prepared as described in the Methods Section in the main text, using M13mp18 circular single-stranded DNA (New England Biolabs, N4040S). A primer strand was added in a mixture with 10 μg M13mp18 circular single-stranded DNA at a ratio of 10:1 in 1x NEB 3.1 buffer, the mixture was heated to 95 ^{o}C and slowly cooled down to room temperature in a thermal cycler. A mixture of prepared circular scaffold (with primer attached), and 10 units of HincII restriction enzyme (New England Biolabs, R0103S) in a total reaction volume of 50 μL in 1x NEB 3.1 buffer were incubated at 37 ^{o}C for 3 hours, then heat inactivated at 65 ^{o}C for 20 minutes in a thermal cycler.

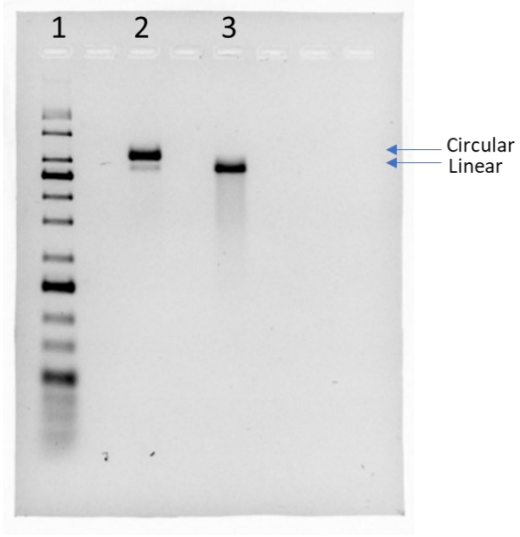

Figure S5.2.1. M13mp18 scaffold gel electrophoresis. Lane 1: GeneRuler 1kbp plus DNA Ladder (ThermoFisher Scientific, SM1331). Lane 2: M13mp18 circular ssDNA scaffold (New England Biolabs, N4040S). Lane 3: M13mp18 linear ssDNA, digested by HincII (New England Biolabs, R0103S). The gel electrophoresis was done using 1% Agarose gel, prepared and performed in 1xTAE buffer at pH 10.5 (40 mM Tris, 20 mM acetic acid, and 2 mM EDTA, pH 10.6) on ice, with an applied voltage of 70V.

The linearized products were characterized by denaturing agarose gel electrophoresis at 1% in 1x TAE buffer (40 mM Tris, 20 mM acetic acid, and 2 mM EDTA, pH 10.5). Upon completion, the agarose gel was submerged in 1xTAE buffer at pH 8 and incubated on incubator at 60 RPM for an hour to bring gel pH back to 8. The gel was then submerged in 2x gel volume de-ionized water with 1x GelRed (Biotium, #41003) for 45 minutes on incubator then store at 4 ^{o}C overnight to post stain. As shown in Figure S5.2.1, linear single-stranded M13 (lane 3) migrate faster than circular single-stranded M13 molecules (lane 2). The disappearance of circular band is an indication of complete cut.

Sequence of linearized M13mp18

The sequence of the M13mp18 scaffold is shown below, showing linearization by HincII (New England Biolabs, R0103S). The underlined sequence represents the region where the primer strand is attached, and the red sequences are the recognition site for HincII restriction enzyme.

GACCTGCAGGCATGCAAGCTTGGCACTGGCCGTCGTTTTACAACGTCGTGACTGGGAAAACCCTGGCGTTACCCAACTTAATCGCCTTGCAGC
ACATCCCCCTTTCGCCAGCTGGCGTAATAGCGAAGAGGCCCGCACCGATCGCCCTTCCCAACAGTTGCGCAGCCTGAATGGCGAATGGCGC
TTTGCCTGGTTTCCGGCACCAGAAGCGGTGCCGGAAAGCTGGCTGGAGTGCGATCTTCCTGAGGCCGATACTGTCGTCGTCCCCTCAAACTG
GCAGATGCACGGTTACGATGCGCCCATCTACACCAACGTGACCTATCCCATTACGGTCAATCCGCCGTTTGTTCCCACGGAGAATCCGACGG
GTTGTTACTCGCTCACATTTAATGTTGATGAAAGCTGGCTACAGGAAGGCCAGACGCGAATTATTTTTGATGGCGTTCCTATTGGTTAAAAAATGAG
CTGATTTAACAAAAATTTAATGCGAATTTTAACAAAATATTAACGTTTACAATTTAAATATTTGCTTATACAATCTTCCTGTTTTTGGGGCTTTTCTGATTAT
CAACCGGGGTACATATGATTGACATGCTAGTTTTACGATTACCGTTCATCGATTCTCTTGTTTGCTCCAGACTCTCAGGCAATGACCTGATAGCCTT
TGTAGATCTCTCAAAAATAGCTACCCTCTCCGGCATTAATTTATCAGCTAGAACGGTTGAATATCATATTGATGGTGATTTGACTGTCTCCGGCCTTT
CTCACCCTTTTGAATCTTTACCTACACATTACTCAGGCATTGCATTTAAAATATATGAGGGTTCTAAAAATTTTTATCCTTGCGTTGAAATAAAGGCTTC
TCCCGCAAAAGTATTACAGGGTCATAATGTTTTTGGTACAACCGATTTAGCTTTATGCTCTGAGGCTTTATTGCTTAATTTTGCTAATTCTTTGCCTTGC
CTGTATGATTTATTGGATGTTAATGCTACTACTATTAGTAGAATTGATGCCACCTTTTCAGCTCGCGCCCCAAATGAAAATATAGCTAAACAGGTTATT
GACCATTTGCGAAATGTATCTAATGGTCAAACTAAATCTACTCGTTCGCAGAATTGGGAATCAACTGTTATATGGAATGAAACTTCCAGACACCGTA
CTTTAGTTGCATATTTAAAACATGTTGAGCTACAGCATTATATTCAGCAATTAAGCTCTAAGCCATCCGCAAAAATGACCTCTTATCAAAAGGAGCAA
TTAAAGGTACTCTCTAATCCTGACCTGTTGGAGTTTGCTTCCGGTCTGGTTCGCTTTGAAGCTCGAATTAAAACGCGATATTTGAAGTCTTTCGGGC
TTCCTCTTAATCTTTTTGATGCAATCCGCTTTGCTTCTGACTATAATAGTCAGGGTAAAGACCTGATTTTTGATTTATGGTCATTCTCGTTTTCTGAACT
GTTTAAAGCATTTGAGGGGGATTCAATGAATATTTATGACGATTCCGCAGTATTGGACGCTATCCAGTCTAAACATTTTACTATTACCCCCTCTGGC
AAAACTTCTTTTGCAAAAGCCTCTCGCTATTTTGGTTTTTATCGTCGTCTGGTAAACGAGGGTTATGATAGTGTTGCTCTTACTATGCCTCGTAATTCC
TTTTGGCGTTATGTATCTGCATTAGTTGAATGTGGTATTCCTAAATCTCAACTGATGAATCTTTCTACCTGTAATAATGTTGTTCCGTTAGTTCGTTTTAT
TAACGTAGATTTTTCTTCCCAACGTCCTGACTGGTATAATGAGCCAGTTCTTAAAATCGCATAAGGTAATTCACAATGATTAAAGTTGAAATTAAACC
ATCTCAAGCCCAATTTACTACTCGTTCTGGTGTTTCTCGTCAGGGCAAGCCTTATTCACTGAATGAGCAGCTTTGTTACGTTGATTTGGGTAATGAAT
ATCCGGTTCTTGTCAAGATTACTCTTGATGAAGGTCAGCCAGCCTATGCGCCTGGTCTGTACACCGTTCATCTGTCCTCTTTCAAAGTTGGTCAGT
TCGGTTCCCTTATGATTGACCGTCTGCGCCTCGTTCCGGCTAAGTAACATGGAGCAGGTCGCGGATTTCGACACAATTTATCAGGCGATGATACA
AATCTCCGTTGTACTTTGTTTCGCGCTTGGTATAATCGCTGGGGGTCAAAGATGAGTGTTTTAGTGTATTCTTTTGCCTCTTTCGTTTTAGGTTGGTGC
CTTCGTAGTGGCATTACGTATTTTACCCGTTTAATGGAAACTTCCTCATGAAAAAGTCTTTAGTCCTCAAAGCCTCTGTAGCCGTTGCTACCCTCGT
TCCGATGCTGTCTTTCGCTGCTGAGGGTGACGATCCCGCAAAAGCGGCCTTTAACTCCCTGCAAGCCTCAGCGACCGAATATATCGGTTATGC
GTGGGCGATGGTTGTTGTCATTGTCGGCGCAACTATCGGTATCAAGCTGTTTAAGAAATTCACCTCGAAAGCAAGCTGATAAACCGATACAATTAA
AGGCTCCTTTTGGAGCCTTTTTTTTGGAGATTTTCAACGTGAAAAAATTATTATTCGCAATTCCTTTAGTTGTTCCTTTCTATTCTCACTCCGCTGAAAC

TGTTGAAAGTTGTTTAGCAAAATCCCATACAGAAAATTCATTTACTAACGTCTGGAAAGACGACAAAACTTTAGATCGTTACGCTAACTATGAGGGC
TGTCTGTGGAATGCTACAGGCGTTGTAGTTTGTACTGGTGACGAAACTCAGTGTTACGGTACATGGGTTCCTATTGGGCTTGCTATCCCTGAAAAT
GAGGGTGGTGGCTCTGAGGGTGGCGGTTCTGAGGGTGGCGGTTCTGAGGGTGGCGGTACTAAACCTCCTGAGTACGGTGATACACCTATTCC
GGGCTATACTTATATCAACCCTCTCGACGGCACTTATCCGCCTGGTACTGAGCAAAACCCCGCTAATCCTAATCCTTCTCTTGAGGAGTCTCAGC
CTCTTAATACTTTCATGTTTCAGAATAATAGGTTCCGAAATAGGCAGGGGGCATTAACTGTTTATACGGGCACTGTTACTCAAGGCACTGACCCCG
TTAAAACTTATTACCAGTACACTCCTGTATCATCAAAAGCCATGTATGACGCTTACTGGAACGGTAAATTCAGAGACTGCGCTTTCCATTCTGGCTT
TAATGAGGATTTATTTGTTTGTGAATATCAAGGCCAATCGTCTGACCTGCCTCAACCTCCTGTCAATGCTGGCGGCGGCTCTGGTGGTGGTTCTG
GTGGCGGCTCTGAGGGTGGTGGCTCTGAGGGTGGCGGTTCTGAGGGTGGCGGCTCTGAGGGAGGCGGTTCCGGTGGTGGCTCTGGTTCCG
GTGATTTTGATTATGAAAAGATGGCAAACGCTAATAAGGGGGCTATGACCGAAAATGCCGATGAAAACGCGCTACAGTCTGACGCTAAAGGCAA
ACTTGATTCTGTCGCTACTGATTACGGTGCTGCTATCGATGGTTTCATTGGTGACGTTTCCGGCCTTGCTAATGGTAATGGTGCTACTGGTGATTTT
GCTGGCTCTAATTCCCAAATGGCTCAAGTCGGTGACGGTGATAATTCACCTTTAATGAATAATTTCCGTCAATATTTACCTTCCCTCCCTCAATCGG
TTGAATGTCGCCCTTTTGTCTTTGGCGCTGGTAAACCATATGAATTTTCTATTGATTGTGACAAAATAAACTTATTCCGTGGTGTCTTTGCGTTTCTTTT
ATATGTTGCCACCTTTATGTATGTATTTTCTACGTTTGCTAACATACTGCGTAATAAGGAGTCTTAATCATGCCAGTTCTTTTGGGTATTCCGTTATTATT
GCGTTTCCTCGGTTTCCTTCTGGTAACTTTGTTCGGCTATCTGCTTACTTTTCTTAAAAAGGGCTTCGGTAAGATAGCTATTGCTATTTCATTGTTTCTT
GCTCTTATTATTGGGCTTAACTCAATTCTTGTGGGTTATCTCTCTGATATTAGCGCTCAATTACCCTCTGACTTTGTTCAGGGTGTTCAGTTAATTCTC
CCGTCTAATGCGCTTCCCTGTTTTTATGTTATTCTCTCTGTAAAGGCTGCTATTTTCATTTTTGACGTTAAACAAAAAATCGTTTCTTATTTGGATTGGG
ATAAATAATATGGCTGTTTATTTTGTAACTGGCAAATTAGGCTCTGGAAAGACGCTCGTTAGCGTTGGTAAGATTCAGGATAAAATTGTAGCTGGGTG
CAAAATAGCAACTAATCTTGATTTAAGGCTTCAAAACCTCCCGCAAGTCGGGAGGTTCGCTAAAACGCCTCGCGTTCTTAGAATACCGGATAAGC
CTTCTATATCTGATTTGCTTGCTATTGGGCGCGGTAATGATTCCTACGATGAAAATAAAAACGGCTTGCTTGTTCTCGATGAGTGCGGTACTTGGTTT
AATACCCGTTCTTGGAATGATAAGGAAAGACAGCCGATTATTGATTGGTTTCTACATGCTCGTAAATTAGGATGGGATATTATTTTTCTTGTTCAGGA
CTTATCTATTGTTGATAAACAGGCGCGTTCTGCATTAGCTGAACATGTTGTTTATTGTCGTCGTCTGGACAGAATTACTTTACCTTTTGTCGGTACTTT
ATATTCTCTTATTACTGGCTCGAAAATGCCTCTGCCTAAATTACATGTTGGCGTTGTTAAATATGGCGATTCTCAATTAAGCCCTACTGTTGAGCGTT
GGCTTTATACTGGTAAGAATTTGTATAACGCATATGATACTAAACAGGCTTTTTCTAGTAATTATGATTCCGGTGTTTATTCTTATTTAACGCCTTATTTA
TCACACGGTCGGTATTTCAAACCATTAAATTTAGGTCAGAAGATGAAATTAACTAAAATATATTTGAAAAAGTTTTCTCGCGTTCTTTGTCTTGCGATT
GGATTTGCATCAGCATTTACATATAGTTATATAACCCAACCTAAGCCGGAGGTTAAAAAGGTAGTCTCTCAGACCTATGATTTTGATAAATTCACTAT
TGACTCTTCTCAGCGTCTTAATCTAAGCTATCGCTATGTTTTCAAGGATTCTAAGGGAAAATTAATTAATAGCGACGATTTACAGAAGCAAGGTTATT
CACTCACATATATTGATTTATGTACTGTTTCCATTAAAAAAGGTAATTCAAATGAAATTGTTAAATGTAATTAATTTTGTTTTCTTGATGTTTGTTTCATCAT
CTTCTTTTGCTCAGGTAATTGAAATGAATAATTCGCCTCTGCGCGATTTTGTAACTTGGTATTCAAAGCAATCAGGCGAATCCGTTATTGTTTCTCCC
GATGTAAAAGGTACTGTTACTGTATATTCATCTGACGTTAAACCTGAAAATCTACGCAATTTCTTTATTTCTGTTTTACGTGCAAATAATTTTGATATGGT
AGGTTCTAACCCTTCCATTATTCAGAAGTATAATCCAAACAATCAGGATTATATTGATGAATTGCCATCATCTGATAATCAGGAATATGATGATAATTC
CGCTCCTTCTGGTGGTTTCTTTGTTCCGCAAAATGATAATGTTACTCAAACTTTTAAAATTAATAACGTTCGGGCAAAGGATTTAATACGAGTTGTCGA
ATTGTTTGTAAAGTCTAATACTTCTAAATCCTCAAATGTATTATCTATTGACGGCTCTAATCTATTAGTTGTTAGTGCTCCTAAAGATATTTTAGATAACC
TTCCTCAATTCCTTTCAACTGTTGATTTGCCAACTGACCAGATATTGATTGAGGGTTTGATATTTGAGGTTCAGCAAGGTGATGCTTTAGATTTTTCATT
TGCTGCTGGCTCTCAGCGTGGCACTGTTGCAGGCGGTGTTAATACTGACCGCCTCACCTCTGTTTTATCTTCTGCTGGTGGTTCGTTCGGTATTTT
TAATGGCGATGTTTTAGGGCTATCAGTTCGCGCATTAAAGACTAATAGCCATTCAAAAATATTGTCTGTGCCACGTATTCTTACGCTTTCAGGTCAG
AAGGGTTCTATCTCTGTTGGCCAGAATGTCCCTTTTATTACTGGTCGTGTGACTGGTGAATCTGCCAATGTAAATAATCCATTTCAGACGATTGAGC
GTCAAAATGTAGGTATTTCCATGAGCGTTTTTCCTGTTGCAATGGCTGGCGGTAATATTGTTCTGGATATTACCAGCAAGGCCGATAGTTTGAGTTC
TTCTACTCAGGCAAGTGATGTTATTACTAATCAAAGAAGTATTGCTACAACGGTTAATTTGCGTGATGGACAGACTCTTTTACTCGGTGGCCTCACT
GATTATAAAAACACTTCTCAGGATTCTGGCGTACCGTTCCTGTCTAAAATCCCTTTAATCGGCCTCCTGTTTAGCTCCCGCTCTGATTCTAACGAG
GAAAGCACGTTATACGTGCTCGTCAAAGCAACCATAGTACGCGCCCTGTAGCGGCGCATTAAGCGCGGCGGGTGTGGTGGTTACGCGCAGC
GTGACCGCTACACTTGCCAGCGCCCTAGCGCCCGCTCCTTTCGCTTTCTTCCCTTCCTTTCTCGCCACGTTCGCCGGCTTTCCCCGTCAAGCT
CTAAATCGGGGGCTCCCTTTAGGGTTCCGATTTAGTGCTTTACGGCACCTCGACCCCAAAAAACTTGATTTGGGTGATGGTTCACGTAGTGGGCC
ATCGCCCTGATAGACGGTTTTTCGCCCTTTGACGTTGGAGTCCACGTTCTTTAATAGTGGACTCTTGTTCCAAACTGGAACAACACTCAACCCTAT
CTCGGGCTATTCTTTTGATTTATAAGGGATTTTGCCGATTTCGGAACCACCATCAAACAGGATTTTCGCCTGCTGGGGCAAACCAGCGTGGACCG
CTTGCTGCAACTCTCTCAGGGCCAGGCGGTGAAGGGCAATCAGCTGTTGCCCGTCTCACTGGTGAAAAGAAAAACCACCCTGGCGCCCAATA
CGCAAACCGCCTCTCCCCGCGCGTTGGCCGATTCATTAATGCAGCTGGCACGACAGGTTTCCCGACTGGAAAGCGGGCAGTGAGCGCAACG
CAATTAATGTGAGTTAGCTCACTCATTAGGCACCCCAGGCTTTACACTTTATGCTTCCGGCTCGTATGTTGTGTGGAATTGTGAGCGGATAACAATT
TCACACAGGAAACAGCTATGACCATGATTACGAATTCGAGCTCGGTACCCGGGGATCCTCTAGAGTC

S5.2.2. 3HB Nanostructure Design and Sequence

Structure design

The caDNAno design of 3HB is shown in Figure S5.2.2. Due to its length and repetitive nature, only a partial design is shown here. The long blue strand represents the M13mp18 scaffold, and the short, coloured arrows are the staple strands, with the arrow side being the 3' end.

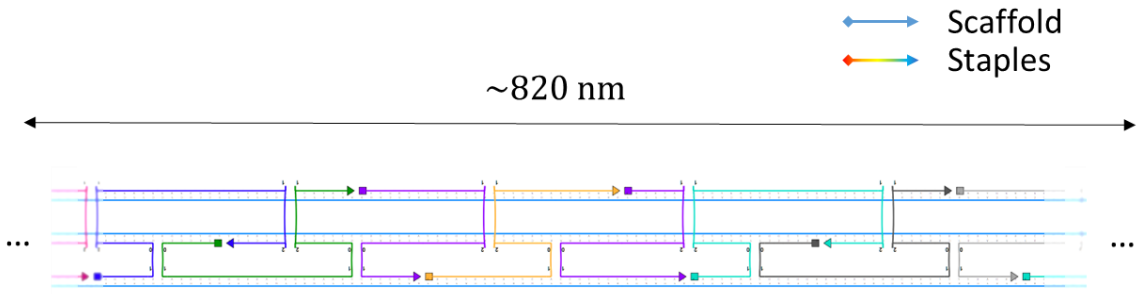

Figure S5.2.2. **caDNAo design of 3HB** on a honey-comb lattice, using M13mp18 scaffold (circular, New England Biolabs, N4040S), linearized at HincII (New England Biolabs, R0103S) site, using 191 staple strands with an average oligo length of 38 nt.

Nanostructure assembly

The 3HB molecules were assembled by mixing the linearized single stranded M13 scaffold with 191 staple strands at a molar ratio of 1:10 in assembly buffer (at final 40 mM Tris, 20 mM acetic acid, 2 mM EDTA, and 16 mM $MgCl_2$, pH 8). The mixture was heated to 95 ^{o}C for 5 minutes, cooled to 90 ^{o}C, ramped from 90 ^{o}C to 60 ^{o}C at a rate of 0.4 ^{o}C per minute, then from 60 ^{o}C to 26 ^{o}C at a rate of 0.03 ^{o}C per minute, and snap cooled to 4 ^{o}C using minicamp Plus Thermal Cycler (ThermoFisher Scientific, #A37835). The nanostructures were subsequently washed three times using 100 kDa Amicon Ultra-0.5 Centrifugal Filter Unit (Millipore Sigma, UFC500396) using the assembly buffer to remove the excess staple oligos. Once assembled, the 3HB molecules were run on a 1% non-denaturing Agarose gel on ice, as shown in Figure S5.2.3, showing one clear band. The excess staple strands were removed by three washes using the assembly buffer (40

mM Tris, 20 mM acetic acid, 2 mM EDTA, and 16 mM MgCl2, pH 8) through 100 kDa Amicon Ultra-0.5 Centrifugal Filter Unit (Millipore Sigma, UFC500396).

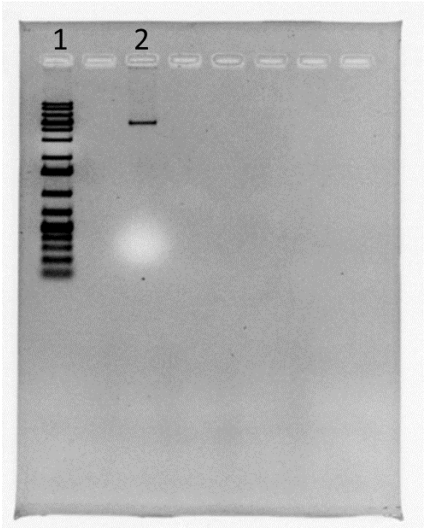

Figure S5.2.3. Gel electrophoresis characterization of 3HB assembly. Lane 1: Generuler 1 kb plus DNA Ladder (ThermoFisher Scientific, SM1331). Lane 2: 3HB. The gel electrophoresis was done using 1% Agarose gel, which was prepared and performed in 1xTAE buffer (40 mM Tris, 20 mM acetic acid, and 2 mM EDTA) at pH 8 on ice, with an applied voltage of 70 V.

Staple strand sequences

Table S5.2.1. Staple strand sequences for 3HB, and primer sequence for HincII restriction enzyme.

Oligo	Sequence	Length
1	CGACGGCGTTATACACCGGAATCATAATTACTAGAAAAAG	40
2	CCCAGTCATAAAGCAGGCGTTAAATAAG	28
3	GTTGGGTAGGGCTTATACCGACCGTGTG	28
4	AAAGGGGGATGTGCATATTTAACCTAAATTTAATG	35
5	CGGTGCGCGAGCCAAGAAAACTTTTTCAAATATATGGCAGAG	42
6	AGGCTGCGCAACTGTAAAGTAAATCGCAAGACAAA	35
7	GTGCCGGACAATAAAGGTTGGGTTATATAACTATACTGTCCA	42
8	TCCAGCCAGCTTTCTAATGCATACCTTTTTAACCT	35
9	GGACGACAACAAGAAGAGTCAATAGTGAATTTATCATAGATA	42
10	TCGTAACCGTGCATTCCTAATGCTTAGATTAAGAC	35
11	TAATGGGTCTTTCCATTAATTAATTTTCCCTTAGATCAATAA	42
12	TCCGTGGGAACAAAACGGGTATTGCTTCTGTAAAT	35
13	CATTAAAGCCGTTTAATGGAAACAGTACATAAATCTCGAGAA	42

14	TGGCCTTCCTGTAGGGAATCATTCATTTGAATTAC	35
15	AACCAATAGGCTTAGAAACAAACATCAAGAAAACAAAATCAG	42
16	AAATTTTTGTTAAAAACGCGAACCTGAGCAAAAGA	35
17	ATTGTAATTGAAGCCAAGTTACAAAATCGCGCAGAACTTGCG	42
18	CAGGAAGATTGTATAGTTGCTTCGCCTGATTGCTT	35
19	TGTACCCACCAACGACAGTAACAGTACCTTTTACATTATCCT	42
20	TAATCGTAAAACTATCCAGAGGGTTTAACGTCAGA	35
21	GAGAGTCATTTATCTTTGCACGTAAAACAGAAATATAAACAG	42
22	ATCTACAAAGGCTAAAACGATGAACCTACCATATC	35
23	AAATTAATTACAGATCCTGATTGTTTGGATTATACGAAAATA	42
24	AATATGATATTCAAAACAGGGGATGGCAATTCATC	35
25	GGGTGAGGAACAAACCAGAAGGAGCGGAATTATCATAACTGA	42
26	TGAGTAATGTGTAGGAGCGCTTTTTGCGGAACAAA	35
27	TTTTTAGGCCCAATGCCCGAACGTTATTAATTTTAAAGAATT	42
28	AGCCTTTATTTCAAACAATGAACAACTCGTATTAA	35
29	AAAACATGAAAAGTACATTTGAGGATTTAGAAGTAGAAGCCC	42
30	AGAGCATAAAGCTAACAAAGTTTAGAGCCGTCAAT	35
31	GGCAAAGGAATACCAGGTTATCTAAAATATCTTTAACGCAAT	42
32	ATTAACATCCAATATGATTAAACAGTTGAAAGGAA	35
33	GAAAAGGAAATACAAATATCAAACCCTCAATCAATTTAGCAA	42
34	AGCTATATTTTCATAACATATGCATCACCTTGCTG	35
35	TTAGATATTTGTCAACAGTGCCACGCTGAGAGCCACGGAATA	42
36	CTGCGAACGAGTAGTTCATATTCAGTATTAACACC	35
37	GAAGTTTAACCGATCCGAACGAACCACCAGCAGAAAAAGGGC	42
38	TAAATATGCAACTATAAATATAAAACATCGCCATT	35
39	AATTGCTGTCACCGTTTGAATGGCTATTAGTCTTTGGTGAAT	42
40	GGTCATTTTTGCGGGGAATTAATACGTGGCACAGA	35
41	TTAGAGAAGCAAGGTGGCCAACAGAGATAGAACCCGCACCAT	42
42	ACCGGAAGCAAACTAATGAAACCAGTAATAAAAGG	35
43	TATCGCGATCAAGTTGAAATGGATTATTTACATTGTCAGTAG	42
44	ATTAAGAGGAAGCCAGACTGTACATTTTGACGCTC	35
45	TTATAGTCTTATTACCGCCAGCCATTGCAACAGGATCGGTCA	42
46	ATCAAAAATCAGGTTTCATAAGTAATATCCAGAAC	35
47	GCTTTAAGCCTCCCTCACTTGCCTGAGTAGAAGAACCACCAC	42
48	ATAAATATTCATTGCTCAGAACTTCTTTGATTAGT	35
49	TTAGACTACCAGAAAAAAGAGTCTGTCCATCACGCCCCTCAG	42

50	TTTGCCAGAGGGGGGCCGCCATAATCAGTGAGGCC	35
51	AAACCAAGCCTTGATTAGACAGGAACGGTACGCCAAGGTCAG	42
52	ATAACCCTCGTTTATAAATCCAGGAGGCCGATTAA	35
53	AAGGAATTTTACCGTATAACGTGCTTTCCTCGTTAGCGCAGT	42
54	TTCAACTAATGCAGATACATGATGGTTGCTTTGAC	35
55	GAAAGATTTTAACGCCACACCCGCCGCGCTTAATGTACTGGT	42
56	AACTAACGGAACAAAGTAACACGGTCACGCTGCGC	35
57	GGACGTTTCGGAACAGAAAGCGAAAGGAGCGGGCGGCCCCCT	42
58	TTTAAGAACTGGCTCATGAAAACGTGGCGAGAAAG	35
59	TTCAACTAGGATTAAAGGGAGCCCCCGATTTAGAGTCAAGAG	42
60	TAGTAAATTGGGCTAGTACCAAAGCACTAAATCGG	35
61	ATAAGGCATAGCCCAACCATCACCCAAATCAAGTTGGGTTGA	42
62	CAACGTAACAAAGCACCGTACAGGGCGATGGCCCA	35
63	AATCTTGACCCTCAAGAACGTGGACTCCAACGTCACCCTCAG	42
64	CATAGGCTGGCTGAAGAGCCAGGAACAAGAGTCCA	35
65	GAAAGAGAACCCATCAAAAGAATAGCCCGAGATAGGCAAGCC	42
66	TCATAAGGGAACCGAGTTTCGTCGGCAAAATCCCT	35
67	ATGTTACCAGACAGTGCCCCAGCAGGCGAAAATCCCCTGTAG	42
68	AATTGTGTCGAAATGTAACGAAGCAAGCGGTCCAC	35
69	CAAAGTATGAATTTAACAGCTGATTGCCCTTCACCCAGACGT	42
70	ACCCCCAGCGATTATGCTAAACTTTTCACCAGTGA	35
71	AGAGGCAAGGAACACGGGGAGAGGCGGTTTGCGTAGAGTGAG	42
72	CACTACGAAGGCACGAATAATATTAATGAATCGGC	35
73	GGAAGTTTCCAAAACACTGCCCGCTTTCCAGTCGGTCCAAAA	42
74	GCTTTGAGGACTAATATCGGTTCACATTAATTGCG	35
75	ACAGCATGCTTGATGCATAAAGTGTAAAGCCTGGGGAATTTC	42
76	GCGGGATCGTCACCCGACAATCACACAACATACGA	35
77	GCTGAGGCTTGCAGGGAGTTAAAGGCCCCACGCATTGTTA	40
78	CCTGTTTAGTATCATATGCCAGTGCCAAGCTTGCATGC	38
79	GCATTTTGGCCTCTTCGCTATTACGCCATAATTTATTTAGTT	42
80	GACGACGAAACCAGGCAAAGCGCCATTCAGTAATTTGTAAAT	42
81	AGTCCTGGACAGTATCGGCCTCAGGAAGATCAACAAAAATCA	42
82	TCGGCTGATAGGTCACGTTGGTGTAGATAAACCAAATCCTTG	42
83	CAAGCAATGTGAGCGAGTAACAACCCGTGCACTCAAATATAT	42
84	ATATAGAAGGAACGCCATCAAAAATAATAGCAAGCAAATTAA	42
85	GGAGGTTACGTTAATATTTTGTTAAAATCCTCCCGGGCGAAT	42

86	GAATCTTCGGTTGATAATCAGAAAAGCCTACAATTTCGGGAG	42
87	CCATATTTGGAGCAAACAAGAGAATCGATACAAAAAAGAAAT	42
88	GCAGCCTTGCCGGAGAGGGTAGCTATTTCAAAAATTTCTGAA	42
89	ACACCCTAAAGGCCGGAGACAGTCAAATGGAGAATTCATATT	42
90	GAGTTAAAACCCTCATATATTTTAAATGAACCCACAAAGTTT	42
91	TTTTTAATATGACCCTGTAATACTTTTGTCTTACCTTAGACT	42
92	AATAACGAATTAGCAAAATTAAGCAATACGAGGAAGGAGCAC	42
93	ACGTAGATGGCATCAATTCTACTAATAGCAGTATGATCTGGT	42
94	AGTTTATCATTTCGCAAATGGTCAATAAGACACCAGCAGCAA	42
95	GACATTCCATTCCATATAACAGTTGATTAAAGACAGATAAAA	42
96	TATCACCGAATATAATGCTGTAGCTCAACATTAAAAATGCGC	42
97	TACCATTGTACCTTTAATTGCTCCTTTTACCAGTATTCTGAC	42
98	CGACAGATTTTAATTCGAGCTTCAAAGCACCGTAAGCAGATT	42
99	TAGCCCCCAGAAGCAAAGCGGATTGCATGGCATTTAAAACGC	42
100	CGGAACCACAGTTCAGAAAACGAGAATGACCAGAGCTCAAAC	42
101	AGCCGCCGGATAGCGTCCAATACTGCGGGCCACCAAAATTAA	42
102	ACGATTGAATAGCGAGAGGCTTTTGCAATTGAGGCGAATCCT	42
103	CTCTGAATACGAGGCATAGTAAGAGCAAATGGAAAGAATCAG	42
104	AATAAGTTCATCAGTTGAGATTTAGGAAAGGAGTGCGCCGCT	42
105	GCCTATTGGGAAGAAAAATCTACGTTAAAGTTAATCTAGGGC	42
106	AAGGATTTTAATCATTGTGAATTACCTTAGACTCCCTTGACG	42
107	TATAAGTTTGCCCTGACGAGAAACACCAGTCGAGATTTTGGG	42
108	AACCGCCACAAGAACCGGATATTCATTAACCGCCAAAGGGCG	42
109	CAATAGGGACAGATGAACGGTGTACAGAAGGGATAGGTTGAG	42
110	CATTCCATTAGCCGGAACGAGGCGCAGATACAACGTGTTTGA	42
111	TAGTAAACAACGGAGATTTGTATCATCGGTCTTTCGCCTGGC	42
112	AATAGAAAAAGAATACACTAAAACACTCTTCAGCGTTGGGCG	42
113	AAAAGGCTCCATTAAACGGGTAAAATACGAAAATCGAAACCT	42
114	TTAAACACGGAACGAGGGTAGCAACGGCTCGAGGTGTGCCTA	42
115	AATAAACAAATTCTTACCAGTACGACGTTGTAAAA	35
116	ATAAATACAACGCTCAACAGTAACGCCAGGGTTTT	35
117	GTTTGAAAATTGAGAATCGCCTGCAAGGCGATTAA	35
118	AATTTCATCTTCTGACAACGCCAACATGGCTGGCG	35
119	GAACGCGGTAATAAGAGAATATTGGGAAGGGCGAT	35
120	GCTGATGCAAATCCCCGACAAAAGGTAAGCCATTC	35
121	CCGGCTTACAACATGTTCAGCCGGCACCGCTTCTG	35

122	TAGGTCTGAGAGACGAACGCGCCTGTTTATCGCAC	35
123	GCTGAGAAAAATAATATCCCACTGCCAGTTTGAGG	35
124	AAAACATAGCGATATTACGAGCATGTAGGGGCGCA	35
125	CGTCGCTTTATCATTCCAAGACGGCGGATTGACCG	35
126	GTGAGTGAATAACCTTAAACCAAGTACCCGGATTC	35
127	CTTTTTTTTATTTTCATCGTACCAGCTTTCATCAA	35
128	TTACATTTAACAATTTACCGCGCCCAATTCGCGTC	35
129	AGATGATTCCGGTATTCTAAGTCAGCTCATTTTTT	35
130	TATTCATTTCAATTGGCGTTTTAGCGAATCGCATT	35
131	TGAATACCTTAAATCAAGATTAAGCAAATATTTAA	35
132	AAACAATAACGGATATTTTGCACCCAGCCCAAAAA	35
133	TGAATATCTAACGAGCGTCTTGCATGTCAATCATA	35
134	TGCGTAGATTTTCACCTAATTTGCCAGTTGAACGG	35
135	AAAATTACCAATCCAAATAAGTCAGGTCATTGCCT	35
136	TAATGGAAGGGTTATTTTTGTTTAACGTTTGAGAG	35
137	AATATAAGAGAATAACATAAACCGTTCTAGCTGAT	35
138	CCTGATTATCAGATAAGCGCATTAGACGCACCATC	35
139	GAAACCAGTCAGAGGGTAATTGTAAAGATTCAAAA	35
140	GAGTAACATTATCAAATATCAGAGAGATCAATGCC	35
141	ATCCTTTAATAAGAGCAAGAACGCAAGGATAAAAA	35
142	TTACAAACAATTCGAATAGCAATAGCTACGGGAGA	35
143	AGATAATAAGCAGATAGCCGAAATCGGTTGTACCA	35
144	TAACAACTAATAGATACCAGAAGGAAACAAGCCTC	35
145	TTGAGGACAAAAGAACTGGCAAATCATACAGGCAA	35
146	CAGTTGGCAAATCAGACTCCTTATTACGTAGTAGC	35
147	AACCTCATACATAAAGGTGGCTTGGGGCGCGAGCT	35
148	ATGAAAAATCTAAAAAAAGAAACGCAAACCTGTTT	35
149	GCCTGCACAATCAATAGAAAAATTTAGTTTGACCA	35
150	CAGAGGTGAGGCGGGGTTTACCAGCGCCCCCAATT	35
151	AAAAATATGAGGGAGGGAAGGAAGTACGGTGTCTG	35
152	GAACTGATAGCCCTTGACGGAAATTATTCATGTTT	35
153	CAATATTACTTGAGCCATTTGATGGCTTAGAGCTT	35
154	CTGAAAGCGTAAGAGAGCCAGCAAAATCGATAAGA	35
155	GACATTCCCGGAAACGTCACCCCAACAGGTCAGGA	35
156	CACCAGTCACACGACCATCGATAGCAGCGAACCAG	35
157	AATCGTCTTGCCTTTAGCGTCCGAAAGACTTCAAA	35

158	TCATGGAAATACCTAGCGCGTTTTCATCCAAAAAG	35
159	AATATTAGCGTTTGCCATCTTCTTTACCCTGACTA	35
160	TATCGGCCTTGCTGTCAAAATCACCGGAACCATAA	35
161	AATAACATCAGAGCCGCCACCAATCCCCCTCAAAT	35
162	CCGTTGTAGCAATACCGCCACCCTCAGAAATCGTC	35
163	ACCGAGTCCACCACCAGAGCCTAATAGTAAAATGT	35
164	GAGAAGTGTTTTTAGCATTGACAGGAGGAAGAAGT	35
165	AGGGATTTATTCACAAACAAACCAGACGACGATAA	35
166	AGCGGGAGCTAAACTCATTAAAGCCAGACACTATC	35
167	GAGCACGTTCCAGTAAGCGTCATACATAACGCCAA	35
168	ACAGGGCGCGTACTGCTTTTGATGATACTACCACA	35
169	GTAACCAGGGTCAGTGCCTTGCATTATTACAGGTA	35
170	GCTGGCAAGTGTAGGTGCCCGTATAAACTAAAACG	35
171	GAAGGGACTATTATTCTGAAACATTATACCAGTCA	35
172	GGGAAAGCCGGCGAGTATTAAGAGGCTGATGCGAT	35
173	AACCCTAGCGGGGTTTTGCTCTGAGATGGTTTAAT	35
174	GTCGAGGTGCCGTAGGCGGATAAGTGCCGAACGAG	35
175	CTACGTGGGAATAGGTGTATCTGCTCATTCAGTGA	35
176	AAAAACCGTCTATCTCAGGAGGTTTAGTCCCAAAT	35
177	CTATTAAGAACCGCCACCCTCCCTTCATCAAGAGT	35
178	TGTTGTTCCAGTTTCCACCCTCATTTTCCCAGGCG	35
179	TATAAATGTACCGTAACACTGAACTGACCAACTTT	35
180	TGGTGGTTCCGAAATCACCAGTACAAACCGGTCAA	35
181	GCTGGTTCCCTCATAGTTAGCCCGCGACCTGCTCC	35
182	CCTGAGAGAGTTGCTCTAAAGTTTTGTCCCTGATA	35
183	GACGGGCTCTGTATGGGATTTTACCAAGCGCGAAA	35
184	CCAGGGTGGTTTTTCAACTTTCAACAGTATCTTTG	35
185	CAACGCGACTAAAGGAATTGCCAACCTAAAACGAA	35
186	GTCGTGCCAGCTGCAATTTTTTCACGTTGTAATGC	35
187	TTGCGCTGGAGCCTTTAATTGAGACTTTTTCATGA	35
188	ATGAGTGAGCTAACTTATCAGCTTGCTTTACAGAG	35
189	GCCGGAAACCGATAGTTGCGCCTCAGCAGCGAAAG	35
190	TCCGCTCACAATTCGACAACAACCATCGCGCTTTT	35
191	TAGCTGTTTCCTGTGTGAAATAACCGATATATTCGGTC	38
HincII Primer	CTGCAGGTCGACTCTAGAGG	20

S5.2.3. Translocation Times *versus* Voltage and Salt-Concentration

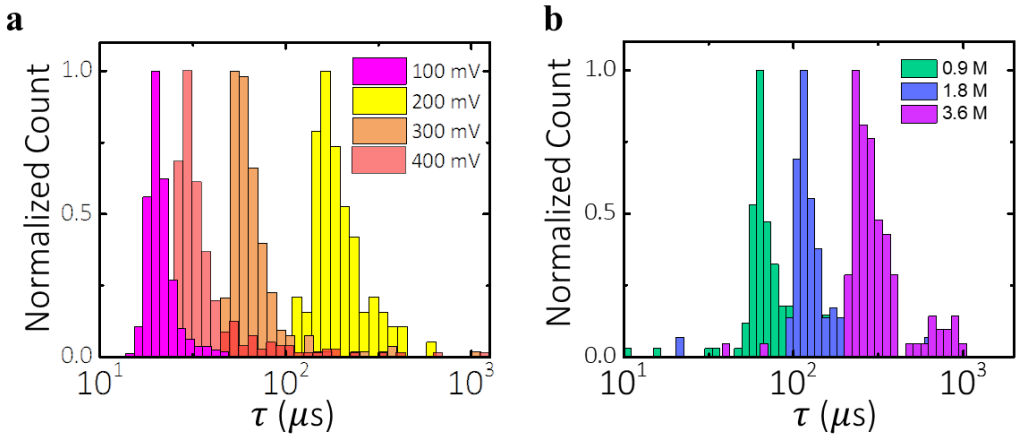

Figure S5.2.4. Salt-concentration and voltage dependence. a) Distribution of single-file translocation times recorded under different voltages in a 13.3 nm nanopore, in 0.9 M LiCl. **b)** Distribution of single-file translocation times recorded under different salt concentrations for a 11.2 nm pore under a 200mV voltage.

S5.2.4. Estimates of Nanostructure Volume – ECD Comparisons

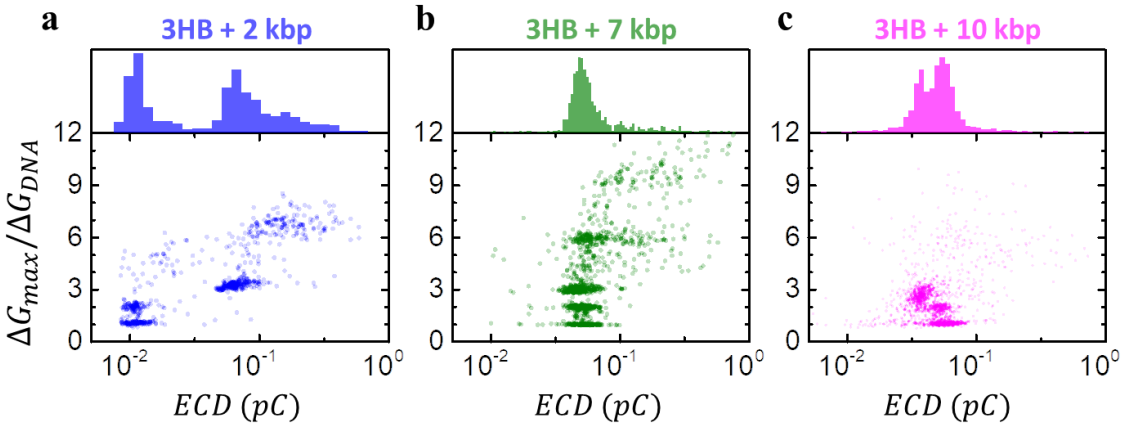

Figure S5.2.5. ECD Comparisons. a) 3HB with 2kbp dsDNA through a 13.3 nm pore in 0.9 M LiCl under a 200 mV bias, N = 630. **b)** 3HB with 7kbp dsDNA through a 11.2 nm pore in 0.9 M LiCl under a 200 mV bias, N = 1189. **c)** 3HB with 10kbp dsDNA through a 25 nm pore in 0.72 M LiCl under a 200 mV bias, N = 1757.

S5.2.5. Strong Correlation of Metastable State and Total Duration

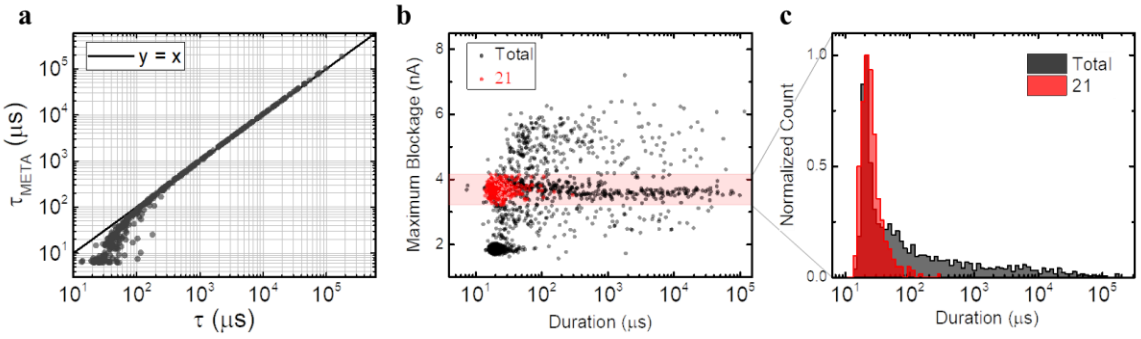

Figure S5.2.6. Metastable state correlation. a) Metastable durations versus total translocation time for 3HB molecules on a log-log plot. A very strong correlation is observed for longer translocations. **b)** Scatter plot of Maximum blockage versus τ for all types of translocation events and versus τ_{21} for folded events contained withing the horizontal red band, N (total) = 1333, and N(21) = 321. **c)** Distributions of τ and τ_{21} for folded events of b). In calculating τ_{21}, the contribution of the metastable state to the total translocation times is omitted. The distribution of τ_{21} is well-described by a log-normal distribution, and the spread of τ_{21} is significantly smaller than that of τ_{total}, and comparable to that of single-file translocation times. This further supports the interpretation that events with $\Delta G_{max} = 2 \times \Delta G_{3HB}$ are indeed folded translocation events preceeded by a metastable state. The data for a-c were acquired using a 13.3 nm pore in 0.9 M LiCl, under a bias of 400 mV.

S5.2.6. Voltage Dependence of Metastable State Duration Distributions

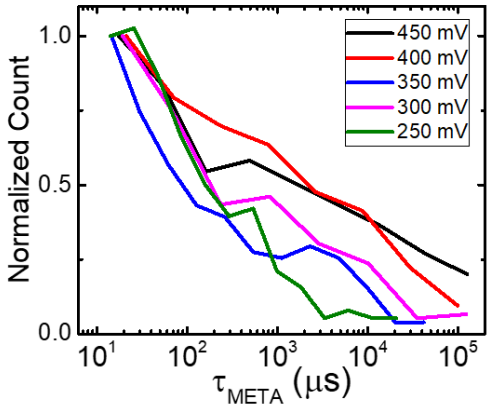

Figure S5.2.7. Distribution of metastable state durations τ_{META} measured at different voltages, in a 13.3 nm nanopore, in a 0.9 M LiCl solution. Distributions are normalized such that the count at the smallest τ_{META} bin is 1.

S5.2.7. Metastable State Power Spectra

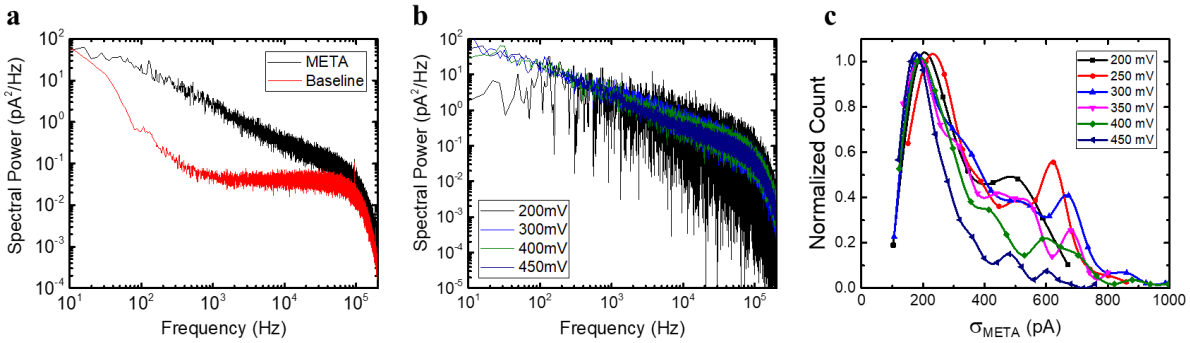

Figure S5.2.8. Spectral Power vs Frequency comparison of **a)** the metastable state and the baseline ionic current, and **b)** the metastable state current measured under different voltages. **c)** Distribution of the standard deviation of individual metastable state current traces. Results were obtained from a 13.3 nm pore, in 0.9 M LiCl.

Figure S5.2.8a plots and compares the Power Spectral Densities (PSD) of the ionic current traces of the open-pore baseline and of the metastable states: $1/f$ noise dominates the metastable state PSD for the entire bandwidth used, unlike the baseline current. Note that the PSD traces for the metastable state were obtained by concatenating the zeroed metastable traces, after which the spectral power was calculated over the entire concatenated trace. Interestingly, Figure S5.2.8b shows that amplitude of the metastable state PSD traces is independent of the applied voltage. Given that the current's root mean square (RMS) is equivalent to the integral of PSDs, Figure S5.2.8b therefore suggests that the RMS of metastable states is voltage independent. To confirm this, Figure S5.2.8c plots the normalized histograms of the metastable state current standard deviation $\sigma_{META} = \langle [I_{META} - \langle I_{META} \rangle]^2 \rangle^{1/2}$, measured for each individual event. Consistent with Figure S5.2.8b, Figure S5.2.8c shows that for every measured voltage, the most probable σ_{META} value is $\approx 200\ pA$.

S5.2.8. Metastable State in Folded and Single-File Translocations

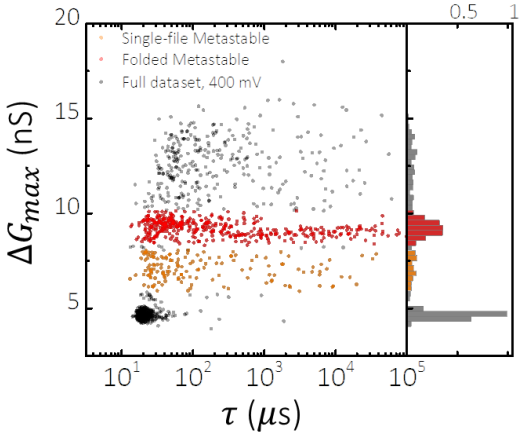

Figure S5.2.9. Folded event characterization. A scatter plot of maximum blockage versus translocation time and a histogram of maximum blockage distribution for 3HB molecules, N = 1330. Events with meta-stable states are highlighted: i) meta-stable followed by a single-file translocation in orange, N = 151; ii) meta-stable state followed by a folded translocation in red, N = 395. The experiment was perform using a 13.3 nm pore in 0.9 M LiCl, with an applied bias of 400 mV.

In addition to folded translocations, metastable states can also precede single-file translocations. Figure S5.2.9 shows the scatter plot of ΔG_{max} *versus* τ for 3HB passing through a 13.3 nm pore in 0.9 M LiCl solution under a 400 V bias. Under these conditions, the metastable states result in deeper blockages than single-file translocations, as demonstrated in Figure 5.1.3e of the main article. Events composed of a metastable state followed by a single-file translocation are therefore identifiable due to their ΔG_{max} values being between those of single-file translocations (ΔG_{3HB}) and folded translocations ($2 \times \Delta G_{3HB}$). These events are highlighted in orange in Figure S5.2.9, whereas folded translocations are highlighted in red.

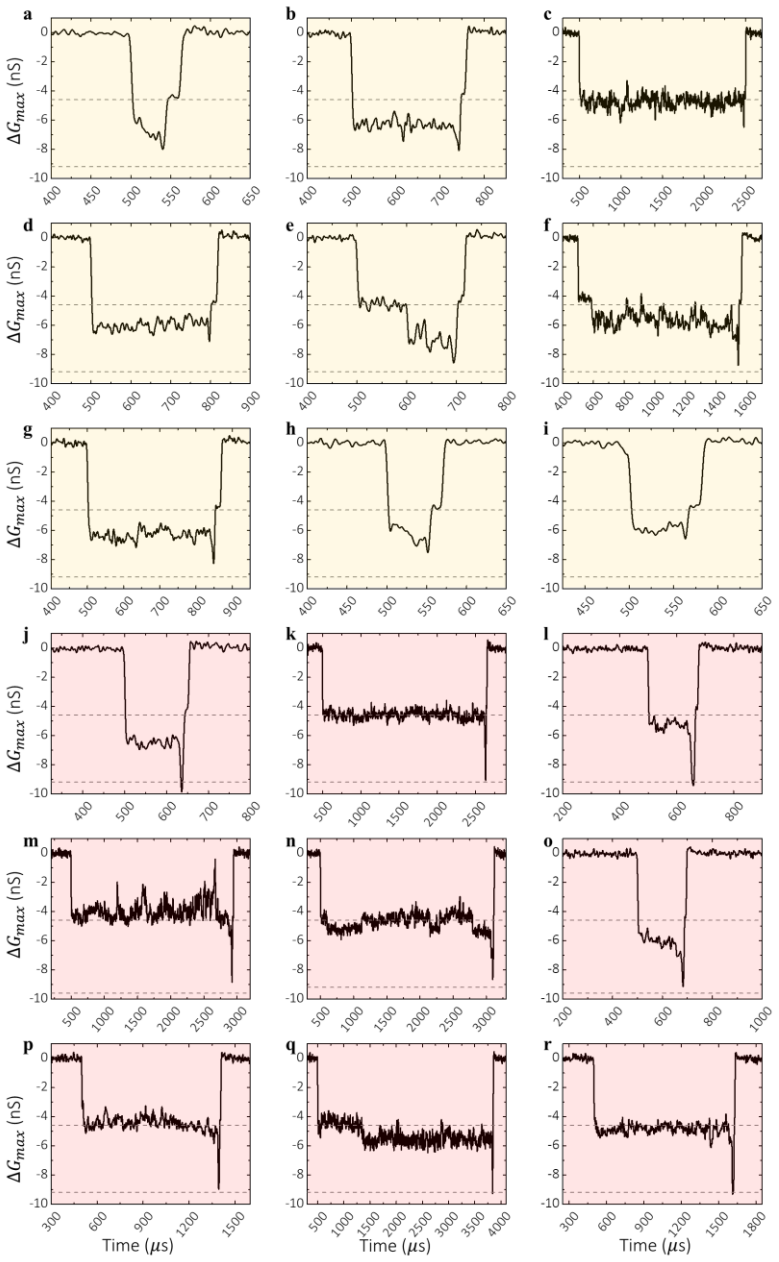

Figure S5.2.10. Current traces of 3HB with meta-stable events. a-i) 3HB current traces of meta-stable state followed by single-file translocation. **j-r)** 3HB current traces of meta-stable state followed by folded translocation. All experiments performed in 0.9 M LiCl, in a 13.3 nm nanopore with an applied bias of 400 mV. The grey dash lines correspond to $\Delta G_{max} = \Delta G_{3HB}$, and $\Delta G_{max} = 2 \times \Delta G_{3HB}$.

Figures S5.2.10a-i show the current traces of nine single-file translocations preceded by metastable states, whereas Figures S5.2.10j-r show folded translocations. For almost all events,

transition from metastable state to the single file blockage state is characterized by a rapid spike, slightly deeper than the metastable state. This spike could either be a folded state too rapid to be well resolved, as sometimes observed, but it could also be an orientation feature, as Wu *et al.* observed when passing the rigid rod-shaped tobacco mosaic virus through nanopores, wherein a rigid molecule enters the pore at an angle and needs to re-orient with the pore to fully enter and traverse.[238] The presence of non-aligned molecules inside nanopores results in deeper blockages than aligned conformations due to the slightly increased cross-sectional area and would therefore be expected from a laterally diffusing 3HB molecule finding and entering by an end.

S5.2.9. Dependence of Metastable State on Experimental Conditions

Pore size

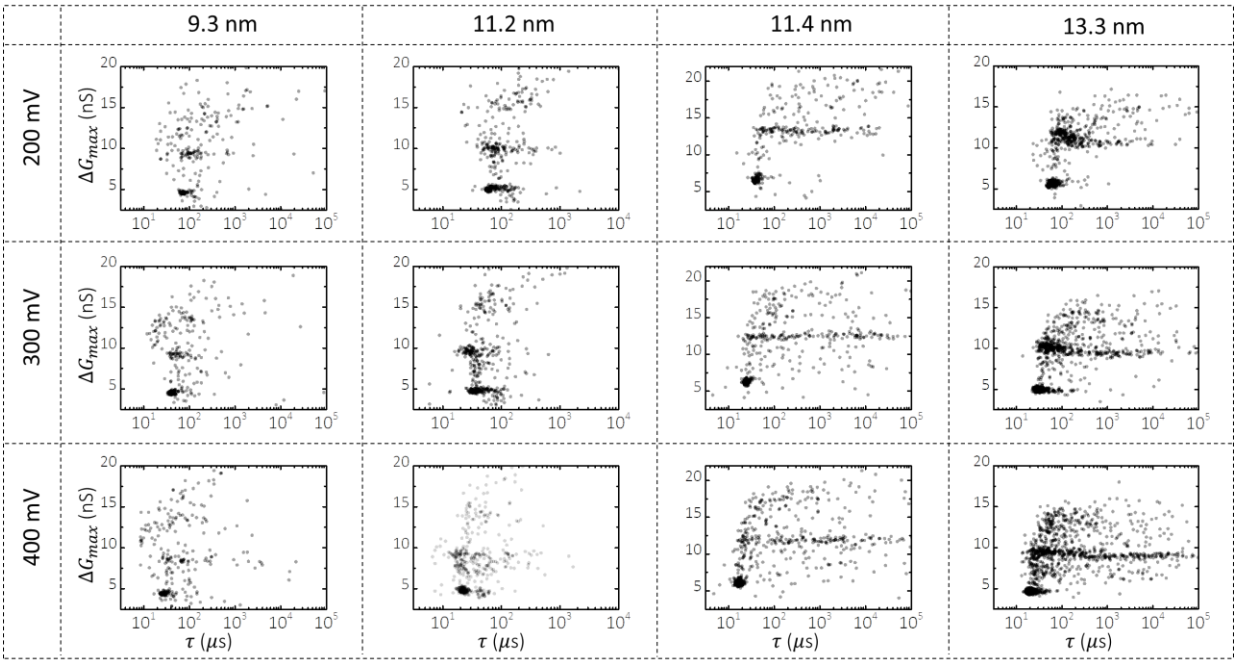

Figure S5.2.11. Pore Size Effects on metastable state. Scatter plots of 3HB translocation events in 0.9 M LiCl under various applied biases and using nanopores of different sizes.

Salt concentration

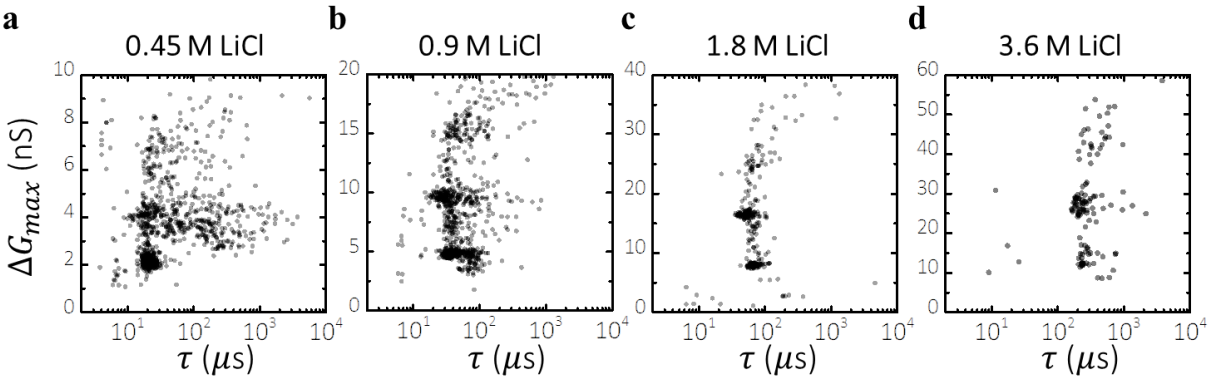

Figure S5.2.12. 3HB translocation in different LiCl concentrations using a single 11.2 nm pore. **a-c)** Under 300 mV in 0.45, 0.9, and 1.8 LiCl salt, N = 948, 885, and 327. **d)** Under 200 mV in 3.6 M LiCl salt, N = 321.

S5.2.10. Gel Electrophoresis for Free-Solution Mobility Extraction

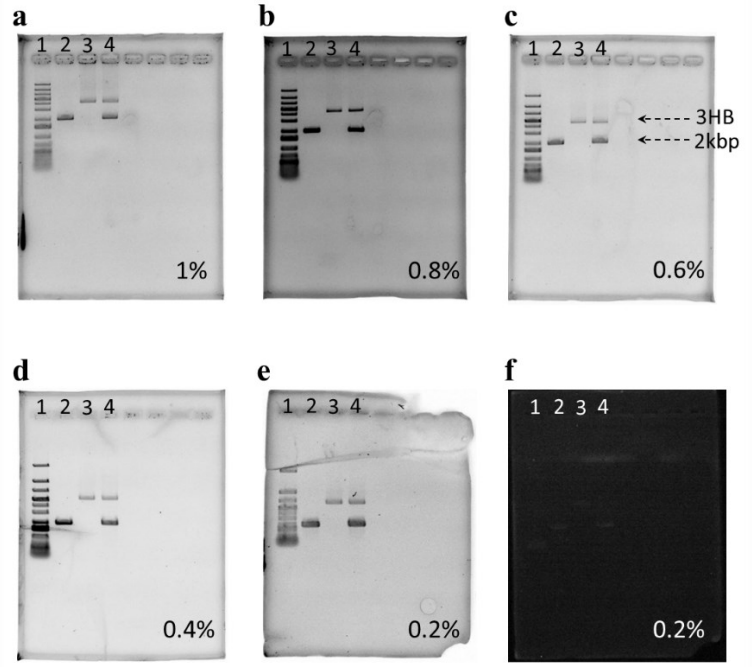

Figure S5.2.13. Free-solution electrophoretic mobility extrapolation. a-e) Gel electrophoresis of 2kbp dsDNA fragments (ThermoFisher Scientific, SM1701) and 3HB in 0.2 – 1 % Agarose gels, post-stained using 1x GelRed (Biotium, #41003). **f)** Gel electrophoresis of 2kbp dsDNA fragments and 3HB in 0.2 % Agarose gel with no staining. Lane 1: Generuler 1 kb plus DNA Ladder (ThermoFisher Scientific, SM1331). Lane 2: 2kbp dsDNA Fragments. Lane 3: 3HB molecules. Lane 4: mixture of 3HB and 2kbp dsDNA fragments. All experiments were performed in 1xTAE buffer (40 mM Tris, 20 mM acetic acid, and 2 mM EDTA) under 70 V for an hour.

S5.2.11. Nanopore Analysis of 3HB Thermal Degradation

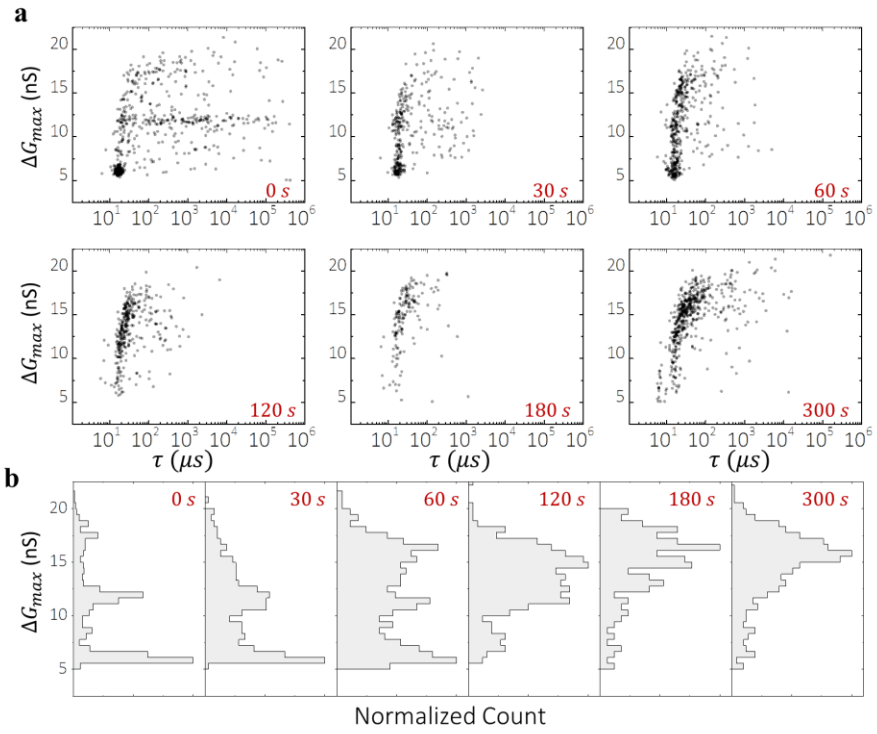

Figure S5.2.14 3HB Thermal Degradation. a) Scatter plots of ΔG_{max} versus τ for 3HB structures heated at 65 C for $0, 30, 60, 120, 180$, and 300 seconds, with N = 599, 313, 629, 314, 150, and 493. **b)** Distributions of ΔG_{max} for translocations of 3HB thermally degraded for different amounts of time, corresponding to the data of a). Single-file 3HB translocations produce a maximum blockage level of $\sim 6\ nS$. All nanopore experiments are performed using a 11.3 nm pore, in 0.9 M LiCl with an applied bias of 400 mV.

5.3 Additional Comment: Non-uniform Nanopore Electric Field Probed by Folded Translocations

As discussed throughout this thesis, especially so in Chapter 2, the electric field in a nanopore system is not uniform. Inside the pore, the field's z-component along the pore axis contains a radial dependence wherein it is strongest at the pore walls and weakest in its center. Because of this field gradient, translocating molecules will preferably translocate along the central axis of the pore, with thermal motion promoting off-axis translocations. During folded dsDNA translocations, multiple segments of the same polymer contour are inside the pore at once. Given the above arguments, it can be suggested that the segments inside the pore are further from the pore axis than the single strand during a single-file passage, thus probing higher electric field amplitudes and blocking more current. This can be generalized stating that n strands inside the pore should block more current than m strands inside the pore for $n > m$, due to the n strands being further away from the pore axis than the m strands. High-order folded translocations can thus be used to probe the non-uniform electric field of nanopores.

This idea has not been pursued nor studied extensively, however this is a phenomena I have observed when working in conditions that allowed higher folding states. An example of such analysis is shown here for the folded states obtained from passing dsDNA through a 15 nm pore under a 300 mV applied voltage, in 1 M LiCl solution. Figure 5.3.1a plots the conductance blockage values measured for different folding states ΔG_n corresponding to n strands inside the pore at once. ΔG_n increases with n as expected, and even fits well to a linear function. Figure 5.3.1b plots $\Delta G_n/(n \times \Delta G_1)$, the blockage of each folding state normalized by $n \times \Delta G_1$, where a value of 1 would be expected for a uniform electric field inside the pore. Values larger than unity are observed with higher values observed for higher n, up to ≈ 1.08 for $n = 4$. In an attempt to

obtain a spatial profile, Figure 5.3.1c plots the percentage of extra blockage induced per strand, i.e. $\left(1-\frac{\Delta G_n}{n\Delta G_1}\right)\times 100\%$, versus the estimated strand distance from the pore center r_o. Values of r_o were calculated using simple geometric considerations under the assumption that cylinders are closely packed inside the pore, as shown in Figure 5.3.1d.

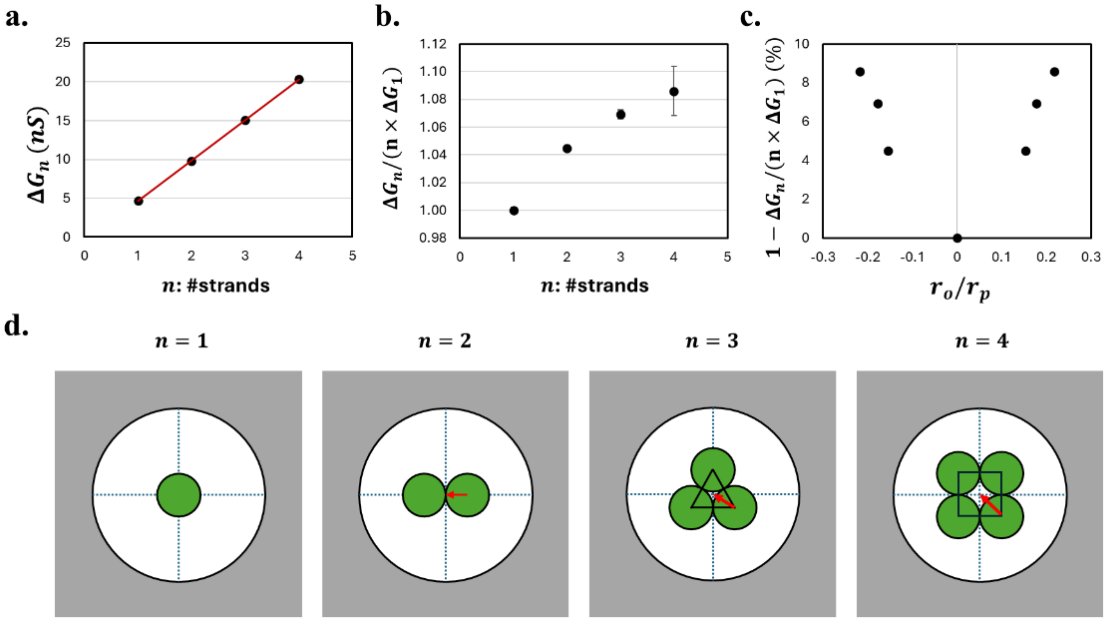

Figure 5.3.1. **Probing nanopore electric fields with folded translocations**. **a)** Conductance blockage measured for different folded states with n strands inside the pore. **b)** Conductance blockage of folded states normalized by $n\times\Delta G_1$, i.e. the blockage expected from a uniform electric field. **c)** Extra percentage blockage *versus* estimated offset distance from the central axis of the pore. **d)** Geometric arguments considered for calculations of r_o.

The slightly higher blockage values observed for higher folded states agree with the above interpretation claiming folded translocations probe higher electric fields near the walls. It should however be noted that in addition to the field, the ionic concentration inside the pore is also non-uniform due to the walls being negatively charged. These types of experiments should be repeated in different pore sizes and salt concentrations before claiming that the minute current blockage variations are both significant, i.e. repeatable, and due to the radial electric field modulations.

Chapter 6. Conclusions and Outlook

6.1. Summary

The work presented in this thesis attempted to reduce the gap of knowledge separating nanopore experiments and theory and was highly motivated by the core idea that a clearly presented experimental description of the physical principles of nanopore sensing could be greatly beneficial in assisting researchers designing better experiments. Boiled down, this thesis revolved around developing a better understanding of the electric field inside a nanopore and its vicinity, and a better understanding of the response of charged molecules to that electric field, whether far away from the pore or confined inside the nanopore. Namely, this was partly achieved in Chapter 2 by developing a mathematical framework harnessing the known properties of electric fields near 2D membranes, which enabled estimating access resistance contributions during the passage of translocating molecules of various shapes and sizes. The response of polymers to the electric field driving nanopore capture and passage was studied by applying salt concentration gradients across the pore (Chapter 3), which imposed experimental conditions that distorted the field non-uniformly in space, and by developing a DNA nanostructure whose translocation signals allowed the estimation of its instantaneous translocation velocity (Chapter 4), and thus of the time-dependent forces throughout the translocation process. Lastly, Chapter 5 investigated the effects of increased rigidity on folded translocation kinetics, demonstrating distinct dynamics compared to those of semi-flexible DNA polymers.

The observations and insights achieved in this thesis have led to complementary ongoing research projects that either make use of models introduced above, or whose analysis is facilitated by the concepts and conclusions reached in this work. Below, I briefly introduce two such projects and show preliminary results, analysis and interpretations.

6.2. Protein Passage Kinetics

A recent goal of solid-state nanopore sensing is to achieve reliable protein fingerprinting capabilities by identifying proteins based on their translocation blockade characteristics. Much progress has been recently achieved, with protein sensing experiments demonstrating the ability of extracting rich information regarding its structure and electrical properties.[28,239,240] Such biosensing endeavours are greatly aided by proteins residing longer inside pores, thus providing better temporal resolution and more statistically relevant current blockage data. Here, I present our preliminary attempts at characterizing the transport of proteins through solid-state nanopores. This work was performed in collaboration with undergraduate student researchers Breeana Elliott, William McLeish and Emma Saunders, who I helped supervise and mentor.

Figure 6.1 shows the translocation characteristics of Green Fluorescent Proteins (GFP) passing through a 6 nm diameter pore of length 12 nm under various applied voltages. GFP is a 27 kDa protein with a very stable beta-barrel structure, well described by a cylinder of length 4.2 nm and diameter 2.4 nm (Figure 6.1a). It has a weak net charge, although contains a heterogeneous distribution of charges. Current traces of GFP translocations are shown in Figure 6.1a under different voltages and characterized in Figure 6.1b which plots the average fractional blockage measured *versus* the corresponding signal duration. Furthermore, Figures 6.1c and 6.1d plot the histograms of fractional blockade traces and the most probable translocation time *versus* voltage, respectively. Figures 6.1c and 6.1d show that average fractional blockades slightly reduce with voltage and that GFP signal durations increase exponentially with time, two observations that are at odds with typical DNA translocation which commonly show a voltage-independent fractional blockage, and whose translocation time reduces inversely proportional to the applied voltage.

These voltage dependencies for GFP translocations have been observed across multiple different pores, with smaller pores showing a more pronounced voltage dependent exponential increase.

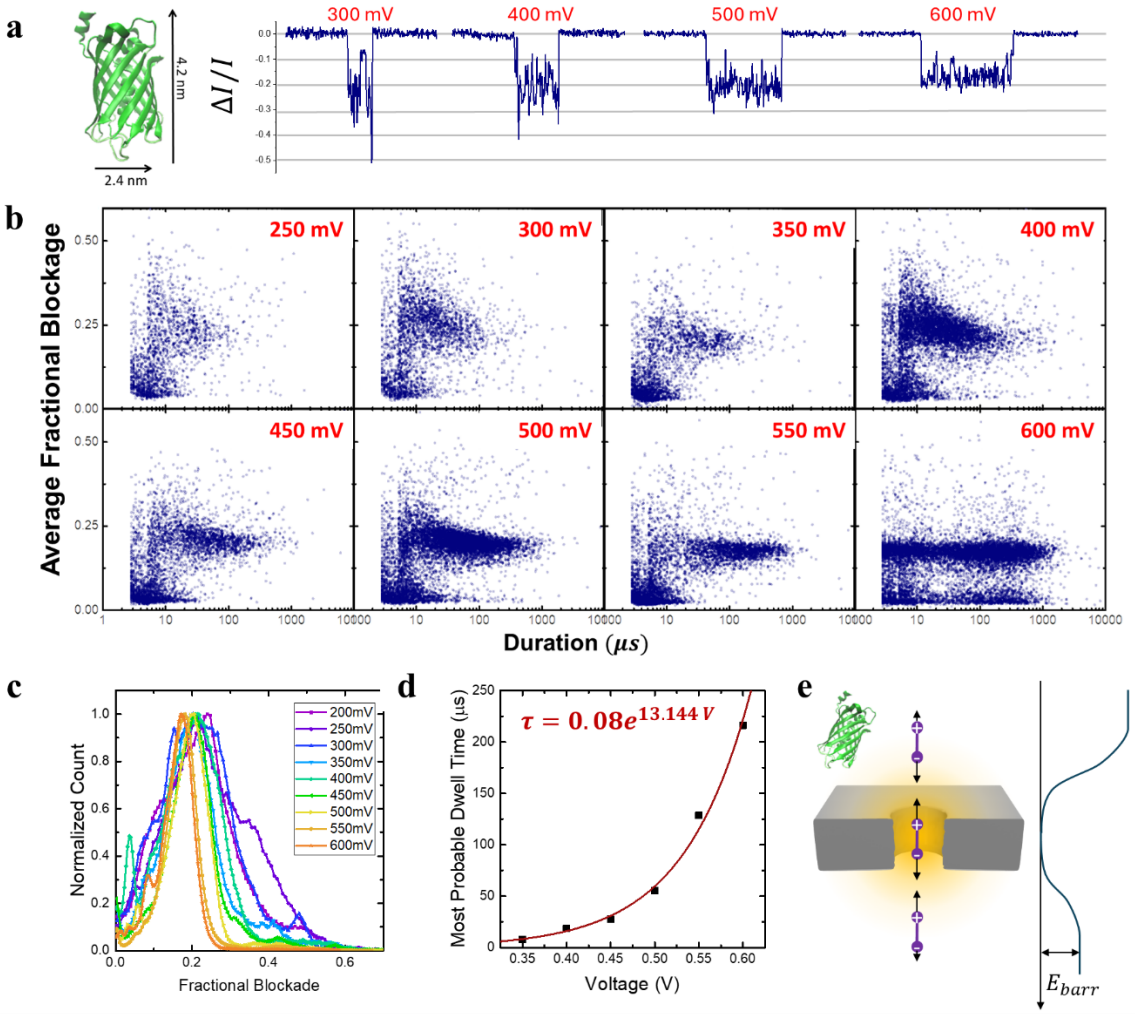

Figure 6.1. GFP capture kinetics. **a)** GFP protein structure and translocation events through a 6 nm pore in 3.6 M LiCl under different applied voltages. **b)** Scatterplots of average fractional blockage vs duration measured across different voltages. **c)** Distributions of GFP translocation current traces. **d)** Most probable signal durations measured for different voltages. Red line is an exponential fit, with the optimal parameters explicitly written. **e)** Schematic of forces on a dipole near a nanopore.

Given that GFP has a weak net negative charge and that both electrophoresis and electroosmosis are expected to increase linearly with voltage, an entirely different process must be at play to explain these observations. A tentative explanation is that, because of its heterogeneous

charge distribution, the observations of Figure 6.1 could result from GFP's dipole moment interacting with the non-uniform electric field in the vicinity of the pore. A zero net-charge dipole aligned with the pore axis would be attracted to the pore whether on the *cis* or *trans* side and feel no force when perfectly centered inside the pore. From this perspective, such a dipole interaction with the pore resembles that of a particle stuck in a free energy well of height E_{barr}. With its small yet non-zero overall net charge, GFP kinetics can be described similarly albeit with a bias towards the trans region, as depicted in Figure 6.1e. The time-to-escape τ of such a process is well-known to scale as $\tau \sim e^{\frac{E_{barr}}{k_B T}}$, from which the fit of Figure 6.1d attributes a barrier height of $E_{barr} = 13.1\ k_B T$.

This dipole-like interaction between the pore and GFP could further help interpret the voltage-dependent fractional blockades given that a dipole will preferably align with the electric field. Under weaker fields, thermal motion will be more important, and as such GFP will explore more orientations, therein broadening and perhaps even deepening the blockage distribution. More work will help clarifying whether dipole interactions really cause this energy-well-like results. If so, this understanding could help develop new methods of trapping proteins that do not rely on complex experimental setups.

6.3. Sizing CBD-Fabricated Pores

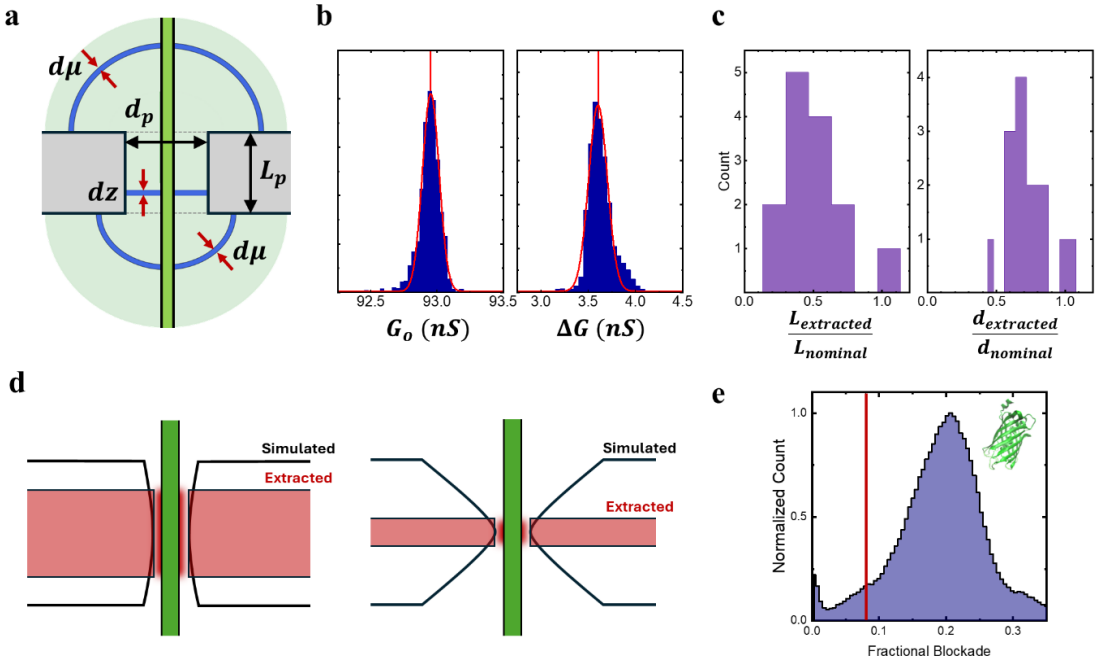

Figure 6.2. Insights into CBD-fabricated pore shapes. a) Modeling of cylindrical obstruction in cylindrical pore. **b)** Distribution of open-pore conductance and conductance blockage for translocations of 5 kbp dsDNA through a 12 nm pore in 3.6 M LiCl under 200mV. **c)** Distribution of extracted thicknesses and pore diameters normalized by their nominal values, as described I the text. **c)** Extracting effective cylindrical pore dimensions from the simulated conductance values of hyperboloid pores. **d)** Fractional blockades from GFP translocations in 3.6 M LiCl in a pore with nominal thickness of 12 nm and corresponding diameter of 6 nm. Red line depicts the fractional blockade expected from nominal protein-pore volume ratio.

Unless mentioned otherwise, the pore diameters reported in this thesis were calculated by assuming a cylindrical pore geometry, with a cylinder length matching the value of the nominal membrane thickness provided by the manufacturer. While TEM images of CBD pores do show an approximate circular opening, this assumed 3D cylindrical shape has however not been experimentally validated. In contrast, the shape of TEM-fabricated pores in membranes thicker than 30 nm, has been reported to be well described by a double cone geometry (Figure 1.2) via TEM tomography.[14] As such, instead of using the nominal thickness L_{nom} for modeling the

conductance states of their pores, an effective thickness L_{eff} is often used instead, commonly and somewhat arbitrarily defined as $L_{eff} = L_{nom}/3$.

As shown in Figures 6.2a-c, the conductance model introduced in Chapter 2 allows using values of open pore conductance G_o and of the conductance blockage ΔG induced by a DNA-like cylindrical obstruction to calculate and extract the diameter d_p and length L_p of the pore, under the assumption of cylindrical pores. When using the model to extract the dimension of CBD-fabricated pores, extracted pores sizes and thicknesses were consistently calculated to be smaller than the nominal values, i.e. the nominal thickness L_{nom} and corresponding diameter d_{nom}, as shown in Figure 6.2c. Given that, as discussed in Section S2.2.7, the conductance model developed tends to overestimate extracted pore dimensions, the results of Figure 6.2c indicate instead that the physical cylindrical assumption of the model might be erroneous.

To study this, values for the open-pore conductance and conductance blockages induced by cylindrical obstructions in non-cylindrical pore geometries were obtained through finite-element simulations, as shown in Figure 6.2d. These conductance values were then fed to the conductance model, under a cylindrical geometry assumption, to see what pore dimensions would be extracted. This was tested on two pores with hyperboloid geometries, with one geometry being more significantly tapered than the other. As per the conductance of the CBD-fabricated pores (Figure 6.2c), the extracted membrane thicknesses, shown in red (to scale) in Figure 6.2d, were thinner than the nominal membrane value, with the more tapered pore resulting in a thinner extracted effective cylinder pore length. Note that the hyperboloid pore shape selected is arbitrary, yet highlights that the pore dimensions extracted when imposing a cylindrical pore shape capture not the nominal thickness but instead the region inside the pore where the electric field is strongest

whose length is the effective cylinder thickness. This of course remains to be tested and further characterized experimentally.

Interestingly, however, the observations and conclusions reached from Figure 6.2 can be similarly obtained for blockage amplitudes from GFP translocations, which are consistently deeper than the values predicted through volumetric assumptions when using nominal nanopore thickness. A $2-5\times$ difference is commonly observed between predicted and observed GFP blockades. A better understanding of pore geometries would thus greatly assist in developing protein sensing applications with CBD-fabricated nanopores.

6.4 Outlook

Figures 6.1 and 6.2 encapsulate the idea that results and insights presented in this thesis can serve as a stepping stone for future research projects, either through facilitating the interpretation of complex translocation kinetics through a better understanding of the underlying forces in the system, or through applying mathematical frameworks to infer physical information about the nanopore system. Two methods introduced in this work show particular potential for future projects, as now described.

The Velocity Profiling Molecule (VPM) method from Chapter 4 presents a simple framework by which nanopore signals from DNA origami structures can be used to study the non-uniform velocities forces underlying the translocation process. Instead of straightforward and symmetric conditions like those of Chapter 4, the structures could be used to study forces arising from pressure, salt or viscosity gradients, for instance. Moreover, by designing a VPM molecule of similar length to the polymer of interest, the velocity profiles can help map temporal signals

into spatial signals, and as such help precisely locate analytes or markers bound along the backbone of a carrier molecule, for example.

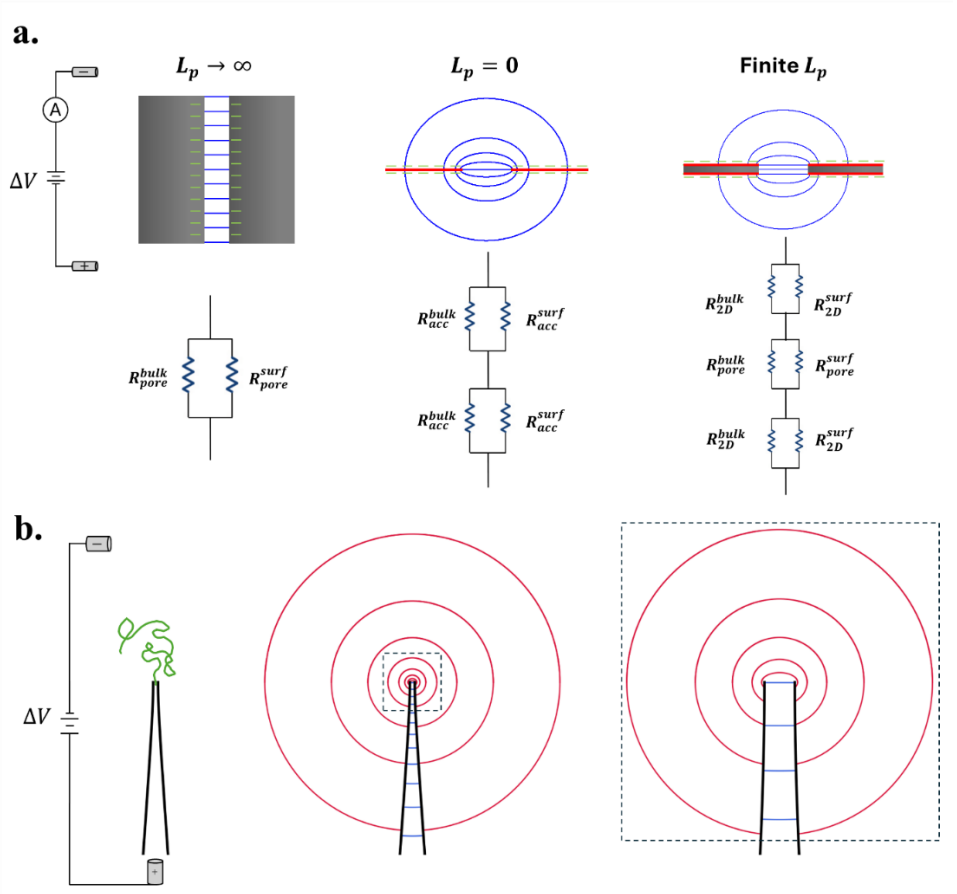

Figure 6.3. Potential applications of oblate spheroidal slicing method. a) Electrokinetic contributions for different pore dimensions. **b)** Example of further applications of oblate spheroidal slicing. A nanopipette is approximated to be a constant-ν hyperboloid. Two oblate spheroidal coordinate mappings are used for the pipette interior (blue) and exterior (red).

Additionally, the oblate spheroidal slicing method developed in Chapter 2 provides a versatile toolset by which access region conductance properties can be determined. Once comfortable with the sometimes-ugly mathematical expressions arising from the framework, this toolset provides the foundation for characterizing unaddressed access region phenomena that are

of high interest with the advent of ultra-thin or 2D membranes providing access-resistance-dominated sensing. For instance, equations modeling surface charge currents only exist for a cylindrical pore's interior. However, the membrane surfaces are charged just like the pore walls, and thus should contribute to the overall current for low-aspect ratio pores, especially in low salt concentrations (Figures 1.8c and 1.9c).[42] Moreover, the curvilinear slicing method is flexible and can be used to model different pore geometries. For instance, under the reasonable assumption that a glass capillary has the shape of a hyperboloid (drawn in Figure 6.3b, and imaged in Figure 1.2f), two sets of oblate spheroidal coordinates can map a nanopipette's interior and exterior extensively, thus allowing for its resistance to be calculated, whether a translocating molecule is inside the pore or entirely in the access region. These two somewhat arbitrary examples show that the conductance model introduced in Chapter 2 is not limited to the specific equations presented in that section, but instead represents a general method applicable to a wide range of previously inaccessible scenarios.

Appendix. Generation of Discrete Wormlike Chains

Here, I discuss how to generate biased random walks whose consecutive steps are not uniformly random, as per an ideal random walk, but instead probabilistically follow the energetic contributions from bending away from neighboring segments, thus following expectations from a semi-flexible polymer with an intrinsic persistence length ℓ_p. Generating Discrete Worm-Like Chains (DWLC) has proven to be very useful in multiple projects of this thesis. Its repeated usefulness and the nice images I generated before realizing this method had already been published 10 years ago[192] are the main reasons why I include this section as an appendix to this thesis.

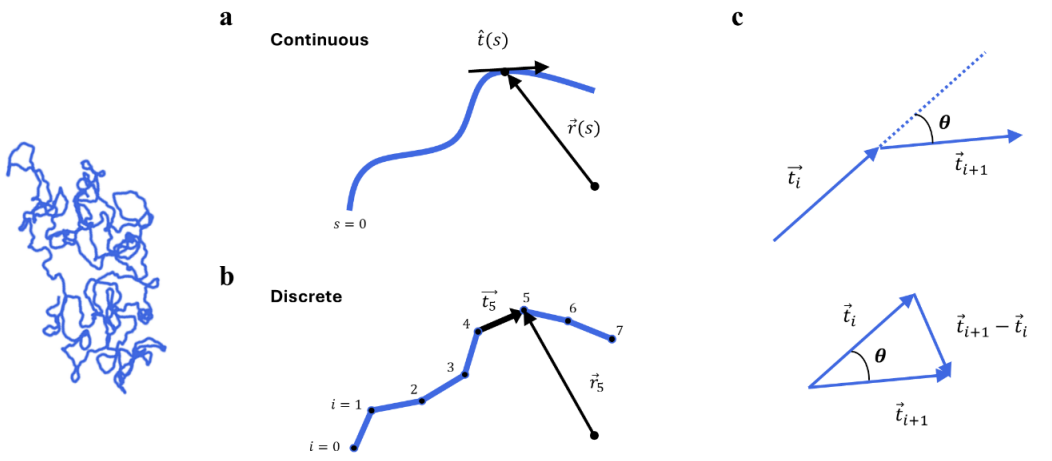

Figure A1. Wormlike chains. Parametrization of worm-like chains (a) and discrete worm-like chains (b). c) geometric interpretation of the discretized double derivative $\partial^2\vec{r}(s)/\partial s^2$.

First consider a continuous semi-flexible polymer of length L with intrinsic Young's modulus Y and cross-sectional moment of inertia I. Let the contour of the polymer be parametrized with $s \in (0, L)$, and the position and tangent vectors at s be defined as $\vec{r}(s)$ and $\hat{t}(s) = \partial\vec{r}(s)/\partial s$, respectively, as shown in Figure A1a. The local bending energy per unit length of such a polymer $u(s)$ has a known form of:

$$u(s) = \frac{1}{2} YI \left| \frac{\partial^2 \vec{r}(s)}{\partial s^2} \right|^2 = \frac{1}{2} k_B T \ell_p \left| \frac{\partial^2 \vec{r}(s)}{\partial s^2} \right|^2 . \quad \text{(A1)}$$

Moreover, it can be shown that the correlation between tangent vectors separated by δs and an angle $\theta(\delta s)$ will follow:

$$\langle \hat{t}(s + \delta s) \cdot \hat{t}(s) \rangle = \langle \cos \theta(\delta s) \rangle = e^{-\frac{k_B T}{YI} \delta s} = e^{-\frac{\delta s}{\ell_p}} . \quad \text{(A2)}$$

Note that the definition of persistence length $\ell_p \equiv YI/k_B T$ was used to obtain the final forms of Equations A1 and A2. The mean square end-to-end radius of WLC polymers of length L is:

$$\langle R_{ee}^2 \rangle = 2\ell_p L \left[1 - \frac{\ell_p}{L} \left(1 - e^{-\frac{L}{\ell_p}} \right) \right] . \quad \text{(A3)}$$

Now, we wish to generate random walks consisting of N steps of size ℓ_s whose properties follow those of wormlike chains, i.e. Eqs. A1-3, when $\ell_s \ll \ell_p$ and those of random walks, i.e. $\langle \hat{t}(s) \cdot \hat{t}(0) \rangle = 0$ and $\langle R_{ee}^2 \rangle = \ell_s^2 N$, when $\ell_s \gg \ell_p$. The contour of a DWLC is parametrized by $i = 1, \dots, i, \dots, N$ such that $\vec{r}_i$ denotes the vector pointing to the end of the i^{th} step and that $\vec{t}_i$ denotes the vector of length ℓ_s linking $\vec{r}_{i-1}$ and $\vec{r}_i$, i.e. $\vec{t}_i = \vec{r}_i - \vec{r}_{i-1}$. To generate a DLWC, we first consider the energetic cost of having an angle of θ between the i^{th} and $(i+1)^{th}$ step. We can approximate this energetic contribution by discretizing Equation A1:

$$U_{step}(\theta) = \int_0^{\ell_s} \frac{1}{2} k_B T \ell_p \left| \frac{\partial^2 \vec{r}(s)}{\partial s^2} \right|^2 ds \approx 2 k_B T \frac{\ell_p}{\ell_s} \sin^2 \theta . \quad \text{(A4)}$$

Equation A4 results from the expression of the discrete second derivative (Figure A1 c):

$$\left| \frac{\partial^2 \vec{r}(s)}{\partial s^2} \right| \approx \frac{|\Delta \vec{r}_{i+1} - \Delta \vec{r}_i|}{\ell_s^2} = \frac{\left| \vec{t}_{i+1} - \vec{t}_i \right|}{\ell_s^2} = \frac{2}{\ell_s} \sin \frac{\theta}{2} . \quad \text{(A5)}$$

The probability of observing an angle θ between two consecutive steps should be proportional to the Boltzmann weight probability evaluated over a sphere of radius ℓ_s:

$$P(\theta)d\theta = Ae^{-\frac{\ell_p}{\ell_s}\sin^2\theta}\ell_s \sin\theta\, d\theta = Ae^{-\frac{\ell_p}{\ell_s}}e^{\frac{\ell_p}{\ell_s}\cos\theta}\ell_s \sin\theta\, d\theta\,. \tag{A6}$$

The rightmost expression of Equation A6 was obtained from the half angle trigonometric identity. An expression for the normalization constant A can be found:

$$\begin{aligned} 1 &= \int_0^\pi P(\theta)d\theta \\ &= A\ell_s e^{-\frac{\ell_p}{\ell_s}}\int_0^\pi e^{\frac{\ell_p}{\ell_s}\cos\theta}\sin\theta\, d\theta \\ &= A\ell_s e^{-\frac{\ell_p}{\ell_s}}\left[-\frac{\ell_s}{\ell_p}e^{\frac{\ell_p}{\ell_s}\cos\theta}\right]_0^\pi \\ &= 2A\frac{\ell_s^2}{\ell_p}e^{-\frac{\ell_p}{\ell_s}}\sinh\frac{\ell_p}{\ell_s} \\ A &= \frac{\ell_p}{2\ell_s^2\sinh\frac{\ell_p}{\ell_s}}e^{\frac{\ell_p}{\ell_s}}\,. \end{aligned} \tag{A7}$$

The expression for the probability density of finding an angle θ between two consecutive steps in a DWLC is thus:

$$P(\theta) = \frac{\ell_p/\ell_s}{2\sinh\frac{\ell_p}{\ell_s}}e^{\frac{\ell_p}{\ell_s}\cos\theta}\sin\theta\,. \tag{A8}$$

Figure A2 plots the function $P(\theta)$ for different values of ℓ_p/ℓ_s. In the limit of $\ell_p/\ell_s \gg 1$, $P(\theta)$ converges to a Dirac-Delta distribution, whereas it converges to $\sin(\theta)/2$ for $\ell_p/\ell_s \ll 1$, as expected for a uniform distribution on the surface of a sphere.

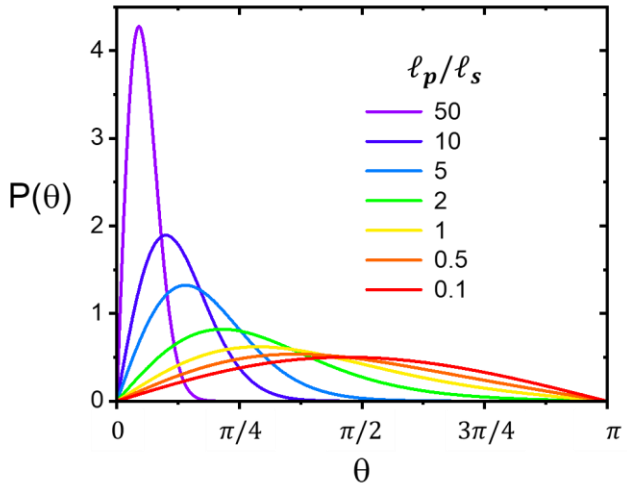

Figure A2. Plots of $P(\theta)$ from Equation A8 for different values of ℓ_p/ℓ_s.

It can further be shown that

$$\begin{aligned}
\langle \cos\theta \rangle &= \int_0^{\pi} \cos\theta \, P(\theta) d\theta \\
&= \frac{1}{2\sinh\frac{\ell_p}{\ell_s}} \int_0^{\pi} \frac{\ell_p}{\ell_s} e^{\frac{\ell_p}{\ell_s}\cos\theta} \sin\theta \cos\theta \, d\theta \\
&= \frac{1}{2\sinh\frac{\ell_p}{\ell_s}} \left[\left(-e^{\frac{\ell_p}{\ell_s}\cos\theta} \right)_0^{\pi} - \int_0^{\pi} \sin\theta \, e^{\frac{\ell_p}{\ell_s}\cos\theta} d\theta \right] \\
&= \frac{1}{2\sinh\frac{\ell_p}{\ell_s}} \left[2\sinh\frac{\ell_p}{\ell_s} - 2\frac{\ell_s}{\ell_p}\sinh\frac{\ell_p}{\ell_s} \right] \\
\langle \cos\theta \rangle &= 1 - \frac{\ell_s}{\ell_p} . \qquad \text{(A8)}
\end{aligned}$$

For small ℓ_s/ℓ_p values, i.e. for step sizes significantly smaller than the persistence length, Equation A8 is equivalent to $\langle \cos\theta \rangle \approx e^{-\ell_s/\ell_p}$, which itself is equivalent to the decaying correlation property of WLC as per Equation A2.

Now, given that the formalism and behavior of DWLC are determined and verified to be consistent with WLC for $\ell_s < \ell_p$, a method is needed to properly and randomly sample θ to

iteratively generate DWLC step by step. To this end, an expression for the Cumulative Density Function density $CDF(\theta)$ can be found:

$$\begin{aligned} CDF(\theta) &= \int_0^{\theta} P(\theta')d\theta' \\ &= \frac{1}{2\sinh\frac{\ell_p}{\ell_s}} \int_0^{\theta} \frac{\ell_p}{\ell_s} e^{\frac{\ell_p}{\ell_s}\cos\theta'} \sin\theta' \, d\theta' \\ &= \frac{1}{2\sinh\frac{\ell_p}{\ell_s}} \left(-e^{\frac{\ell_p}{\ell_s}\cos\theta'} \right)_0^{\theta} \\ CDF(\theta) &= \frac{e^{\frac{\ell_p}{\ell_s}} - e^{\frac{\ell_p}{\ell_s}\cos\theta}}{e^{\frac{\ell_p}{\ell_s}} - e^{-\frac{\ell_p}{\ell_s}}} \, . \end{aligned} \tag{A9}$$

With the CDF of $P(\theta)$ determined, it is possible to perform an inverse transform sampling, wherein a random uniformly distributed variable $r \in U(0,1)$ is randomly generated and assigned as $r = CDF(\theta)$. The corresponding value of θ is then found by inverting Eq. A9:

$$\theta(r) = \cos^{-1}\left(1 + \frac{\ell_s}{\ell_p}\ln\left(1 - r\left(1 - e^{-2\frac{\ell_p}{\ell_s}}\right)\right)\right). \tag{A10}$$

Given $\vec{r}_{i-1}$ and $\vec{t}_{i-1}$, two angles are required to randomly generate the 3D position of $\vec{r}_i$: the polar angle θ, as discussed above, and the azimuthal angle ϕ which describes the rotation about the $\hat{t}_{i-1}$ axis. Given that only bending energy is considered for WLC and torsional contributions are omitted, the azimuthal angle between steps is uniformly distributed over the 2π domain, i.e. $\phi \in U(0, 2\pi)$. Figure A3 shows 1000 randomly generated $\vec{r}_2$ vectors given $\vec{r}_0 = (0,0,0)$ and $\vec{r}_1 = (\sqrt{3}\ell_s, \sqrt{3}\ell_s, \sqrt{3}\ell_s)$ for various values of ℓ_p/ℓ_s. As expected, flexible scenarios, i.e. $\ell_p \ll \ell_s$,

appear to be randomly distributed over the ℓ_s sphere, as per ideal random walks. As rigidity increases however, randomly generated $\vec{r}_2$ coordinates get increasingly concentrated around the same point parallel to the previous step, as expected from a rigid rod.

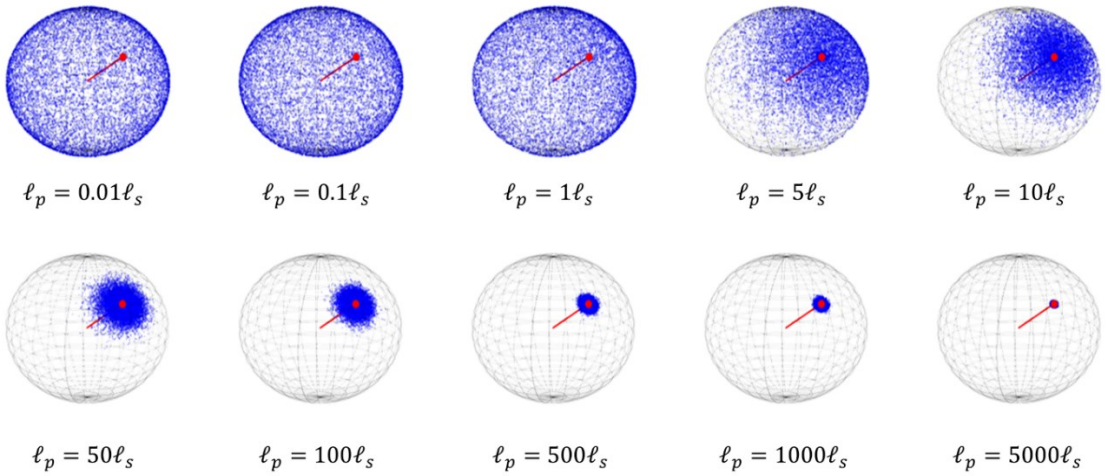

Figure A3. Randomly generated DWLC step. 1000 randomly generated $\vec{r}_2$ vectors for $\vec{r}_0 = (0,0,0)$ and $\vec{r}_1 = (\sqrt{3}\ell_s, \sqrt{3}\ell_s, \sqrt{3}\ell_s)$ with different values of ℓ_p/ℓ_s values. The red line indicates the direction of $\vec{t}_1$.

Following the above points, an N-step discrete worm-like chain with steps of length ℓ_s and a persistence length of ℓ_p can thus be generated iteratively by following these steps:

1. Generate a random first step, uniformly distributed along the surface of a sphere of radius ℓ_s centered at the starting coordinate, e.g. $(x_0, y_0, z_0) = (0,0,0)$.
2. For the i^{th} step part of any the next N-1 steps, repeat the following:
    a. Randomly generate $r \in U(0,1)$;
    b. Calculate corresponding $\theta_i(r)$ from Eq. A10;
    c. Randomly generate $\phi_i \in U(0,2\pi)$;
    d. Determine coordinates of the position vector $\vec{r}_i = (x_i, y_i, z_i)$ from θ_i and ϕ_i;

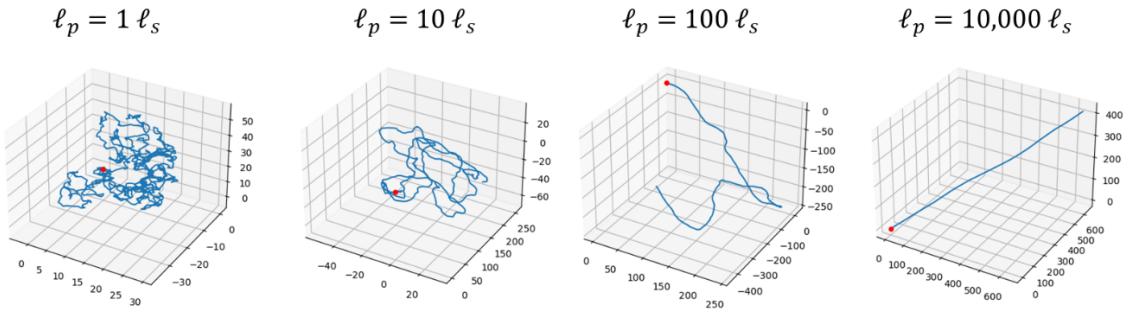

Figure A4. 1000-step discrete worm-like chains with different persistence lengths.

Figure A4 shows four examples of DWLC of the same length, 1000 steps, generated with different persistence length values ℓ_p/ℓ_s, using the steps outlined above. As intended by design, randomly generated DWLCs with higher rigidities look like rigid rods, whereas those with lower persistence lengths like purely random walks.

To confirm that the generated DWLCs follow the long-range statistics of wormlike chains in addition to the short-range ones (Eq. A8), the above algorithm was used to generate 5000 DWLCs consisting of $N = 5000$ steps using a wide range of persistence lengths. For each simulation, the step size was manually changed to ensure $\ell_s \ll \ell_p$, and thus provide a proper comparison with WLCs. The mean square end-to-end distance $\langle R_{ee}^2 \rangle$ was calculated for chains of different rigidities, as shown in Figure A5 which plots values of $\langle R_{ee}^2 \rangle / N^2 \ell_s^2$ against the corresponding normalized persistence lengths values $\ell_p / N\ell_s$. Alongside the values from simulated DLWCs, Figure A5 plots corresponding $\langle R_{ee}^2 \rangle / L$ values expected from WLC statistics (Eq. A3), showing great agreement.

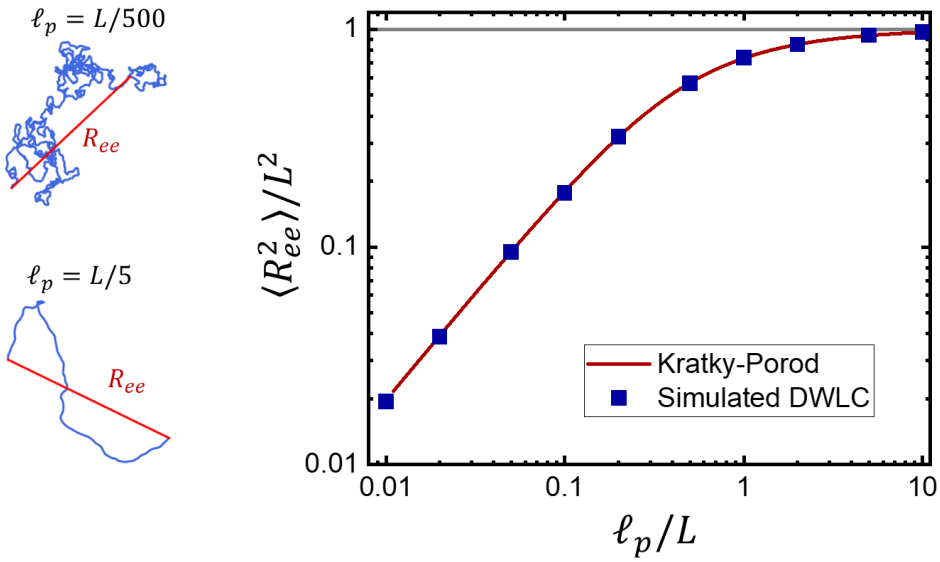

Figure A5. DWLC vs WLC statistics. Scatterplot of mean square end-to-end distance $\langle R_{ee}^2 \rangle / (N\ell_s)^2$ of DWLCs calculated from 5000 randomly generated walks plotted against the corresponding normalized persistence length $\ell_s / N\ell_s$. For all simulations, the step size ℓ_s was significantly smaller than the persistence length ℓ_p. The red curve corresponds to Eq. A2.

References

1. Deamer, D., Akeson, M. & Branton, D. Three decades of nanopore sequencing. *Nat Biotechnol* **34**, 518–524 (2016).

2. Lindsay, S. The promises and challenges of solid-state sequencing. *Nat Nanotechnol* **11**, 109–111 (2016).

3. Alfaro, J. A. *et al.* The emerging landscape of single-molecule protein sequencing technologies. *Nat Methods* **18**, 604–617 (2021).

4. Xue, L. *et al.* Solid-state nanopore sensors. *Nat Rev Mater* **5**, 931–951 (2020).

5. Mayer, S. F., Cao, C. & Dal Peraro, M. Biological nanopores for single-molecule sensing. *iScience* **25**, (2022).

6. Zhang, M., Chen, C., Zhang, Y. & Geng, J. Biological nanopores for sensing applications. *Proteins: Structure, Function, and Bioinformatics* 1–14 (2022) doi:10.1002/prot.26308.

7. Zhang, S. *et al.* Bottom-up fabrication of a proteasome–nanopore that unravels and processes single proteins. *Nat Chem* **13**, 1192–1199 (2021).

8. Cao, C. *et al.* Single-molecule sensing of peptides and nucleic acids by engineered aerolysin nanopores. *Nat Commun* **10**, 4918 (2019).

9. Robertson, J. W. F., Kasianowicz, J. J. & Banerjee, S. Analytical Approaches for Studying Transporters, Channels and Porins. *Chem Rev* **112**, 6227–6249 (2012).

10. Crnković, A., Srnko, M. & Anderluh, G. Biological nanopores: Engineering on demand. *Life* **11**, 27 (2021).

11. Tabard-cossa, V. Instrumentation for Low-Noise High-Bandwidth Nanopore Recording 3. 59–93 (2013) doi:10.1016/B978-1-4377-3473-7.00003-0.

12. Xing, Y., Rottensteiner, A., Ciccone, J. & Howorka, S. Functional Nanopores Enabled with DNA. *Angewandte Chemie - International Edition* vol. 62 Preprint at https://doi.org/10.1002/anie.202303103 (2023).

13. Lo, C. J., Aref, T. & Bezryadin, A. Fabrication of symmetric sub-5 nm nanopores using focused ion and electron beams. *Nanotechnology* **17**, 3264–3267 (2006).

14. Min, B., Kim, J., Wanunu, M., Bell, D. C. & Meller, A. Rapid Fabrication of Uniformly Sized Nanopores and Nanopore Arrays for Parallel DNA Analysis. 3149–3153 (2006) doi:10.1002/adma.200601191.

15. Kwok, H., Briggs, K. & Tabard-Cossa, V. Nanopore fabrication by controlled dielectric breakdown. *PLoS One* **9**, e92880 (2014).

16. Ivanov, A. P. *et al.* On-demand delivery of single DNA molecules using nanopipets. *ACS Nano* **9**, 3587–3594 (2015).

17. Hall, A. R. *et al.* Hybrid pore formation by directed insertion of α-haemolysin into solid-state nanopores. *Nat Nanotechnol* **5**, 874–877 (2010).

18. Hernández-Ainsa, S., Misiunas, K., Thacker, V. V., Hemmig, E. A. & Keyser, U. F. Voltage-dependent properties of DNA origami nanopores. *Nano Lett* **14**, 1270–1274 (2014).

19. Xing, Y., Dorey, A., Jayasinghe, L. & Howorka, S. Highly shape- and size-tunable membrane nanopores made with DNA. *Nat Nanotechnol* **17**, 708–713 (2022).

20. Li, J. *et al.* Ion-beam sculpting at nanometre length scales. *Nature* **412**, 166–169 (2001).

21. Storm, A. J., Chen, J. H., Ling, X. S., Zandbergen, H. W. & Dekker, C. Fabrication of solid-state nanopores with single-nanometre precision. *Nat Mater* **2**, 537–540 (2003).

22. Waugh, M. *et al.* Solid-state nanopore fabrication by automated controlled breakdown. *Nat Protoc* **15**, 122–143 (2020).

23. Steinbock, L. J., Bulushev, R. D., Krishnan, S., Raillon, C. & Radenovic, A. DNA Translocation through Low-Noise Glass Nanopores. *ACS Nano* **7**, 11255–11262 (2013).

24. Tahvildari, R., Beamish, E., Tabard-Cossa, V. & Godin, M. Integrating nanopore sensors within microfluidic channel arrays using controlled breakdown. *Lab Chip* **15**, 1407–1411 (2015).

25. Nicoli, F., Verschueren, D., Klein, M., Dekker, C. & Jonsson, M. P. DNA translocations through solid-state plasmonic nanopores. *Nano Lett* **14**, 6917–25 (2014).

26. Bayley, H. & Martin, C. R. Resistive-pulse sensing - from microbes to molecules. *Chem Rev* **100**, 2575–2594 (2000).

27. Waduge, P. *et al.* Nanopore-Based Measurements of Protein Size, Fluctuations, and Conformational Changes. *ACS Nano* **11**, acsnano.7b01212 (2017).

28. Houghtaling, J. *et al.* Estimation of Shape, Volume, and Dipole Moment of Individual Proteins Freely Transiting a Synthetic Nanopore. *ACS Nano* **13**, 5231–5242 (2019).

29. Tripathi, P. *et al.* Electrical unfolding of cytochrome c during translocation through a nanopore constriction. *Proc Natl Acad Sci U S A* **118**, (2021).

30. Carson, S., Wilson, J., Aksimentiev, A. & Wanunu, M. Smooth DNA Transport through a Narrowed Pore Geometry. *Biophys J* **107**, 2381–2393 (2014).

31. Schneider, G. F. & Dekker, C. DNA sequencing with nanopores. *Nat Biotechnol* **30**, 326–328 (2012).

32. Tripathi, P., Firouzbakht, A., Gruebele, M. & Wanunu, M. Threading single proteins through pores to compare their energy landscapes. *Proc Natl Acad Sci U S A* **119**, 1–9 (2022).

33. Tripathi, P., Firouzbakht, A., Gruebele, M. & Wanunu, M. Direct Observation of Single-Protein Transition State Passage by Nanopore Ionic Current Jumps. *J Phys Chem Lett* 5918–5924 (2022) doi:10.1021/acs.jpclett.2c01009.

34. Bell, N. A. W. & Keyser, U. F. Digitally encoded DNA nanostructures for multiplexed, single-molecule protein sensing with nanopores. *Nat Nanotechnol* **11**, 645–651 (2016).

35. Tabard-Cossa, V. *et al.* Single-molecule bonds characterized by solid-state nanopore force spectroscopy. *ACS Nano* **3**, 3009–3014 (2009).

36. Ren, R. *et al.* Nanopore extended field-effect transistor for selective single-molecule biosensing. *Nat Commun* **8**, (2017).

37. Plesa, C. *et al.* Fast translocation of proteins through solid state nanopores. *Nano Lett* **13**, 658–663 (2013).

38. Beamish, E., Kwok, H., Tabard-Cossa, V. & Godin, M. Precise control of the size and noise of solid-state nanopores using high electric fields. *Nanotechnology* **23**, 405301 (2012).

39. Briggs, K., Kwok, H. & Tabard-Cossa, V. Automated fabrication of 2-nm solid-state nanopores for nucleic acid analysis. *Small* **10**, 2077–86 (2014).

40. Tang, W., Fried, J. P., Tilley, R. D. & Gooding, J. J. Understanding and modelling the magnitude of the change in current of nanopore sensors. *Chem Soc Rev* 5757–5776 (2022) doi:10.1039/d1cs00972a.

41. Kowalczyk, S. W., Grosberg, A. Y., Rabin, Y. & Dekker, C. Modeling the conductance and DNA blockade of solid-state nanopores. *Nanotechnology* **22**, 315101 (2011).

42. Smeets, R. M. M. *et al.* Salt dependence of ion transport and DNA translocation through solid-state nanopores. *Nano Lett* **6**, 89–95 (2006).

43. Lin, K. *et al.* Surface Charge Density Inside a Silicon Nitride Nanopore. *Langmuir* (2021) doi:10.1021/acs.langmuir.1c01504.

44. Hall, J. E. Access Resistance of a Small Circular Pore. *Journal of General Physiology* **66**, 531–532 (1975).

45. Vodyanoy, I. & Bezrukov, S. M. Sizing of an ion pore by access resistance measurements. *Biophys J* **62**, 10–11 (1992).

46. Maxwell, J. C. *A Treatise on Electricity and Magnetism*. vol. 1 (Oxford: Clarendon Press, 1873).

47. DeBlois, R. W. & Bean, C. P. Counting and Sijzing of Submicron Particles by the Resistive Pulse Technique. *J Sci Instrum* **25**, 86 (1970).

48. Li, J., Gershow, M., Stein, D., Brandin, E. & Golovchenko, J. A. DNA molecules and configurations in a solid-state nanopore microscope. *Nat Mater* **2**, 611–615 (2003).

49. Tabard-Cossa, V., Trivedi, D., Wiggin, M., Jetha, N. N. & Marziali, A. Noise analysis and reduction in solid-state nanopores. *Nanotechnology* **18**, 305505 (2007).

50. Smeets, R. M. M., Keyser, U. F., Dekker, N. H. & Dekker, C. Noise in solid-state nanopores. *Proc Natl Acad Sci U S A* **105**, 417–21 (2008).

51. Smeets, R. M. M., Dekker, N. H. & Dekker, C. Low-frequency noise in solid-state nanopores. *Nanotechnology* **20**, 095501 (2009).

52. Fragasso, A., Pud, S. & Dekker, C. 1/F Noise in Solid-State Nanopores Is Governed By Access and Surface Regions. *Nanotechnology* **30**, (2019).

53. Balijepalli, A. *et al.* Quantifying short-lived events in multistate ionic current measurements. *ACS Nano* **8**, 1547–1553 (2014).

54. Charron, M., Briggs, K., King, S., Waugh, M. & Tabard-Cossa, V. Precise DNA Concentration Measurements with Nanopores by Controlled Counting. *Anal Chem* **91**, 12228–12237 (2019).

55. Meller, A. & Branton, D. Single molecule measurements of DNA transport through a nanopore. *Electrophoresis* **23**, 2583–2591 (2002).

56. Wanunu, M., Morrison, W., Rabin, Y., Grosberg, A. Y. & Meller, A. Electrostatic focusing of unlabelled DNA into nanoscale pores using a salt gradient. *Nat Nanotechnol* **5**, 160–165 (2010).

57. Grosberg, A. Y. & Rabin, Y. DNA capture into a nanopore: interplay of diffusion and electrohydrodynamics. *J Chem Phys* **133**, 165102 (2010).

58. Muthukumar, M. Mechanism of DNA Transport Through Pores. *Annu Rev Biophys Biomol Struct* **36**, 435–450 (2007).

59. Muthukumar, M. Theory of capture rate in polymer translocation. *Journal of Chemical Physics* **132**, (2010).

60. Nakane, J., Akeson, M. & Marziali, A. Evaluation of nanopores as candidates for electronic analyte detection. *Electrophoresis* **23**, 2592–2601 (2002).

61. Chen, P. *et al.* Probing Single DNA Molecule Transport Using Fabricated Nanopores. *Nano Lett* **4**, 2293–2298 (2004).

62. Rowghanian, P. & Grosberg, A. Y. Electrophoretic capture of a DNA chain into a nanopore. *Phys Rev E Stat Nonlin Soft Matter Phys* **87**, 1–8 (2013).

63. Bell, N. A. W. W., Muthukumar, M. & Keyser, U. F. Translocation frequency of double-stranded DNA through a solid-state nanopore. *Phys Rev E Stat Nonlin Soft Matter Phys* **93**, 1–10 (2016).

64. Ling, D. Y. & Ling, X. S. On the distribution of DNA translocation times in solid-state nanopores: an analysis using Schrödinger's first-passage-time theory. *J. Phys.: Condens. Matter* **25**, 375102 (2013).

65. Li, J. & Talaga, D. S. The distribution of DNA translocation times in solid-state nanopores. *J Phys Condens Matter* **22**, 454129 (2010).

66. Muthukumar, M. & Katkar, H. H. Reading nanopore clocks in single-molecule electrophoresis experiments. *Biophys J* **108**, 17–19 (2015).

67. Chen, K. *et al.* Dynamics of driven polymer transport through a nanopore. *Nat Phys* **17**, 1043–1049 (2021).

68. Saito, T. & Sakaue, T. Dynamical diagram and scaling in polymer driven translocation. *The European Physical Journal E* **34**, 135 (2011).

69. Rowghanian, P. & Grosberg, A. Y. Force-Driven Polymer Translocation through a Nanopore: An Old Problem Revisited. *J Phys Chem B* **115**, 14127–14135 (2011).

70. Sarabadani, J., Ikonen, T. & Ala-Nissila, T. Iso-flux tension propagation theory of driven polymer translocation: The role of initial configurations. *J Chem Phys* **141**, 214907 (2014).

71. Ikonen, T., Bhattacharya, A., Ala-Nissila, T. & Sung, W. Influence of pore friction on the universal aspects of driven polymer translocation. *EPL (Europhysics Letters)* **103**, 38001 (2013).

72. Ikonen, T., Bhattacharya, A., Ala-Nissila, T. & Sung, W. Unifying model of driven polymer translocation. *Phys Rev E Stat Nonlin Soft Matter Phys* **85**, 1–7 (2012).

73. Storm, A. J. *et al.* Fast DNA translocation through a solid-state nanopore. *Nano Lett* **5**, 1193–1197 (2005).

74. Briggs, K. *et al.* DNA Translocations through Nanopores under Nanoscale Preconfinement. *Nano Lett* **18**, 660–668 (2018).

75. Mihovilovic, M., Hagerty, N. & Stein, D. Statistics of DNA capture by a solid-state nanopore. *Phys Rev Lett* **110**, 1–5 (2013).

76. Kirby, B. J. *Micro- and Nanoscale Fluid Mechanics: Transport in Microfluidic Devices*. (Cambridge University Press, Cambridge, 2010). doi:DOI: 10.1017/CBO9780511760723.

77. Sinden, R. R., Pearson, C. E., Potaman, V. N. & Ussery, D. W. DNA: Structure and function. in *Advances in Genome Biology* (ed. Verma, R. S.) vol. 5 1–141 (JAI, 1998).

78. WATSON, J. D. & CRICK, F. H. C. Molecular Structure of Nucleic Acids: A Structure for Deoxyribose Nucleic Acid. *Nature* **171**, 737–738 (1953).

79. Mills, J. B. & Hagerman, P. J. Origin of the intrinsic rigidity of DNA. *Nucleic Acids Res* **32**, 4055–4059 (2004).

80. Lu, Y., Weers, B. & Stellwagen, N. C. DNA persistence length revisited. *Biopolymers* **61**, 261–275 (2001).

81. Rubinstein, M. & Colby, R. H. *Polymer Physics*. (Oxford University Press, 2003). doi:10.1093/oso/9780198520597.001.0001.

82. Nkodo, A. E. *et al.* Diffusion coefficient of DNA molecules during free solution electrophoresis. *Electrophoresis* **22**, 2424–2432 (2001).

83. Stellwagen, N. C., Gelfi, C. & Righetti, P. G. The free solution mobility of DNA. *Biopolymers* **42**, 687–703 (1997).

84. Zhou, Y., Dong, J. & Wang, Q. Fabricating higher-order functional DNA origami structures to reveal biological processes at multiple scales. *NPG Asia Materials* vol. 15 Preprint at https://doi.org/10.1038/s41427-023-00470-3 (2023).

85. Rothemund, P. W. K. Folding DNA to create nanoscale shapes and patterns. *Nature* **440**, 297–302 (2006).

86. Douglas, S. M. *et al.* Rapid prototyping of 3D DNA-origami shapes with caDNAno. *Nucleic Acids Res* **37**, 5001–5006 (2009).

87. Farahpour, F., Maleknejad, A., Varnik, F. & Ejtehadi, M. R. Chain deformation in translocation phenomena. *Soft Matter* **9**, 2750–2759 (2013).

88. Shah, A. *et al.* A Universal Approximation for Conductance Blockade in Thin Nanopore Membranes. *Nano Lett* (2023) doi:10.1021/acs.nanolett.3c04997.

89. Willmott, G. R. & Parry, B. E. T. Resistive pulse asymmetry for nanospheres passing through tunable submicron pores. *J Appl Phys* **109**, (2011).

90. Carlsen, A. T., Zahid, O. K., Ruzicka, J., Taylor, E. W. & Hall, A. R. Interpreting the conductance blockades of DNA translocations through solid-state nanopores. *ACS Nano* **8**, 4754–4760 (2014).

91. He, Y., Tsutsui, M., Scheicher, R. H., Miao, X. S. & Taniguchi, M. Salt-Gradient Approach for Regulating Capture-to-Translocation Dynamics of DNA with Nanochannel Sensors. *ACS Sens* **1**, 807–816 (2016).

92. Kowalczyk, S. W., Wells, D. B., Aksimentiev, A. & Dekker, C. Slowing down DNA translocation through a nanopore in lithium chloride. *Nano Lett* **12**, 1038–1044 (2012).

93. Zhang, H. *et al.* Slowing down DNA translocation through solid-state nanopores by pressure. *Small* **9**, 4112–4117 (2013).

94. Yeh, L. & Joo, S. W. Slowing down DNA translocation through a nanopore by lowering fluid temperature. 3458–3465 (2012) doi:10.1002/elps.201200142.

95. Rivas, F., DeAngelis, P. L., Rahbar, E. & Hall, A. R. Optimizing the sensitivity and resolution of hyaluronan analysis with solid-state nanopores. *Sci Rep* **12**, (2022).

96. Verschueren, D. V., Jonsson, M. P. & Dekker, C. Temperature dependence of DNA translocations through solid-state nanopores. *Nanotechnology* **26**, 234004 (2015).

97. Bell, N. A. W., Chen, K., Ghosal, S., Ricci, M. & Keyser, U. F. Asymmetric dynamics of DNA entering and exiting a strongly confining nanopore. *Nat Commun* **8**, 380 (2017).

98. McMullen, A., Araujo, G., Winter, M. & Stein, D. Osmotically Driven and Detected DNA Translocations. *Sci Rep* **9**, 1–10 (2019).

99. Shi, X. *et al.* Sustained unidirectional rotation of a self-organized DNA rotor on a nanopore. *Nat Phys* **18**, 1105–1111 (2022).

100. Plesa, C., Van Loo, N., Ketterer, P., Dietz, H. & Dekker, C. Velocity of DNA during translocation through a solid-state nanopore. *Nano Lett* **15**, 732–737 (2015).

101. van Dorp, S., Keyser, U. F., Dekker, N. H., Dekker, C. & Lemay, S. G. Origin of the electrophoretic force on DNA in solid-state nanopores. *Nat Phys* **5**, 347–351 (2009).

102. Keyser, U. F. *et al.* Direct force measurements on DNA in a solid-state nanopore. *Nat Phys* **2**, 473–477 (2006).

103. Bulushev, R. D., Marion, S. & Radenovic, A. Relevance of the Drag Force during Controlled Translocation of a DNA-Protein Complex through a Glass Nanocapillary. *Nano Lett* **15**, 7118–7125 (2015).

104. Bulushev, R. D. *et al.* Measurement of the position-dependent electrophoretic force on DNA in a glass nanocapillary. *Nano Lett* **14**, 6606–6613 (2014).

105. Galla, L. *et al.* Hydrodynamic slip on DNA observed by optical tweezers-controlled translocation experiments with solid-state and lipid-coated nanopores. *Nano Lett* **14**, 4176–4182 (2014).

106. Li, K. *et al.* Metrology of Individual Small Viruses. *Adv Mater Interfaces* **2300385**, 1–10 (2023).

107. Roelen, Z., Briggs, K. & Tabard-Cossa, V. Analysis of Nanopore Data: Classification Strategies for an Unbiased Curation of Single-Molecule Events from DNA Nanostructures. *ACS Sens* **8**, 2809–2823 (2023).

108. Wen, C., Zhang, Z. & Zhang, S. L. Physical Model for Rapid and Accurate Determination of Nanopore Size via Conductance Measurement. *ACS Sens* **2**, 1523–1530 (2017).

109. Frament, C. M., Bandara, N. & Dwyer, J. R. Nanopore surface coating delivers nanopore size and shape through conductance-based sizing. *ACS Appl Mater Interfaces* **5**, 9330–9337 (2013).

110. Rodríguez-Manzo, J. A., Puster, M., Nicolaï, A., Meunier, V. & Drndić, M. DNA Translocation in Nanometer Thick Silicon Nanopores. *ACS Nano* **9**, 6555–6564 (2015).

111. Charron, M., Roelen, Z., Wadhwa, D. & Tabard-Cossa, V. Pore Dimension Calculator. https://www.tcossalab.net/porecalc/ (2024).

112. Zanjani, M. B., Engelke, R. E., Lukes, J. R., Meunier, V. & Drndić, M. Up and down translocation events and electric double-layer formation inside solid-state nanopores. *Phys Rev E* **92**, 022715 (2015).

113. Jodeyri, Z. & Taghipoor, M. Multivariate analysis of nanoparticle translocation through a nanopore to improve the accuracy of resistive pulse sensing. *Physical Chemistry Chemical Physics* **26**, 5097–5105 (2024).

114. Smythe, W. R. Off-axis particles in coulter type counters. *Review of Scientific Instruments* **43**, 817–818 (1972).

115. Inge Berge, L., Jossang, T. & Feder, J. Off-axis response for particles passing through long apertures in Coulter-type counters. *Meas Sci Technol* **1**, 471–474 (1990).

116. Ying, C., Houghtaling, J. & Mayer, M. Effects of off-axis translocation through nanopores on the determination of shape and volume estimates for individual particles. *Nanotechnology* **33**, (2022).

117. Gershow, M. & Golovchenko, J. A. Recapturing and trapping single molecules with a solid-state nanopore. *Nat Nanotechnol* **2**, 775–779 (2007).

118. Don, M. The Coulter Principle: Foundation of an Industry. *JALA: Journal of the Association for Laboratory Automation* **8**, 72–81 (2003).

119. Henriquez, R. R., Ito, T., Sun, L. & Crooks, R. M. The resurgence of Coulter counting for analyzing nanoscale objects. *Analyst* vol. 129 478–482 Preprint at https://doi.org/10.1039/b404251b (2004).

120. Howorka, S. & Siwy, Z. Nanopore analytics: Sensing of single molecules. *Chem Soc Rev* **38**, 2360–2384 (2009).

121. Das, N., Ropmay, G. D., Joseph, A. M. & Roychaudhuri, C. Modeling the Effective Conductance Drop Due to a Particle in a Solid State Nanopore towards Optimized Design. *IEEE Trans Nanobioscience* **19**, 598–608 (2020).

122. Terejánszky, P., Makra, I., Fürjes, P. & Gyurcsányi, R. E. Calibration-less sizing and quantitation of polymeric nanoparticles and viruses with quartz nanopipets. *Anal Chem* **86**, 4688–4697 (2014).

123. Charron, M., Roelen, Z., Wadhwa, D. & Tabard-Cossa, V. Improved Conductance Blockage Modeling of Cylindrical Nanopores, from 2D to Thick Membranes. *Nano Lett* (2024) doi:10.1021/acs.nanolett.4c02538.

124. Yusko, E. C. *et al.* Real-time shape approximation and fingerprinting of single proteins using a nanopore. *Nat Nanotechnol* **12**, 360–367 (2017).

125. Hinkle, P. *et al.* A hybrid resistive pulse-optical detection platform for microfluidic experiments. *Sci Rep* **7**, (2017).

126. Qin, Z., Zhe, J. & Wang, G. X. Effects of particle's off-axis position, shape, orientation and entry position on resistance changes of micro Coulter counting devices. *Meas Sci Technol* **22**, (2011).

127. Ren, R. *et al.* Multiplexed detection of viral antigen and RNA using nanopore sensing and encoded molecular probes. *Nat Commun* **14**, (2023).

128. Chen, K., Zhu, J., Bošković, F. & Keyser, U. F. Nanopore-based dna hard drives for rewritable and secure data storage. *Nano Lett* **20**, 3754–3760 (2020).

129. Chen, K. *et al.* Digital Data Storage Using DNA Nanostructures and Solid-State Nanopores. *Nano Lett* **19**, 1210–1215 (2019).

130. Bošković, F. & Keyser, U. F. Nanopore microscope identifies RNA isoforms with structural colours. *Nat Chem* **14**, 1258–1264 (2022).

131. Zhu, J. *et al.* Image Encoding Using Multi-Level DNA Barcodes with Nanopore Readout. *Small* **17**, 2100711 (2021).

132. Charron, M., Roelen, Z., Wadhwa, D. & Tabard-Cossa, V. Nanopore Signal Generator. tcossalab.net/signalGenerator.

133. Schneider, G. F. *et al.* DNA translocation through graphene nanopores. *Nano Lett* **10**, 3163–3167 (2010).

134. Merchant, C. A. *et al.* DNA translocation through graphene nanopores. *Nano Lett* **10**, 2915–2921 (2010).

135. Pore, L. *et al.* Single-nanoparticle detection using a low-aspect-ratio pore. *ACS Nano* **6**, 3499–3505 (2012).

136. Liu, K. *et al.* Geometrical Effect in 2D Nanopores. *Nano Lett* **17**, 4223–4230 (2017).

137. Garaj, S., Liu, S., Golovchenko, J. A. & Branton, D. Molecule-hugging graphene nanopores. *Proc Natl Acad Sci U S A* **110**, 12192–12196 (2013).

138. Liu, K., Feng, J., Kis, A. & Radenovic, A. Atomically thin molybdenum disulfide nanopores with high sensitivity for dna translocation. *ACS Nano* **8**, 2504–2511 (2014).

139. Davenport, M. *et al.* The role of pore geometry in single nanoparticle detection. *ACS Nano* **6**, 8366–8380 (2012).

140. Roelen, Z. & Tabard-Cossa, V. Synthesis of length-tunable DNA carriers for nanopore sensing. *PLoS One* **18**, (2023).

141. Logsdon, G. A., Vollger, M. R. & Eichler, E. E. Long-read human genome sequencing and its applications. *Nat Rev Genet* **21**, 597–614 (2020).

142. Garalde, D. R. *et al.* Highly parallel direct RNA sequencing on an array of nanopores. *Nat Methods* **15**, 201–206 (2018).

143. Branton, D. *et al.* The potential and challenges of nanopore sequencing. *Nat Biotechnol* **26**, 1146–1153 (2008).

144. Chuah, K. *et al.* Nanopore blockade sensors for ultrasensitive detection of proteins in complex biological samples. *Nat Commun* **10**, (2019).

145. Sze, J. Y. Y., Ivanov, A. P., Cass, A. E. G. & Edel, J. B. Single molecule multiplexed nanopore protein screening in human serum using aptamer modified DNA carriers. *Nat Commun* **8**, 1–10 (2017).

146. Morin, T. J. *et al.* A handheld platform for target protein detection and quantification using disposable nanopore strips. *Sci Rep* **8**, 14834 (2018).

147. Varongchayakul, N., Song, J., Meller, A. & Grinstaff, M. W. Single-molecule protein sensing in a nanopore: a tutorial. *Chem Soc Rev* **47**, 8512–8524 (2018).

148. Raveendran, M., Lee, A. J., Sharma, R., Wälti, C. & Actis, P. Rational design of DNA nanostructures for single molecule biosensing. *Nat Commun* **11**, 1–9 (2020).

149. Ouldali, H. *et al.* Electrical recognition of the twenty proteinogenic amino acids using an aerolysin nanopore. *Nat Biotechnol* **38**, 176–181 (2020).

150. Nivala, J., Marks, D. B. & Akeson, M. Unfoldase-mediated protein translocation through an α-hemolysin nanopore. *Nat Biotechnol* **31**, 247–250 (2013).

151. Brinkerhoff, H., Kang, A. S. W., Liu, J., Aksimentiev, A. & Dekker, C. Multiple rereads of single proteins at single-amino acid resolution using nanopores. *Science (1979)* **374**, 1509–1513 (2021).

152. Lucas, F. L. R., Versloot, R. C. A., Yakovlieva, L., Walvoort, M. T. C. & Maglia, G. Protein identification by nanopore peptide profiling. *Nat Commun* **12**, 1–9 (2021).

153. Schmid, S., Stömmer, P., Dietz, H. & Dekker, C. Nanopore electro-osmotic trap for the label-free study of single proteins and their conformations. *Nat Nanotechnol* **16**, 1244–1250 (2021).

154. Cao, C. *et al.* Aerolysin nanopores decode digital information stored in tailored macromolecular analytes. *Sci Adv* **6**, 2–10 (2020).

155. Boukhet, M. *et al.* Translocation of Precision Polymers through Biological Nanopores. *Macromol Rapid Commun* **38**, 1–6 (2017).

156. Palyulin, V. V., Ala-Nissila, T. & Metzler, R. Polymer translocation: The first two decades and the recent diversification. *Soft Matter* **10**, 9016–9037 (2014).

157. Dubbeldam, J. L. A., Rostiashvili, V. G., Milchev, A. & Vilgis, T. A. Forced translocation of a polymer: Dynamical scaling versus molecular dynamics simulation. *Phys Rev E* **85**, 41801 (2012).

158. Ikonen, T., Bhattacharya, A., Ala-Nissila, T. & Sung, W. Influence of non-universal effects on dynamical scaling in driven polymer translocation. *J. Chem. Phys* **137**, 85101 (2012).

159. Ivica, J., Williamson, P. T. F. & de Planque, M. R. R. Salt Gradient Modulation of MicroRNA Translocation through a Biological Nanopore. *Anal Chem* **89**, 8822–8829 (2017).

160. Nova, I. C. *et al.* Investigating asymmetric salt profiles for nanopore DNA sequencing with biological porin MspA. *PLoS One* **12**, 1–14 (2017).

161. Bello, J. *et al.* Increased dwell time and occurrence of dsDNA translocation events through solid state nanopores by LiCl concentration. *Electrophoresis* **40**, 1082–1090 (2019).

162. He, Y. *et al.* Mechanism of how salt-gradient-induced charges affect the translocation of DNA molecules through a nanopore. *Biophys J* **105**, 776–782 (2013).

163. Chou, T. Enhancement of charged macromolecule capture by nanopores in a salt gradient. *Journal of Chemical Physics* **131**, (2009).

164. Jeon, B. J. & Muthukumar, M. Polymer capture by α-hemolysin pore upon salt concentration gradient. *Journal of Chemical Physics* **140**, (2014).

165. Vollmer, S. C. & De Haan, H. W. Translocation is a nonequilibrium process at all stages: Simulating the capture and translocation of a polymer by a nanopore. *Journal of Chemical Physics* **145**, (2016).

166. Seth, S. & Bhattacharya, A. How capture affects polymer translocation in a solitary nanopore. *Journal of Chemical Physics* **156**, (2022).

167. Qiao, L., Szuttor, K., Holm, C. & Slater, G. W. Ratcheting Charged Polymers through Symmetric Nanopores Using Pulsed Fields: Designing a Low Pass Filter for Concentrating Polyelectrolytes. *Nano Lett* **23**, 1343–1349 (2023).

168. Wong, C. T. A. A. & Muthukumar, M. Polymer capture by electro-osmotic flow of oppositely charged nanopores. *Journal of Chemical Physics* **126**, (2007).

169. Rankin, D. J., Bocquet, L. & Huang, D. M. Entrance effects in concentration-gradient-driven flow through an ultrathin porous membrane. *Journal of Chemical Physics* **151**, (2019).

170. Lee, C. *et al.* Osmotic flow through fully permeable nanochannels. *Phys Rev Lett* **112**, 1–5 (2014).

171. Anderson, J. Colloid Transport By Interfacial Forces. *Annu Rev Fluid Mech* **21**, 61–99 (1989).

172. Sakaue, T. Dynamics of polymer translocation: A short review with an introduction of weakly-driven regime. *Polymers (Basel)* **8**, 1–12 (2016).

173. Meller, A., Nivon, L. & Branton, D. Voltage-driven DNA translocations through a nanopore. *Phys Rev Lett* **86**, 3435–3438 (2001).

174. Tanaka, K. & Reita Tamamushi. A Physico-chemical Study of Concentrated Aqueous Solutions of Lithium Chloride. *Zeitschrift für Naturforschung A* **8**, 55 (1991).

175. He, L., Karau, P. & Tabard-Cossa, V. Fast capture and multiplexed detection of short multi-arm DNA stars in solid-state nanopores. *Nanoscale* **11**, 16342–16350 (2019).

176. Sarabadani, J. *et al.* Driven translocation of a semi-flexible polymer through a nanopore. *Sci Rep* **7**, 1–8 (2017).

177. Lu, B., Albertorio, F., Hoogerheide, D. P. & Golovchenko, J. A. Origins and consequences of velocity fluctuations during DNA passage through a nanopore. *Biophys J* **101**, 70–79 (2011).

178. de Haan, H. W., Sean, D. & Slater, G. W. Reducing the variance in the translocation times by prestretching the polymer. *Phys Rev E* **98**, 22501 (2018).

179. Sean, D., de Haan, H. W. & Slater, G. W. Translocation of a polymer through a nanopore starting from a confining nanotube. *Electrophoresis* **36**, 682–691 (2015).

180. Bandara, Y. M. N. D. Y., Karawdeniya, B. I., Hagan, J. T., Chevalier, R. B. & Dwyer, J. R. Chemically Functionalizing Controlled Dielectric Breakdown Silicon Nitride Nanopores by Direct Photohydrosilylation. *ACS Appl Mater Interfaces* **11**, 30411–30420 (2019).

181. Eggenberger, O. M., Ying, C. & Mayer, M. Surface coatings for solid-state nanopores. *Nanoscale* **11**, 19636–19657 (2019).

182. Lin, C.-Y. *et al.* Modulation of Charge Density and Charge Polarity of Nanopore Wall by Salt Gradient and Voltage. *ACS Nano* **13**, 9868–9879 (2019).

183. Firnkes, M. *et al.* Electrically facilitated translocations of proteins through silicon nitride nanopores: conjoint and competitive action of diffusion, electrophoresis, and electroosmosis. *Nano Lett* **10**, 2162–2167 (2010).

184. Forstater, J. H. J. H. *et al.* MOSAIC: A modular single-molecule analysis interface for decoding multistate nanopore data. *Anal Chem* **88**, 11900–11907 (2016).

185. Wang, X. & Seeman, N. C. Assembly and characterization of 8-arm and 12-arm DNA branched junctions. *J Am Chem Soc* **129**, 8169–8176 (2007).

186. Sarabadani, J. & Ala-Nissila, T. Theory of pore-driven and end-pulled polymer translocation dynamics through a nanopore: an overview. *Journal of Physics: Condensed Matter* **30**, 274002 (2018).

187. Fologea, D., Uplinger, J., Thomas, B. & Mcnabb, D. S. Slowing DNA Translocation in a Solid-State Nanopore. 20–23 (2005) doi:10.1021/nl051063o.

188. Charron, M., Philipp, L., He, L. & Tabard-Cossa, V. Elucidating the dynamics of polymer transport through nanopores using asymmetric salt concentrations. *Nano Res* (2022) doi:10.1007/s12274-022-4886-3.

189. Wanunu, M., Sutin, J., McNally, B., Chow, A. & Meller, A. DNA translocation governed by interactions with solid-state nanopores. *Biophys J* **95**, 4716–4725 (2008).

190. He, L. *et al.* DNA origami characterized via a solid-state nanopore: insights into nanostructure dimensions, rigidity and yield. *Nanoscale* **15**, 14043–14054 (2023).

191. Doi, M., Edwards, S. F. & Edwards, S. F. *The Theory of Polymer Dynamics*. (Clarendon Press, 1988).

192. Tree, D. R., Muralidhar, A., Doyle, P. S. & Dorfman, K. D. Is DNA a good model polymer? *Macromolecules* **46**, 8369–8382 (2013).

193. Sandler, S. E. *et al.* Sensing the DNA-mismatch tolerance of catalytically inactive Cas9 via barcoded DNA nanostructures in solid-state nanopores. *Nat Biomed Eng* **8**, 325–334 (2024).

194. Seeman, N. C. Nucleic acid junctions and lattices. *J Theor Biol* **99**, 237–247 (1982).

195. Dey, S. *et al.* DNA origami. *Nature Reviews Methods Primers 2021 1:1* **1**, 1–24 (2021).

196. Seeman, N. C. & Sleiman, H. F. DNA nanotechnology. *Nat Rev Mater* **3**, 1–23 (2017).

197. Ke, Y., Ong, L. L., Shih, W. M. & Yin, P. Three-dimensional structures self-assembled from DNA bricks. *Science (1979)* **338**, 1177–1183 (2012).

198. Wintersinger, C. M. *et al.* Multi-micron crisscross structures grown from DNA-origami slats. *Nat Nanotechnol* 1–9 (2022) doi:10.1038/s41565-022-01283-1.

199. Douglas, S. M., Chou, J. J. & Shih, W. M. DNA-nanotube-induced alignment of membrane proteins for NMR structure determination. *Proc Natl Acad Sci U S A* **104**, 6644–6648 (2007).

200. Liedl, T., Högberg, B., Tytell, J., Ingber, D. E. & Shih, W. M. Self-assembly of three-dimensional prestressed tensegrity structures from DNA. *Nature Nanotechnology 2010 5:7* **5**, 520–524 (2010).

201. Gu, H., Yang, W. & Seeman, N. C. DNA scissors device used to measure mutS binding to dna mis-pairs. *J Am Chem Soc* **132**, 4352–4357 (2010).

202. Andersen, E. S. *et al.* Self-assembly of a nanoscale DNA box with a controllable lid. *Nature 2009 459:7243* **459**, 73–76 (2009).

203. Chhabra, R., Sharma, J., Liu, Y. & Yan, H. Addressable molecular tweezers for DNA-templated coupling reactions. *Nano Lett* **6**, 978–983 (2006).

204. Li, S. *et al.* A DNA nanorobot functions as a cancer therapeutic in response to a molecular trigger in vivo. *Nature Biotechnology 2018 36:3* **36**, 258–264 (2018).

205. Hansen, C. H., Yang, D., Koussa, M. A. & Wong, W. P. Nanoswitch-linked immunosorbent assay (NLISA) for fast, sensitive, and specific protein detection. *Proc Natl Acad Sci U S A* **114**, 10367–10372 (2017).

206. Shrestha, P. *et al.* Single-molecule mechanical fingerprinting with DNA nanoswitch calipers. *Nature Nanotechnology 2021 16:12* **16**, 1362–1370 (2021).

207. Mathur, D. & Medintz, I. L. Analyzing DNA Nanotechnology: A Call to Arms for the Analytical Chemistry Community. *Anal Chem* **89**, 2646–2663 (2017).

208. Woeste, S. & Demchick, P. New version of the negative stain. *Appl Environ Microbiol* **57**, 1858–1859 (1991).

209. De Carlo, S. & Harris, J. R. Negative staining and cryo-negative staining of macromolecules and viruses for TEM. *Micron* **42**, 117–131 (2011).

210. Stirling, J. W., Curry, Alan. & Eyden, Brian. *Diagnostic Electron Microscopy : A Practical Guide to Tissue Preparation and Interpretation*. (John Wiley & Sons, 2013).

211. Harris, J. R. & De Carlo, S. Negative Staining and Cryo-negative Staining: Applications in Biology and Medicine. *Methods in Molecular Biology* **1117**, 215–258 (2014).

212. Douglas, S. M. *et al.* Self-assembly of DNA into nanoscale three-dimensional shapes. *Nature* **459**, 414–418 (2009).

213. Castro, C. E. *et al.* A primer to scaffolded DNA origami. *Nature Methods 2011 8:3* **8**, 221–229 (2011).

214. Dietz, H., Douglas, S. M. & Shih, W. M. Folding DNA into twisted and curved nanoscale shapes. *Science (1979)* **325**, 725–730 (2009).

215. Alibakhshi, M. A. *et al.* Picomolar Fingerprinting of Nucleic Acid Nanoparticles Using Solid-State Nanopores. *ACS Nano* **11**, 9701–9710 (2017).

216. Beamish, E., Tabard-Cossa, V. & Godin, M. Identifying Structure in Short DNA Scaffolds Using Solid-State Nanopores. *ACS Sens* **2**, 1814–1820 (2017).

217. Confederat, S., Sandei, I., Mohanan, G., Wälti, C. & Actis, P. Nanopore fingerprinting of supramolecular DNA nanostructures. *Biophys J* **121**, 4882–4891 (2022).

218. He, L. *et al.* Digital immunoassay for biomarker concentration quantification using solid-state nanopores. *Nature Communications 2021 12:1* **12**, 1–11 (2021).

219. Beamish, E., Tabard-Cossa, V. & Godin, M. Digital counting of nucleic acid targets using solid-state nanopores. *Nanoscale* **12**, 17833–17840 (2020).

220. Beamish, E., Tabard-Cossa, V. & Godin, M. Programmable DNA Nanoswitch Sensing with Solid-State Nanopores. *ACS Sens* **4**, 2458–2464 (2019).

221. Hernández-Ainsa, S. *et al.* DNA origami nanopores for controlling DNA translocation. *ACS Nano* **7**, 6024–6030 (2013).

222. Briggs, K., Bouhamidi, M. Y., He, L. & Tabard-Cossa, V. Efficient Simulation of Arbitrary Multicomponent First-Order Binding Kinetics for Improved Assay Design and Molecular Assembly. *ACS Measurement Science Au* **2**, 139–146 (2021).

223. Doricchi, A. *et al.* Emerging Approaches to DNA Data Storage: Challenges and Prospects. *ACS Nano* **16**, 17552–17571 (2022).

224. Kundukad, B., Yan, J. & Doyle, P. S. Effect of YOYO-1 on the mechanical properties of DNA. *Soft Matter* **10**, 9721–9728 (2014).

225. Japaridze, A., Benke, A., Renevey, S., Benadiba, C. & Dietler, G. Influence of DNA binding dyes on bare DNA structure studied with atomic force microscopy. *Macromolecules* **48**, 1860–1865 (2015).

226. Kowalczyk, S. W. & Dekker, C. Measurement of the docking time of a DNA molecule onto a solid-state nanopore. *Nano Lett* **12**, 4159–4163 (2012).

227. McMullen, A., De Haan, H. W., Tang, J. X. & Stein, D. Stiff filamentous virus translocations through solid-state nanopores. *Nature Communications 2014 5:1* **5**, 1–10 (2014).

228. Lee, C., Kim, K. S., Kim, Y. J., Lee, J. Y. & Kim, D. N. Tailoring the Mechanical Stiffness of DNA Nanostructures Using Engineered Defects. *ACS Nano* **13**, 8329–8336 (2019).

229. Penth, M., Schellnhuber, K., Bennewitz, R. & Blass, J. Nanomechanics of self-assembled DNA building blocks. *Nanoscale* **13**, 9371–9380 (2021).

230. Afrasiabian, N. & Denniston, C. The journey of a single polymer chain to a nanopore. *Soft Matter* **16**, 9101–9112 (2020).

231. Qiao, L. & Slater, G. W. Capture of rod-like molecules by a nanopore: Defining an 'orientational capture radius'. *Journal of Chemical Physics* **152**, (2020).

232. Qiao, L. & Slater, G. W. Capture and translocation of a rod-like molecule by a nanopore: orientation, charge distribution and hydrodynamics. *Physical Chemistry Chemical Physics* **24**, 6444–6452 (2022).

233. Dorfman, K. D. DNA electrophoresis in microfabricated devices. *Rev Mod Phys* **82**, 2903–2947 (2010).

234. Chrambach, A. & Rodbard, D. Polyacrylamide Gel Electrophoresis. *Science (1979)* **172**, 440–451 (1971).

235. He, L. *et al.* Digital Immunoassay Protocol for Solid-State Nanopore Sensing. *Protoc Exch* (2021).

236. Carlsen, A. T., Briggs, K., Hall, A. R. & Tabard-Cossa, V. Solid-state nanopore localization by controlled breakdown of selectively thinned membranes. *Nanotechnology* **28**, 085304 (2017).

237. Briggs, K. CUSUM v3.3.3 Nanopore Analysis Software Suite. (2020) doi:10.5281/zenodo.595675.

238. Wu, H. *et al.* Translocation of Rigid Rod-Shaped Virus through Various Solid-State Nanopores. *Anal Chem* **88**, 2502–2510 (2016).

239. Awasthi, S., Ying, C., Li, J. & Mayer, M. Simultaneous Determination of the Size and Shape of Single α-Synuclein Oligomers in Solution. *ACS Nano* **17**, 12325–12335 (2023).

240. Yusko, E. C. *et al.* Controlling protein translocation through nanopores with bio-inspired fluid walls. *Nat Nanotechnol* **6**, 253–260 (2011).